Integration and Characterisation of Superconducting thin films and high spin orbit coupling InSb 2DEGs

Thomas Patrick Robinson

A Thesis submitted for the purposes of a
Doctor of Philosophy.

29/06/2023

Abstract:

One theoretical route towards fault proof quantum computing is the realisation of Majorana Zero Modes (MZMs) at the ends of $InSb$ nanowires coupled to conventional s-wave superconductors. The high spin-orbit coupling within the $InSb$ is predicted to result in a proximity superconducting state that exhibits elements of $p_x + ip_y$ superconducting pairing, which required to support a topological state hosting MZMs. Nanowire devices initially showed promise, however material concerns and analytical complications have led to several notable retractions. Additionally, direct experimental evidence of the necessary $p_x + ip_y$ superconduting state remains under debate.

This thesis explores an alternate material approach towards the same end - high mobility $InSb$ two-dimensional electron gases (2DEGs). $InSb$ 2DEGs with additional electrical confinement via gating are relatively underexplored scalable alternative. The top-down integration of high-quality superconducting films and characterisation of the size, quality, temperature and field dependence of the resulting proximity induced state is requisite for this. A series of $300 \times 600 \mu m$ Nb contacts on an InSb 2DEG with increasing spacings were fabricated. Gap sizes spanned the range $1.5 - 8\mu m$, comparable to the ballistic length of the 2DEGs. Measurement with both AC and DC measurement techniques observed a conductance dip, supressed as a function of temperature, with a $T_c \approx 7.5K$, in agreement with our Nb. A dip was seen in all gaps up to and including $8\mu m$. These features were found to be consistent with the BTK theory for a SN junction with a high degree of interfacial roughness, and a large proportion of interfacial scattering. Proximity superconductivity extending across such a long junction is indicative of successful induction of superconductivity with the 2DEG layer via top-down films, despite poor interfacial quality.

Subsequent magnetic field measurements result in an alteration on the conductance spectra, that persisted after the removal of the field. Thermal cycling to T_{room} was required to change this alteration. This behaviour, and the required temperature range is believed to be indicative of field induced alteration of trapped charge states at the SN interface.

This work presents low energy muon spin relaxation measurements on a superconductor/high spin orbit coupling $InSb$ 2DEG for the first time. Measurements on $50nm\ Nb$ film deposited on an $InSb$ 2DEG failed due to defects within the Nb precluding measurement of Meissner screening and showed no evidence of proximity induction. Measurements of a $50nm\ Pb/InSb$ with a modified 2DEG structure showed Meissner screening extending deep within the sample, well into the $InSb$ layers. This was indicative of successful proximity induction via a second superconducting film. This screening profile was supressed by the application of a higher field. Secondary measurements and subsequent analysis indicate this suppression was a direct response to the magnitude of the applied field, and distinct from the field induced alteration seen in the electrical measurements. Such a suppression is possible evidence of $p_x + ip_y$ superconducting elements, however this work cannot fully resolve that from other possible elements. Despite this, evidence of successful induction of proximity superconductivity with two different SC films opens many immediate directions for further analysis and material improvements for similar devices.

Table of Contents

List Of Figures:

List of Symbols and common abbreviations:

Symbol	Definition
$\hat{a}_m^\dagger$	Fermionic Creation Operator
$\hat{a}_n$	Fermionic Annihilation Operator
t	Nanowire 'hopping' potential
μ	Chemical potential
Δ	Superconducting energy gap
γ_{2n} and γ_{2n-1}	Majorana Operators
δ_{nm}	Kronecker Delta function
$|0\rangle$ and $|1\rangle$	Bra-Ket notation for unoccupied and occupied states
MZM	Majorana Zero Mode
SOC	Spin-Orbit Coupling
$\boldsymbol{a_1, a_2}$ and $\boldsymbol{a_3}$	Lattice translation vectors.
$\boldsymbol{b_1, b_2, b_3}$.	Reciprocal lattice vector
FCC	Face-Centred Cubic structure
$\hbar$	Reduced Planck Constant
m_e	Electron mass
$u_{\boldsymbol{k}}(\boldsymbol{r})$	Periodic potential for Bloch's theorem
E_f	Fermi Energy
E_g	Semiconductor Band Gap
m^*	Effective mass of charge carriers
Γ, X, W, L	Brilloin Zone locations
Δ_{SO}	Spin-Orbit band splitting
$D_{3D}(E)$	3D Density of States
μ_n	Carrier mobility
n, p	Carrier concentration for electrons, holes
q	Carrier charge

τ_c	Mean free scattering time
v_d	Carrier drift velocity
l_c	Carrier mean free path length
$D_{2D}(E)$	2D Density of States
2DEG	Two-Dimensional electron gas
n_i, p_i	Intrinsic carrier concentrations for electrons, holes
g_e	Electron g-factor
μ_B	Bohr Magneton
$\sigma_x, \sigma_y, \sigma_z$	Pauli Spin matricies
$\boldsymbol{\sigma} = \boldsymbol{x}\sigma_x + \boldsymbol{y}\sigma_y + \boldsymbol{z}\sigma_z$	Pauli spin vector
α_k	Rashba coefficient
n_s	Superconducting carrier number density
ε_o	Vacuum permittivity
$\mathbf{B}$	Magnetic field
$\boldsymbol{E}$	Electric field
μ_o	Vacuum permeability
$\boldsymbol{j}$	Supercurrent density
λ_L	London Penetration Depth
$\boldsymbol{A}$	Magnetic vector potential
T_c	Critical Temperature of Superconductor
ξ_N, ξ_S	Coherence Length (Normal, Superconducting)
H_c	Critical Magnetic Field (Type I Superconductor)
H_{c1}, H_{c2}	Upper and Lower Critical Magnetic fields (Type II Superconductor)
κ	Ginzburg-Landau Ratio
$c_{k\sigma}^\dagger$	Bogoluibov creation operator for quasiparticle of moment $\boldsymbol{k}$ and spin, σ
$c_{k\sigma}^\dagger$	Bogoluibov creation operator for quasiparticle of moment $\boldsymbol{k}$ and spin, σ

$V_{kk'}$	Interaction potential
Δ_k, Δ	Superconducting energy gap
k_b	Boltzmann Constant
Δ_{prox}	Proximity induced superconducting energy gap
$\lambda_{prox}.$	Proximity induction length.
v_f	Fermi velocity
E_{th}	Thouless energy
BTK	Blonder-Tinkham- Klapwjik
$A(E), B(E), C(E), D(E)$	BTK coefficients
Z	Dimensionless BTK Barrier height
G_o	Normal state conductance
R_N	Normal state resistance
ICP	Inductively Coupled Plasma
RIE	Reactive Ion Etching
MBE	Molecular Beam Epitaxy
TLM	Transition Line Measurement
SC	Superconductor
R_s	Sheet Resistance
R_c	Contact Resistance
n_{sheet}	Sheet carrier concentration
G	Conductance
Γ	Dynes scattering term
π^+	Pion
μ^+	Positive Muon
v_μ	Muon neutrino
μSR	Muon spin relaxation, resonance or rotation
γ_μ	Muon Gyromagnetic Ratio
$P(t)$	Muon polarisation function
σ	Depolarisation rate

P_o	Initial polarisation
$A(t)$	Muon Asymmetry Function
ZF	Zero Field
$LE - \mu SR$	Low energy μSR
ϕ_o	Magnetic flux quanta
χ'	Magnetic susceptibility
A_o	Initial Asymmetry
r_{rms}	Root mean squared surface roughness

Acknowledgements

To begin, we first must see the end. I find it strange to be here, finally after so much time and effort. It is no small thing to call this the most involved, challenging and the most rewarding experience of my life so far. And there are many, perhaps even too many, people that I wish to thank as part of it.

Next, I thank my peers here at Cardiff through the years. Thanks to Amber and Jess, both as office mates, and for the assistance with my Masters all those years ago. My extended group through the years, George, George, Dave, Andrea, Sam, James, Jake and Ffion – in many respects I wish I'd gotten more of a chance to work with you all. I also thank those in my cohort, who helped make those early days less intimidating, Ali, Virginia and Gerwyn. Special thanks to Gerwyn for putting up with me as a housemate for that first year as well. And the as yet unmentioned academic staff for the conversations, advice, and assistance they have given over the years in no particular order, I thank Daryl Beggs, Dave Westwood, Emyr MacDonald, Sam Ladak, Chris Dunscombe, Matt Smith and Sara Gillgrass.

Words cannot express enough gratitude to my supervisory team. Phil, for giving me the chance for this, for all the practical advice I still use and your eternally cheery manner. You are dearly missed. Craig – Your help with easing that transition, the constant expertise and advice with fabrication and measurements. Thanks for the patience, for saving multiple near failed experiments, and for always finding time. Sean – it's not uncharitable to say this work wouldn't have been finished without you stepping in. I know taking over from Phil was not easy, (and I probably didn't help!) but you were a fantastic supervisor. You have constantly gone above and beyond for this, and you have made me a better researcher as a result. I won't say working with you has always been fun or even pleasant, but I have gained more skills and knowledge than I would've thought possible going in.

Moving to the more personal acknowledgements, I thank all the staff at Little Man Coffee Shop over the years. It was my home away from home, and my true office. There are more of you than I can name, but Seb, Dylan, Beth, Cole, Tim, Dom, Izzy, Corrie, Connor, Brandon, Connor, Heide, and of course Sophie Dally, I thank you all. For the coffee, the conversations, and the friendships. Many good nights, and many long working days that you made all the easier.

I thank my family. My Mum and Dad for always being there when needed and have been unconditional and unwavering in their support and belief. My brother, Joe, his wife and children – Whilst I have not been able to see you and them as much as I wished, they have been bundles of joy all the same, and the rest of my extended

family. I give a special mention to Alf and my Grandad, though they are not here to see the end of this, I know would've been chuffed to be mentioned.

Most importantly, I thank those closest to me, without whom I am sure I would've left long before finishing this. Julie - for 4 years of being the best, albeit bananas, housemate I could've have had. You made home truly feel homely. Lotte - a literal decade of friendship, of general silliness and madness, and of out of the blue gifts at the perfect time. There are too many little moments to list. Clara - sorry for locking you in the lab and breaking your Mac-book – Hopefully I've made up for that at this point. Oh, and you know the day-to-day annoyance, emotional support and all else that comes with friendship. Work would not have, been the same without you. Finally, Tristan and Megan – without you both, I would not have started down this road to begin with. Hours of conversation, of wild tales, of moments of genius, of laughing till my stomach hurts. And of mornings watching the sunrise. To all of you, I cannot thank you enough, I love you all very dearly.

"The glory of the heavens was ever beyond the grasp of those who never thought to reach for it. But if I have gained anything from all of this, it is the courage to stretch out my hand."

Natsuko Ishikawa - 2019

Chapter 1: Context and Introduction:

1.1: The Kitaev Chain, topology and material requirements.

Amongst many different fields there is a strong research focus towards Quantum Computing [1] [2]. Although quantum computers exist currently, they are limited in scale, and the field is far from creating practical commercial devices [2]. To form the basis for practical application, it must be possible to produce Qubit arrays that are both large, and thus scalable, as well fault proof, allowing the reliable storage of information free of decoherence and interactions with the outside world. The choice of Qubit is often the limiting factor [1] [2]. One such proposed Qubit to circumvent the issues is the Majorana Zero Mode, or MZM [3].

MZMs are spinless, massless and chargeless quasiparticles locatable at the ends of topological superconducting wires. The idea of a Majorana particle originated from the works of Ettore Majorana in 1937 [4]. His work, an alternative representative basis of the Dirac equation, argued that an additional class of massive fermion should exist – A chargeless, spin-half particle that was its own anti-particle, or charge conjugate. Although at the time of writing, no detected particle obeys this relation, the idea of a particle being its own charge conjugate found a place in theoretical condensed matter physics.

Motivated by a desire to search for a suitable foundation for error free quantum computing, Alexi Kitaev created a toy model [5]. He theoretically constructed, a spin-less semiconductor nanowire as a chain of N electron sites. A superconductor is in contact with the surface such that superconductivity will be induced in the nanowire via the proximity effect. To describe and manipulate this system, we use fermionic creation and annihilation operators, $a^\dagger$ and a.

These obey the following relations:

$$\hat{a}_m^\dagger \hat{a}_n + \hat{a}_n \hat{a}_m^\dagger = \left[\hat{a}_m^\dagger, \hat{a}_n\right]_+ = \delta_{nm}$$

$$\hat{a}|0\rangle = 0 \qquad\qquad \hat{a}^\dagger|1\rangle = 0$$

$$\hat{a}|1\rangle = |0\rangle \qquad\qquad \hat{a}^\dagger|0\rangle = |1\rangle$$

A particle can be added to an empty state $|0\rangle$, but not an occupied state, and a particle can be removed from an occupied state, but not an empty one. Exchanging the positions of any two particles will cause the system to accumulate a phase of -1. Additionally, there exists a number operator, N, defined as $N = a_n^\dagger a_n$, that serves to 'count' the number of particles in a state. For fermionic system like Kitaev's, this means it will act on the states $|0\rangle$ and $|1\rangle$ to give values of 0 or 1 respectively.

Kitaev described his chain as follows by

$$H = \sum_n -t\left(a_n^\dagger a_{n+1} + a_{n+1}^\dagger a_n\right) + \mu\left(a_n^\dagger a_n + \frac{1}{2}\right) + \Delta a_n a_{n+1} \qquad (1.1)$$
$$+ \Delta^* a_n^\dagger a_{n+1}^\dagger$$

Where μ is the chemical potential in the wire, Δ is the superconducting gap, Δ^* is it's complex conjugate, and t is the hopping potential, an energy associated with an electron moving an adjacent unoccupied site in the chain. n is an integer number in the range $j = 1, 2 \dots N$, noting the nth site in the chain. Each of the terms carries meaning corresponding to physical interactions in the chain. The first term represents the energy cost associated with moving a particle from one site in the chain to its nearest neighbour site. The second represents the total energy of the wire in the absence of other phenomena, taking the form of the Hamiltonian for a chain of harmonic oscillators. The final two terms represent the superconductivity, pairing two adjacent particles that can be added or removed in said pairs only.

Kitaev's argument involved replacing the fermionic operators a and $a^\dagger$ with a superposition of two other operators:

$$\hat{a}_n^\dagger = \gamma_{2n-1} + i\gamma_{2n}$$

$$\hat{a}_n = \gamma_{2n-1} - i\gamma_{2n}$$

Each possible fermionic site, whether empty or occupied, could be resolved as a superposition of a pair of other sites. These operators can be rearranged to give γ in terms of fermion operators:

$$\gamma_{2n} = -i(a_n - a_n^\dagger) \tag{1.2a}$$

$$\gamma_{2n-1} = a_n + a_n^\dagger \tag{1.2b}$$

This γ operators can be easily shown to be invariant under charge conjugation. They are, as far as the idea can be transferred across to Condensed Matter Physics, their own anti-particle. Additionally, these operators anti-commute. These conditions are described by:

$$\gamma_n^\dagger = \gamma_n$$

$$\hat{\gamma}_m\hat{\gamma}_n + \hat{\gamma}_n\hat{\gamma}_m = [\hat{\gamma}_m, \hat{\gamma}_n]_+ = 2\delta_{nm}$$

The combination of these two conditions were sufficient for Kitaev to label these as so called Majorana Operators. Furthermore, these Majorana operators can be shown to obey unusual particle statistics. If we act twice on the ground state $|0\rangle$ with (1.2b)

$$\gamma_{2n-1}\gamma_{2n-1}|0\rangle = \gamma_{2n-1}^\dagger(a_n + a_n^\dagger)|0\rangle$$

$$= (a_n + a_n^\dagger)|1\rangle + 0$$

$$= |0\rangle$$

Acting twice with a γ_{2n-1} on a state returned the initial state. This behaviour is also true of γ_{2n}, and the complex conjugate of both operators. This is in contrast with the behaviour of both Fermion and Boson operators. A fermi operator acting on $|0\rangle$ twice would give 0, as the pauli exclusion principle forbids two particles sharing the same state. A bose operator would give $|2\rangle$ up to a some constant. Since operator behaviour

is in part informed by the particle statistics, this suggested that the particles these operators describe obey neither Fermi-Dirac statistics, nor Bose-Einstein statistics. They are instead predicted to be a so called anyon, obeying non-Abelian particle statistics [6] [7]

Substituting our operators from (1.2a) and (1.2b) into (1.1) gives

$$H = \frac{i}{2} \sum_n \mu(\gamma_{2n-1}\gamma_{2n}) \, (t + |\Delta|)\gamma_{2n}\gamma_{2n+1}$$

$$+ (-t + |\Delta|)\gamma_{2n-1}\gamma_{2n+2}$$

(1.3)

whereas before there were N electron sites, we now have 2N Majorana sites. The summation now occurs between $n = 1, 2, \ldots, N$. This can be considered in two limits. The first sets $t = |\Delta| = 0, \mu < 0$ to give:

$$H = -\frac{i}{2} \sum_n \mu(\gamma_{2n-1}\gamma_{2n}) = -\sum_n \mu \left(a_n^\dagger a_n + \frac{1}{2} \right)$$

(1.4a)

The superconducting gap is closed, particle motion across the chain is supressed, and all that is left, unsurprisingly, is the terms describing a normal nanowire. The substitution of fermion operators for Majorana operators offers no new physics in this limit and is instead an unnecessary mathematical complication. The second limit is the case of $\mu = 0, |\Delta| = t > 0$. This leads to:

$$H = it \sum_n \gamma_{2n}\gamma_{2n+1} = -2t \sum_{n=1}^{N-1} \left(\widetilde{a_n}^\dagger \widetilde{a_n} + \frac{1}{2} \right)$$

(1.4b)

where $\widetilde{a_n} = \gamma_{2n} + i\gamma_{2n+1}$. If a fermion can be described as a composite of two coupled Majorana's, this limit serves to adjust which Majorana's couple to constitute a fermion. Note the indices in the summation. Two of the Majorana operators have vanished from

the Hamiltonian, γ_1 and γ_{2N}. These two configurations (1.4a) and (1.4b) are visualised in Figure 1 below:
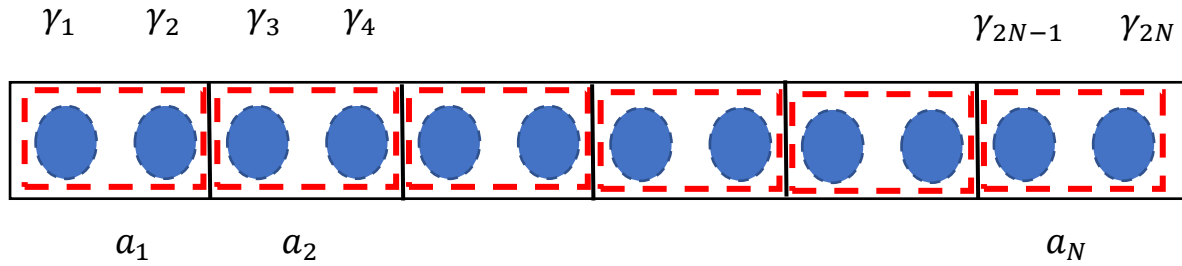
Figure 1: Visualisation of (1.4a). Blue dots indicate Majorana sites. Black rectangles indicate the original fermion site in the chain. Red dotted line indicates the Majorana pairing corresponding to a fermion in the chain.
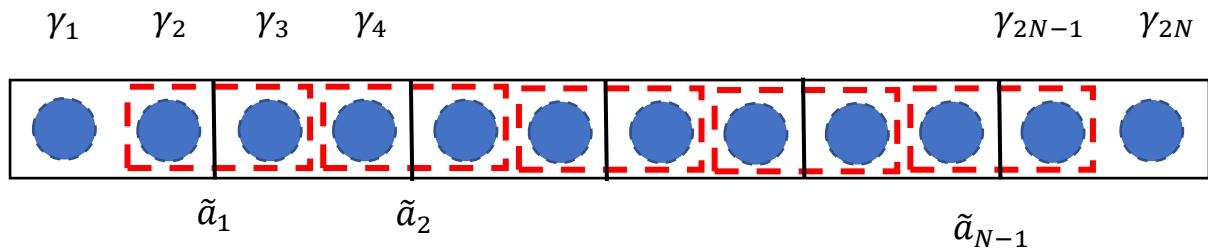
Figure 2: Visualisation of (1.4b). Features are as labelled above. Note the pairing, now instead of pairing along one state, Majorana's now pair across sites. This leads to two unpaired sites either end of the chain. The unpaired Majorana's are Majorana Zero Modes.

The missing Majorana's in (1.4b) correspond to either end of the chain visualised in Figure 2. The total energy of the system in this phase must no longer depend upon them. The Majorana's occupying them are thus required to be zero energy states. These zero energy edge states are the MZMs. Further analysis by Kitaev showed that these states should exist up to the limit $2|t| > |\mu|$ for $\Delta \neq 0$. If $2|t| < |\mu|$, then the orientation in Figure 1 exists, and no MZMs will be present.

Kitaev also suggested that because the Majorana's are located at either end of the chain, they are protected from interacting by a tunnelling probability that decreases exponentially through the wire. He reasoned this would protect them from many sorts of quantum computational errors [5]. For instance, increasing the length of the wire would decrease the likelihood of the states interacting with the outside environment,

as it would be required to interact with both ends of the chain. Additionally, the as mentioned unusual particle statistics allow MZMs to function as qubit, via successive exchanges of MZMs in nanowire networks [3] [8]. This process is known as braiding [9]

1.2 Experimental realisation of MZMs:

The Kitaev Model suggested the existences of MZMs. It gave a simplified platform for realising them, and it offered some potential experimental signatures to detect them. However, the initial idea of the chain was un-physical to fabricate in a real device. The Kitaev model was spinless and as a result exhibited a specific type of superconducting pairing $p_x + ip_y$ p-wave pairing. P-wave superconductors are not abundant in nature, and spinless p-wave superconductivity is absent entirely [10] [11]. This was an issue, as the presence of spin allowed for the possibility of degenerate Majorana edge states. It was however, found that via the right combination of broken symmetries one could replicate this superconducting state [12]. A quick succession of 2010 papers showed that a semiconductor nanowire with high spin-orbit coupling, proximity-induced with conventional s-wave superconductivity, and undergoing Zeeman splitting could host Majorana's [13] [14] [15] [16]. The s-wave superconductivity in combination with spin orbit coupling induced the necessary superconducting energy gap, allowing for the formation of a triplet $p_x + ip_y$ state. The Zeeman effect broke time-reversal symmetry, lifting Kramer's degeneracy. This combination suggested that detection possibilities existed in relatively simple to fabricate experimental set-ups. The final proposal required only a thin film of s-wave superconductor deposited on a nanowire [17].
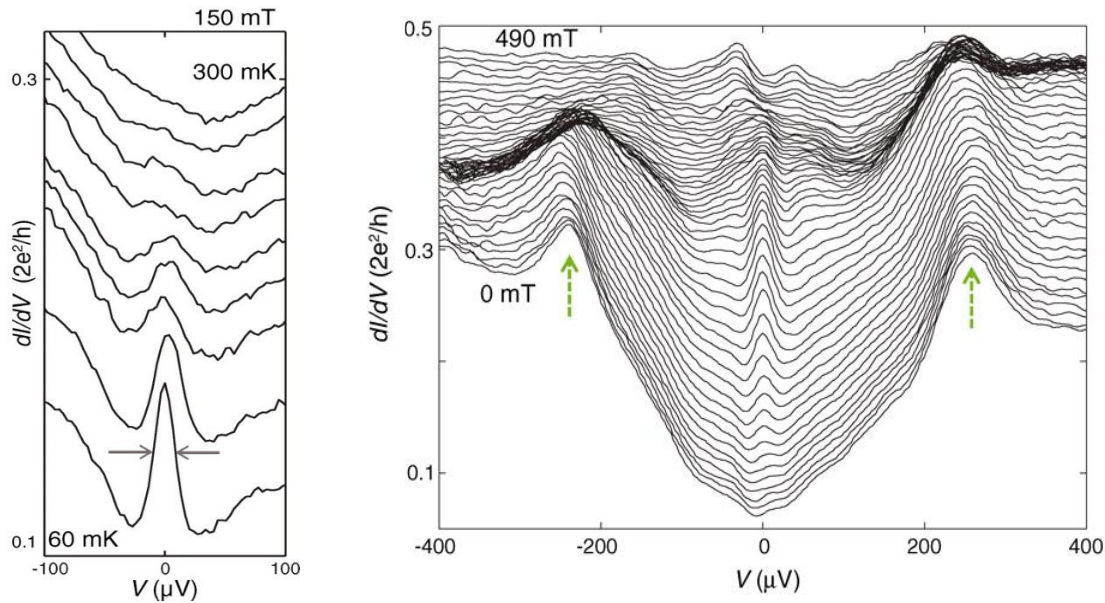
Figure 3: Experimental results from Delft [18]. Left) Conduction measurements as a function of applied fate voltage of increasing temperatures at constant finite field, B=150mT. (Right) Conduction measurements as a function of applied gate voltage of increasing B-field at constant finite temperature, T=70mK. In both cases, traces are offset from the lower most example for the sake of clarity.

A version of this device design was then used by a group at TU Delft in 2012, where they reported possible signatures of Majorana's [18]. They fabricated a gated InSb nanowire, in contact with two electrodes. One was gold, and the other superconducting NbTiN. Measurements of conductance, G, as a function of gate voltage were performed for varying temperatures and applied magnetic fields. Figure 3 shows the key result a zero-bias peak appearing at finite fields. The peak remained at zero bias as magnetic field increased before vanishing at high field. The peak amplitude rapidly decayed away as temperature increased. They deemed such observations inconsistent with other possible topologically trivial zero-bias effects, such as Andreev Bound States.
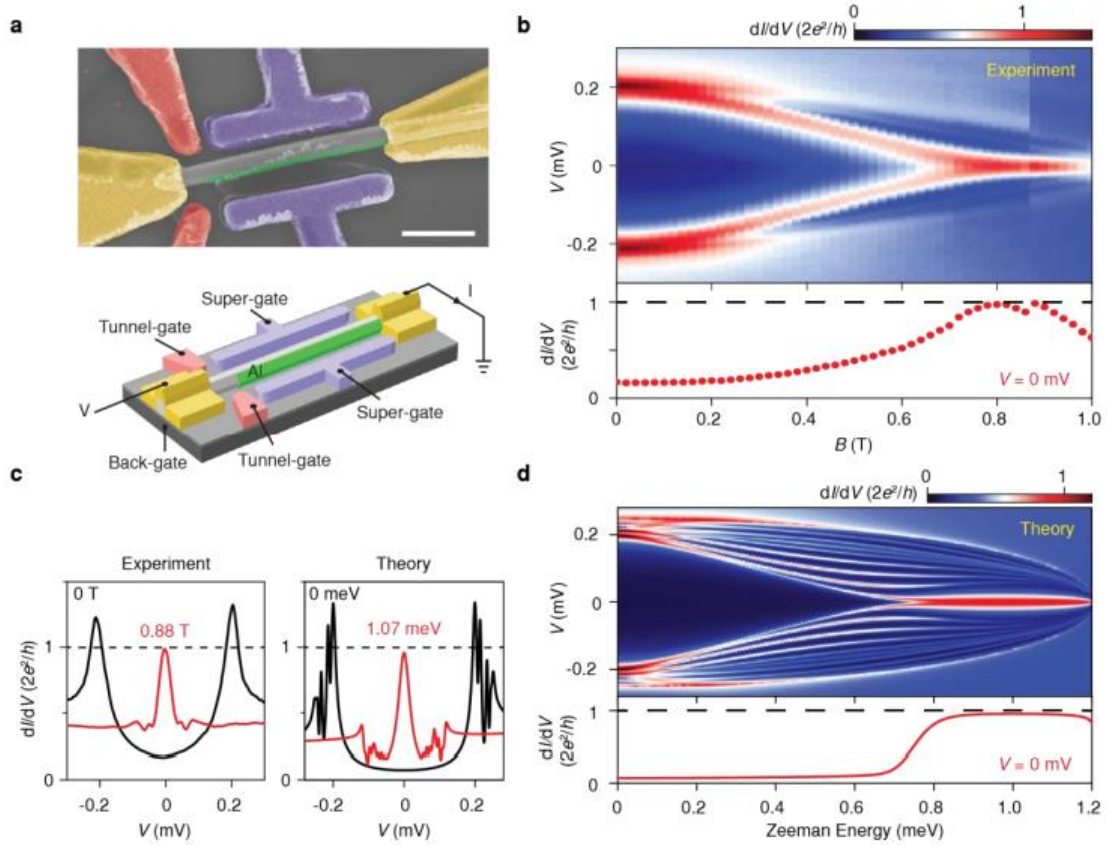
Figure 4: Quantized MZM Conductance device [19] a) False colour SEM of fabricated InSb nanowire with 10nm AL (green) shell side deposited. Tunnel gates (red), super-gates (Blue) and electrical contacts (gold) are 10/100nm Cr/Au. b) Measured device conductance spectra as a function of externally applied magnetic field at T=20mK. Red dots indicate the line cut through V=0. c) Conductance spectra at B=0T and B=0.88T and corresponding theoretical calculations of measured device. d) Theoretical calculations of full field dependant conductance spectra.

Advances in material quality in the fabrication of their nanowires lead to a further publication suggesting the observation of zero bias peaks with conductance quantisation consistent with theoretical predictions [19]. Their device is shown in Figure 4a showing the fabricated InSb/Al nanowire. Electrical control of the hopping potential, t and overall chemical potential μ of the wire are achieved via the tunnel gates, and so called "Super-gates", which alter the potential of the whole superconducting wire, respectively. This device showed the emergence of a zero-bias peak at finite field, with a quantised value of $\frac{2e^2}{\hbar}$, which stayed constant over increasing field. This showed strong agreement with the theoretical expectations (Figure 4d).
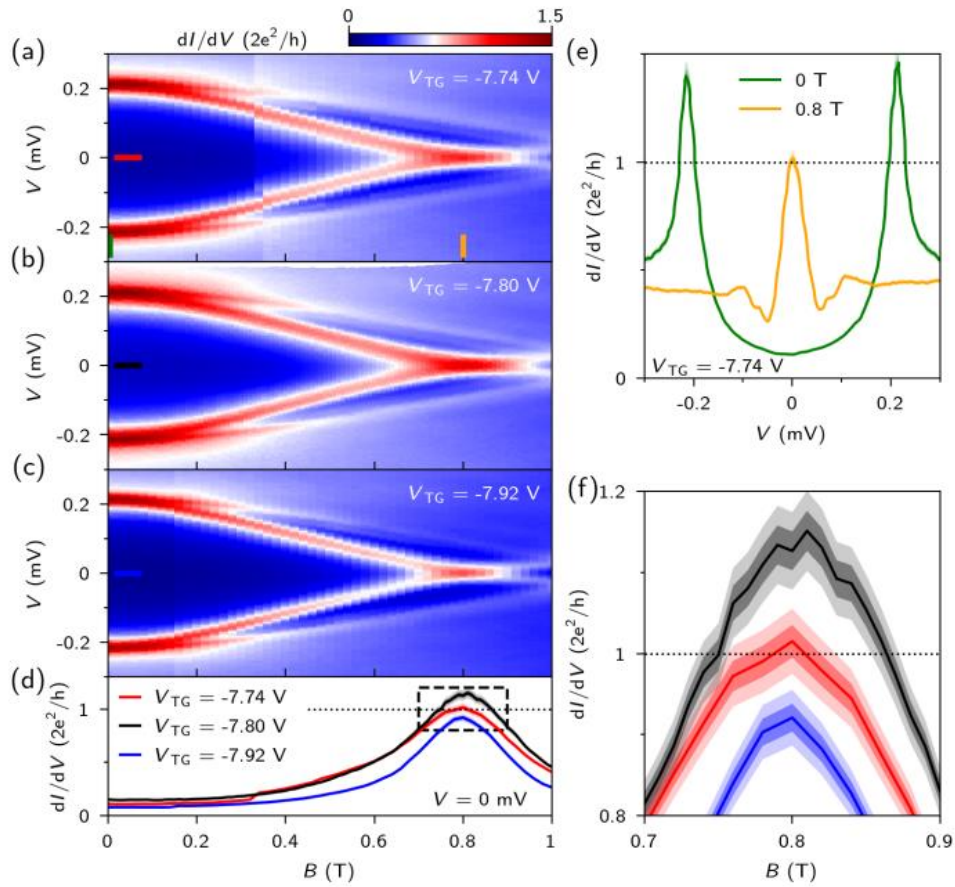
Figure 5: a-c) Conductance measurements of Al/InSb nanowire featured in Figure 4, at different tunnel gate voltage as a function of external magnetic field. .d) Zero bias line cuts of (a-c) at zero applied bias voltage. e) Conductance spectra of a at select external fields f) Zoomed view of d) focusing on the supposed conductance plateau. All figures adapted from [20]

However, in the following years the paper was retracted, citing analytical over-reach and data misinterpretation [21] [22]. It was found that an improper calibration of the device conductance with respect to the gate voltages incorrectly represented both the robustness of the conductance plateau, as well as its overall value. For instance, Figure 5a-c shows the effect of changing tunnel gate on the conductance spectra. In each, a conductance plateau is observable at equivalent field regimes, however each showed different conductance values (Figure 5d). A conductance peak corresponding to an MZM should, after formation, be robust against such variations, with a consistent amplitude and position owing to its quantised nature. Additionally, the change in bias peak height varied non systematically with V_{TG}. The combination of these factors

deemed the initial claim of quantised conductance to be unsubstantiated, and thus lead to the retraction of the paper [20] [21].

Measurements of the height, width and position of the conductance peak, were later deemed to be insufficient as sole measurements to confirm MZM signatures [23]. The evolution of trivial Andreev Bound states could be found to mimic the evolution of an MZM peak with field and could be present in the system without the necessary $p_x \pm ip_y$ superconducting state. Three contact conductance measurements that independently measure the local conductance at either end of the wire found large variations in results between the two ends of a wire, eliminating the possibility of the detected modes being MZMs [24]. Further theoretical analysis on the existing nanowires suggested large improvements in material quality were needed to realise MZM's in a detectable fashion. Several other retractions of papers in the fabrication of nanowire networks have followed [25]. Recent nanowire devices coupled to quantum dots have shown progress but remain limited in scope, and significant material improvements remain to fully realise MZMs [26] [27] [28] [29]. Additionally, theory dictates that the proximity superconductivity in high SOC materials should exhibit experimental signatures of both s-wave and $p_x \pm ip_y$ superconductivity. Experimental confirmation of such a state in a readily manipulatable form, required for the system to become predominantly $p_x \pm ip_y$ remains inconclusive. Most recently in 2023, however, experimental signatures consistent with this SC pairing have been observed in using $InSb$ quantum dots in combination with $InSb$ nanowires [26] [27] [30] [31] [32]. By precisely tuning Quantum Dot energy levels, and coupling them to a nanowire exhibiting superconductivity, the spin composition of an individual Cooper pair can be measured [26]. Such measurements showed evidence of a mixed s-wave and $p_x + ip_y$ state. A similar experimental set-up has been claimed to have realised a minimal two site Kitaev chain [27] .

It is in this state the field lies. Despite recent progress, the scientific and technological interest in the field remains great, and significant progress is being made, but much work is still required to support the pursuit and realisation of these complex devices. This includes conclusive experimental confirmation of the $p_x \pm ip_y$ superconducting state, the capacity to manipulate and control it, as well as realisation of such a state in

a scalable material platform. All of these elements are needed to allow for the fabrication of a full Kitaev chain and the subsequent design and fabrication of quantum computational networks from them.

This work looks at two areas around this area of work. Firstly, we look at the fabrication and measurement of a series of InSb 2DEG/Nb superconductor heterostructures as the basis of a scalable material substitute for InSb nanowires [33] [34]. Previous work looking at proximity superconductivity in high mobility $InSb$ 2DEGs primarily utilised a side-deposited approach of the superconducting film [35] [36]. This work focuses on proximity induction of superconductivity via top-down films, instead. This alternative material route opens the possibility for future side-gated devices, expanding the range of technological applications, that would other otherwise be impossible with top-down films. Successful measurement of top-down induction of proximity superconductivity in a high SOC QW is a significant achievement for moving in this direction.

Secondly, we consider investigations into the interface between the high SOC semiconductor and the s-wave superconductor in search of evidence of the induced $p_x + i p_y$ pairing via Muon Spin Relaxation (μSR) measurements. Such measurements occurred in both Nb/InSb heterostructure and Pb/InSb heterostructures. To the best of this authors knowledge, this is the first time μSR measurements have been performed on a superconductor/ high SOC InSb 2DEG heterostructure. As discussed, prior works had considered the nature of proximity superconductivity primarily through electrical measurements, such as tunnelling conductance, and Quantum Dot spin filters. These works utilised side deposition of the SC material, rather than top down, and as such they were incapable of having the required measurement geometry for μSR. The potential for direct measurement of the nature of the superconducting pairing, means this work thus offers a unique experimental perspective as to the nature of the induced superconductivity. This perspective is free from many of the issues limiting purely electrical measurements and the work supports future use of method in the field.

Finally, the work detailed here features several contributions from sources other than this author. Specific contributions will be noted later in relevant sections, but an

overview is provided here. InSb 2DEGs were grown at the National Epitaxy Centre and were designed and initially characterized via Hall Effect Measurements by previous members of this group. Metal deposition of superconducting materials was performed by collaborators at Bristol University and University of Copenhagen. Atomic Force Microscopy measurements used to characterise surface roughness were also performed by a prior student. The original work of this author is thus – Characterisation measurements of deposited superconducting material. Fabrication and measurement of superconducting/semiconductor structures from these deposited films, along with subsequent analysis. Measurement of μSR on both Nb and Pb film devices was performed by myself, with assistance from the onsite collaborator Zaheer Salman. All all subsequent analysis was performed by the author of this work.

The work is structured as follows:

- Chapter 2: A theoretical overview of Semiconductor 2DEG heterostructures, superconductivity, and proximity induced superconductivity. This includes theoretical description and associated experimental features.

- Chapter 3: A description of the most common experimental and sample fabrication techniques. An overview of cleanroom processing for a variety of the samples measured within the thesis.

- Chapter 4: Fabrication, characterisation and measurement of an Nb/InSb 2DEG TLM junction.

- Chapter 5: Low energy Muon Spectroscopy measurements of Nb and Pb/InSb heterostructures.

- Chapter 6: Low energy Muon Spectroscopy measurements of Pb/InSb heterostructures, and subsequent analysis of internal field.

- Chapter 7: Summary of key findings, future work, and concluding remarks.

Theory of Semiconductor 2DEGs, Superconductors and the Proximity effect.

This chapter seeks to overview the fundamental theory required to understand the experimental work that follows. We will overview the formation of solids and the band structures that dictate their electrical properties. We will look at semiconductor heterostructures, and the formation and physics of semiconductor 2DEGs. Then, we will introduce and consider the history and formulation of superconductivity. This will include observed measurable properties, and a brief discussion of the underlying theoretical models. Finally, we will consider the integration of superconductors and semiconductors via a discussion of the proximity effect, and a theoretical description as to how to model the resulting interface.

2.1: Crystalline Structure of InSb

The physical properties of materials arise as a result of their underlying atomic structure. The atoms in solids form crystalline repeating fundamental cells, or unit cells. This is formed by a combination of the physical arrangement of the atomic sites in real space, or the lattice, and the constituent set of atoms that occupy these atomic sites, the basis.
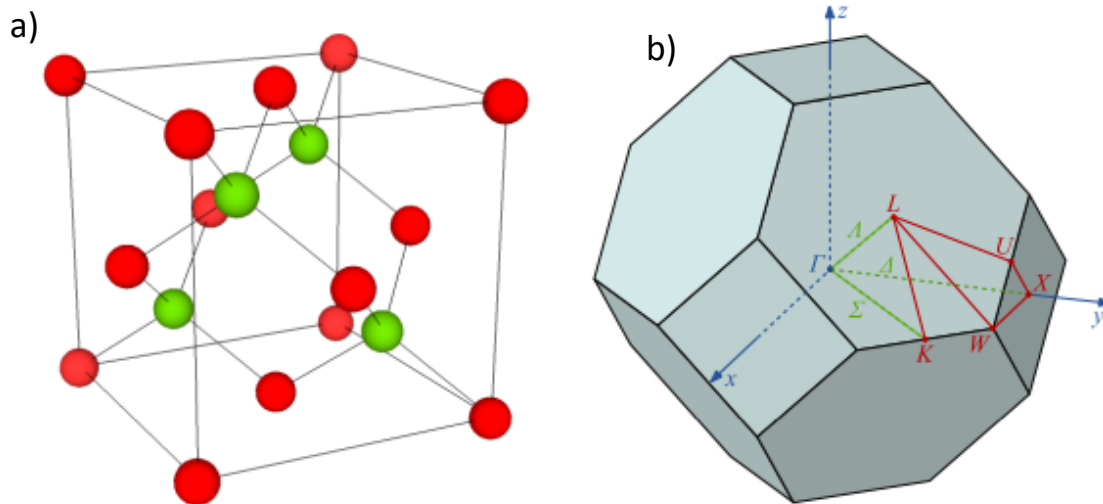
Figure 6: a) Primitive cell of Zincblende Crystal Structure of InSb. Red and green dots indicate the two different elements comprising the intersecting FCC lattices. b) The FBZ of the equivalent Zincblende crystal structures. Figures adapted from [37].

The lattice can be described in terms of a set of translation vectors, a_1, a_2 and a_3 between next nearest lattice points. There are a finite number of combinations of these vectors, known as the Bravais lattices. In 3 dimensions there are 14 of them [38]. Of these, three are Cubic, with a single magnitude primitive vector, a, along all three axes. These three are Simple Cubic, Body-Centred Cubic (BCC), and a Face-Centred Cubic (FCC) [39].

InSb, like many III-V semiconductors forms a Zincblende structures [40]. Two interpenetrating FCC lattices, containing In and Sb atoms respectively, intersect with an offset of one quarter of the atomic length. Each atom in the lattice will form tetrahedrally orientated bonds with the nearest atoms. The offset results in these bonds forming between opposing atoms. The primitive cell of a such a structure is illustrated in Figure 6a.

Although the lattice is a description of the structure in physical space much information can be gained by instead considering it in reciprocal space, or k-space. The periodic nature of the crystal lattice means that fourier transformations can be used to define an equivalent reciprocal lattice, with its own set of vectors, b_1, b_2, b_3. The equivalent to the unit cell in k-space is the First Brillouin Zone (FBZ). The FBZ for a Zincblende

primitive cell is shown in Figure 6b. It encompasses all parts of reciprocal space closer to a given reciprocal lattice point than they are to any other reciprocal lattice point. [41]

2.2: Electronic Band Structure and Electrical conduction through semiconductors.

Mapping the FBZ thus allows mapping of much of the overall crystal, and correspondingly much of electrical structure and properties of the material. We can start with the time independent Schrodinger Equation.

$$H\Psi(\boldsymbol{r}) = -\frac{\hbar^2}{2m_e}\frac{\partial^2}{\partial \boldsymbol{r}^2}\Psi(\boldsymbol{r}) + V(\boldsymbol{r})\Psi(\boldsymbol{r}) = E\Psi(\boldsymbol{r}) \tag{2.1}$$

Where $\boldsymbol{r}$ is a 3-dimensional spatial vector and $V(\boldsymbol{r})$ is the potential. The simplest non-trivial solution to this, is that of the free electron model ($V(\boldsymbol{r}) = 0$ for all $\boldsymbol{r}$). This, unsurprisingly, gives solutions of the form:

$$E(k) = \frac{\hbar^2}{2m}k^2 \tag{2.2}$$

$E(k)$ is known as the dispersion relation. Whilst the free electron model has many advantages in describing the electrical behaviour of metals, it is insufficient to describe semiconductors or insulators. In reality the assumption that electrons are entirely free of potential is untrue – Electrons will experience a periodic potential from the lattice itself.

We can account for the periodicity of the lattice in two ways: Firstly, Ψ must obey periodic boundary conditions – Because the lattice is periodic, and the wavefunction must be continuous over all space, it must match itself at either side of the unit cell. Secondly, because the atoms within a crystal lattice are periodically spaced, electrons within the lattice will experience a periodic potential. The atomic nucleus contributes an attractive potential that is periodic on the same length scale as the lattice.
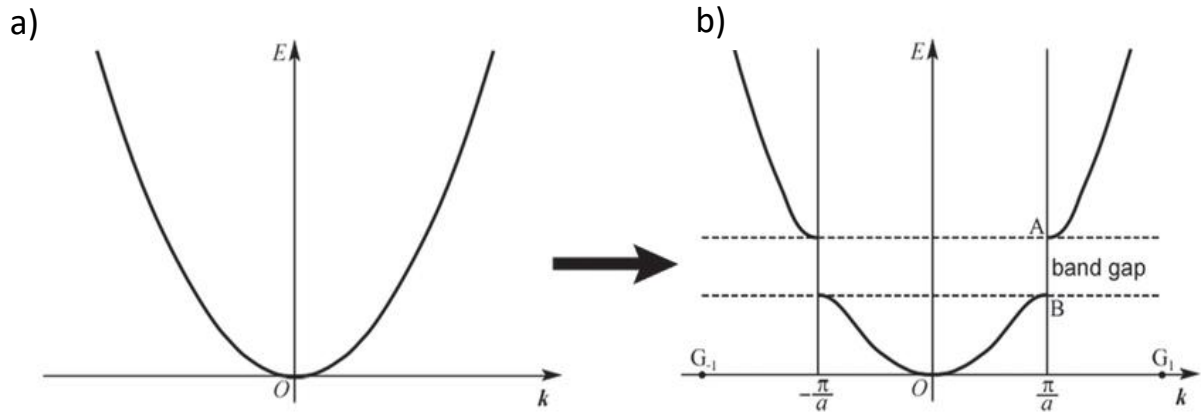
Figure 7:a) Free Electron model dispersion relationship, given by eq.2.2. b) Nearly free electron model. The addition of the periodic potential opens forbidden regions, or 'band gaps'. [42]

According to Bloch's Theorem, the solutions to this will be given by: $\psi_k(r) = u_k(r)e^{ik.r}$, where $u_k(r)$ is periodic such that $u_k(r) = u_k(r + T)$ where T is a translation vector of the lattice [43] [39] [41]. These Bloch solutions leads to energy gaps in the dispersion relation. These are regions of energy in which there are no valid solutions, and thus are forbidden for occupancy by electrons. The energies constrained by these forbidden regions are known as energy bands, and the forbidden region known as a band gap (Figure 7b).

The band structure largely determines the electrical properties of the material. Materials contain a large density of electrons. At $T = 0K$, these will, from the lowest energy state, fill up the electron bands up to some maximum energy level, the fermi energy E_f. The location of E_f within the band structure distinguishes the 'ease' of conduction, and thus the classification of the material. If E_f falls within an electron band, then there is a wealth of accessible, unoccupied energy states. Conduction occurs easily, and thus the material will be a metal.

If E_f instead falls within a band gap then all the bands below E_f (Valance Bands) will be occupied, and all the above E_f bands (Conductance Bands) will be unoccupied. The material is said to be 'gapped' with a band gap energy, E_g, defined as the energy

range between the bottom of the Valance Band and the top of the conduction band. The dispersion relation for carriers in the conduction band would now be given by

$$E_{Carrier}(g) = E_g + \frac{\hbar^2 k^2}{2m^*}$$

(2.3)

m^* is the effective mass of the charge carriers, which is the mass a charge carrier with the material effectively has, accounting for interactions between charge carriers and the crystal, inferable by its response to an applied field. Electrons moving from occupied to unoccupied states now requires an increase in energy, which leads to a suppression in conductance relative to an ungapped metal. The wider the gap, the less conductive the material will be. This gap classifies semiconductors and insulators, with the distinction between those two then being the size of the energy gap. The exact energies serving as a distinction between the two is a matter of some debate.
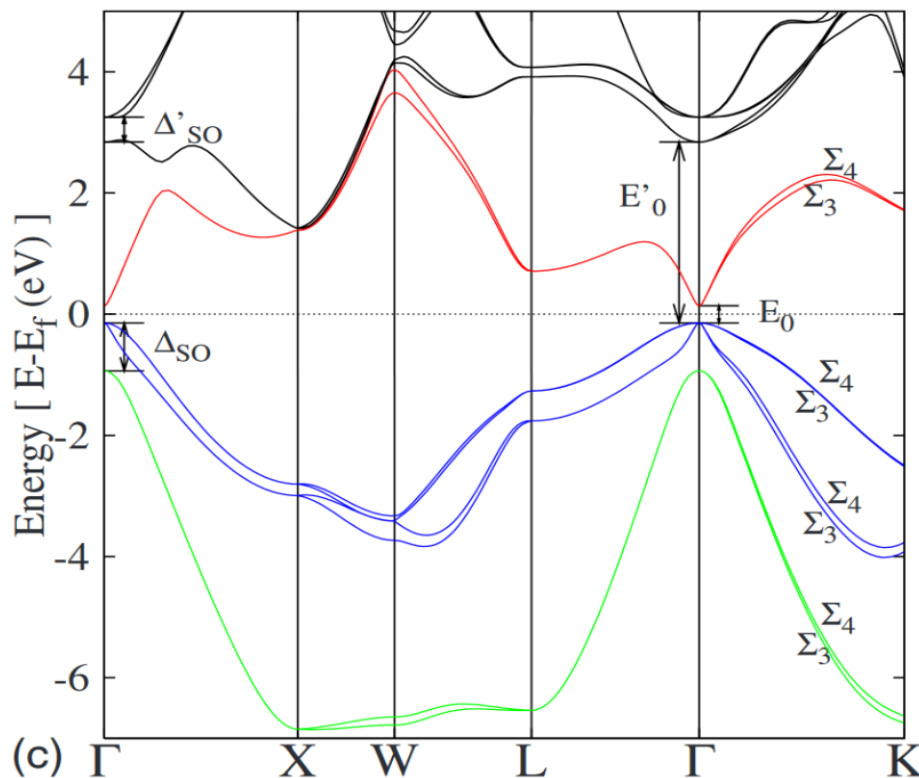
Figure 8:InSb Band Structure. Calculation shows a single electronic band (red), and 3 hole bands; two light hole (blue) bands, and a heavy hole band (green). Figure is adapted from [44], which includes details of calculation.

Mapping the periodicity of real structures to a potential function is often complex and prohibits an analytical solution. Calculations of the electronic structure require

numerical methods. An example of such a numerical calculation for InSb is presented in Figure 8. The solid lines corresponding to $\Gamma, X W$ and L different co-ordinate points in the Brillouin Zone (Figure 6b), with Γ being the centre. Δ_{SO} indicates spin band splitting induced by spin orbit coupling within the material which we shall elaborate upon later.
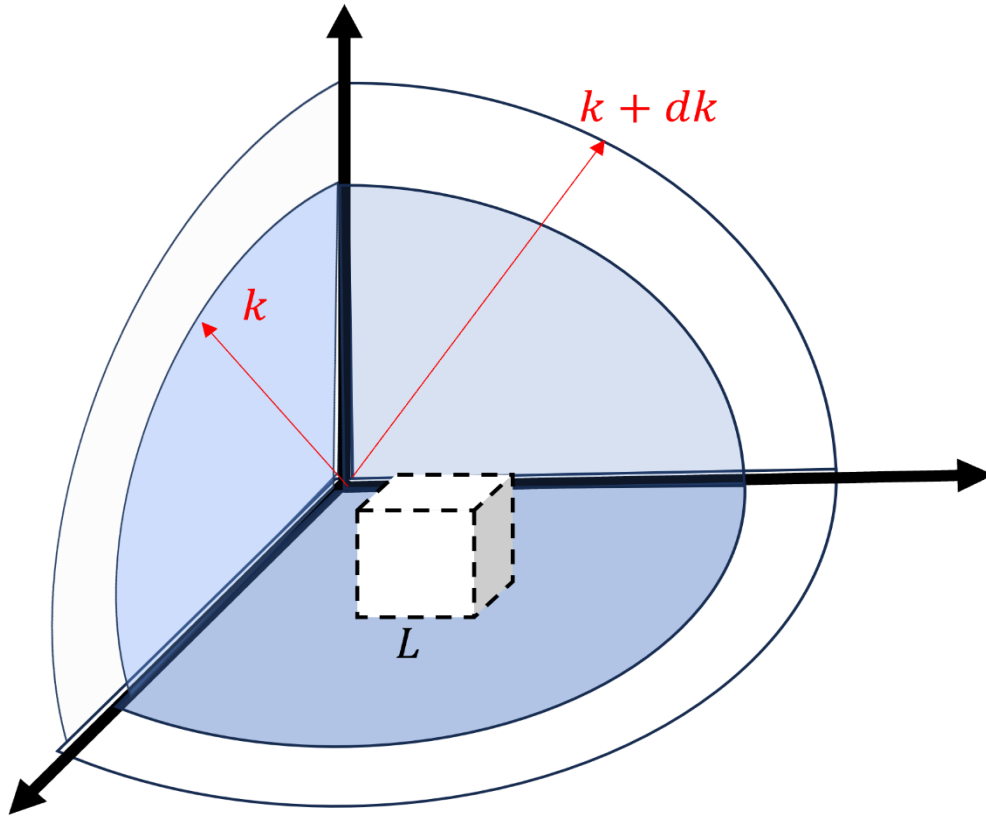
Figure 9: Reciprocal space spheres of radius k and $k + dk$. States defined as occupying the volume L^3 are encompassed by the spheres.

We can also define the density of states (DOS) for a given material from dispersion relation, that being the total number of states available in the system at a given energy, E. For a 3D bulk material, the DOS can be found by considering an infinitesimally small shell contained between a sphere of radius, k, and a sphere of radius $k + dk$ (Figure 9). A given 3D state occupies and volume of k space of $\Omega_{3D}(k) = \left(\frac{2\pi}{L}\right)^3$. The k-space volume of the shell is given by:

$$V_{shell} = \frac{4}{3}\pi(k + dk)^3 - \frac{4}{3}\pi k^3 = 4\pi k^2 dk$$

18

Given we know both the volume of an infinitesimally small shell of k-space, and the volume of an individual state, we can calculate the total number of states by dividing one by the other, i.e:

$$N(k) = \frac{V_{shell}}{V_{state}} = \frac{4\pi k^2 dk}{\left(\frac{\pi}{L}\right)^2}$$

From 2.3, assuming the material obeys a parabolic band structure, we can define the relationships:

$$k = \sqrt{\frac{2m^*E}{\hbar^2}} \qquad\qquad dk = \frac{1}{2}\sqrt{\frac{2m^*}{\hbar^2}}E^{-1/2}dE \qquad (2.4)$$

And then substitute k for E in (2.7) giving:

$$N(E) = \frac{4\pi}{\left(\frac{2\pi}{L}\right)^3}\frac{2m^*E}{\hbar^2}\frac{1}{2}\sqrt{\frac{2m^*}{\hbar^2 E}}dE$$

$$N(E) = \frac{L^3}{2\pi^2}\left(\frac{2m^*}{\hbar^2}\right)\sqrt{E} \qquad (2.5)$$

$N(E)$ is the number of states available in a given volume, L^3. Accounting for the spin degeneracy of the system, and converting to a density by dividing by the area, gives a final expression of the density of states $D(E)$:

$$D(E) = \frac{1}{2\pi^2}\left(\frac{2m^*}{\hbar^2}\right)^{\frac{3}{2}}\sqrt{E} \qquad (2.6)$$

For an unbound 3D system, unsurprisingly the number of available states increases with the total energy of the system.

In addition to the size of the band gap and carrier density, an additional important physical parameter is the electrical mobility. Consider a slab of semiconductor under a bias. A voltage difference between two segments of the semiconductor will cause a net acceleration of carriers from one lead to the other. The velocity of this motion will be dictated by several material scattering factors, such as impurities, phonon scattering, and electron-electron interactions. The overall drift current density will be given by:

$$J_n = qn\mu_n E \tag{2.7}$$

where q is the carrier charge, n is the carrier concentration and μ_n is known as the carrier mobility.

The mobility serves as a measure of the velocity of carriers in response to an applied field. It relates the mean free time between scattering events, τ_c, to the carrier drift velocity, v_d by [41] [45]:

$$v_d = -\mu E = e \frac{\tau_c}{m_e^*} E \tag{2.8}$$

μ_n is thus dependant on both the material quality, which will affect τ_c, and the intrinsic electrical structure of the material, which dictates m^*. The higher the mobility, the faster the carriers move in response to an applied field, and the longer the τ_c. High mobility materials, such as InSb, with low temperature mobilities as high as $200,000 m^2 V^- s^{-1}$, are thus desirable for technological applications in high-speed electronics [46] [47]. Additionally, long τ_c often means a correspondingly long mean free path, l_c which as we will see is a desirable trait for proximity superconductivity systems. Mean free paths of up to $2.5 \mu m$ have been observed in InSb devices [46].

2.3: 2DEG Heterostructures:

Modification of bulk semiconductor band structure via dimensional confinement can radically change the physics present within the system. In our case, this is done via the growth of a semiconductor heterostructure comprised of alloys of InSb. InSb is an III-V compound semiconductor. It has the smallest band gap ($E_g = 0.17eV$ @ $300K$), and lowest effective mass ($0.014m_e$) of any III-V semiconductor, as well as the largest lattice constant ($a_o = 6.48\mathring{A}$) [48]. It additionally has the highest room temperature mobilities (~$78,000cm^{-2}V^{-1}s^{-1}$) and ballistic lengths of III-V semiconductors. [46] InSb 2DEGs have also been shown to possess high Rashba spin orbit coupling, and correspondingly large electronic g-factors [49].

Through careful growth techniques, typically Molecular Beam Epitaxy, it is possible to create a structure consisting of two alloys of $Al_xIn_{1-x}Sb$ (where $0 \leq x \leq 1$) either side of a piece of InSb. AlSb has a different lattice constant and a significantly larger band gap ($1.7eV$ vs $0.18eV$) compared to InSb. The lattice constant of the $Al_xIn_{1-x}Sb$ alloy will sit between the two, in relation to the relative fraction of Al. This is described empirically by Vegard's law:

$$a_{alloy} = xa_a + (1-x)a_b \tag{2.9}$$

Where a_a and a_b are the lattice constants of two given materials, and a_{alloy} is the lattice constant of the resulting alloy [50] [51]. Although something of an approximation, for small fractions (x<0.4%), $Al_xIn_{1-x}Sb$ obeys this relation well.
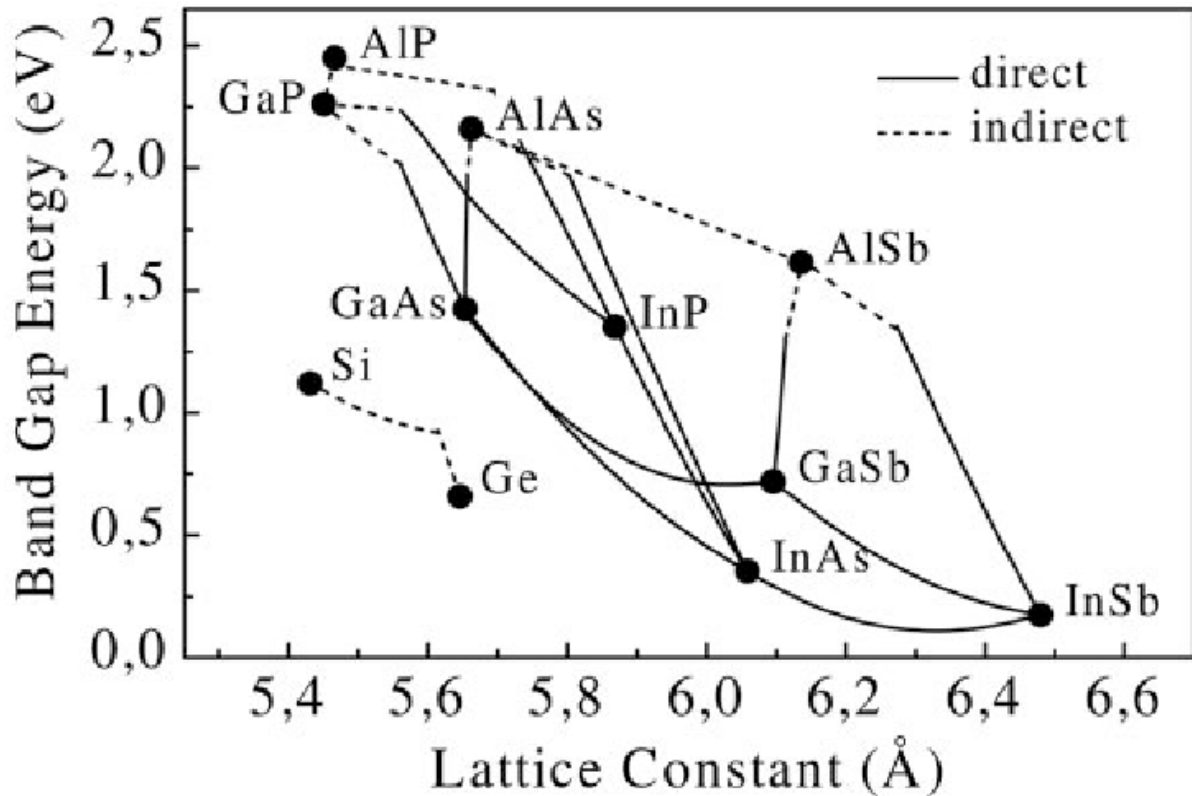
Figure 10: Band-Gap Energy vs Lattice Constant for III-V Semiconductor materials. Dots indicate a given III-V material, whereas the lines between dots indicate the resulting properties of constituent alloys between two III-V. Dashed line indicates indirect band gap materials and alloys. Figure adapted from [52]

Additionally, E_g will also change similarly for a III-V alloy, although not obey Vegard's law. Figure 10 shows the relationship between the lattice constant and E_g of many III-V semiconductors. From this, it can be readily seen that $Al_xIn_{1-x}Sb$ will have a larger E_g than bulk $InSb$. If 'slabs' of $Al_xIn_{1-x}Sb$ are brought adjacent to either side of a slab on $InSb$, then alignment of E_f between these materials will lead to formation of a potential well in the $InSb$, with the larger E_g of $Al_xIn_{1-x}Sb$ serving as a potential barrier either side.
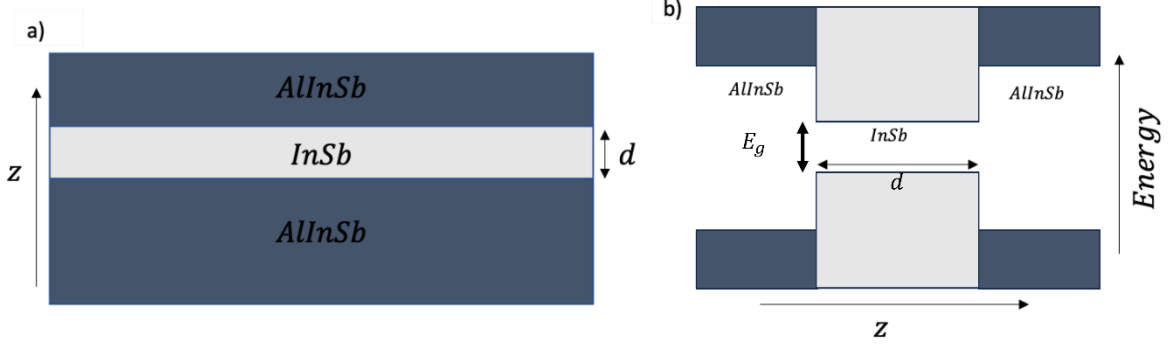
Figure 11: a) Simplified InSb 2DEG structure, comprising layers of AlInSb surrounding an InSb layer of thickness d. b) Resulting band edge structure – Conduction and valence bands are separated by the band gap, E_g.

If the InSb layer is sufficiently narrow, then as mentioned, energetic confinement along z-direction will form a rudimentary quantum well (Figure 11b). The quantum well will lead to the formation of discretised confined states along the direction of growth, z [41]. However, this confinement will not exist along the other two principal directions and will behave according to eq. 2.2. Additionally, the confinement within the well will be dependent upon the well width [41]. Accordingly, for a suitably confining well, the electrons in the system are- essentially 2D, and the electron population within the well is known as a Two-Dimensional Electron Gas, or 2DEG [53].

This confinement to 2D alters the density of states. We can take a similar approach as to the 3D case, considering a small shell at the surface of this circle, defined as the area between a circle of radius k and that of radius $k + dk$. The k-space area of the shell is given by:

$$\pi(k + dk)^2 - \pi k^2 = 2\pi k dk$$

A given 2D state in this shell occupies an area of k space of $\Omega_{2D}(k) = \left(\frac{\pi}{L}\right)^2$, allowing calculation of the total number of states via:

$$N(k) = \frac{A_{total}}{A_{state}} = \frac{2\pi k dk}{\left(\frac{\pi}{L}\right)^2}$$

Eq. 2.7. can be substitute into this, giving:

$$N(E) = \frac{2\pi}{\left(\frac{\pi}{L}\right)^2} \sqrt{\frac{2m^*E}{\hbar^2}} \frac{1}{2} \sqrt{\frac{2m^*}{\hbar^2 E}} dE$$

$$N(E) = \frac{m^* L^2}{2\pi\hbar^2} \tag{2.10}$$

Accounting again for the spin degeneracy of the system, and converting to a density by dividing by the area, this gives a final expression of the density of states $D(E)$:

$$D(E) = \frac{m}{\pi\hbar^2} \tag{2.11}$$

From (2.10) and (2.11), we can see that for a 2D system $D(E)$ is constant, although this can differ for materials with non-parabollic band structures, which can be the case for $InSb$ structures [37]. Dimensional confinement has altered the form of the DOS from the 3D case from $D(E) \propto E^{1/2}$ to $D(E) \propto E^0$. Confinement in other dimensions further alters the form of the DOS.

(a) bulk (3D)   **(b)** quantum well (2D)   **(c)** quantum wire (1D)   **(d)** quantum dot (0D)
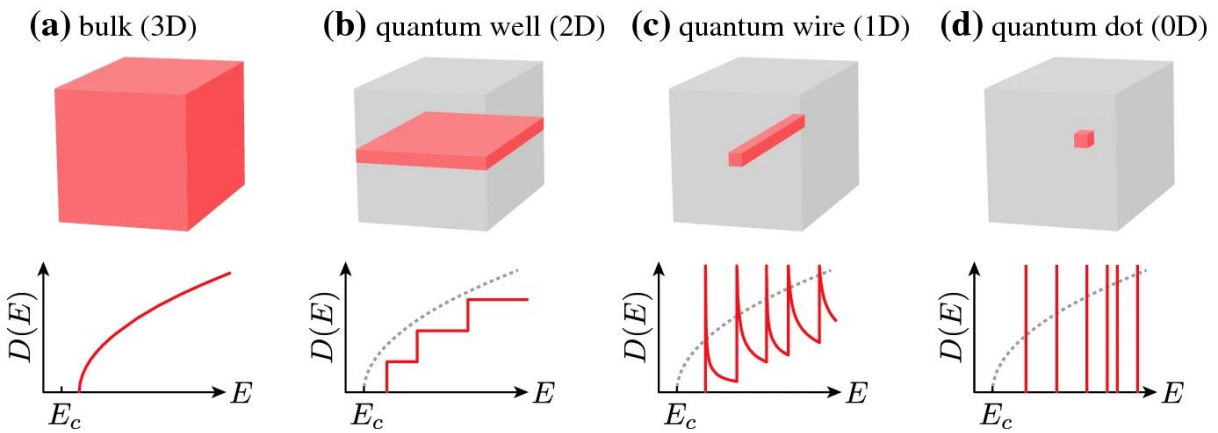
Figure 12: Density of State expressions for increasing degrees of dimensional confinement, going from unconfined bulk material to fully confined quantum dots [54]. Dotted line in b), c) and d) indicates the comparative bulk density of states shown in a)

Figure 12 illustrates the density of states for different degrees of energetic confinement, from the two-dimensional quantum well, to the so called 'zero dimensional' quantum dot. Confinement from the 3D bulk increasingly discretises the DOS, leading to fully discrete energy levels in quantum dots. Figure 12b, the QW

shows the DOS as a series of steps. Physically, this arises from the previously discussed confinement. Accessing one of the energy levels within the growth plane of the Quantum Well can, in many cases, give access to all the other states in the other two planes. The 2DEG thus gives a relatively high degree of available states for smaller energy requirements than the equivalent 3D system. This confinement has been of use for development of technologies, including the development of quantum cascade lasers, and for creating high electron mobility transistors [55] [56] [57] [58].
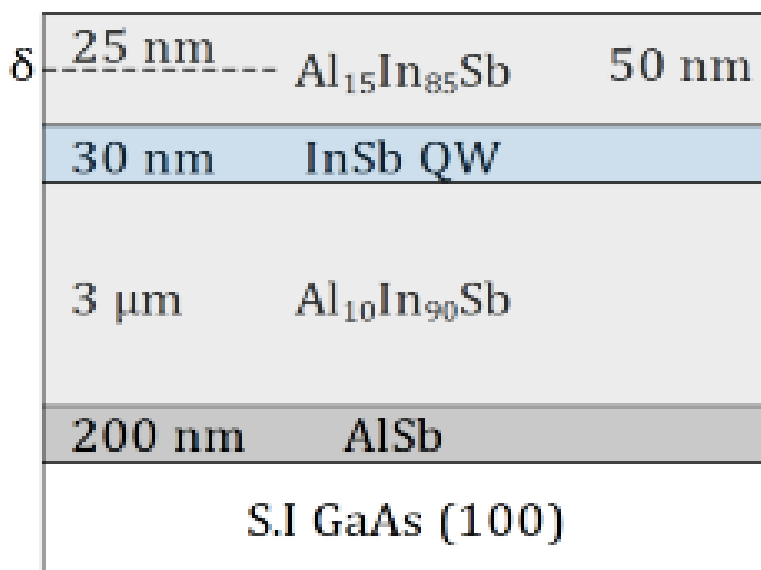
Figure 13: Typical InSb/AlInSb QW heterostructure. Delta indicates the approximate location of the doping layer [37].

The Quantum Wells typically used in this work are $InSb/AlInSb$ heterostructures with a Te δ-doping layer, grown on GaAs substrate [59] [60]. The GaAs substrate is severely lattice mismatched with the InSb, which causes strain. To compensate for this, a thick buffer layer of $Al_{0.1}In_{0.9}Sb$ is grown. Strain induced defects emerge within $\sim100s$ of nm of the surface. The thick buffer serves to localise these well away from the active 2DEG layer by allowing them to self-annihilate [61]. Upon this, a heterostructure of $Al_{0.15}In_{0.85}Sb/InSb/Al_{0.1}In_{0.9}Sb$ is formed to create a confined high mobility InSb quantum well.

To increase the carrier concentration within the 2DEG, remote modulation doping with Te is performed [62]. Doping semiconductors increases carrier concentrations via the

intentional introduction of defects. Undoped semiconductor will have equal concentrations of electrons and holes:

$$n_i \cdot p_i = n_i^2 \tag{2.12}$$

By introducing elements within different periodic table groups to the bulk of the material, one can alter this. If, for instance one introduced a group VI element, such as Te to bulk III-V, $InSb$, the Te would have an excess of electrons relative to the rest of the material, increasing electron carrier density, whilst decreasing the hole density.

$$p \cdot n = n_i^2 \tag{2.13}$$

These dopants are still defects, and thus whilst they improve carrier concentration, they can introduce added scattering centres – either directly from added distortions in the lattice, or from increased charge screening from the nuclei. Remote doping addresses this, by introducing the dopants spatially separate from the conduction channel [55]. The Te is localised in the middle of the $Al_{15}In_{85}Sb$ top cap layer. Charge carriers from these Te atoms will be delocalised from their atoms, and enter the QW, which minimises the role that these Te atoms can play. This has allowed the realisation of $InSb$ QW with high carrier concentrations, without compromising carrier mobility [62].

2.4: Spin Orbit Coupling in Semiconductor 2DEGS:

The semiconductor material is nominally spin-degenerate – for each state of energy E_k there exist two electrons of opposing spin. However, in real materials there exist interactions between the electrons, the lattice, and the wider outside environment that can remove this degeneracy. The most obvious example would be applying an external magnetic field. This field will induce a Lorentz force on moving charges within the material, causing phenomena such as the Hall effect, but also Zeeman splitting of the spin states with an associated energy $E = \pm\frac{1}{2}g\mu_o B$, the Zeeman energy. The two spin states are split into separate energy bands [41].

There exists a similar phenomenon for electrons moving in an electrical field in the absence of a B-field. Electrons moving in an electrical field will experience an 'effective' magnetic field, given by:

$$B = -(\boldsymbol{v} \times \boldsymbol{E})/c \qquad (2.14)$$

Where $\boldsymbol{v}$ is the velocity of the electron, and $\boldsymbol{E}$ is the electrical field.
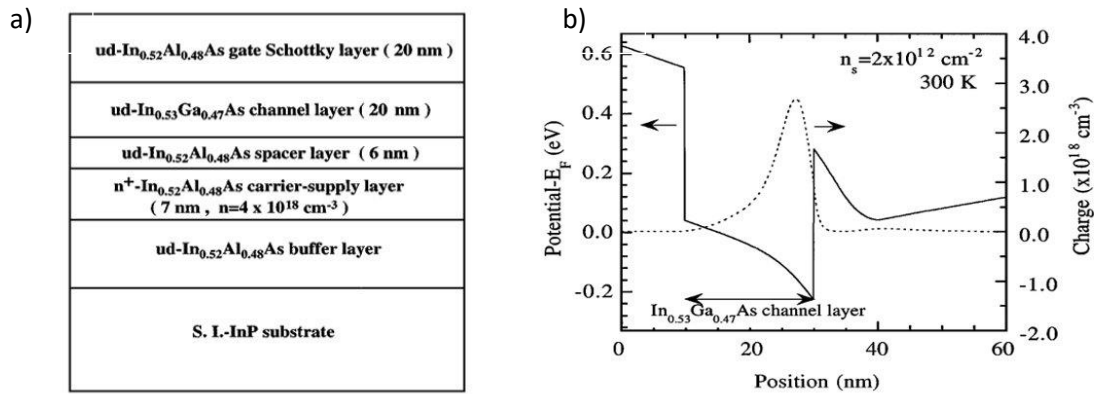
Figure 14: a) InGaAs/InAlAs QW structure detailing layer composition and thicknesses. B) Schrodinger Poisson simulations of a). Solid line indicates the calculated band edge energy, indicating the formation of the QW within the channel layer. Dotted line indicates the resulting charge distribution within the well. [63]

Such an electric field can often arise from inversion symmetry breaking within a material causing a non-uniform electrical environment along a given material axis. This can be intrinsic to the crystal structure, which is known as Bulk Inversion Asymmetry [64]. Or it can also be purposefully introduced owing to the difference in potentials between different surfaces in a material. This later case is known as Structural Inversion Asymmetry.

Figure 14 shows an example of a InGaAs/InAlAs QW heterostructure, and its corresponding band diagram as calculated via Schrodinger Poisson simulations. Charge within the QW layer is shown to be distributed asymmetrically along the direction of growth, arising from localised doping inducing band bending [63]. The charge causes an electrical field that acts on the carriers in the QW. As such, the resulting effective 'B' field will lead to an associated energy coupling term:

$$H_{so} = \frac{g\mu_B}{2c}(\boldsymbol{v} \times \boldsymbol{E}) \cdot \boldsymbol{\sigma} \qquad (2.15)$$

Where g is the electronic g factor, μ_B is the Bohr magneton, and $\boldsymbol{\sigma}$ are the spin matrices. If $\boldsymbol{E}$ is entirely aligned along growth direction, and thus perpendicular to carrier motion, then 2.15 reduces to:

$$H_{so} = \frac{g\mu_B}{2c}((v_x E_z)\sigma_x - (v_y E_z)\sigma_y)$$

$$H_{so} = \frac{g\mu_B E_z}{2m_e c}\begin{pmatrix} 0 & p_x - ip_y \\ p_x + ip_y & 0 \end{pmatrix} \qquad (2.16)$$

This is known as Rashba Spin Orbit Coupling (Rashba SOC) [65] [66].
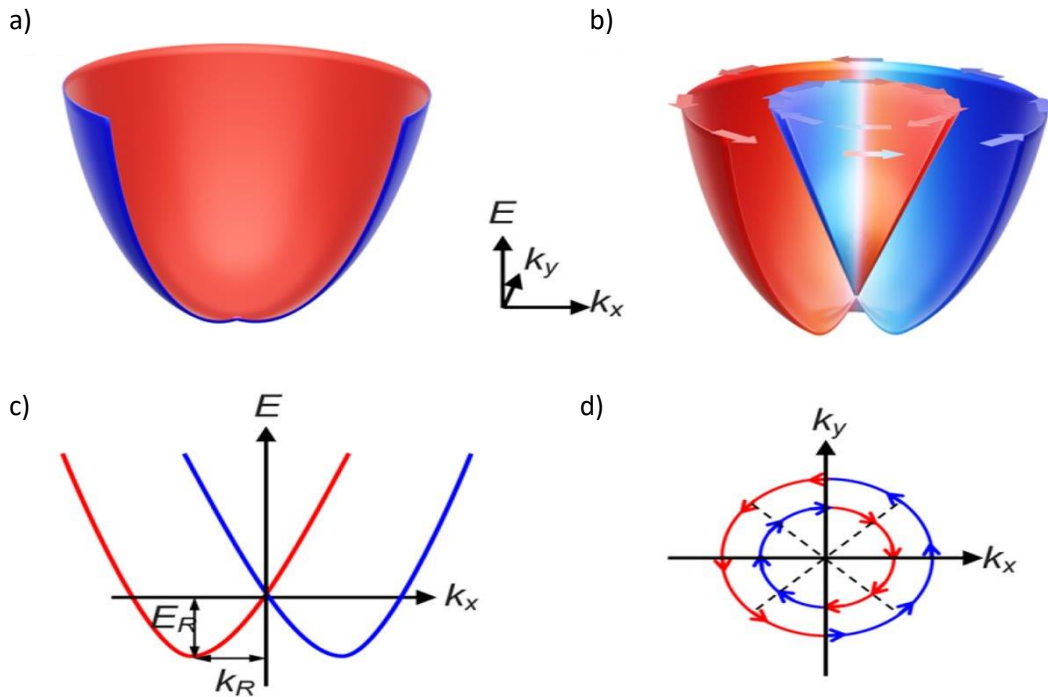
Figure 15: Rashba Spin-Orbit Coupling Diagrams red and blue indicate different spin states. Adapted from [66] a) 3D Spin texture of a spin degenerate system b) As a) but with an added Rashba term. c) 1D Dispersion relation of Rashba SOC. d) Spin texture of Rashba splitting – a slice of b) at fixed energy.

The addition of the Rashba term adds an additional momentum dependence to the system, shifting the two spin bands. This lifts the spin degeneracy of the p_x and p_y bands of the system at all points of k-space except for $k = 0$ (Figure 15b and c). The strength of the Rashba coupling can be described by the Rashba coefficient:

$$\boldsymbol{\alpha_k} = \frac{2E_R}{k_R} \tag{2.17}$$

Where E_R and k_R are defined as the energy and momentum minima of the shifted bands (Figure 15c).

The lifting of the spin degeneracy has applications for spintronic technologies, such as spin polarisers and spin filters, and for investigations of the Spin Hall Effect [67] [68] [69] [70] [71]. The strength of the Rashba term can be controlled via gating to alter the strength of the internal field by altering the electric field within the QW [63] [72] [73]. This allows for the manipulation of spins without the application of an external magnetic field, opening possibilities for local control of the spin states [68]. Significant steps towards spin Field Effect Transistors have been made using Rashba SOC materials [74] [75]. Additionally, SOC is seen as a necessary component for the practical realisation of $p_x + ip_y$ superconducting pairing necessary for MZMs in 1D and 2D semiconductor-superconductor hybrids [15].

Our discussion up to now has been focused primarily on semiconductors. This is only one half of the materials used and necessary for this work. We must now consider the other, superconductors. This will overview the history and underlying physics of superconductors, as well as the superconductor-semiconductor interface, and proximity superconductivity.

2.5: Superconductivity and The London Equations:
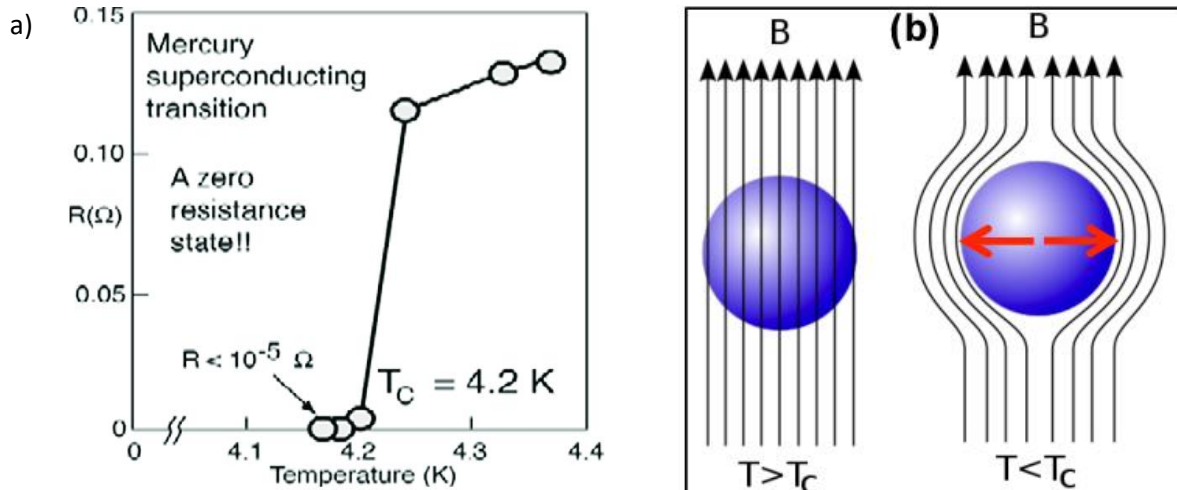
Figure 16: a) Resistance vs Temperature for mercury [76] b) Illustration of the Meissner effect – an example superconductor with an external magnetic field. Below T_c, the field is expulsed from within the superconductor [77].

Superconductivity was first observed in 1911 by Onnes [78] [79]. By cooling liquid Mercury with liquid helium, Onnes observed a sharp drop of the resistance of the Mercury to zero below a certain critical temperature, T_c (Figure 16a). The zero-resistance state was also supressed above a critical current, I_c. Later observations by Meissner and Oschenfeld found this zero-resistance state was accompanied by a complete expulsion of Magnetic Flux within the bulk of the superconducting material below T_c [80] (Figure 16b). This observation distinguished superconductors from perfect conductors – in a perfect conductor, any magnetic field applied above T_c would remain in the bulk of the material regardless of it then being cooled below T_c.

Both observed properties found a phenomenological explanation in the work of Fritz and Heinz London [81]. They developed the so-called London equations:

$$\frac{\partial \boldsymbol{j}}{\partial t} = \frac{n_s e^2}{m_e} \boldsymbol{E} \qquad (2.18a)$$

$$\nabla \times \mathbf{j} = -\frac{n_s e^2}{m_e} \mathbf{B} \qquad (2.18b)$$

where $\mathbf{j}$ is the supercurrent density, $\mathbf{E}$ and $\mathbf{B}$ are the electric and magnetic fields respectively within the superconductor and n_S is the number density of superconducting carriers. Eq. 2.18a relates the time dependence of $\mathbf{j}$ and an applied $\mathbf{E}$. As such, it states that a constant current may flow in the absence of an Electric field, i.e. perfect conductivity. The physical implication of the second is less immediately obvious. However, by taking the second Maxwell Equation:

$$\nabla \times \mathbf{B} = \mu_o \left(\mathbf{J} + \varepsilon_o \frac{\partial \mathbf{E}}{\partial t} \right) \qquad (2.19)$$

In most instances, $\mathbf{J}$ will be large relative to $\varepsilon_o \frac{\partial E}{\partial t}$. As such we can approximate $\frac{\partial E}{\partial t} = 0$. We can then take curl of the eq. 2.19, and substitute $\nabla \times \mathbf{J}$ from eq. 2.18b to obtain:

$$\nabla \times \nabla \times \mathbf{B} = -\frac{\mu_o n_s e^2}{m_e} \mathbf{B} \qquad (2.20)$$

Through use of the vector identity:

$$\nabla \times (\nabla \times \vec{v}) = \nabla(\nabla \cdot \vec{v}) - \nabla^2 \vec{v}$$

And Gauss's law ($\nabla \cdot \mathbf{B} = 0$) (2.18b) can be reduced to the following differential equation:

$$\nabla^2 \mathbf{B} = \frac{\mu_o n_s e^2}{m} \mathbf{B} \qquad (2.21)$$

Eq. 2.21 will have solutions for $\boldsymbol{B}$ that decay away exponentially from the surface of the superconductor with a length scale of $\lambda_L = \sqrt{\frac{m}{\mu_o n_s e^2}}$. Physically, this describes the observed Meissner effect. Applied Magnetic flux will only be present within a small region of the sample close to the surface. This length scale is the so-called London Penetration depth. Additionally, eq. 2.18b also describes that an applied field will lead to the inducement of a supercurrent density in opposition to the applied field. If as observed, the field decreases as a function of sample depth, then eq. 2.18b states that $\boldsymbol{J}$ must also decrease. As such, the supercurrent is also constricted to the surface of the superconductor, along the same length scale, λ_L. This supercurrent serves as a 'Screening' current – shielding the bulk of the sample from the magnetic field.

This showed the Meissner effect was the fundamental property of a superconductor. The expulsion of flux naturally led to the inducement of a supercurrent, rather than vice versa. Whilst instructive, the London equations were still only an estimate, as λ_L as predicted by the theory was found to a factor of two out of experimentally measured values.

2.6: Ginzburg-Landau theory

The London equations were expanded upon in 1950 by Ginzburg and Landau [82] They sought to build an explanation as to why the superconducting state is destroyed by the application of a sufficiently high magnetic field or current. Ginzburg-Landau theory proposed the existence of ψ, an effective wavefunction of superconducting electrons, defined such that $\psi^*\psi = n_s$. For a full derivation we refer the reader to the following resources [82] [83]. They considered the change in Free Energy, F, of a 1D superconductor with a series expansion in powers of $|\psi|^2$ as:

$$F = F_n + \alpha|\psi|^2 + \frac{\beta}{2}|\psi|^4 + \frac{1}{2m}(-i\hbar\nabla - 2e\boldsymbol{A})|\psi|^2 + \frac{|\boldsymbol{B}|^2}{2\mu_o} \quad (2.22)$$

Where F_n is the normal state free energy, α and β are constants, and $\boldsymbol{A}$ is the magnetic vector potential determined by $\boldsymbol{B} = \nabla \times \boldsymbol{A}$. ψ is only non-zero below T_c, so in the non-

superconducting region, the free energy is the normal state energy, plus a potential magnetic contribution. Minimising F with respect to the variables of the system, $\boldsymbol{A}$ or ψ, will give the 'steady-state' equation of that parameter. For instance, in the case of a spatially uniform ψ ($\nabla\psi = 0$) in the absence of a magnetic field ($\boldsymbol{A} = 0$), finding the minima $\frac{\partial F}{\partial \psi^*} = 0$ will give:

$$\frac{\partial F}{\partial \psi^*} = (\alpha + \beta|\psi|^2)\psi = 0 \qquad (2.23)$$

Eq. 2.23 has roots of $\psi = 0$ or $|\psi| = \sqrt{-\frac{\alpha}{\beta}}$. The first root is the free energy minimum of the normal state, whereas the latter is the minimum for superconductivity. These roots have corresponding solutions of $F = 0$ or $F = -\frac{\alpha^2}{2\beta}$ respectively. Because $\beta > 0$, we know that α must be negative below T_c for the second root to give a real number. Because as previously mentioned it was experimentally known n_s (and hence ψ) decreases as T increases, α was inferred to be a function of the form $\alpha(T) = a\sqrt{T - T_c}$ where a is a constant of proportionality.

Looking at the general case eq. 2.22, F can be minimised with respect to either ψ or $\boldsymbol{A}$. Minimising with respect to ψ gives:

$$\alpha\psi + \beta\psi|\psi|^2 + \frac{1}{4m}\left(\frac{\hbar}{i}\nabla + \frac{2e}{c}\boldsymbol{A}\right)^2\psi = 0 \qquad (2.24a)$$

Whilst minimising with respect to $\boldsymbol{A}$ gives:

$$\boldsymbol{j} = -\frac{e\hbar}{2mi}(\psi^*\nabla\psi - \psi\nabla\psi^*) - \frac{2e^2\boldsymbol{A}}{mc}|\psi|^2 \qquad (2.24b)$$

Eq. 2.24a is analogous to the Schrodinger equation and allows for calculation of ψ over space for a given potential. It also allows definition of the boundary conditions between a superconductor and an insulator, where $\psi(x) = 0$ for all x and T. It thus

allowed for description of spatial variation in n_s. Eq. 2.24b allowed calculation of the resulting supercurrent as a function of flux.

In addition to these expressions, Ginzburg-Landau theorem defined two characteristic length scales for superconductors, λ and ξ. The first, λ is the penetration depth. It is the same physical concept as λ_L, however, it is defined as

$$\lambda = \sqrt{\frac{m}{4\mu_o e^2 n_s}}$$

(2.25)

Which differs from ψ_L by a factor of a half. This difference was in agreement with experimental observations [84]. The second, ξ, is the coherence length, depends upon the phase of the material. In the normal phase

$$\xi_N = \sqrt{\frac{\hbar}{2m|\alpha|}}$$

(2.26a)

Whereas in the superconducting phase:

$$\xi_S = \sqrt{\frac{\hbar}{4m|\alpha|}}$$

(2.26b)

The coherence length is the distance over which ψ can vary gradually without an energy requirement and is thus the length scale over which ψ can change without destroying the superconducting state. The coherence length was first proposed by Pippard as an extension of the London equations [85], following from experimental measurements of Sn-In alloys that saw an abnormally large penetration depth [86].

2.7: Type I and Type II Superconductors:
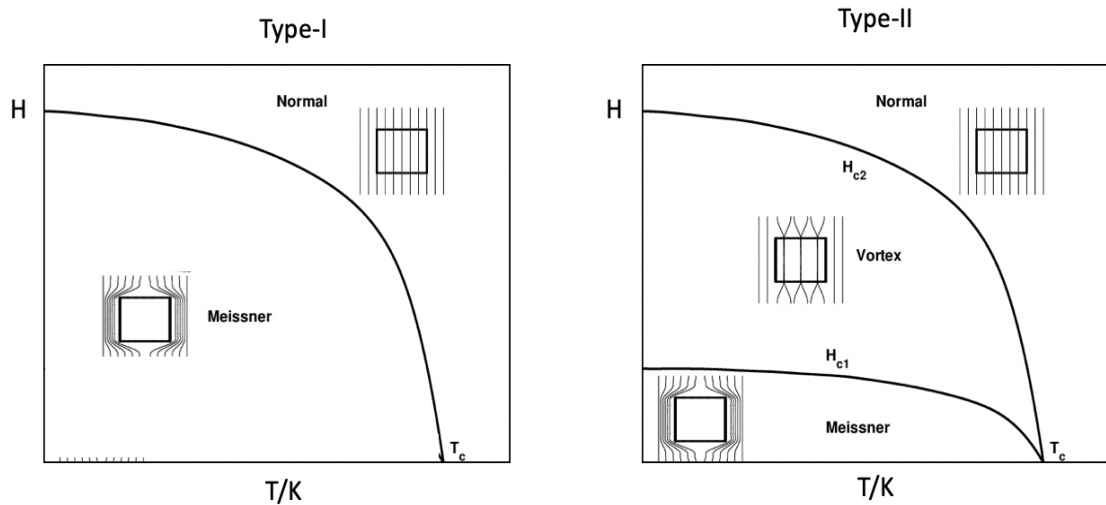
Figure 17: Critical Fields of Type-I and Type-II superconductors as a function of temperature. Inset images give a depiction of the field penetrations for each state [87]

Two distinct magnetic responses can be seen in so-called 'conventional' superconductors, Type I and Type II. Type I superconductors exhibit the field behaviour previously described. They have characteristic critical values, T_c and H_c. Below these values, Type I superconductors have zero resistance, and expel all applied magnetic flux. Type II was first observed by Shubnikov and Rjabinin [88]. Type two again show a single T_c, but now has two distinct critical fields, H_{c1} and H_{c2}, where $0 < H_{c1} < H_{c2}$. Below H_{c1}, Type II behave as per Type I. However, in the region $H_{c1} < H < H_{c2}$, there is partial leakage of flux into the bulk of the superconductor before the Superconducting state collapses completely for $H > H_{c2}$.

An explanation owing to the formation of magnetic vortexes was given by Abriskosov [89]. The difference in behaviour is attributable to the free energy of the interface between the superconducting and normal phases. In type I, this is positive, and the energy of the system is lowest when the contact area between superconducting and normal phases is minimised. In type II, it is negative [90]. It becomes favourable to maximise the contact area. The superconducting lattice becomes needled with cylinders of the normal phase, which allows partial penetration of flux, and the formation of magnetic vortexes around them. As the flux increases, the number of these cylinders increases eventually occupying the entirety of the volume of the

material and destroying the superconducting state entirely. The ratio of the two Ginzburg-Landau length scales eq. 2.25 and eq. 2.26 $\kappa = \frac{\lambda}{\xi}$ can be used to distinguish between and classify these types of superconductors. For type I, it obeys the ratio will take the values $0 < \kappa < \frac{1}{\sqrt{2}}$ and Type II for $\kappa > \frac{1}{\sqrt{2}}$ [84].

2.8: BCS Theory:

The Ginzburg-Landau theory offered a description consistent with some experimental observations, but it did not offer a microscopic description to the underlying cause of the Meissner state. Following from Pippard, John Bardeen proposed that a gap in the electron density of states would describe both the Meissner effect, and Pippard's measurements of a long coherence length [91]. From this, Leon Cooper proposed the existence of so called 'Cooper Pairs' [92]. An arbitrarily small net attractive force between two electrons could allow for the formation of a bound state between them. This bound state would obey some bose-like properties, forming a degenerate ground state that is separated from unbound single particle states by a small energy gap. [92] Additional evidence as to the source of this attraction came from the observation of the dependence of critical temperature on isotope mass of a series of Mercury samples [93] [94]. The phonon energy within a solid is inversely dependant on the mass of its atoms, which will differ between differing isotopes of the same material. By measuring a variation of T_c between two isotopes of Hg in proportion to the difference in mass, there was strong evidence that the attractive force would be an electron-phonon interaction [95]
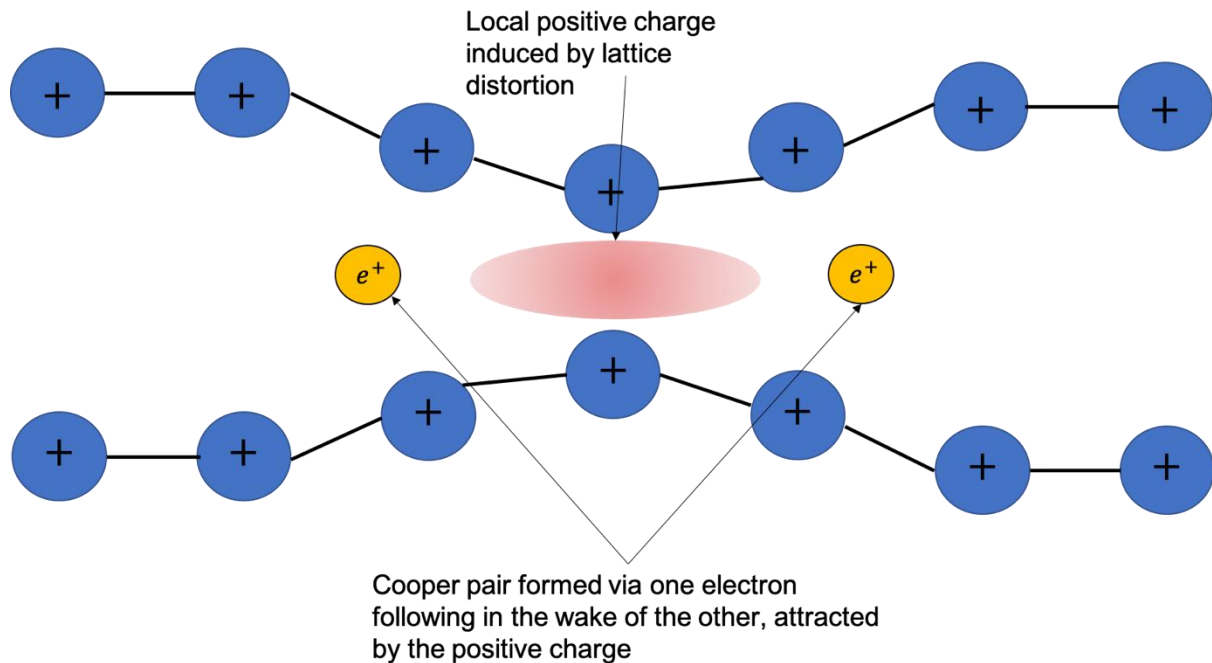
Figure 18: Schematic representation of a physical image of the Cooper Pair formation – an electron moving through a crystal lattice.

For a simple physical image of these cooper pairs, consider the case of an electron moving through a lattice (Figure 18). The atoms in the lattice are positively charged. There will exist an attractive force between the electron and the lattice. This causes a slight lattice distortion, as atoms are slightly pulled towards the electrons. The distorted lattice will, until it relaxes, create a region that is electrically positive relative to the lattice around it. If the relaxation time is long relative to the electron velocity, then a second electron can be attracted towards it. In effect, one electron will follow in the others wake, bound by the induced phonon. The length over which these two electrons are 'correlated' is equivalent to ξ_s, the coherence length discussed previously.

These elements were finally combined in 1957 by Bardeen, Cooper and Schrieffer, producing the BCS theory [96]. This proposed that a virtual phonon interaction between electrons lead to the formation of Cooper Pairs between electrons of opposite spin and momentum, e.g. $(k \uparrow, -k \downarrow)$. The process will be briefly overviewed here, before focusing on the results and findings. The original BCS derivation used a variational argument, whereas this shall focus on an alternative method proposed first by Bogoluibov [97]. For a detailed derivation, the reader is referred to the following book by Michael Tinkham [84].

The superconducting Hamiltonian can be written as:

$$H = \sum_{k\sigma} \xi_k c_{k\sigma}^\dagger c_{k\sigma} + \frac{1}{N} \sideset{}{'}\sum_{kk} V_{kk'} c_{k\uparrow}^\dagger c_{-k\downarrow}^\dagger c_{-k'\downarrow} c_{k'\uparrow}$$

(2.27)

where $V_{kk'}$ is the interaction potential between an electron with momentum k and k', and $\xi_k = \frac{\hbar^2 k^2}{2m}$. $c_{k\sigma}^\dagger$ is the creation operator describing the formation of a particle with momentum k and spin σ, and $c_{k\sigma}$ is the corresponding annihilation operator. The first term describes the normal state energy of the system whereas the second describes the energy resulting from the destruction and creation of a cooper pairs via creation and destruction of the composite quasiparticles. The cooper pair in this instance is created by particle of momentum and spin $k \uparrow$ and $-k \downarrow$. This pairing of particles with opposing spin and momentum is known as s-wave pairing and is the most commonly occurring pairing in nature. This second term can be expanded giving a first approximation for the gap function:

$$\Delta_k = -\frac{1}{N} \sum_{k'} V_{kk'} \langle c_{-k'\downarrow} c_{k'\uparrow} \rangle$$

Where the notation $\langle ... \rangle$ indicates the average value of the bracketed term. The initial Hamiltonian (2.27) can be expressed using this new gap function

$$H = \sum_{k\sigma} \xi_k c_{k\sigma}^+ c_{k\sigma} - \sum_k (\Delta_k c_{k\uparrow}^+ c_{-k\downarrow}^+ + \Delta_k^* c_{-k'\downarrow} c_{k'\uparrow})$$

$$+ \sum_k \Delta_k \langle c_{k\uparrow}^+ c_{-k\downarrow}^+ \rangle$$

(2.28)

This is solved by diagonalization via the use of a Bogoliubov transformation:

$$c_{k\uparrow} = u_k^* \gamma_{k\uparrow} + v_k \gamma_{-k\downarrow}^+$$

$$c_{-k\downarrow}^+ = u_k \gamma_{-k\downarrow}^+ - v_k^* \gamma_{k\uparrow}$$

$$|u_k|^2 + |v_k|^2 = 1$$

The Bogoliubov transformation describes a mixing of electronic and hole states, with the relative weighting of each being given by the coefficients v_k and u_k. Substitution into eq. 2.28 lets us diagonalize the equation

$$2\xi_k u_k v_k - \Delta_k u_k^2 + \Delta_k^* v_k^2 = 0 \qquad (2.29)$$

which in turn allows us to solve for the two coefficients u_k and v_k in terms of energy

$$|u_k|^2 = 1 - |v_k|^2 = 1 - \left(\frac{\xi_k}{E_k}\right) \qquad (2.30)$$

where $E_k = (\xi_k^2 + \Delta_k^2)^{\frac{1}{2}}$. This leads to the diagonalized Hamiltonian:

$$H = \sum_k (\xi_k - E_k + \Delta_k \langle c_{k\uparrow}^+ c_{-k\downarrow}^+ \rangle) + \sum_{k\sigma} E_k \gamma_{k\sigma}^+ \gamma_{k\sigma} \qquad (2.31)$$

The first term is a constant. The second describes the energy associated with adding excited quasiparticles, $\gamma_{k\sigma}$, to the system. These excitations will have an energy of:

$$E_k = \pm\sqrt{\xi_k^2 - \Delta^2} \qquad (2.32)$$

From which, Δ_k can be seen as an energy gap in the quasiparticle density of states.

BCS theory was shown be consistent with experimental observations, such as the Isotope Effect, and various thermo-dynamical properties such as changes in the specific heat capacity. [96]. It was further shown that the Ginzburg-Landau equations were derivable from BCS theory [98]. BCS theory was thus inherently consistent with the Meissner Effect, and by extension the electrical properties of a superconductor. The zero-temperature energy gap, $\Delta(0)$ is predicated to be proportional to T_c, given by

$2\Delta = 3.5k_bT_c$ at $T = 0$, rapidly decaying to $\Delta = 0$ as T approaches T_c. [99]. Near the limit $T \approx T_c$ the temperature dependence of the gap is approximated by:

$$\Delta(T) \approx \Delta(0)(1 - T/T_c)^{\frac{1}{2}} \tag{2.33}$$

The exponent of this equation can be used as an indication as to the quality of a superconductor. $1/2$ is the expected exponent for a well-behaved BCS superconductor. The presence of defects can alter this relation, to higher order powers of $e.g. 3/2$ $5/2$. A similar relationship exists for describing $I_c(T)$:

$$I_c(T) = I_c(0)\left(1 - \frac{T}{T_c}\right)^{0.5} \tag{2.34}$$

and similar inferences as to SC quality can be made from this.

It is also possible to calculate the density of single particles states in the superconductor, $N_s(E)$. Because a superconductor is in many ways a metal with a gap around E_f, we can equate the DOS of the superconductor to that of the normal state, $N_s(E)dE = N_n(\xi)d\xi$. From this, the superconducting DOS can be described by:

$$\frac{N_s(E)}{N(0)} = \begin{cases} \dfrac{E}{(E^2 - \Delta^2)^{\frac{1}{2}}} & E > \Delta \\ 0 & E < \Delta \end{cases} \tag{2.35}$$

where $N(0)$ is the density of states in the normal phase around $E = 0$. Around $E \approx \Delta$, the DOS is enhanced relative to the normal state, owing to the sudden formation and dissipation of Cooper pairs.
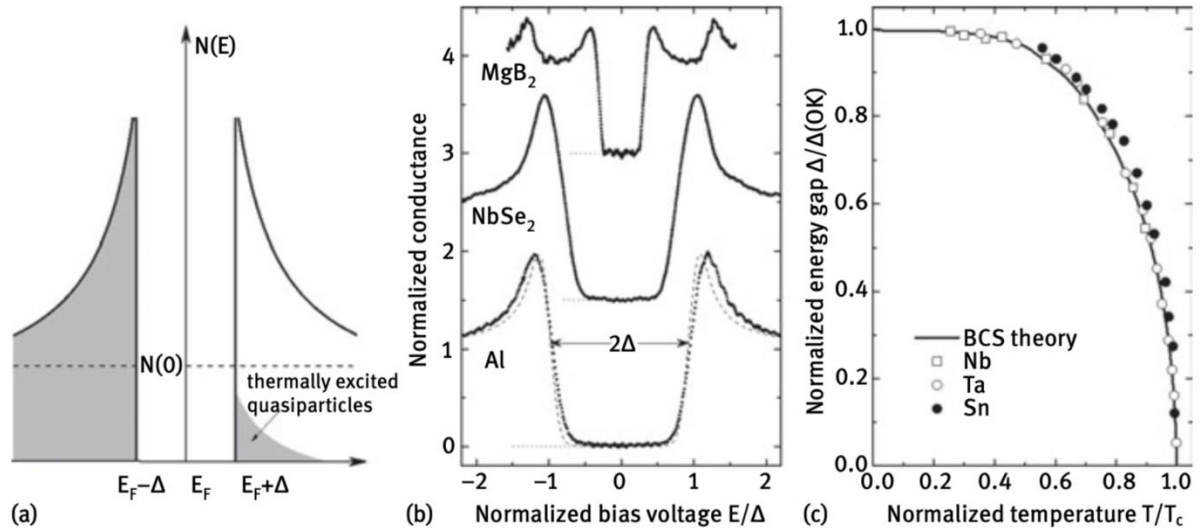
Figure 19: a) Superconducting density of states forming within a conventional metal. Finite temperature causes some excitation of single carriers above the energy gap. b) Measured Conductance through tunnelling spectroscopy for a variety of superconductors, offset from Al for visual clarity. c) Extracted Δ modelled to an 'ideal' BCS function for measured SCs in b) [100]

Figure 19a shows the single particle density of states for a superconductor for $0 < T < T_c$. An energy gap of 2Δ is opened around E_f, as per eq. 2.32. Measurement of the density of states, such as through measurements of the tunnelling conductance in the SC (Figure 19b) can be used to directly measure the size of the energy gap. The temperature dependence of the energy gap can then be used to characterise the resulting superconductor state. Ideal BCS superconductors can be modelled via eq. 2.33, such as is the case for Nb and Ta in Figure 19c.

2.9: Andreev Reflection and the Proximity Effect:

Although a superconductor is gapped, it is possible for unpaired electrons to conduct through a superconductor, via a process called Andreev reflection. Consider a heterojunction comprised of a normal and superconducting material, or NS junction. An electron incident from N to the S, with an energy $E < \Delta$. From a strictly single particle picture, transmission from N to S within this energy range is forbidden. There are no unoccupied states on the S side of the interface, forbidding the e^- from entering. Additionally, for a perfect interface, there is nothing allowing the electron to scatter and change momentum away from the surface. However, Andreev showed that in the case

of a superconductor, an unusual form of reflection occurs at the interface. [101]. Rather than simply reversing the component of the velocity normal to the interface, Andreev noted that all components reversed.
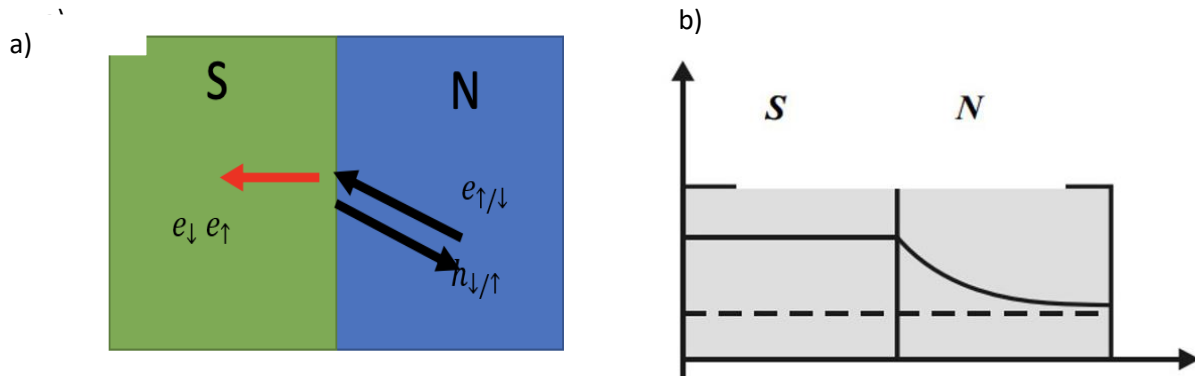
Figure 20: a) Andreev Reflection at an NS interface – an incident electron in a given spin state incident upon the interface is reflected as a hole. b) Amplitude of Superconducting wavefunction decaying exponentially away from the interface [102].

The incident particle (hole) is reflected as a hole (particle) along the path of approach Figure 20a. This process is equivalent to two electrons passing from the N to S as a Cooper Pair, carrying a total charge of $2e$ per reflection event [103].

Furthermore, when N and S regions are in close contact, it has been observed that superconductivity will extend some length into the normal material. This is known as the proximity effect. It has been observed in a multitude of materials, of widely varying structures. Cooper Pairs from the superconductor can be seen to 'leak' into the normal region [104], remaining coherent some finite length into N. This leakage is in fact attributable to the 'rigidity' of the superconducting wavefunction characterised by the Ginzburg-Landau equations (2.24a and 2.24b). Because the wavefunction cannot immediately change due to energy constraints, it will have a finite value some length into the normal phase. From (2.24b), a finite value of the wavefunction will lead to a finite supercurrent density within that region as well. It can be shown to hold even in the absence of an attractive potential between pairs that would allow the formation of new Cooper pairs. [104] There will exist an effective superconducting gap, Δ_{prox}. As with the bulk superconductor, Δ_{prox} will be proportionate to the local cooper pair density, that reduces away from the NS interface of a length scale λ_{prox}. [103]

The proximity effect is closely related to Andreev Reflection [103]. The incident electron, and it's retro-reflected hole form a phase correlated pair. The length scale over which this pair remains correlated will determine λ_{prox} [104]. The energy scale of this coherence is typically related to the Thouless Energy of the N material:

$$E_{\text{th}} = \frac{\hbar v_f l_c}{2L^2}$$
(2.36)

Where L^2 is the length of the normal region of the device [35] [105]. Owing to the dependence on l_c, the carrier mean free path, the coherence and thus the proximity length will directly depend upon the scattering properties of N material. The further from the interface, the greater the likelihood of a given pair having experienced a scattering event, the lower the pair density and thus $\Delta_{prox}(\infty) \to 0$. Materials with high mobilities, μ are expected to exhibit long λ_{prox}. This can reach the order of microns in such materials, including recently in InSb 2DEGs [35] [106] [107].
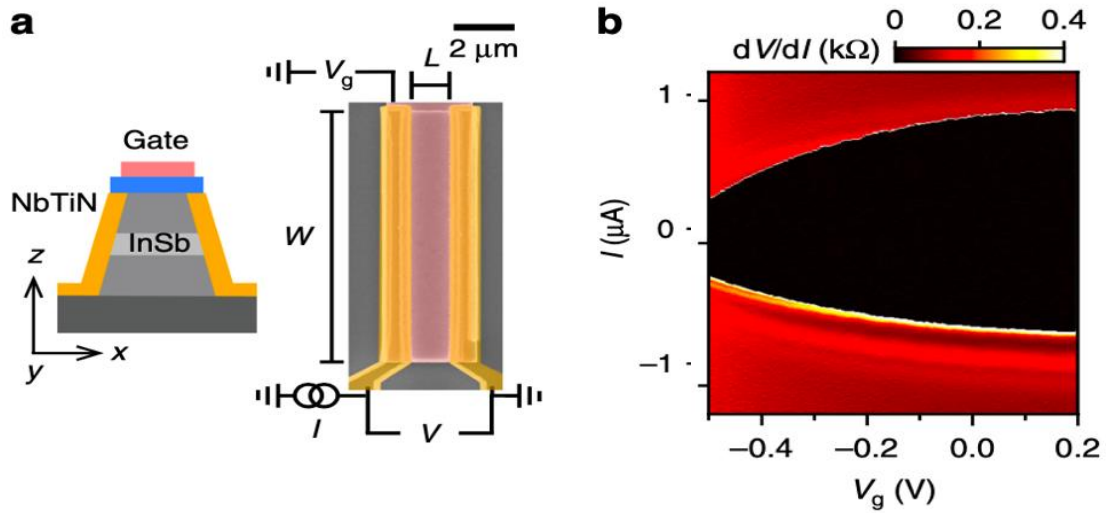
Figure 21: a) SC/InSb 2DEG heterostructure devices consisting of an InSb 2DEG with side deposition of NbTiN superconductor. Device is top gated, allowing depletion of the 2DEG carriers Measured device has dimensions $L = 1.1\mu m$, $W = 9.7\mu m$ b) Conductance measurements of device as a function of gate voltage. All figures reproduced from [35]

Figure 21 shows a measurement of such a long-range proximity induction. A top gated InSb 2DEG structure, the exact structure detailed here [108], was side deposited with NbTiN superconductor. The measured conductance (Figure 21b) showed successful induction of a superconducting gap within an $InSb$ 2DEG [35]. Such an induction was seen a across a variety of junction sizes ranging from 0.7 to $4.7\mu m$. Side deposition of the $NbTiN$ with the 2DEG ensures direct electrical contact to, and likely a relatively clean interface between the SC and the 2DEG. However, side deposition prevents the usage of side gates, such as those seen in Figure 4, to electrically confine the 2DEG. Electrical confinement to 1D is a requirement to realise devices hosting MZMs from 2DEGs and utilising them for computation. The confinement is required to ensure spatial localisation of the MZMs, and minimise unwanted interactions between MZMs. For top-down deposition, as is necessary to produce such side-gated devices, interfacial quality can have a significant impact on the conductance spectra.

2.10: BTK Theory:

The interface between two real materials is often non-ideal. It is highly likely that the interface between the N and S states will have some degree of impurity arising from

the fabrication process, such as interfacial roughness or the presence of defects between layers. The ability to characterise the interface, and assess its impact on the resulting device properties thus becomes an important consideration for experimental work considering the SN or NS interface. This problem was approached for small-scale tunnel junction devices by Blonder, Tinkham, and Klapwjik [109]. We refer reader to the following sources for a full derivation [109] [110] and will instead summarise the approach here:

$$A(E) + B(E) + C(E) + D(E) \equiv 1$$
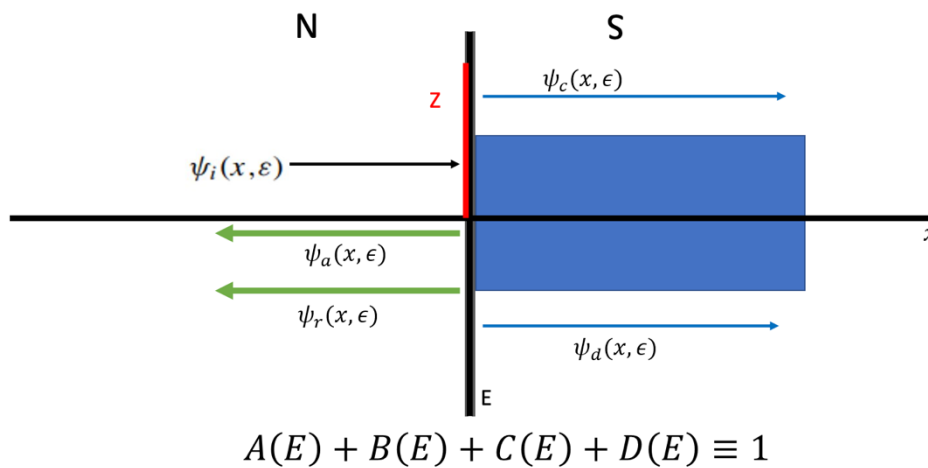
Figure 22: Illustration of the BTK theorem. An NS interface with some interfacial barrier, Z, localised entirely at the interface. An electron incident upon the interface from the N material, $\psi_i(x, \epsilon)$, has 4 possible outcomes: Andreev Reflection (A), conventional reflection (B), transmission as an electron-like (C) or hole-like quasiparticle (D).

Infinitely long 1D slices of N and S state material are brought together to form an NS interface (Figure 22). As outlined above there exists a gap of magnitude 2Δ centred around the fermi energy in S. Quasiparticles are said to be incident at the interface moving from N → S. The outcomes will depend upon the energy of the quasiparticles. If $|E| < \Delta$, single particle transmission is forbidden, and the particle will Andreev reflect. If $|E| > \Delta$ the particle will instead transmit across the barrier, although some finite probability of Andreev reflection remains. For a perfect interface, with no scattering sources, only these possibilities exist.

If the interface is non-ideal, there will be added scattering sources, such as interfacial roughness, or defects. These allow for conventional reflection in addition to Andreev reflection. To model this, a dimenionless potential barrier is added in the form of a δ

function, of height Z, localised at the interface ($x = 0$). The wavefunctions for the various processes at the interface are:

$$\psi_{incident} = \begin{pmatrix} 1 \\ 0 \end{pmatrix} e^{ik_e x} \tag{2.37a}$$

$$\psi_{reflected} = a \begin{pmatrix} 0 \\ 1 \end{pmatrix} e^{ik_h x} + b \begin{pmatrix} 1 \\ 0 \end{pmatrix} e^{-ik_e x} \tag{2.37b}$$

$$\psi_{transmitted} = c \begin{pmatrix} u \\ v \end{pmatrix} e^{ik'_e x} + d \begin{pmatrix} u \\ v \end{pmatrix} e^{-ik'_h x} \tag{2.37c}$$

Where a, b, c and d are the probability amplitude coefficients of Andreev reflection, normal reflection, and a pair of transmission processes, respectively. Solving for these four coefficients in turn give us the probabilities of each of these processes (e.g. $A = |a|^2$,) for a given incident quasiparticle. Solving the problem also requires that two boundary conditions be satisfied:

$$\psi_N(0) = \psi_S(0) \equiv \psi(0) \tag{2.38a}$$

$$\frac{\hbar}{2m}(\psi'_S - \psi'_N) = H\psi(0) \tag{2.38b}$$

Eq. 2.38a states the wavefunction must be continuous across the interface. Eq. 2.38b is the differential boundary condition across a delta potential. Additionally, the total probability of the four outcomes must sum to 1. The problem can then be solved by substituting in the requisite wavefunctions from eq. 2.37 into eq. 2.38a and eq. 2.28b and performing a series of substitutions to eliminate all the transmission coefficients one at a time and solve for the remaining one. This gives expressions for the various amplitudes as a function of both energy and barrier height. These are listed in Table 1:

Table 1: BTK Coefficient expressions for energies above and below the gap

	$E < \Delta$	$E > \Delta$
$A(E)$	$\dfrac{\Delta^2}{E^2 + (\Delta^2 - E^2)(1 + 2Z^2)^2}$	$\dfrac{u_o^2 v_o^2}{\gamma^2}$
$B(E)$	$1 - A$	$\dfrac{(u_o^2 - v_o^2)Z^2(1 + Z^2)}{\gamma^2}$
$C(E)$	0	$\dfrac{u_o^2(u_o^2 - v_o^2)(1 + Z^2)}{\gamma^2}$
$D(E)$	0	$\dfrac{v_0^2(u_o^2 - v_o^2)Z^2}{\gamma^2}$

Where $\gamma^2 = [u_o^2 + Z^2(u_o^2 - v_o^2)]^2$. Equations $A(E)$ and $B(E)$ are visualised in Figure 23 for example barrier heights of $Z = 0.0$ and $Z = 0.5$
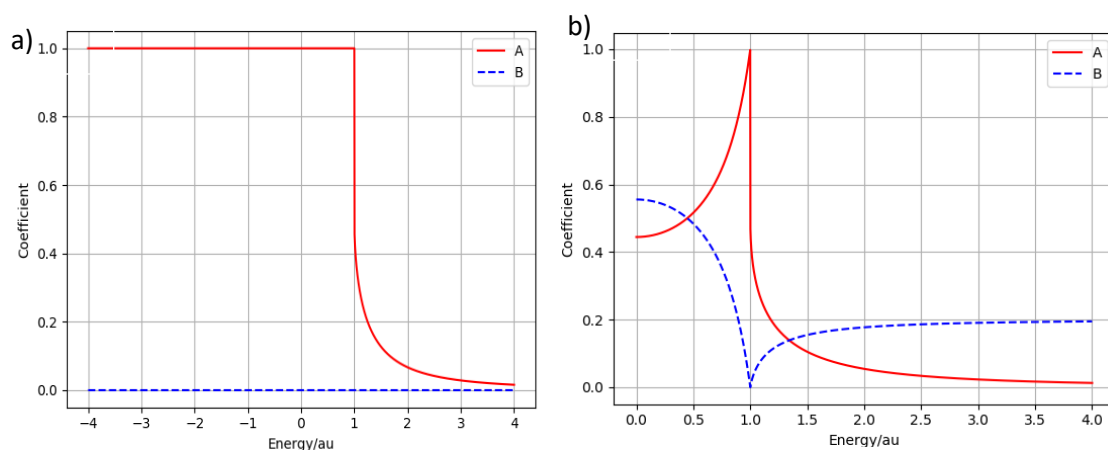
Figure 23: BTK Coefficients A and B as a function of energy. a) BTK Coefficients A and B calculated for a barrier height of Z=0. Energy scale is normalised to units of Δ=2.532meV b) Z=0. All other factors held constant.

As the barrier height increases, the probability of Andreev Reflection decreases whilst the probability of normal reflection increases. This holds for all sub gap energies, save for $E = \Delta$. Here Andreev Reflection, even when taken to extremes limits of Z, will still occur with a significant probability.

Although not the first to treat this as a tunnelling problem, BTK theory expanded upon prior works by calculating I-V curves from these coefficients [111] [112]. They considered the relative difference in carrier populations caused by the application of a finite voltage. This is then filtered using the BTK coefficients to describe the proportion of electrons at a given energy contributing to net current flow by passing through the barrier. This gave the expression:

$$I = \frac{G_o}{e} \int^{\infty} [f(E) - f(E + eV)][1 + A(E) - B(E)] \, dE \qquad (2.39)$$

Where G_o is the normal state conductance, $f(E) = \frac{1}{e^{\frac{E-mu}{k_b T}} + 1}$, V is the applied voltage. Calculation of this at different voltages allows for the calculation of IV characteristics, and in turn differential conductance curves.
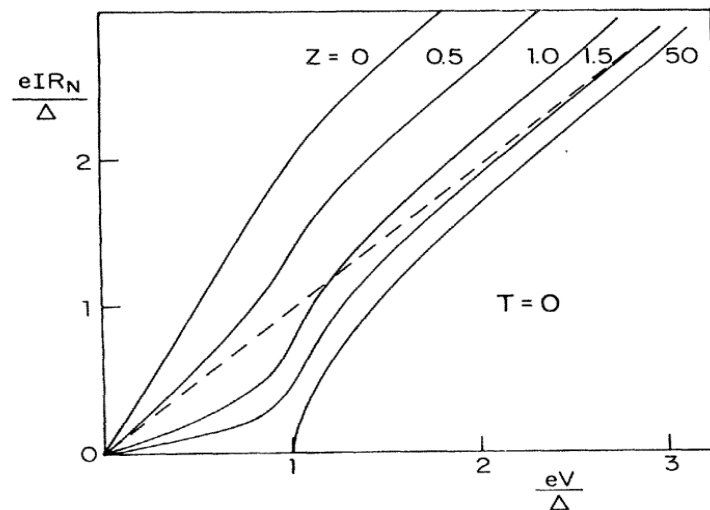
Figure 24: IV curves as a function of Z. Current values at each step are calculated using (16) and are normalised for the sake of comparison. The dotted line is an extrapolation of the conductance at high energies to the intercept [109].

Figure 24 shows calculated IV curves for various barrier heights. The increasing barrier height serves to increase the resistance, and hence decrease the conductance, of the superconducting region. A large barrier, such as the $z = 50$, practically supresses current flow through the junction during the superconducting region. Additionally, the conductance can be seen to be asymptotic as show by the dotted line

in Figure 22. The conductance will deviate highly from the normal state, until approaching high carrier energies. The difference in currents between the normal state and the superconducting state is known as the excess current, or $I_{excess} = (I_{NS} - I_{NN})_{eV \ll \Delta}$. In terms of the co-efficients, this is described by:

$$I_{excess} = \frac{1}{eR_N[1 - B(\infty)]} \int_0^\infty [A(E) - B(E) + B(\infty)]dE \qquad (2.40)$$

Measurement of the excess current through the junction in theory allows for quantification of the quality of the junction as a function of temperature. In practice, it is a difficult value to measure. Measurement of I_{excess} requires precise measurement of the normal state resistance. This often requires the application of voltages many times larger than the energy gap to ensure the sample is in the purely normal resistive state, which will contribute to sample heating [109].
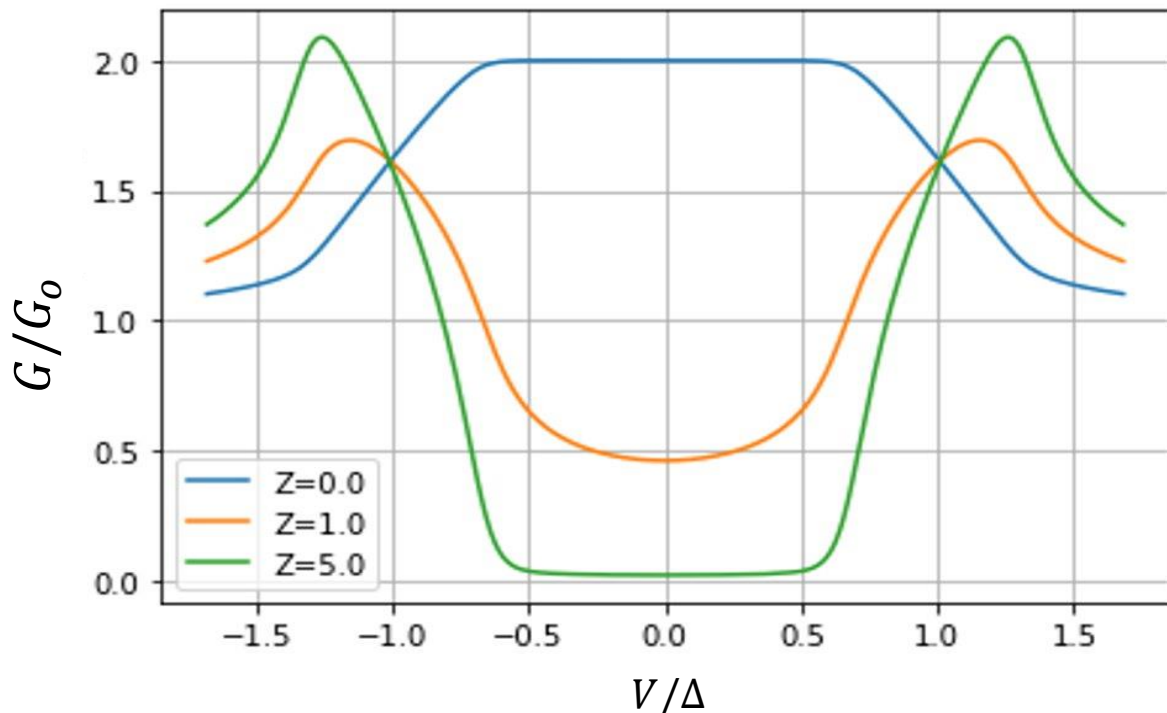
Figure 25: Normalised conductance calculated for an arbitrary N-S junction via the BTK theorem for a series of barrier heights, Z.

Eq 2.40 can also be used for measurements of conductance, illustrated in Figure 25. Injection of the electrons into a superconductor through a perfect interface should lead

to a conductance of twice the normal state conductance, i.e. the carriers are injected as a Cooper pair of two electrons via Andreev reflection. As established, the presence of a barrier supresses the probability of Andreev Reflection lowering the conductance. Sufficiently high barriers can supress the conductance within the energy gap below the conductance of the normal state for an equivalent barrier.

Differential Conductance is an easily measured experimental quantity via AC modulation techniques. With the appropriate measurement set-up, this theory allows for non-intrusive qualitative measurement of interface quality and superconductor gap simultaneously. This analysis has been used extensively in point contact measurements of superconductors, and variations of the theory have been applied to wide varieties of S-N-S junctions [113] [114] [115] [116] [117]. Additional amendments to the theory have extended it to alternate superconducting gap functions with different symmetries. [118] [119]. It is particularly useful in combination with fabrication, as it allows for efficient and qualitative assessment of device quality.

2.11: Superconducting Pairing in Proximity Superconducting Materials:

Finally, we want to combine all this together to consider how the proximity superconductor state can exhibit exotic superconducting pairing required for topological technologies. In section 2.7, we described BCS theory and the formation of a superconducting state for a cooper pair of two electrons of opposing spin and momentum owing to it being energetically favourable. The pairing of opposite spin states means that the pairing function describing this is a spin-singlet state.

It is not the only possible spin momentum combination possible for a superconductor. It is also possible to generate spin-triplet pairing states, pairing electrons in spin combinations of ↑↑, ↓↓ and ↑↓. The wave functions describing these states will exhibit different parity – spin singlet states will be even parity, and the spin triplet states odd parity. Other than s-wave, the pairing most relevant to this work is the $p_x + ip_y$ triplet pairing state, owing to its necessary role in realising MZMs. Innate $p_x + ip_y$ is exceedingly rare in nature [10]. However as mentioned, the proximity superconducting

state induced in a high SOC material by a conventional s-wave superconductor has been shown theoretically to exhibit this pairing [120].
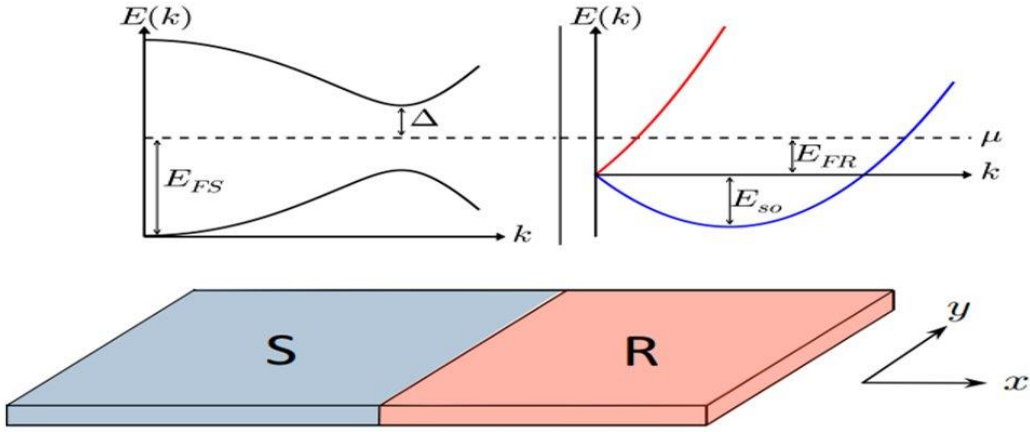
Figure 26: Interface between a superconductor S, and a high Rashba SOC material. Pictured above is the dispersion relation for each material. Blue and red in the Rashba material indicate the two spin states. [121]

The triplet state arises in these materials from the lifting of spin degeneracy, which SOC does at all points other than $k = 0$. We can, as we did with eq. 2.37 in describing the BTK equation, consider an electron incident at the interface between a high Rashba SOC material and a superconductor (Figure 26). A full derivation of such a system can be found in [121]. To briefly summarise the approach undertaken, consider an incident wave ψ_i, we can write the waves on each side of the interface as:

$$\psi_{N(x,E)} = \psi_i + a_\uparrow(E)\begin{pmatrix}0\\0\\1\\0\end{pmatrix}e^{ik_{\uparrow h}^L x} + a_\downarrow(E)\begin{pmatrix}0\\0\\0\\1\end{pmatrix}e^{ik_{\downarrow h}^L x} + r_\uparrow(E)\begin{pmatrix}1\\0\\0\\0\end{pmatrix}e^{ik_{\uparrow h}^L x}$$

$$+ r_\downarrow(E)\begin{pmatrix}0\\1\\0\\0\end{pmatrix}e^{ik_{\downarrow h}^L x}$$

$$\psi_{S(x,E)} = t_1(E) \begin{pmatrix} u_o \\ 0 \\ 0 \\ v_o \end{pmatrix} e^{iq_+x} + t_2(E) \begin{pmatrix} 0 \\ u_o \\ -v_o \\ 0 \end{pmatrix} e^{iq_+x} + t_3(E) \begin{pmatrix} v_o \\ 0 \\ 0 \\ u_o \end{pmatrix} e^{-iq_-x}$$

$$+ t_4(E) \begin{pmatrix} 0 \\ -v_o \\ u_o \\ 0 \end{pmatrix} e^{-iq_-x}$$

Where ψ_N describes the total wavefunction incident from the Rashba material, ψ_S is total wave wavefunction incident from the superconductor, $a_{\uparrow/\downarrow}$ is the probability coefficient of Andreev reflection for electrons in the two spin states, $r_{\uparrow/\downarrow}$ the probability coefficient of regular reflection, and t_n are the probability coefficients for transmission of carriers from the S into the Rashba material. In all cases ψ is a four-component wave function, describing the ↑/↓ spin states of particle like and hole like states. We can apply the same boundary conditions to the problem as 2.29, for an incident spin up electron:7

$$\psi_i = \begin{pmatrix} 1 \\ 0 \\ 0 \\ 0 \end{pmatrix} e^{ik_{\uparrow e}^R x} \qquad \text{(2.41a)}$$

And an incident spin down electron:

$$\psi_i = \begin{pmatrix} 0 \\ 1 \\ 0 \\ 0 \end{pmatrix} e^{ik_{\downarrow e}^R x} \qquad \text{(2.41a)}$$

Solving these boundary conditions gives expressions for the amplitudes of Andreev and normal reflection as:

$$a_\downarrow(E) = -\frac{v_{F\uparrow}}{v_{F\downarrow}} a_\uparrow(E) \qquad \text{(2.42a)}$$

$$r_\uparrow(E) = \frac{(u_o^2 - v_o^2)(v_{F\uparrow}v_{F\downarrow} - v_{FS}^2) + v_{FS}(v_{F\uparrow} - v_{F\downarrow})}{(u_o^2 - v_o^2)(v_{F\uparrow}v_{F\downarrow} - v_{FS}^2) - v_{FS}(v_{F\uparrow} - v_{F\downarrow})} r_\downarrow(E) \qquad \text{(2.42b)}$$

Where $a_{\uparrow/\downarrow}$ and $r_{\uparrow/\downarrow}$ are Andreev and normal reflection amplitudes for an incident electron in one of the two spin states, $v_{F\uparrow/\downarrow}$ is the fermi velocity in the normal material

for carriers with the two spin states, and v_{FS} is the fermi velocity in the superconductor. Eq. 2.42a states Fermi velocity mismatch between electrons in the two spin states, which arises from the lifted degeneracy, can make Andreev reflection for one state more favourable than other. Eq. 2.42b states similarly for regular reflection,

Additionally, this opens the possibility for the formation of a triplet pairing wave function, defined as:

$$\Delta(x, x', E) = \frac{1}{2}[\Delta_{\uparrow\downarrow}(x, x', E) + \Delta_{\downarrow\uparrow}(x, x', E)] \sim v_{\uparrow}(x, E)u_{\downarrow}^*(x', x, E) \qquad (2.43)$$
$$+ v_{\downarrow}(x, E)u_{\uparrow}^*(x', E)$$

Which is the average of the pairing function of the two opposing spin states. The wavefunctions defined in 2.41 can be substituted into this pairing term:

$$\Delta_t(x, x', E) \approx a_{\uparrow}\left[e^{-ik_{\downarrow e}^R x'} + r_{\downarrow}^* e^{-ik_{\downarrow e}^L x'}\right]e^{ik_{\uparrow h}^L x} \qquad (2.44)$$
$$+ a_{\downarrow}\left[e^{-ik_{\uparrow e}^R x'} + r_{\uparrow}^* e^{-ik_{\uparrow e}^L x'}\right]e^{ik_{\downarrow h}^L x}$$

And finally, the relations found in 2.43 can be substituted into 2.44 to give a final triplet pairing function:

$$\Delta_t(x, x', E) \approx a_{\uparrow}\left[e^{-ik_{\uparrow e}^R x}e^{-ik_{\downarrow e}^L x'} - \frac{v_{F\uparrow}}{v_{F\downarrow}}e^{-ik_{\downarrow e}^L x}e^{ik_{\uparrow h}^R x'}\right] + a_{\uparrow}r_{\downarrow}(e^{ik_{\uparrow h}^L x}e^{-ik_{\downarrow e}^L x'}) \qquad (2.45)$$

$$-a_{\uparrow}r_{\downarrow}(\left(\frac{v_{F\uparrow}}{v_{F\downarrow}}\frac{sgn(E-\Delta)(u_o^2-v_o^2)(v_{F\uparrow}v_{F\downarrow}-v_{FS}^2)+v_{FS}(v_{F\uparrow}-v_{F\downarrow})}{sgn(E-\Delta)(u_o^2-v_o^2)(v_{F\uparrow}v_{F\downarrow}-v_{FS}^2)-v_{FS}(v_{F\uparrow}-v_{F\downarrow})}\right)e^{ik_{\downarrow h}^L x}e^{-ik_{\uparrow}}$$

This pairing is only non-zero when $v_{F\uparrow} \neq v_{F\downarrow}$, i.e. when spin degeneracy is lifted. Triplet SC thus arises directly from lifted spin degeneracy. SC-Ferromagnetic systems, with completely lifted spin degeneracy, have shown experimental signatures of triplet SC [122] [123].

As discussed, in section 2.9 when considering the proximity effect, the properties of the proximity SC state will be determined by the electrical properties of the N material. As such, the electron population comprising a SC state induced in a QW with high

SOC will itself experience high SOC. In Rashba materials, the SOC only lifts spin degeneracy for finite momentum. Proximity SC in Rashba materials should thus be comprised of a mixed state between conventional singlet and triplet SC pairing elements, even if the superconductor itself is purely a singlet state [124] [125].This mixed state forms the basis for high SOC devices to form the basis to host MZMs providing the system can be tuned such that it is predominantly a triplet state [126].

The two components exhibit different responses to an externally applied magnetic field [122]. The singlet component should be supressed. In physical terms, the applied field causes spin alignment with the field, making formation of ↑↓ pairs energetically less favourable. Associated with this suppression will be the formation of a screening current, opposing the field within the proximity SC as described by eq. 2.21 .

The triplet component will be resistant to this field and may even exhibit a slight enhancement. Again, the alignment of the spins with the field will make it energetically favourable to form Cooper pairs with the same spins. Instead of a screening component, an anti-screening current will form, increasing the local magnetic field [10] [127]. The larger the triplet component within the material, the greater this enhancement, and the larger the anti-screening current. As such a predominantly triplet SC may see a net increase in Magnetic field within the proximity material comparative to the size of the external field [128]. Magnetic field is thus a vital component in the realisation of MZMs, as by lifting the remaining spin degeneracy, the system can be shifted to predominantly host triplet SC [126].

As such, measurement of the magnetic field within a high SOC proximity superconductor, as well as the variation of the magnetic field response can allow for some inference as to the mixed state nature of the induced SC state. Characterisation of the exact field behaviour, and the H_c of the induced state is of vital experimental importance.

Chapter 3: Fabrication methods and measurement techniques

3.0: Overview:

Many of the samples measured within this work required device fabrication within the ICS cleanroom facilities at Cardiff. This chapter seeks to overview the top-down fabrication techniques used to provide full context for the work that will follow. Additionally, this chapter will cover the commonly used measurement apparatus and techniques used in later chapters.

3.1: Photolithography:

Fabrication of micro-electronics and optical devices can be done in primarily two routes – top down or bottom-up [129] [130]. Bottom-up fabrication techniques involve gradually building up a complex structure layer by layer, or directly growing such structures, such as growth of nanowires via Vapor-Liquid-Solid techniques. [131]. This work instead used top-down fabrication methods. Top-down fabrication involves taking a complex substrate, and selectively removing elements, typically via etching, to leave a final device. In our case, we use $InSb$ heterostructures grown by molecular beam epitaxy, or MBE [132]. MBE utilizes a series of evaporators containing different elemental or compound sources. The sources are heated, to produce a flux of a given element, and the resulting flux at a substrate is controlled via a series of shutters. This allows for selective and controlled growth of a sample. MBE has extensive usage for the growth of $InSb$ wafers. [59] [133] [134] [135]. From these grown wafers, to make our devices, it is necessary to define an active area, or structure. This is done via lithography, and in our case, photolithography.
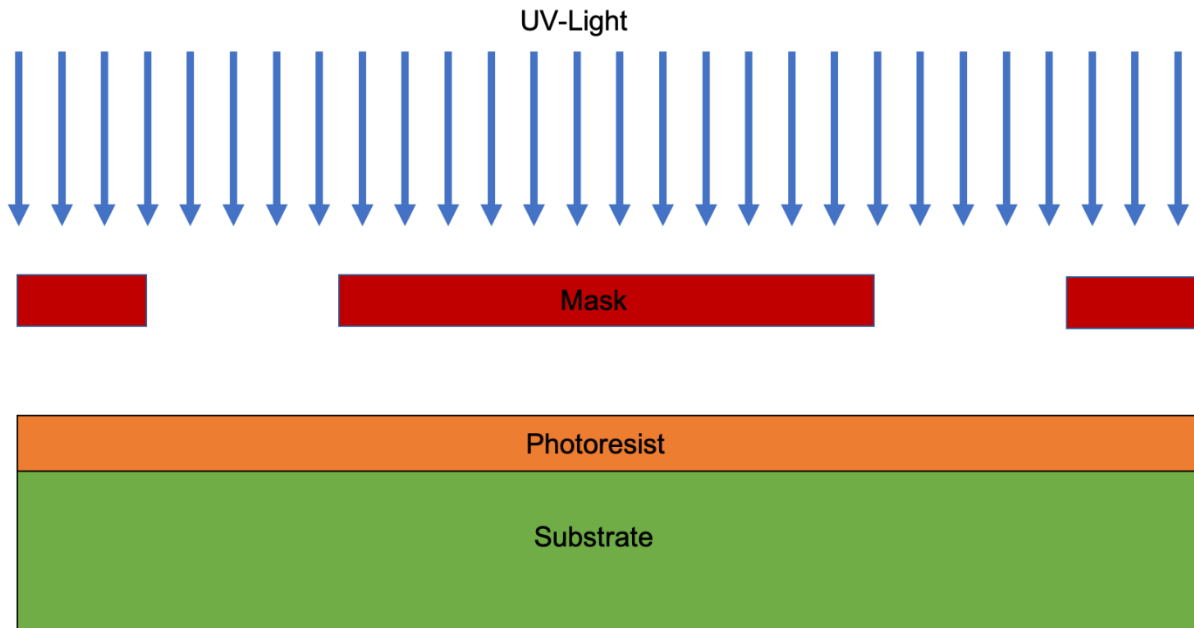
Figure 27: Schematic overview of Photolithography

Photolithography uses light exposure, typically through a mask, to define a structure in a thin layer of polymer (Figure 27). The polymer, known as a photoresist, is applied to the surface of the sample. High energy light, typically in the UV range, is shone perpendicularly to sample surface through a mask. The mask functions as a stencil, allowing light through some areas of the sample, whilst shielding others from exposure.
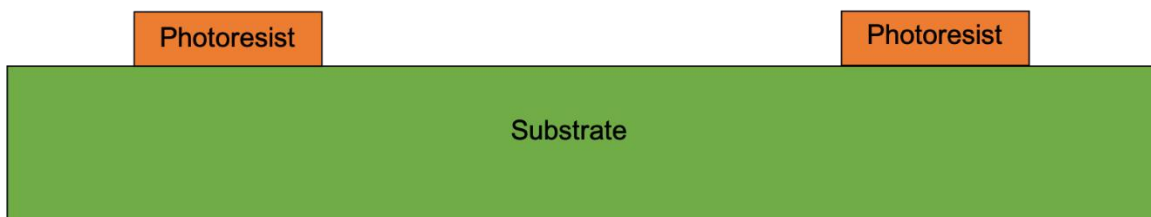
Figure 28: Post exposure and development of the lithography undertaken in Figure 26.

This exposure defines the desired device within the photoresist. The light is sufficiently energetic to alter the polymer chains within the photoresist. By soaking the sample post exposure in solvent, the undesired polymer can be removed, leaving only select segments of photoresist as defined by the mask (Figure 28). This process is known as 'developing'.

3.1.1: Sample Preparation

Sample cleanliness and surface preparation are important for high quality photolithography. The presence of defects, dirt or excess photoresist from previous fabrication stage on the sample surface can greatly impact the resulting lithography. Mask alignment often requires close contact with the wafer surface for high resolution lithography, as diffraction through the mask grating can smear out features if there is uneven separation between the mask and sample.
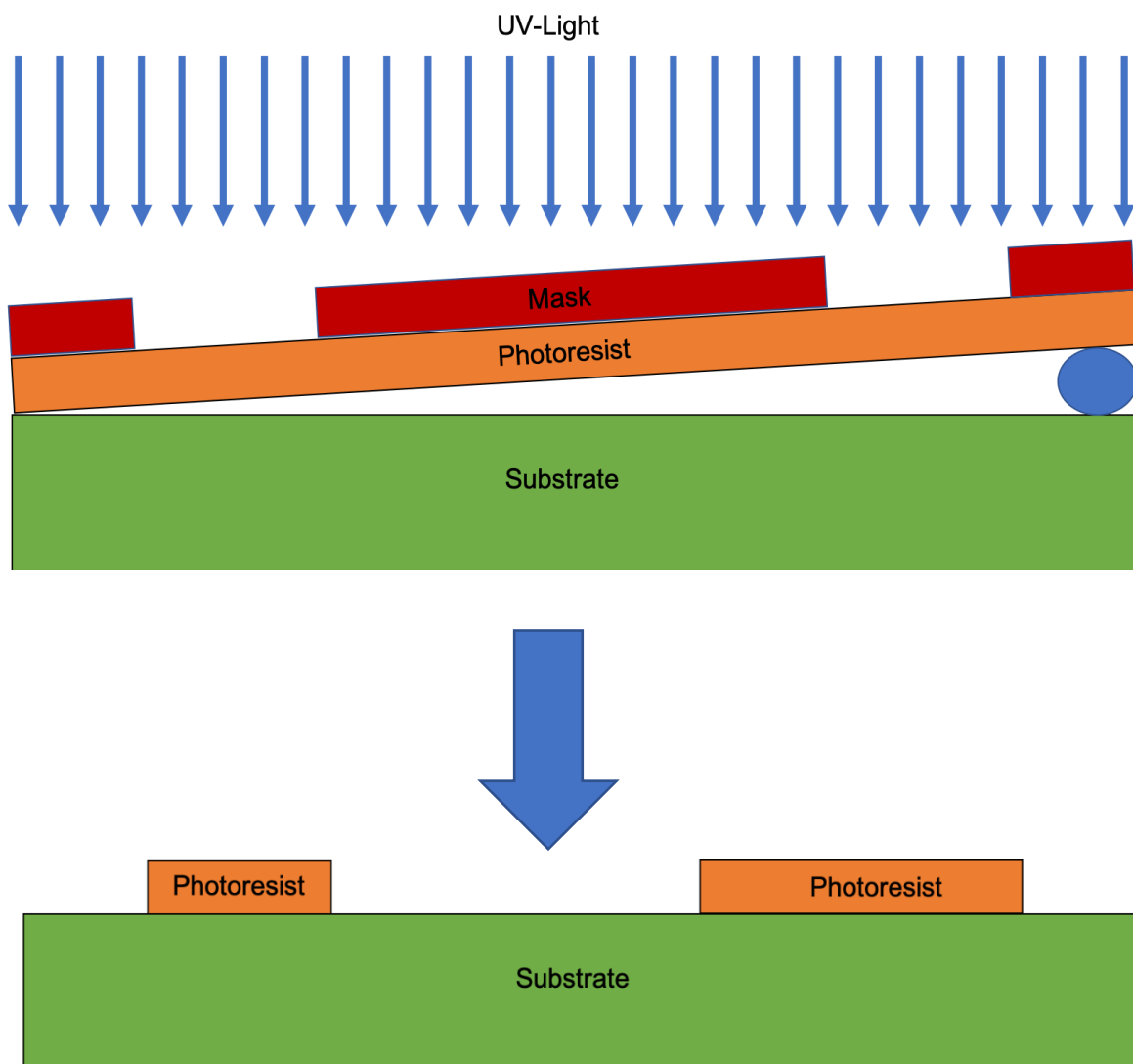
Figure 29: An example of mask misalignment owing to the presence of surface defects (Blue circle). Bottom) Resulting lithographic features – feature size is now non-uniform owing to diffraction.

If for example, there exists some dirt underneath the resist, when contact between with the mask may leave it non-parallel to the sample surface (Figure 29). As different

elements of the mask have different separations from the surface, diffraction will result. This will lead to non-uniform feature sizes across a sample and will lower the overall possible resolution. Additionally, for small features, large defects may damage the ultimate device structure – by being present where a feature is desired. As such, extensive sample cleaning is required prior to any fabrication to ensure a high-quality device.

The standard cleaning procedure used is a solvent clean: submersion of the sample in Acetone followed by Isopropanol alcohol (IPA). Acetone dissolves many possible organic dirt molecules present on the sample. An IPA rinse/soak removes the acetone and prevents the formation of any acetone residue on the surface. If necessary, this step can be augmented with the use of an ultrasonic bath to add a more abrasive element.

Additionally – water can interfere with photoresist. Many photoresists are hydrophobic, and as such water can reduce adhesion [136]. To prevent this, samples are baked on a hot plate over $100^o C$ for several minutes, to evaporate any moisture. In the case of $InSb$ structures, some care must be taken with the temperature of this bake. High temperatures can cause elements of the structure to diffuse, undermining the integrity of the 2DEG [137]. For all sample processing undertaken throughout this work, care is taken to keep the $InSb$ temperature at or below $100^o C$.

3.1.2 Positive and Negative Resist:
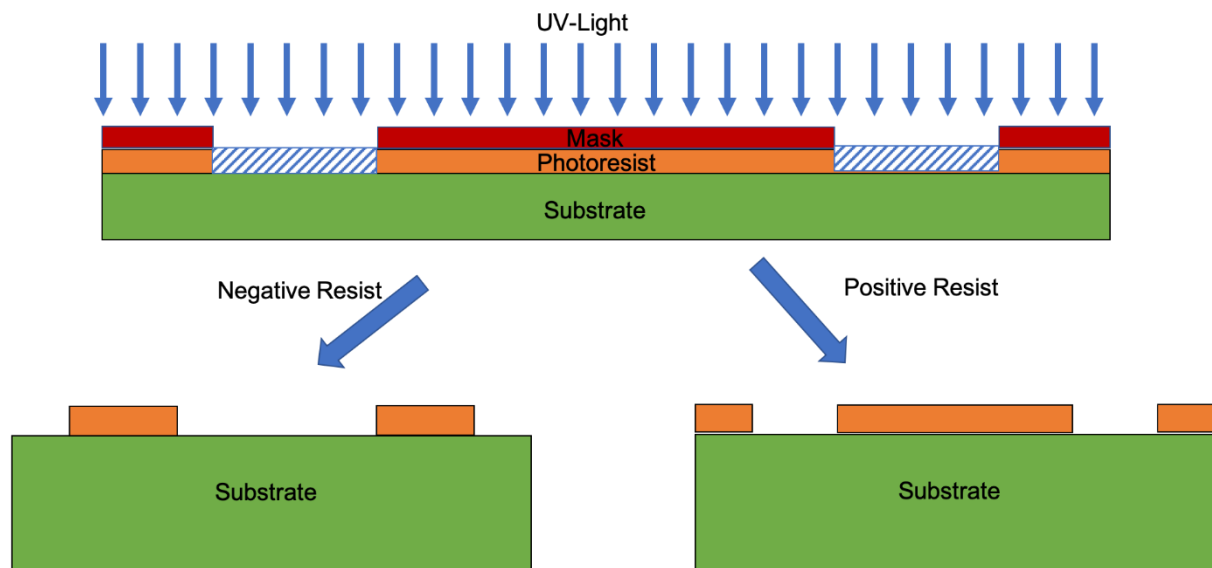
Figure 30: Exposure and Development with positive and negative resist.

With a suitably clean sample surface, photoresist can be applied. Photoresists typically consist of a polymer suspended in solvent [138]. Two main types of photoresist exist, positive tone and negative tone. Functionally, they differ in their response to UV exposure (Figure 30). Positive (negative) tone-resist, when exposed to light becomes more soluble (insoluble) to the resist developer [139] [140] [141]. As such, exposure will create holes(mask). This difference arises from the chain lengths of the polymers present in each – positive resist consists of long chains that are broken down by UV exposure, whilst negative resist consistent of short chains linked in response to light exposure [142] [139]. Choice of resist depends upon the feature being designed – negative resist can allow for higher resolution of smaller features. This work uses the negative tone resists, AZ2020 and AZ2070.

Resists are applied via spin coating [143] – Samples are coated in the resist, and then spun at high speeds. In our case, typical spins of ~ 5000 RPM for upwards of 30-45s were undertaken. The process leads to a generally uniform film of resist across the sample, with a tendency of increased thickness occurring at sample edges, known as edge beading [144]. Resist thickness – which has a significant impact on feature resolution and can be a limiting factor for processes such as metal deposition – is largely determined by this spinning process. Thinner resists, such as AZ2020 can lead to higher resolution optical features but limit the thickness of deposited metals [138]

[145] [141]. Once spun, the resist coated sample is often baked once again to evaporate any remaining solvents within the resist. Additionally, resist adhesion can be improved via the application of an adhesion promoter prior to the resist, applied in much the same manner as the resist itself [146]. Where relevant, this work used TI Prime as an adhesion promoter.

3.1.3: Exposure and Development:

The photoresist is patterned via exposure to light the wavelengths of which is dictated by the resist of choice [147] [148] [149]. Typical photolithography, as discussed, uses UV light shone through photomasks - glass plated with Cr to block light in select segments [150]. The masks are defined with specific patterns to work with specific resist tones. Mask Aligners are used to bring mask and sample into alignment, such SUSS MicroTec MJB3 and MJB4 Mask Aligners. These operate largely as outlined in 3.1.1, generating light via a 350W Mercury lamp and allow for precise control of mask separation and exposure time as necessary [137].

Rather than use these more traditional techniques, this work instead uses a Durham Magneto Optics direct writer (DMO). The DMO allows maskless photolithography [151] [152]. Instead of using a mask and exposing the sample surface uniformly through it, the DMO uses a laser on a moveable stage. The stage can be moved, allowing specific areas of the sample to be exposed at different times, known as image projection [153]. This DMO can take a predefined pattern and map it onto a wafer surface – exposing each element of the wafer surface according to the pattern. Although the total exposure time is longer than that of mask lithography, the design can be modified without requiring the fabrication of a new mask. This makes it ideal for fast prototyping of new designs and structures. This made it the preferred process for the fabrication of our novel superconducting devices, as it allowed adjustment of the design in response to various difficulties and successes in the fabrication process.

Post exposure samples are again baked, to set the altered polymer chains, and thus set the pattern. Following that, the resist is soaked in a developer, which serves to

remove the unexposed negative tone resist. This work used AZ726 as the developer of choice with typical total development times of $90s$.

3.2: Etching:

The patterns are defined in photo resist to protect certain elements of a wafer from further processing steps. Chemical etching is one such step – often a requirement to electrically isolate devices from the surrounding substrate. The etching utilizes chemical reactions to gradually strip away elements of the substrate. The resist functions as a mask for this process. Resists are such that it etches more slowly than the surrounding substrate – a property known as etch selectivity. By doing so, one can etch exposed areas of a sample without damaging the material underneath the substrate. There are two branches of chemical etching utilized in micro-electronic fabrication, wet and dry, and both will be considered here [154] [155].

3.2.1: Wet chemical etching:
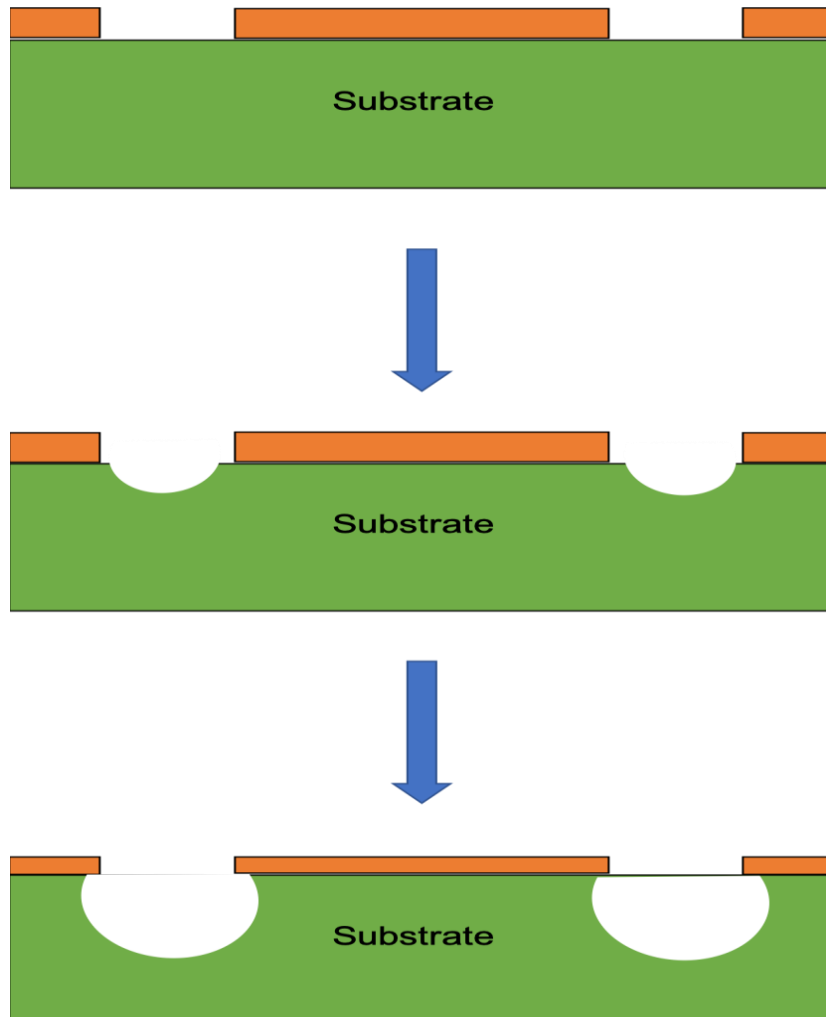
Figure 31: Wet etch example. a) Structure defined by photolithography. b) Etching begins in the unmasked areas of the susbtrate. c) final etch profile, indicating the undercut of the resist, and the slight etching of the resist layer.

Wet etching typically involves submersion in solutions of acid. They are often isotropic, etching in all directions without bias [156]. The isotopy of a wet etch often depends on the given crystallographic orientation [157]. For this work, we can consider purely isotropic etches, an example of this is included within Figure 31. The isotropic etch leads to undercutting of the resist. The undercutting can be used purposefully, to create air-bridge gates and contacts of structures [158]. However, for deeper etches, this can lead to issues with undercutting undermining the device, leading to collapse,

or 'float off' of the intended structure, and critical failure of the process. Wet etching is a commonly used etching technique for III-V semiconductors such as $InSb$. [159] [160] [161] [134] In this work, wet chemical etching is performed using a citric acid etch designed for surface treatment of $InSb$ samples [162] [163].

3.2.2: Dry Etching – RIE and ICP:
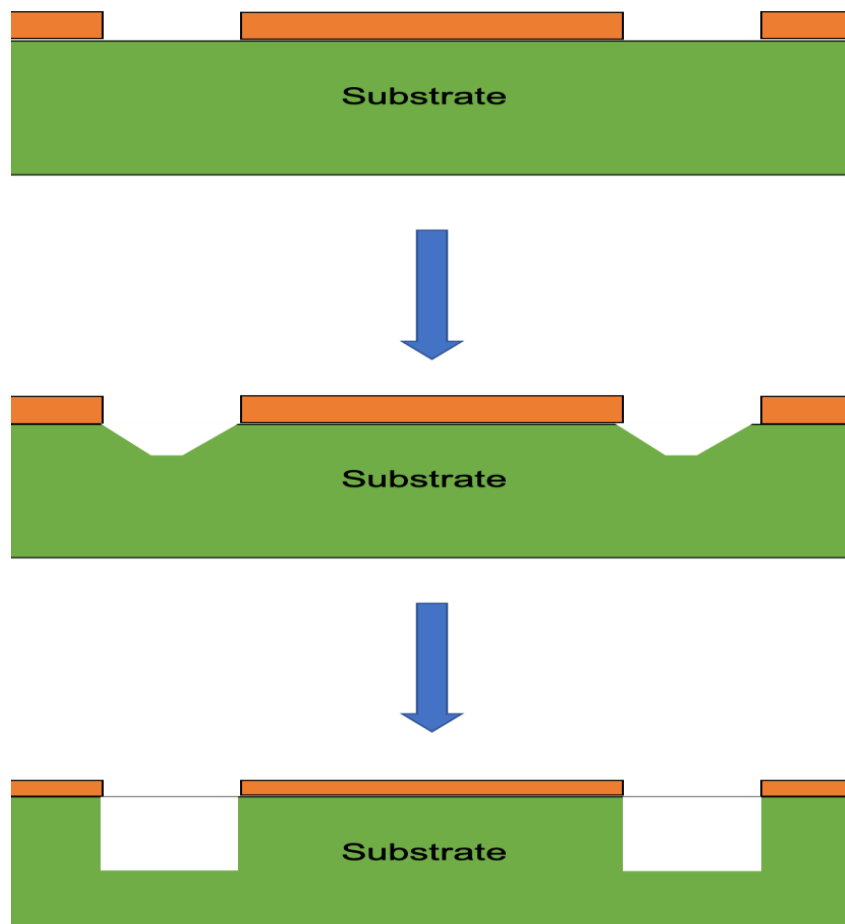
Figure 32: Dry etch example a) a) Structure defined by photolithography. b) Etching begins in the unmasked areas of the substrate. c) final etch profile, indicating the sharp side walls and the slight etching of the resist layer

Dry etching, rather using a liquid solution of acids, uses mixtures of gases [164] [165]. The dry etch process undertaken in this work primarily uses Reactive Ion Etching (RIE) with an Inductively Coupled Plasma (ICP) [166] [167]. A gas of a given chemistry is pumped into a sample chamber. Within the chamber, exist two electrodes – with the

sample placed to lie upon the negative electrode. An rf voltage is applied between these electrodes which ionizes the gas to form a plasma. The ions within the plasma, which are positively charged, are then accelerated towards the negative electrode. This acceleration gives the ions high kinetic energy. This added kinetic energy gives the ion sufficient energy to overcome the activation energy of the etch process. The rf voltage causes this acceleration to happen repeatedly, etching the sample as it does. In an ICP system, versus others such as an Capacitively Coupled Plasma, the gas is ionized away from the sample – allowing for the sample electrode to be biased independently of the requirements to ionize the plasma, allowing higher plasma densities at lower biases [168] [169]. A more detailed overview of RIE, including practical concerns with the usage of RIE systems can be found in the following source [170]

One advantage of dry etching relative to wet etching is that the etch profile is typically anisotropic, with minimal undercutting [171]. This leads, ideally, to sharp side walls in the etch. Again, whilst advantageous for preservation of fine features, it prevents potential applications from the undercutting, and well as having typically lower etch rates than equivalent wet chemical processes [155].

3.3: Superconducting Thin film deposition:

In order to have superconductor/semiconductor heterostructures, SC films must be deposited upon the 2DEG structures, ideally of high quality. Metal deposition for this work primarily occurred via two different apparatus in two different sites.

Deposition of these films was performed by sputtering [172] [173]. Sputtering utilises bombardment of a target source via a high energy gas or plasma. In a similar fashion as to the ICP discussed in section 3.2.2, the target is to be the negative electrode, and the sample set to the positive electrode. The gas is ionized by collisions and directed at the target by the electrical charge. The ion bombardment causes energy transfer from the gas to the atoms in the target, which is sufficient to eject them from the surface of the target. The released atoms can be directed towards a given sample substrate, where they condense, coating it in the targeted material. The ion bombardment also

causes the release of so called 'secondary electrons' from the target [174]. Sputtering is a commonly used technique for the deposition of thin films atop semiconductors [175] [176]. Many varieties of sputtering techniques exist, which use a variety of power sources and orientation [174]. For this work, an important type is Magnetron Sputtering.

Magnetron Sputtering aligns a magnetic field parallel to the target surface. The magnetic field constrains the secondary electrons to the vicinity of the target surface [177]. The secondary electrons, through further collisions increase the local density in the region around the targets surface. This in turn increases the ion bombardment rate, which improves the overall efficiency of the deposition process [177]. Magnetron sputtering thus allows for higher deposition rates, at lower operating pressures and voltages [177].

For the deposition of the Nb, a custom ultra-high vacuum sputtering kit utilising DC Magnetrons was used at Bristol University, details of which can be found here [178]. This equipment offered a wide range of metals, including but not limited to Al, Co, Fe, Hf, Tb, Nb, Ti and Zr. The system exhibited deposition rates typically greater than $1 \dot{A}s^{-1}$ allowing for growth of 25mm diameter uniform films with a variety of thicknesses extending up to $\sim \mu m$. InSb 2DEG samples were mounted on Molybdenum plates, loaded, and pumped to system pressures of less than $< 10^{-9}mbar$. In order to prevent the previously mentioned diffusion of $InSb/AlInSb$ layers above $100^{o}C$, sputtering occurred with the sample held at room temperature. Some warming is likely to have occurred during sputtering but is unlikely to have significantly increased the sample temperature. 99.999% Pure inert Ar gas, with a sputtering pressure of $8 \times 10^{-3}mbar$ and sputtering power between 20-50W was used to deposit the Nb. Film thickness was measured externally post deposition via x-ray reflectivity measurements. Additionally, a sample used for characterisation of Nb etch process was deposited at UC Santa Barbara.

The Pb was deposited at the Neils Bohr Institute in a dedicated metal deposition chamber connected to a solid-source Varian GEN-II MBE system, used for similar deposition in [179]. The $InSb$ sample is mounted on a GaAs substrate using a Ga

droplet for loading purposes. The Pb deposition was performed using in-situ electron beam evaporation of a Pb target via a Thermionics HCL e-Gun kit. For deposition, samples were cooled to nominal substrate temperatures of -153^oC, though due to the sample mounting method, the actual surface temperature of the sample was found to be $\sim 20^oC$. Pb deposition rates were measured in-situ with a INFICON quartz crystal to be $1.4nm/s$. The same equipment was used to deposit an additional Al layer atop the Pb, to both protect the sample surface, and prevent dewetting of the Pb during sample removal [180]. During this deloading, the Al layer was purposefully allowed to oxidise to Al_2O_3 to function as an additional protective layer for the Pb surface.

3.4: Sample Packing and wire bonding.

Once fabricated, samples are mounted into $1cm^2$ 20 pin gold ceramic chip carriers, adhered to the base with GE Varnish. GE varnish ensures good thermal contact to ceramic base, which is ideal for cryogenic measurements. Inner cavity size limited maximum sample size to $\approx 0.5cm^2$.

Figure 33:West Bond wire bonder used for gold-to-gold contacts.

Bonds from sample to the contact pads used a West Bond wedge bonder (Figure 33). The bonder was modified to be purely manual, with minimal abrasive force. This is primary used for gold-to-gold bonds and is particularly useful in cases where the sample contact pad consists of thin gold layers. More abrasive bonders, with added mechanical force, could often tear off deposited gold contacts if the layers were thin. Additionally, this was used to bond the connections to the gold pin contacts on the chip carriers. The sample stage is heated, and the wire is adhered to a heated crystal tip. The crystal tip is then pressed against the sample contact pad. The combination of heat and pressure melts the gold wire into the contact pad, forming strong electrical contacts whilst minimizing abrasion. Silver conductive epoxy was used to bond to the sample surface

3.4: Optistat Cryostat:
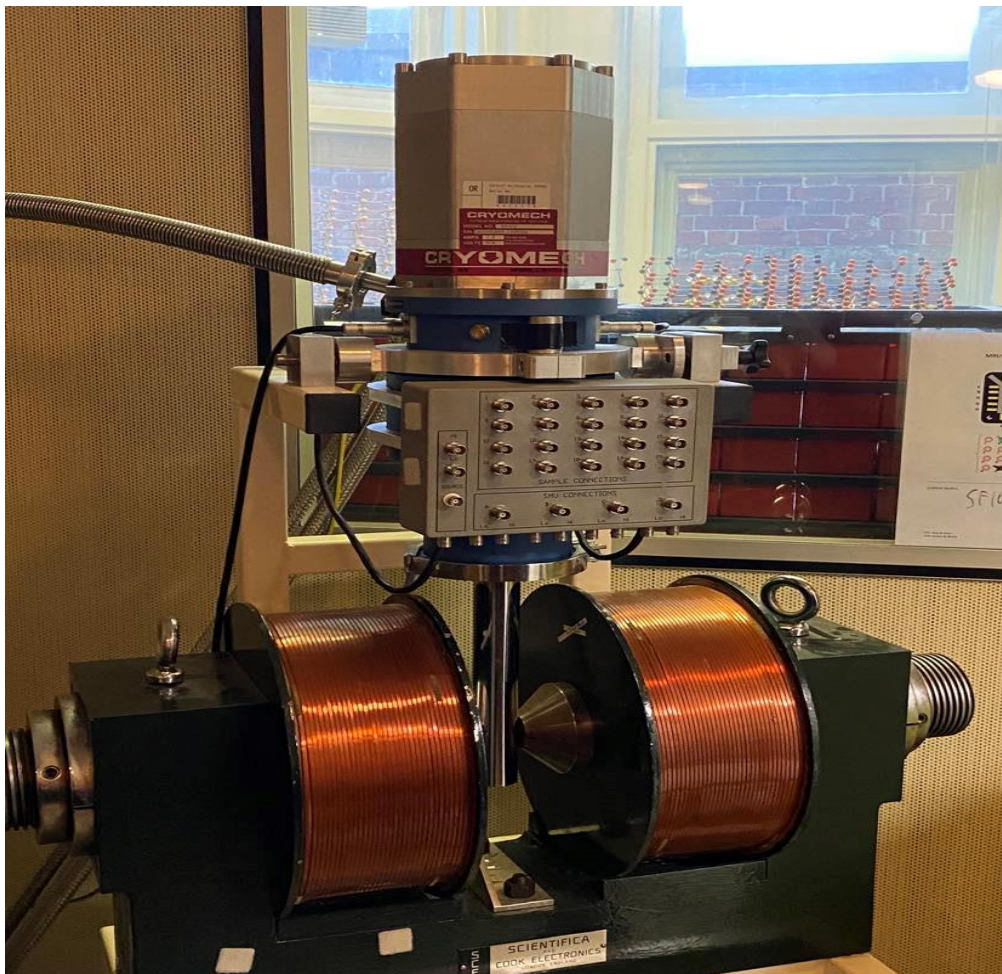
Figure 34: Optistat cyrostat system in sealed state. Featured are the cold head, attached to the cold finger, which is orientated between the poles of two magnets. Sample sits at the end

of the cold finger, such that it lies in the centre of the two poles. Breakout box allows connections to the sample configured as per the 20pin carrier chips. Additional tri-axial and BNC connections for voltage and current supply are also present.

The bonded samples chips are mounted into a Oxford Instruments Optistat AC-V12 cryogenic system (Figure 34). The sample environment is held under vacuum by a Aerlikon Leybold vacuum turbolab 80 basic turbomolecular pump with an oilless compressing backing pump to achieve a base pressure below $5 \times 10^{-5} mbar$. A combination of Cryomech, Inc PT403 cold head and a water cooled Cryomech Inc CP830 helium gas compressor provides the cooling power. It is a liquid cryogen free system, capable of reaching base temperatures of $2.8K$ within a few hours.

The pulse tube cryostat cools via the expansion of the flow of He gas through the system. The compressor compresses the gas, sending it to the cryogenic environment. Expansion of the gas extracts heat from thermally coupled cold plates, then cycling it out, where a heat exchange cools the incoming gas, and warms and compresses the outgoing gas. The system contains two cold plates. The first is connected directly to the cold head, which i combination with the pulse tube cools from 75K to 40K.

Figure 35: Second cold plate – Heater and thermometer are mounted in the copper blocks for thermal contact with the plate and cold finger.

The second cold plate then reaches base temperature. A copper cold finger with the sample mounting is attached to the second cold plate for good thermal contact. Also attached are a resistive heater and a Rhodium-Iron thermometer. The thermometer is calibrated to control the sample temperature, and the heater is controlled remotely with a Mercury iTC Temperature Controller. The Mercury is programmable via USB, accepting fully autonomous control via Python.
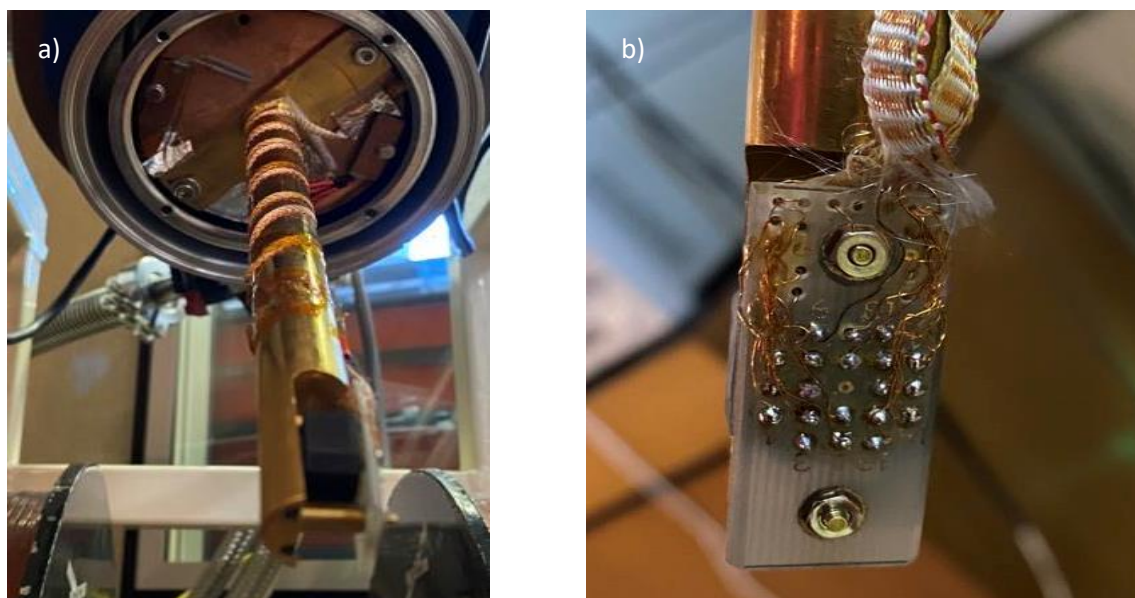
Figure 36: a) Sample holder puck, mounted at the end of the cold finger. Wires from the sample are wound round the cold finger leading to the breakout box for electrical connection. b) back of the sample holder. Screws fix holder in place, flush against a cooper block for thermal contact. Electrical contact between the wound wires and sample holder occurs here.

The sample holder is mounted in a puck, with wires thermally anchored to the cold finger to minimise excess heat conduction along the wires (Figure 36). Wires then exit the cryostat via 10 pin Fischer connectors. The cold finger can be rotated up to 45° out of the pole of the magnets to allow for easier sample loading and un-loading.

When unrotated, the cold finger sits between the poles of two large magnets (Figure 34). The sample holder is aligned such that the field is produced such that it goes through the cross section of any loaded sample. Current for the field is controlled via a combination of Magnetic Relay Unit, and an Agilent technologies N5751A DC power supply. Field values are calibrated via a polynomial generated via measurements with a Hall Probe between the coils. It is capable of generating fields of up to 0.8T can be

generated with suitable poles. As with the temperature controller, the magnet is controlled remotely via python.

3.5: DC and AC measurement techniques
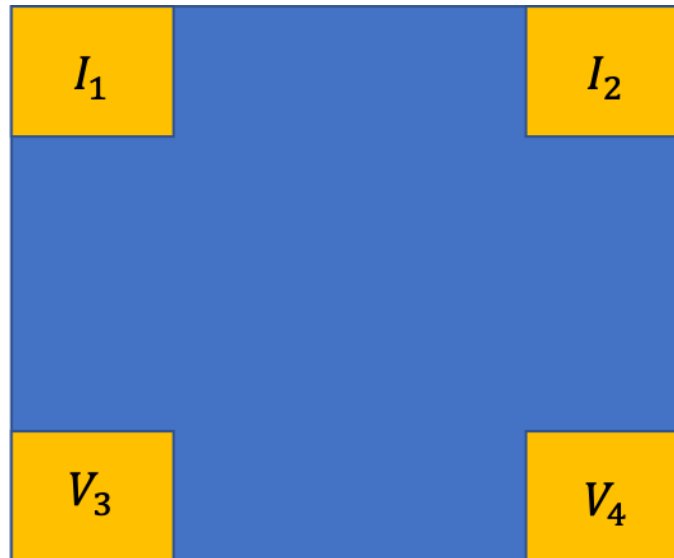
Figure 37: Van der Pauw measurement geometry. Four equivalent electrical contacts (yellow) are placed in each corner of a square sample (blue). Current is supplied from $I_1 \rightarrow I_2$ and voltage measured from $V_3 \rightarrow V_4$.

Where possible, measurements of superconducting samples utilised a four-contact measurement technique with a Van der Pauw measurement geometry [181] [182] (Figure 37). Current is supplied along one edge of the sample, e.g. $(I_1 \rightarrow I_2)$. The contact at V_3 will be an equipotential with the contact at I_1. Similarly, V_4 will be an equipotential with I_2. As a result, measurement of voltage V_{34} will give a measurement of the sample voltage without sourcing a current from either contact. From this, sample resistance can be found via:

$$R_{12,34} = \frac{V_{34}}{I_{12}}$$

(3.1)

This method allows direct measurement of the sample resistance, rather than the combination of sample, wire and contact resistances.

DC electric measurements utilized two different sets of equipment. A combination of a Keithley 6221 AC and DC current source and a Keithley 2182A nanovoltmeter. The

other was an Agilent Technologies E5270B 8 slot precision measurement mainframe. In such a case, the Agilent was used to both source the current and record the voltage.

Additionally, AC measurements were undertaken as part of this work. For this, a Stanford Research Systems Model SR830 lock-in amplifier was used as an AC voltage source, typically at $13.7 Hz$. A bias resistance was placed between the voltage source and the sample, allowing control of the size of the supplied AC current. The AC voltage response is then also measured via the Lock-In amplifier. Measurement of the AC voltage response then allows calculation of the resistance across the sample. With the application of an additional DC current source and an additional bias resistance, an offset current could be supplied as necessary. This allows direct measurement of sample resistance as a function of applied bias, and resultingly measurement of the sample conductance. This allows, for instance, for measurement of the energy gap in a superconductor. For such measurements, the offset is provided via an DC output on the lock-in amplifier, providing DC voltages in the range $\pm 10V$.

In both AC and DC measurements, automation of the measurements were performed using python code, via GPIB connection, often in combination with control of the system temperature and magnet.

Chapter 4: Fabrication and measurement of Gapped Nb/InSb Heterostructures.

4.0: Motivation and context

As discussed at length in Chapters 1 and 2, there is a great deal of technological and scientific interest in the construction of devices supporting proximity SC in high SOC materials [23] [33]. Many existing approaches to this problem involve the fabrication and usage of hybrid SC-semiconductor nanowires [15] [33]. However, nanowires are often difficult to fabricate, and fabrication of defect free nanowire networks remain challenging [183] [184]. 2DEGs with additional electrical confinement via gating are a scalable, and potentially controllable alternative approach to realise 1D conducting states [185] [186][101]. 2DEG fabrication is well suited for industry, and the ability to selectively restrict and confine segments of material gives full control of the resulting device [27]. Successful inductions of SC into active layers of 2DEGs have been measured, and it is a growing field of work [186][101] [27] [35]

As part of this, development of top-down fabrication of proximity superconducting devices is an important material step for future work, as well as allowing for detailed characterisation of the induced state. This work focuses specifically on the attempted fabrication and measurement of Transition Line Measurement, or TLM, devices using an $InSb$ 2DEG and a Nb superconducting film.

4.1: Transmission Line Measurements as a probe of superconductivity:

A Transmission Line Measurement is a measurement technique typically utilised to measure the contact resistance between an electrical contact and a semiconductor

[187] [188] [189]. It serves as a quantitative assessment for the quality of a contact, which is useful for fabrication of quality Ohmic contacts [190].
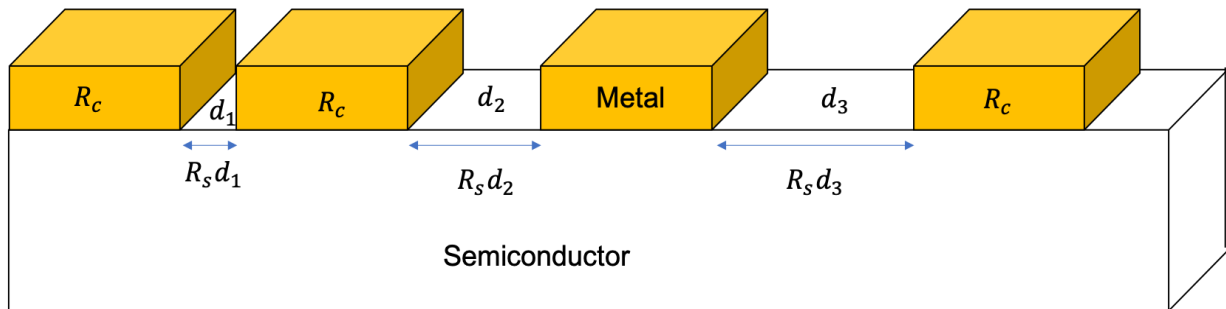
Figure 38: Schematic diagram of a TLM measurement. A series of identical metallic contacts, with contact resistances R_c, deposited on a semiconductor substrate, with sheet resistance R_s, separated by spacings $d_1, d_2 \dots d_n$, where $d_n < d_{n+1}$.

TLM measurement use a series of identical conductive contacts, often metals, with increasing spacings (Figure 38). The total resistance, R_{Tot} measured between any pair of contacts will be given by [187]:

$$R_{Tot} = \frac{R_s}{Z} d + 2R_c \qquad (4.1)$$

Where R_s is the sheet resistance of the material, R_c is the contact resistance, Z is the width of the contact pads, and d is the separation between pads, or resistive length. R_c will typically include both the resistance between the metal and the semiconductor, as well as any resistance between the pad and the electrical contact used for measurement, e.g. a bonded gold wire. Thus, measurement across pad separations will allow extraction of both R_s and R_c separately [191].
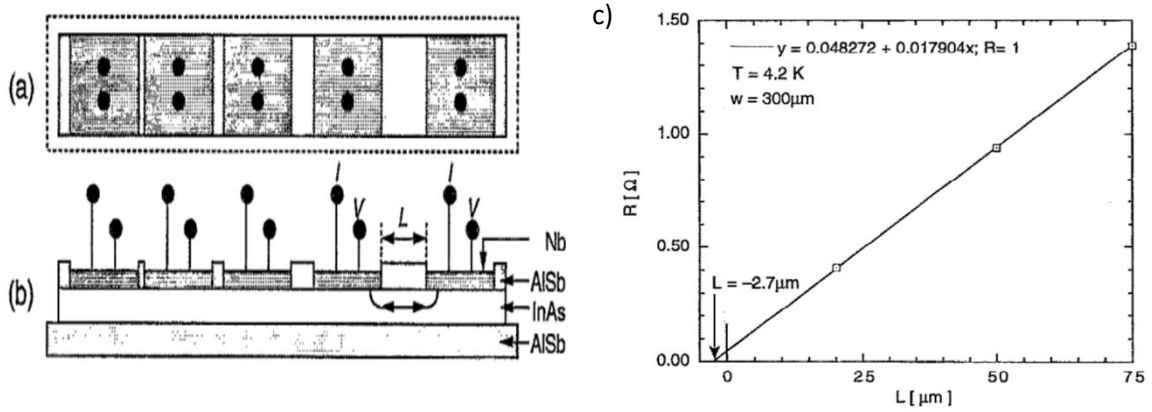
Figure 39: Superconducting TLM structure a) Top down view b) Cross sectional view [192]. c) Zero bias resistance vs gap length of a) at $T = 4.2K$, below T_c.

Such a device can be made with superconducting contact pads. Figure 39 has an example of such a device using Nb contact pads sunken into an $AlSb/InAs$ heterostructure to allow for adjacency between the SC and the $InAs$ QW. If the contact pads are made of superconducting material, below T_c, the pads will go to superconducting, reducing R_c. Additionally, if there is proximity superconductivity extending some length, λ_{prox}, into the semiconductor, the effective resistive length between the contact pads, d, will be reduced. This will in turn lower R_s. In the limiting case where the proximity SC covers the entire pad separation, $d \approx 2\lambda_{prox}$, we should in fact expect there to be no measured R_s. A plot of R vs d for various gap sizes will thus be shifted relative to the normal state, and the x-intercept should correspond to λ_{prox}. Figure 39c is data from such a measurement, across SC gaps in the range of $20 - 200\mu m$ giving $\lambda_{prox} = 3.0 \pm 0.5\mu m$ [192].

The aim of this chapter of work, was thus to fabricate a set of TLMs with superconducting pads. With such a set of devices, we seek to characterise the induced superconducting state across a series of different gap widths, and estimate λ_{prox}.

4.2: Quantum Well Characterisation
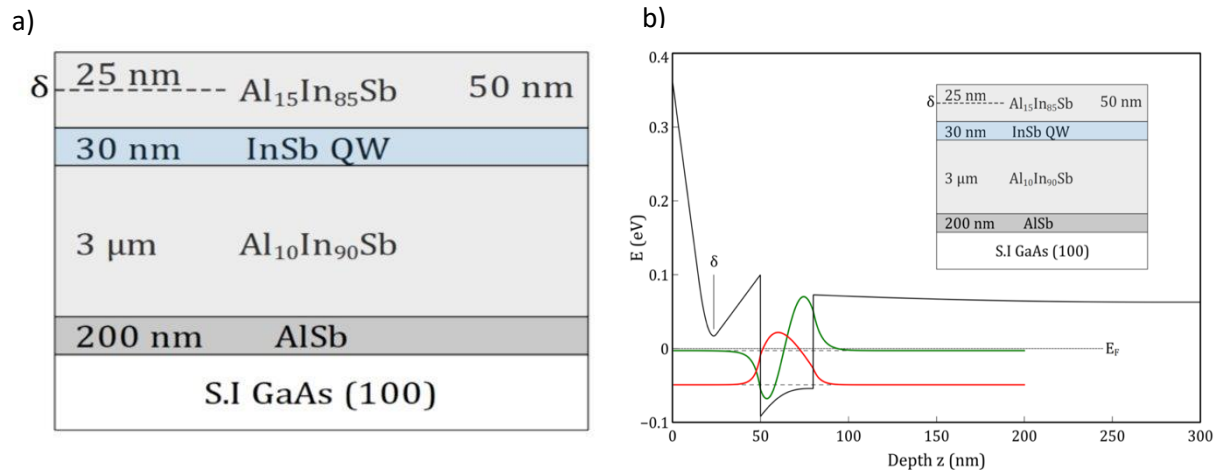
Figure 40: a) Cross section of 2DEG Structure used. δ indicates approximate location of the Te doping layer. b) Schrodinger-Poisson simulations of such a typical QW structure. Red (Green) line indicates first (second) bound state within the QW. Both figures adapted from [37], which includes full details of the modelling.

Typical 2DEGs used throughout this work consist of an $InSb$ quantum well (QW) electrically confined by layers of $Al_xIn_{1-x}Sb$ either side of it. A Te delta doping layer (Figure 40a) is localised within a few nm in the middle of the top cap to remote dope the well and enhance the conductivity. Schrodinger-Poisson modelling of the band structure of such structures are shown in Figure 40b, suggested good electrical confinement within the QW [37]. For sufficiently high levels of doping, confinement can be sufficient to allow a second sub-band of states. In this example, the sub band exists within the QW, however for highly doped samples it can instead be localized to the δ doping layer instead. This modelling is reproduced from [37], and further discussions of such calculations can be found in [137]. Characterisation of 2DEG properties was performed via Hall measurements.
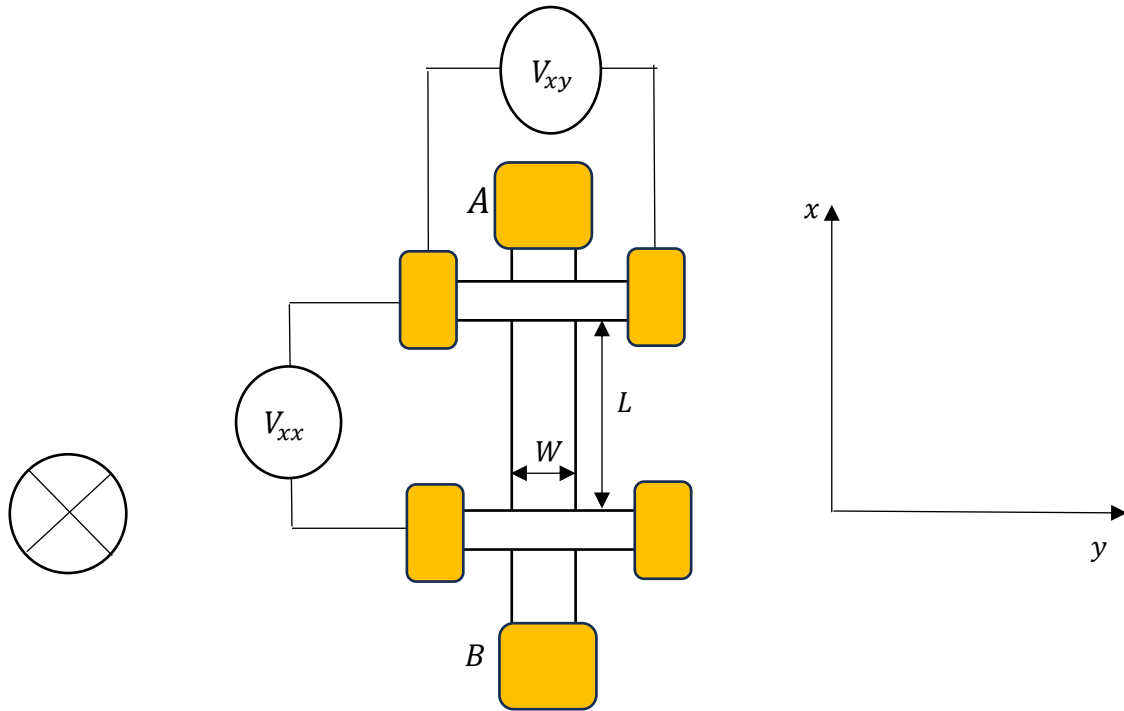
Figure 41: Schematic of Hall Effect measurements undertaken on a typical Hall Bar sample. A magnetic field is applied into the page aligned along the Z axis, and voltages across (V_{xy}) and along the bar are recorded (V_{xx}). Contact pads are indicated by the yellow squares.

A constant current, I_x is sent along a Hall bar via contacts A and B (Figure 41). Because they are moving in a B field, the carriers experience a Lorentz Force, F, given by:

$$F = q\boldsymbol{E} + q(\boldsymbol{v} \times \boldsymbol{B})$$

(4.2)

Where q is the carrier charge and $\boldsymbol{v}$ is the electron drift velocity. $\boldsymbol{B}$ can be aligned entirely along z without any loss of generality, express eq. 4.2 as:

$$F = q\boldsymbol{E_y} + q(\boldsymbol{v_x B_z})$$

The electrons experience a net force in the y direction owing to the B field, causing a charge imbalance between the two sides of the 2DEG. This charge imbalance leads to an electrical field E_H in opposition to F, and measurable voltage, V_{xy} Eventually, the system will reach an equilibrium state, where the induced Electrical Field and Lorentz Force are equal and opposite, i.e.

$$\frac{eV_{xy}}{W} = e(v_x B_z)$$

We can express v_x in terms of the electrical current flowing through the 2DEG using:

$$I_x = nev_x w$$

Where n is the carrier density of electrons. Thus:

$$V_{xy} = \left(\frac{I_x B_z}{nte}\right) \tag{4.3}$$

Where t is the thickness of the conducting bar. For 2DEGs, due to the dimensional confinement along the growth axis, this thickness can be disregarded, and the extracted carrier density will be the sheet carrier density, n_{sheet}. Assuming constant current, a measurement of V_{xy} as a function of applied magnetic field will allow extraction of n. Furthermore, by measuring the resistance along the Hall Bar, R_{xx} and finding the resistivity ρ_{xx} we can use, $\sigma = ne\mu$ to calculate the mobility of our samples. This analysis thus gives large amounts of information from a relatively simple measurement technique and has long been used to characterise $InSb$ and other semiconductor materials [193].

Fabricated samples contained Hall bars with dimensions $L = 200\mu m$, $W = 40\mu m$, and $L = 100\mu m$, $W = 20\mu m$. Hall bars used in this work were fabricated, and temperature characterisation were undertaken by prior members of our research group, the full details of which can be found here [37] [137]. Sample chips containing 20 total Hall Bars were mounted in 20 pin gold pin chip carriers, with electrical connections created by manually bonded gold wires to 10/300nn Zn/Au contacts deposited by evaporation. Measurements occurred in the Optistat 12A cryostat environment. A current of $I_x = 2\mu A$ was supplied via a Keithley 2100. V_{xx} and V_{xy} were recorded via a Keithley 6212B multimeter. Magnetic fields up to 0.85T were supplied perpendicularly to the sample cross section. Measurements utilized δ-mode averaging, recording 32 points for DC

currents of $\pm I_x$, alternating between positive and negative, to average out thermal variations during measurements.
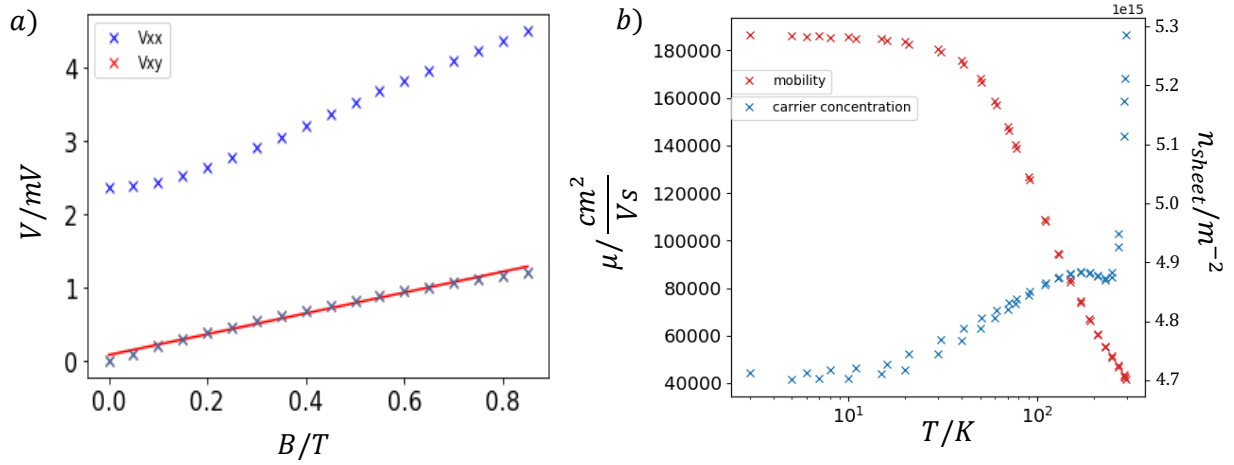
Figure 42: a) Hall Voltage, and longitudinal voltage as a function of field. A straight line is deemed a satisfactory fit to the measured Hall Voltage. b) Extracted mobility (red) and carrier concentration (blue) of measured Hall Bar. Temperature characterisation was performed part of work prior to this thesis [137] [37].

Figure 42a shows a Hall measurement at 293K, with a linear fit to V_{xx}, From these measurements we obtain n at $T = 293K\ of\ 5.28 \times^{15}\ m^{-2}$, and μ in the range $50,000\frac{cm^2}{Vs}$. Measurements across the full temperature range Figure 42b gave mobilities and carrier concentrations of $n_{sheet} = 4.71 \times 10^{15}\ m^{-2}$ and $\mu = 187,000\frac{cm^2}{Vs}$ respectively at 3K. These are consistent with high quality InSb 2DEGs present within the literature [194] [195]. With characterised 2DEGs available, we can now consider the deposition and characterisation of our other material component, the superconductor.

4.3: Superconducting Thin Film Deposition and Characterisation

A wide variety of superconductors have been trialled in the literature with $InSb$ structures. Common choices include Al, Nb and $NbTiN$ [196] [35] [197] [33]. Other less common choices include Pb and Sn [198] [199]. For our purposes, Nb and Al were the main options owing to ease of availability. Al is a constituent component with our 2DEGs. As such, there was the possibility of having a fresh 2DEG grown with an

epitaxially deposited layer of Al on the surface grown in situ [196]. This would have ensured a clean interface between the Al and the $InSb$. However, Al has $T_c \approx 1.2K$, which is outside the available range of the Optistat Cyrostat, adding significant experimental complications [200]. Additionally, there were some concerns about the potential degradation of such Al thin films. Previous works had shown that Al thin films directly onto $InSb$ heterostructures often exhibit degradation [201] [202]. In the extreme case, even samples stored under vacuum can fully hybridise the Al thin film within a few months although some success had been found in minimising this via the addition of a buffer layer on the order of a few monolayers [202]. As the facilities and time needed to redesign and optimise our 2DEGs to incorporate such a monolayer were not available, we decided on using Nb as our superconductor of choice.

Additionally, the choice was made to have the superconducting film deposited on top of the 2DEG structure. Many of the other works in the field, such as the $InSb$ nanowires discussed in Chapter 1 (Figure 4), and the $InSb$ 2DEGs discussed in Chapter 2 (Figure 21) utilised side deposition of superconductor [18] [35]. However, as discussed there, top deposition will be a necessity to utilise the side gates required to realise a controllable 1D conductance state in an InSb 2DEG.

Nb was deposited at Bristol university as described in Chapter 3. An initial film thickness of $100nm$ was chosen after examination of the literature. The film thickness was measured in situ and verified via surface profilometry. For this, a spot of PMMA photoresist was placed on the surface of $InSb$ 2DEG heterostructure prior to deposition. This was removed post deposition, and the resulting step height between the Nb and the $InSb$ surface measured. Additionally, to consider any initial substrate effects on the films, a control sample was deposited in the same process. This consisted of an Nb film grown on a glass substrate. The samples were mounted in the Optistat cryostat and cooled to base of 3.0K.4-terminal IVs were taken as a function of temperature using a Keithley 2100A power supply, and a Keithley 6221B multimeter.
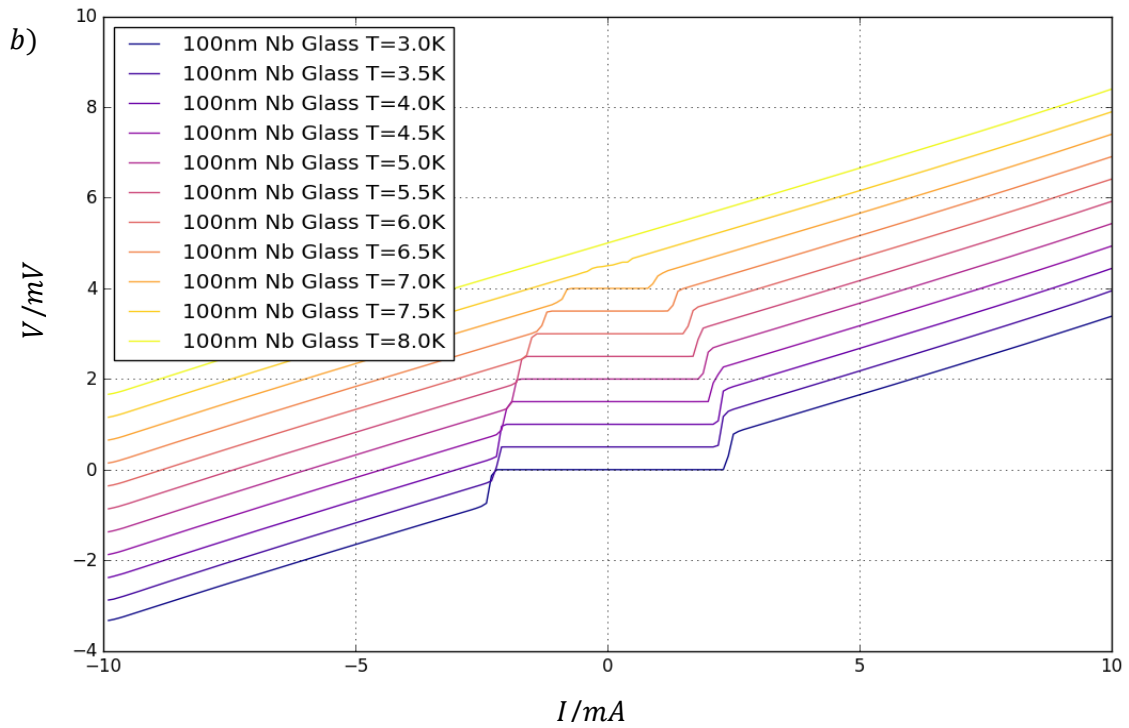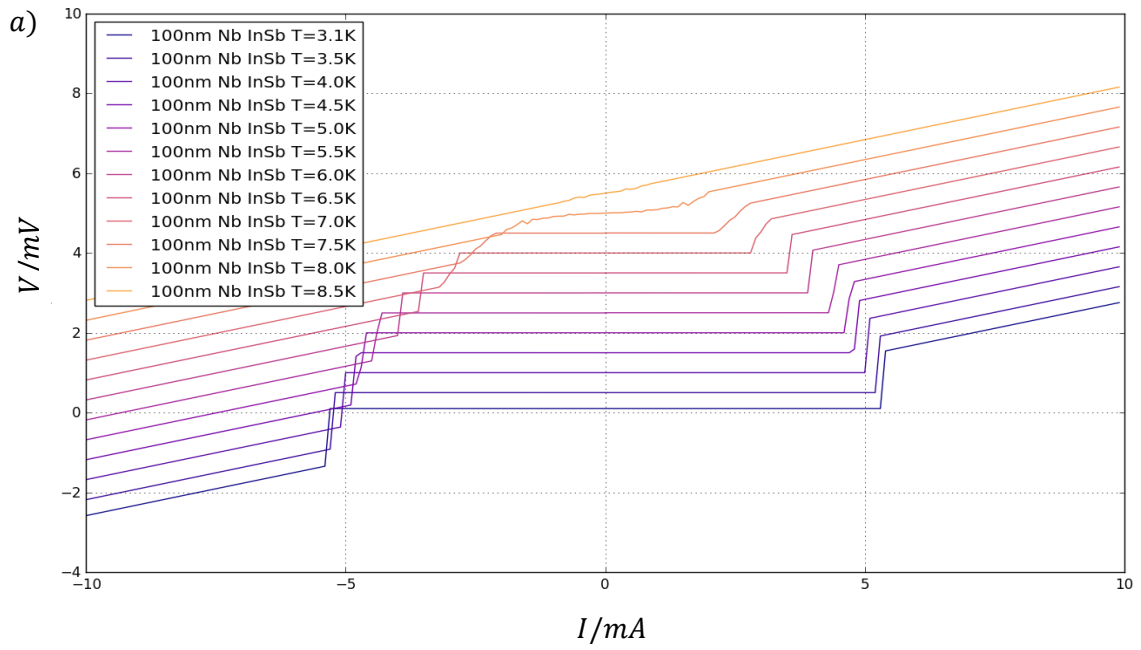
Figure 43: Measured voltage vs supplied current as a function of temperature. for 100nm Nb film on a) InSb substrate b) Glass Substrate. In both cases, curves are offset from $T = 3.0K$ for visual clarity.

Figure 43 presents the IVs for films on each substrate. In each case a clear sharp transition from nominally zero resistance to a regular resistive state can be seen. This transition is suppressed entirely above 7K for Glass, and 8.0K from glass. This suggests a slight enhancement for the $InSb\ 2DEG$, possibly due to the higher conductance of the substrate. In either case, this is less than the stated value for pure bulk Nb ($Tc = 9.26K$). I_c values are extracted for each temperature and plotted as a function of temperature.
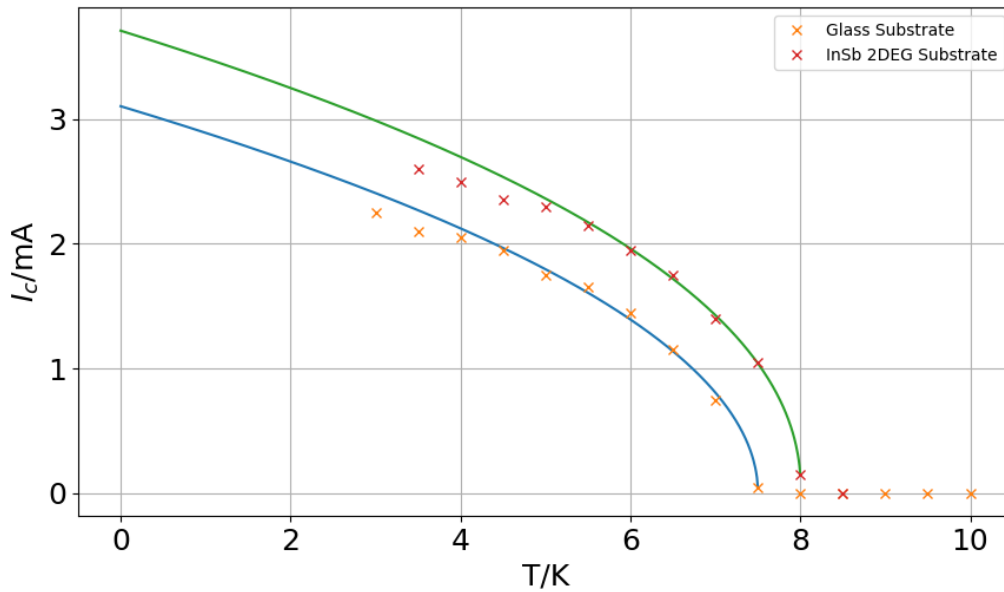
Figure 44: Extracted I_c vs T for 100nm Nb film on Glass and InSb substrates.

These data are fitted to eq. 2.34 (Figure 44). In both cases, the data near T_c are well modelled by this equation. Fit parameters are displayed in Table 2.

Table 2: Fit parameters for 100nm Nb deposited on InSb and glass substrates.

Substrate	$I_c(0)/mA$	T_c/K	n
$Glass$	3.10 ± 0.03	7.50 ± 0.23	0.49 ± 0.07
$InSb$	3.70 ± 0.10	8.00 ± 0.31	0.46 ± 0.05

The film deposited upon $InSb\ 2DEG$ is found to have a higher T_c than that on the glass. Additionally, I_c is also greater for $InSb$ vs glass. This suggests a slight enhancement of the superconductor quality on the $InSb\ 2DEG$, possibly due to the significantly higher conductance of it as a substrate. In consideration of the power in the fit, which should

be nominally ~ 0.5 for well-behaved Nb, a slight deviation is seen for the glass. However, both broadly agree, and thus the Nb appears to be a well-behaved s-wave SC.

4.4: Fabrication of gapped Nb/InSb QW structures:

Having characterised the bulk Nb film, we can now move to fabrication of the desired structure.
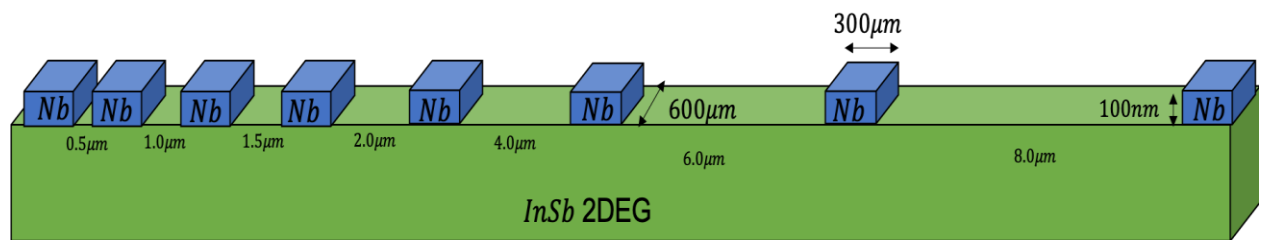
Figure 45: $Nb/InSb$ TLM schematic $600 \times 300\mu m$ contact pads defined and etched from a $100nm$ Nb (blue) film deposited on an $InSb$ 2DEG (green) with increasing spaced gap between them.

Figure 45 is schematic of the planned device. It is comprised of a series of $300x600\mu m$ Nb contact pads, separated by gaps of increasing width. Pad sizes were chosen to allow bonding of two electrical contacts per pad for the purposes of four terminal measurements. Gap widths spanned the range of $0.5 - 8\mu m$. Our chosen gaps were significantly smaller than those of [192], which covered the range $2 - 200\mu m$. Shorter lengths were chosen for ours, such as to be around the ballistic length of our 2DEG to consider the limiting case $d \leq 2\lambda_{prox}$ in greater detail.
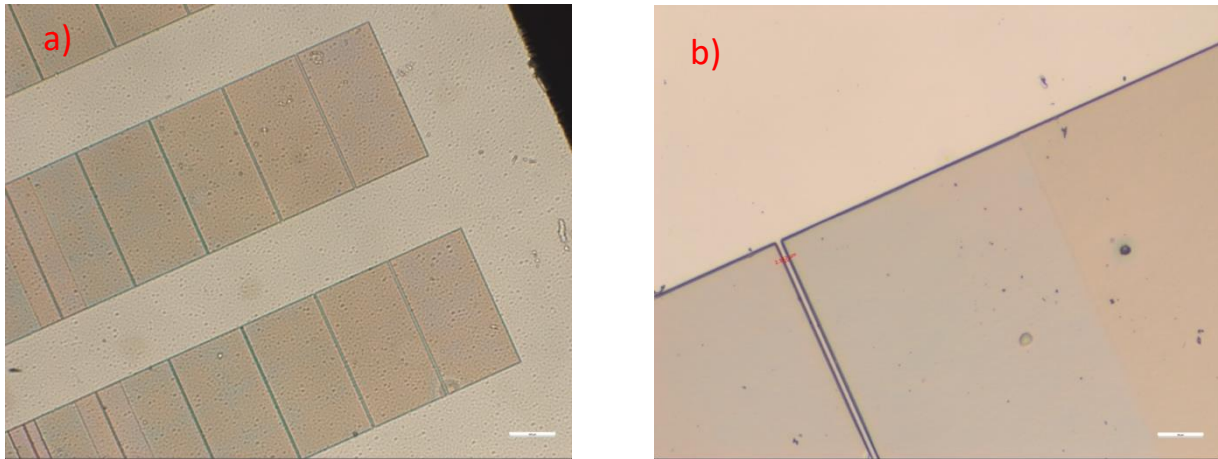
Figure 46: Examples of lithographically defined structure examined under microscope. a) Overview of three patterned structures. b) Examination of the nominally $2\mu m$ gap. Visual inspection indicates actual gap size of $2.182\mu m$.

Devices were defined via optical lithography. TI prime followed by AZ nLOF 2020 resist was spun onto solvent cleaned sample surfaces at 5000 rpm. A Durham Magneto Optics MicroWriter was used for exposure of the resist to pattern our design with maskless lithography. Finally, following a post exposure bake, it was developed in AZ-726 developer. Examples of the lithographic pattern are presented in Figure 46. Visual inspection via microscope shows the sharp edges with clear definition of the gaps (Figure 46b).

In order to fabricate the gaps, an etch process for etching Nb had to be established. Existing processes known to us for etching Nb had the potential to be unsuitable for $InSb$ as a substrate, as they had been designed for etching Nb on Si substrates. As such, one of the first priorities was establishing a Nb etch recipe that would be functional for all intended devices going forwards.

4.4.1: Cl Etching:

In the first instance, a Cl based dry etch chemistry was trialled. Dry etch chemistry was chosen due to the desire for sharp walls in the trenches. The omni-directional nature of wet chemistry methods could lead to undercutting, and non-sharp features in our films. The etch was undertaken using an ICP RIE system. A nominal etch rate $50nm$ per minute was monitored in situ via end pointing – monitoring the change in reflectivity of a piece of the bulk Nb via a laser spot. The $InSb$ substrate was less reflective than

the Nb layer, and as such a sharp decrease in reflectivity would correspond to a total etch of the Nb film.
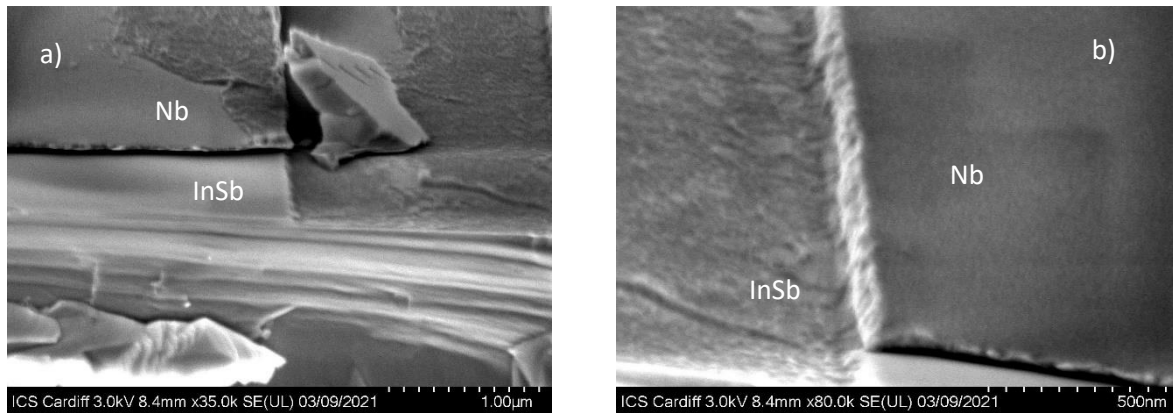
Figure 47: SEM images of Cl chemistry ICP etched Nb films. a) Angled SEM image of film sidewall. A large piece of debris is visible within the etched trench. b) SEM image of a different side wall of the same device.

Figure 47 shows SEM images of the resulting etch structure. This combined with visual inspection indicated that the Nb has been successfully etched. However, the Cl chemistry also etched the underlying $InSb$ layers. This can be seen most clearly in Figure 47a. The topmost darker layer indicated the Nb film, and the underlying brighter layers are that of the $InSb$ layers. The etch can be seen to have eaten well into the $InSb$. A total etch depth was estimated to be $\sim 500nm$, which is well past the active QW layer. This was well beyond the active QW layer, and as such the device non-viable.

From this, the etch rate was re-evaluated, and another set of devices was fabricated. However, SEM images showed the Nb had been negligibly etched within the gaps, despite fully etching around them. This issue arose from varying width of the gaps. The etch rate of RIE has a known dependence upon the surface area of the feature being etched [203] [204]. This phenomena is known as RIE lag. [205] [206] It is most pronounced for sub-micron feature sizes, and for low aspect ratio features – those with low depths and long width, much like our device. Any estimation of the etch rate from the bulk Nb surrounding the device would not correspond to the etch rate of the gaps. Additionally, this would mean the different sized gaps would etch at different rates. This would result in it being extremely difficult, if not impossible, to fabricate the wide

array of gaps sizes desired here with a Cl etch. To suitably etch the $100nm$ within the smallest gaps would result in an over-etching of the large gaps. The combination of these two factors ultimately led the abandonment of the Cl dry etch, in favour of an alternate etch chemistry.

4.4.2: C_4F_8 Etching:

The alternative chemistry chosen was a F based one, which had been shown to work for Nb films in the literature [207] [208]. Ideally, the chosen gas, C_4F_8 wouldn't etch the $InSb$ structures, allowing for sufficiently long etch time to remove the Nb from all the gaps without compromising the conductivity of the underlying 2DEG. For this, a fabrication trial was proposed. This trial needed to demonstrate two things: that the chosen chemistry would etch the Nb and would not etch the $InSb$. Two samples were prepared for this. One consisted of a 100nm Nb film deposited on a Si film at UC Santa Barbara. This film had been deposited as a control sample, equivalent to the previously discussed glass sample.
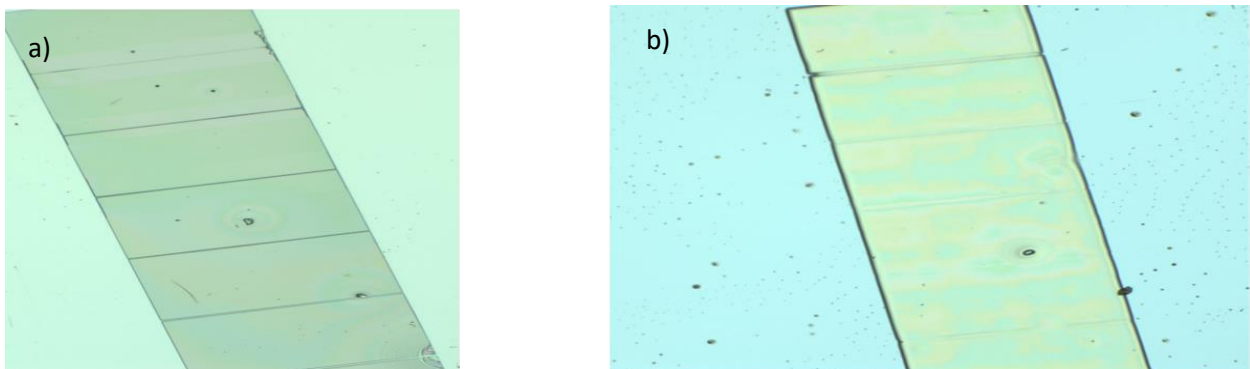
Figure 48: TLM device patterned via negative resist optical lithography on an $100nm\ Nb/Si$ sample a) Post exposure, but pre C_4F_8 etch b) post C_4F_8 etch, prior to resist removal. .

Optical microscope images were taken pre and post etch and presented in Figure 48. This visual inspection showed increased contrast between the TLM structure and the substrate, indicative of a change in height between the pattern and the substrate. The defined gaps in Figure 48a are smeared out post etch. This is attributable to resist reflow caused by high RIE power during the etch. Subsequent etches with a lowered

power rectified this issue. The resist was then removed via NMP solvent, and the sample inspected.
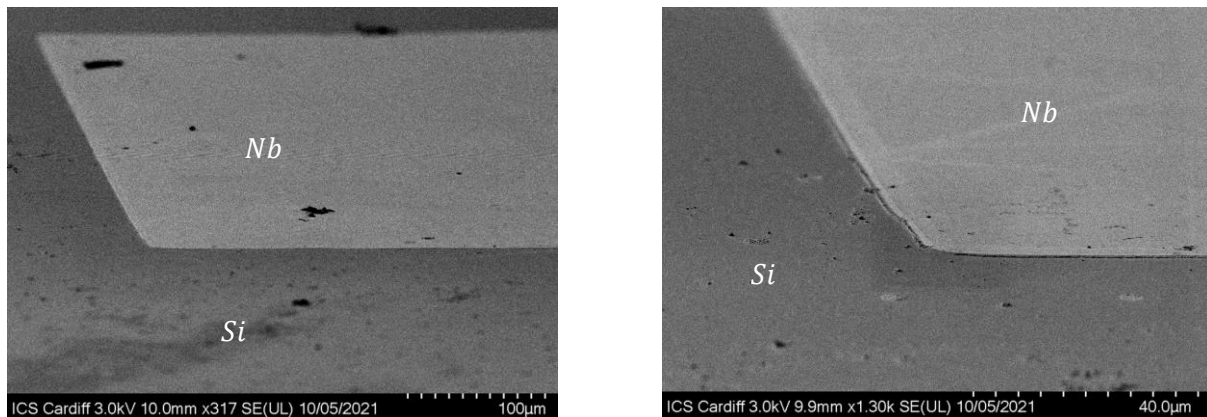
Figure 49: SEM images of TLM device patterned Nb on Si etched via C_4F_8

The SEM images confirm the initial visual inspection. Clear contrast between the substrate and Nb is visible in both images. Surface profilometry further supports this, giving a measured height difference of 111.6nm. As such, it was reasonable to conclude the Fl chemistry had and would etch the Nb.
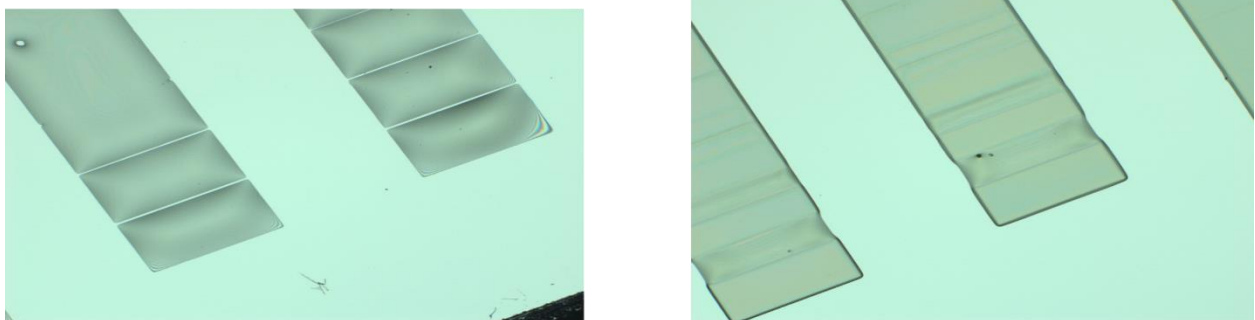
Figure 50: TLM device patterned via negative resist optical lithography on a piece of $InSb$ wafer a) Post exposure, but pre C_4F_8 etch b) post C_4F_8 etch, prior to resist removal.

The second sample used in the trial was a piece of bare $InSb$ wafer. The same TLM design was patterned onto it as the Nb/Si sample (Figure 50a). This sample was loaded at the same time as the Nb/Si sample and was thus subject to the same etch conditions. As before, this results in resist reflow because of the etch power (Figure 50b). The resist was then removed, and the sample subsequently examined under SEM
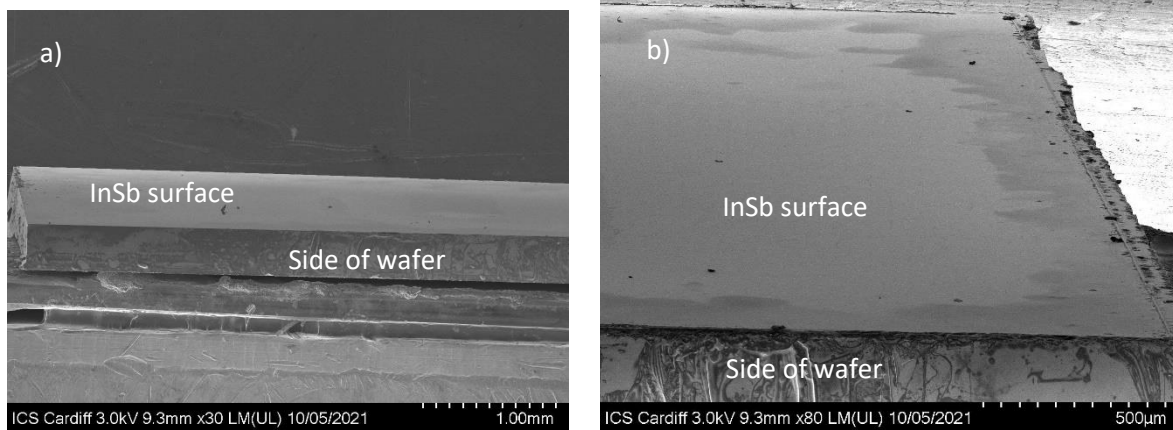
Figure 51: SEM Images of post FI etched InSb surface. a) 'planar view' of InSb surface. b) tilted view.

The SEM images post resist removal (Figure 51) show no indication of etching. The planar view (Figure 51a) shows no indication of the lithographic structure defined, in contrast to Figure 51b supports this, taking instead a tilted view of the sample surface. Although there is some surface roughness, visible as the darker regions towards the edge of the sample, there is no trace of a raised structure comparable to the Nb/Si (Figure 49). Surface profilometry also supported no etching of the $InSb$. As such it was concluded the C_4F_8 does not etch the $InSb$, as was thus a viable etch chemistry for our devices.

4.4.3: Final device fabrication:

With the etch process established, fabrication of samples for measurements was undertaken. 3 TLMs were patterned on a $1cm^2$ square piece of the 100nm Nb/InSb QW material previously characterized. The TLMs were patterned using the Durham Magneto-Optics Direct Writer on negative resist TI prime/AZ2020 as discussed previously. Samples were then etched via the C_4F_8 RIE process established within 5.5.2. Etch process was monitored in situ via end-pointing – a sharp transition in reflectivity was seen after $150s$. Total etch time of 7 minutes was undertaken to adequately allow the smallest gaps to etch.
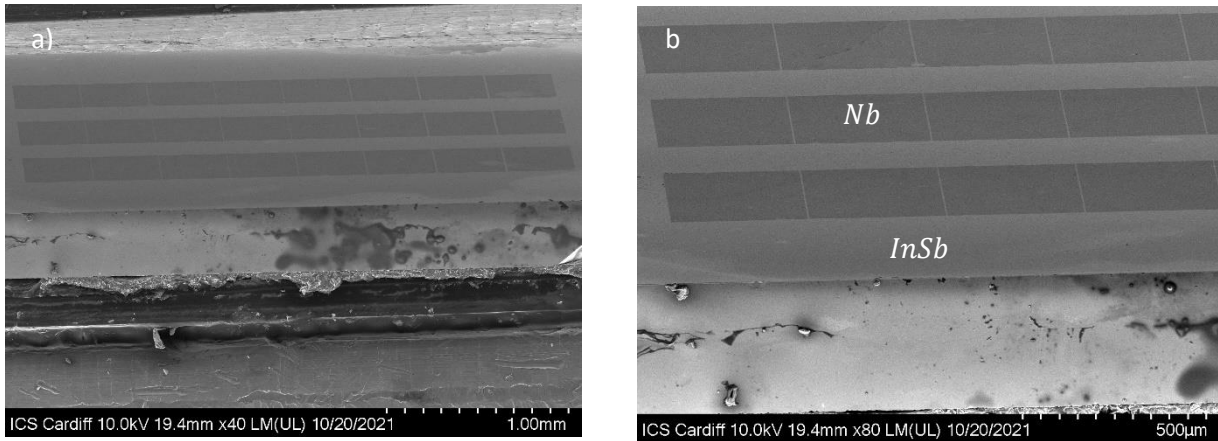
Figure 52: SEM images of fabricated TLMs of the $100nm$ $Nb/InSb$ samples a) Full view of sample. b) Zoomed view of sample to show gaps.

Initial inspection of sample via SEM shows three sets of fabricated TLMs (Figure 52a). Gaps between contact pads are clearly visible (Figure 52b). Surface profilometry from the substrate to the pads gave an etch height of $\sim100nm$, meaning full etch of the Nb and minimal etch of the $InSb$. To further ensure the Nb within the gaps is fully etched, we also used the SEM for a visual inspection.
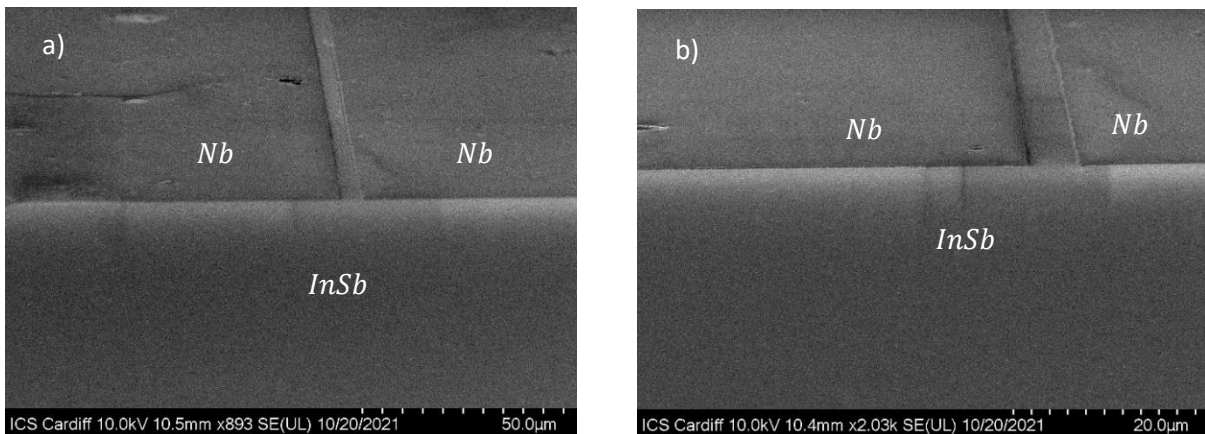
Figure 53: SEM images of gaps etched in the $100nm$ $Nb/InSb$ sample via C_4F_8 a) Examination of $2\mu m$ gap b) As a) but at high magnification.

Figure 53 shows inspection of the gaps via SEM. Clear contrast can be seen between the trench walls and the trench. The trench additionally appears to be continuous with the surrounding substrate, with no step or lip distinguishing it. The combination of these observations with the surface profilometry and endpoint reflectivity was sufficient evidence for the gaps being fully etched out, and thus the sample was usable for measurements. Final Gap sizes were found via SEM inspection as follows: $1.5, 1.75, 2.0, 4.0, 6.0, 8.0\mu m$.

4.5: Electrical measurement of gapped structures – Initial Characterisation:

An individual TLM structure was scribed out from the fabricated trio and mounted in a 20-pin chip package carrier. Samples were bonded via 2 Al wires to each pad, to allow four-contact measurements between any gap. The sample was then mounted within the Optistat Cryostat – However upon loading it was found several bonds failed, precluding 4 terminal measurements. Two terminal measurements were possible across each gap, and as such low temperature measurements were undertaken.
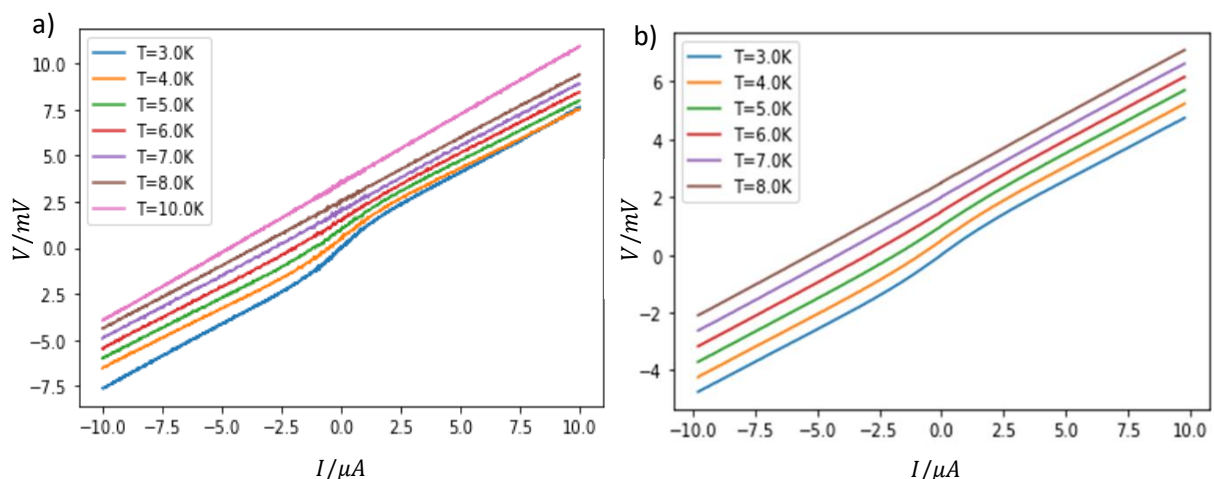
Figure 54: a) IV measurement across 1.5um Junction performed using Agilent for increasing temperatures. b) as a) but measured using a Keithley 2100 and 6221 in conjunction. Both a) and b) curves are offset from T=3.0K line via a linear scaling factor for visual clarity.

Initial measurements consisting of 2 terminal IVs, Figure 54a with an with an Agilent E52070B and Figure 54b measured with a combination of Keithley 2100 multimeter, and 6221 current source. Neither showed a zero-resistance region as per the bulk Nb film (Figure 43). However, in both cases, a distinct non-linear region was observable centred around $I = 0\mu A$. This non-linear region and was higher resistance than 'linear' regions and was suppressed as a function of temperature..

Given the small current values covered by the feature, and the overall small shift of the feature, the differential resistance of the sample was also measured, using an

SR830 lock-in amplifier. A $0.01 \mu A$ $13.7 Hz$ excitation signal was supplied via the lock-in. DC offset currents were then also supplied by the lock-in in the range $\pm 10 \mu A$.
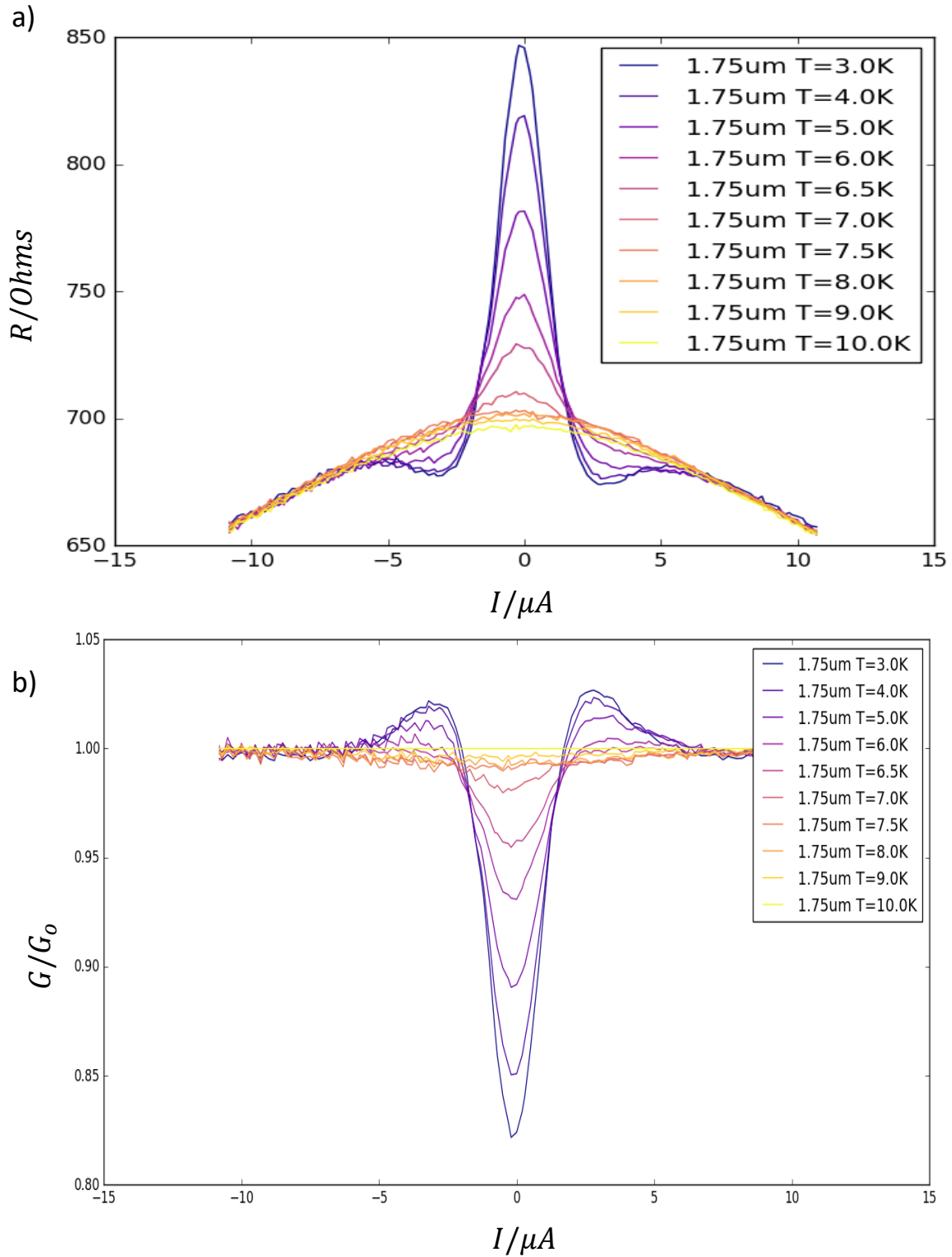
Figure 55: a) Differential resistance measurements of $1.75 \mu m$ gapped Nb/lnSb heterostructure. b) Measured Conductance normalised with respect to $T = 10.0K$ data.

Figure 55a shows the differential resistance measurement taken via the lock-in as a function of temperature. A sharp peak in resistance, accompanied by a pair of onset troughs is observable. Both sets of features are suppressed via increasing temperature, being fully supressed by $T \approx 7.0K$. Conversion of resistance to conductance, and then normalizing with respect to $T = 10K$ data (Figure 55b) shows, unsurprisingly, a slight suppression in conductance centred around $I = 0\mu A$. This feature shape is generally consistent with the the BTK model previously discussed in Section 2.10 for high interfacial barriers – the conductance peaks should correspond approximately with the limits of the superconducting gap. This serves as initial indicative evidence for potential induction of superconductivity across the gap.

4.5.1: R vs T:
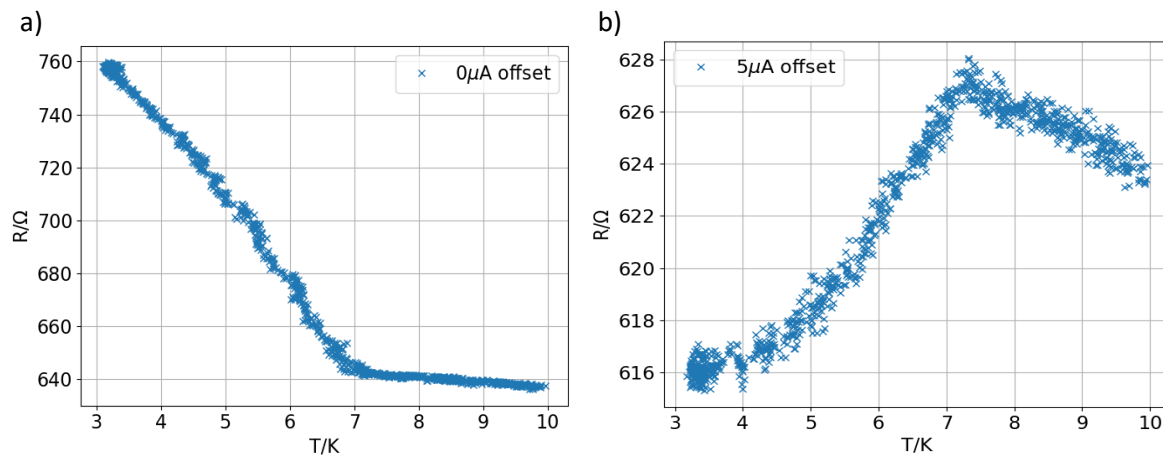
Figure 56: Differential resistance vs Temperature measured via a lockin amplifier supplying a $0.01\mu A$ $13.7Hz$ ac current at a fixed DC bias. a) Measurement at $I_{bias} = 0.0\mu A$ b) Measurement at $I_{bias} = 5\mu A$ offset.

The temperature dependence of these features was examined in greater depth via R(T) measurements at select DC bias. Fixed bias currents I_{bias} were applied to examine either the central peak (Figure 56a), or one of the onset trough (Figure 56b). At these biases, T was gradually raised in $0.1K$ intervals every 1s. As the temperature could not be stably controlled to these small temperature steps, measurements of R and T were recorded in 0.1s intervals, in effect recording R as the sample gradually heated. Temperature was recorded using the mercury ITC, whilst Resistance was recorded via the lock-in. From these, $R(T)$ supported the electrical measurements (Figure 55) indicating a T_c of around $T \approx 7.0K$ for both features.

4.5.2: Niobium contact characterisation:

As the signal measured in this experiment required injection into the InSb via the Nb contact pad, eliminating the possibility that measured signal was simply a manifestation of the pad superconductivity was required. For this, a two terminal differential resistance measurement of one of the contacts was performed.
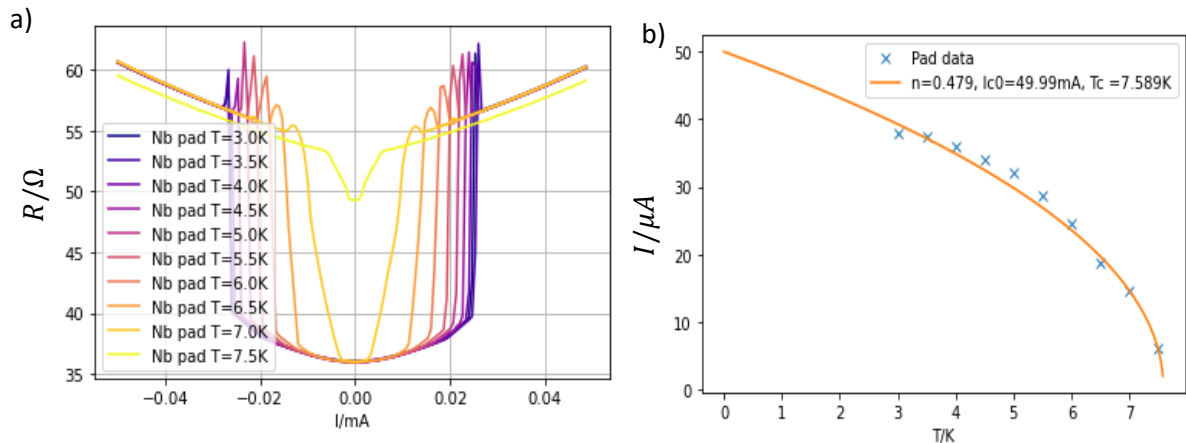
Figure 57: a) 2 terminal differential resistance of a Nb pad as a function of I_{bias} with a lockin amplifier supplying an $0.01mA$ $13.7Hz$ ac current b) Extracted I_c as a function of temperature.

The measured differential resistance of the Nb pad is presented in Figure 57a. A clear $SC \rightarrow N$ transition is visible. This gave T_c between $T = 7.5K$ and $T = 8.0K$. which agrees with the bulk film measurement in Figure 43. The finite resistance in the SC state is expected to arise from the combination of contact and wire resistances still present within the two-terminal measurement. I_c was extracted from these data and fit to eq. 2.34 as per Figure 43. The pad still exhibited well-behaved S-wave SC (exponent of 0.47 vs 'pure' exponent of 0.5). A slight suppression of T_c was observed ($T_{c_{pad}} = 7.589K$ vs $T_{c_{bulk}} = 8.00$), but it was deemed reasonable the fabrication process undertaken had not substantially damaged or reduced the quality of the Nb. The transitions seen in the pads occur at significantly larger applied DC currents to that of the feature measured across the gap (mA vs μA).

The combination of all these measured factors leads to the following hypothesis: The measured feature across the $1.5\mu m$ gap is evidence of proximity induced superconductivity extending some length into the $InSb$ layers. As no surface preparation was undertaken before SC deposition, it is likely there is a high degree of

interfacial roughness and surface defects between the Nb and $InSb$. This would suggest, in the language of the BTK model, that there will be a large barrier between the SC and the N regions. As discussed in Section 2.10, large barriers can suppress the conduction within the SC state to be below that of the normal state. Thus, poor interfacial quality can create the reduction in conductivity observed in our device. With that in mind, two things follow: Qualitative analysis of this induced state to allow characterization, and then evaluation of the temperature dependence.

5.4.3: Modelling of induced SC state and full temperature sweeps.

In the first instance, an attempt to model the SC state was performed with the basic BTK model, outlined in eq. 2.39. This sought to obtain an approximate value for Δ and for Z, the dimensionless barrier height. However, fitting with this basic model failed to find satisfactory values. As such, a numerical test was performed, taking a fixed value

of $\Delta = 0.05\text{mA}$ and taking a wide range of Z's to achieve an estimate for an appropriate guess value.
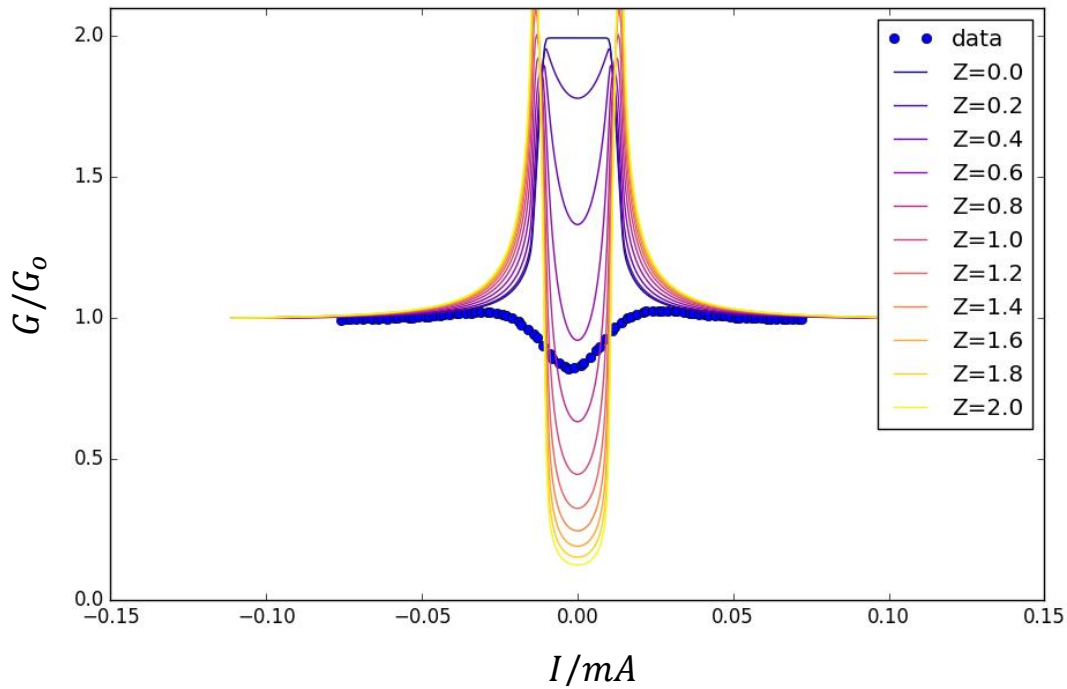
Figure 58: Numerical BTK calculations for various barrier heights Z. Blue dots indicate the experimental data for $1.5\mu m$ gap.

No values of Z were seen to be suitable (Figure 58). The conventional BTK model was thus a non-satisfactory choice for modelling our junctions. Consulting with the literature, suggested that a modification to the theory may be more appropriate. For the case of superconductors exhibiting high degrees of in-elastic scattering, arising from roughness at the surface, can lead to added breaking of cooper pairs incident at the interface. This can be modelled by an additional added to the energy within the BTK model [116].

$$E \rightarrow E + i\Gamma \qquad\qquad (4.4)$$

Where Γ corresponds to the pair breaking processes of this added scattering [209]. The scattering serves to smear out the BTK Conductance curves. For systems with this high degree of scattering, an approximation of the conductance can be made:

$$G(E) = \alpha \frac{E - i\Gamma}{((E - i\Gamma)^2 - \Delta^2)^{0.5}} \tag{4.5}$$

This is known as the Dynes model and is a phenomenological fit that has been used for many SC system, quantifying both the size of the induced SC and the additional scattering [210] [211] [212] [213] [214] [215]. The minimal surface preparation used in the fabrication of our TLMs makes a high degree of interfacial roughness between the InSb and Nb likely, and as such, the Dynes model is an appropriate choice of model. Differential Resistance measurements of all the gaps on our devices were performed as a function of temperature, and the Dynes model applied to model them.
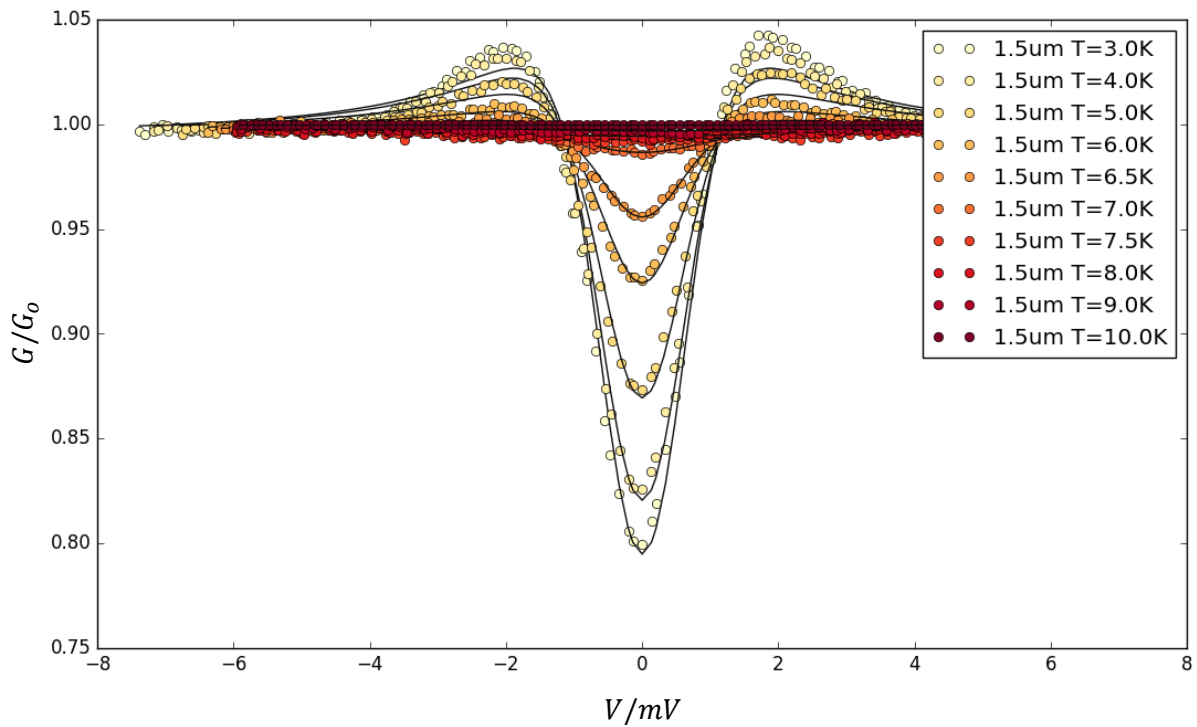
Figure 59: Normalised conductance as a function of applied voltage of a 1.5μm gap
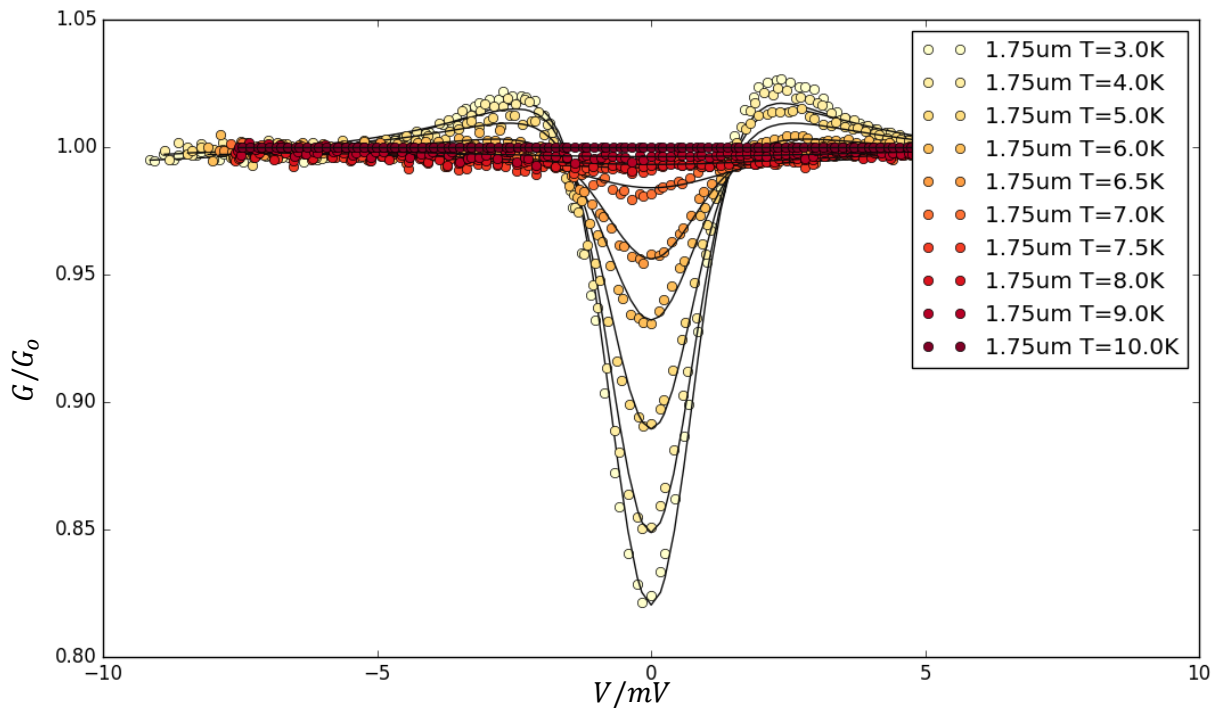
Figure 60: Normalised conductance as a function applied voltage of a 1.75μm gap.
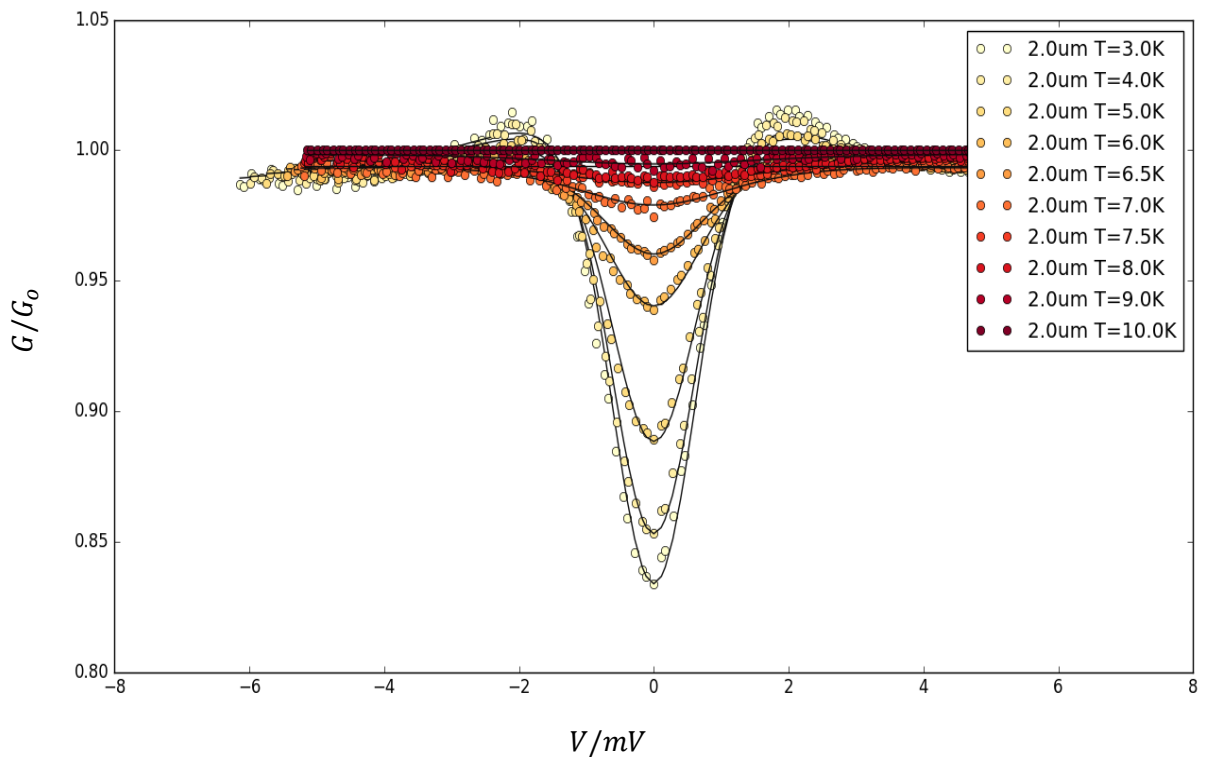
Figure 61: Normalised conductance as a function applied voltage of a 2.0μm gap.
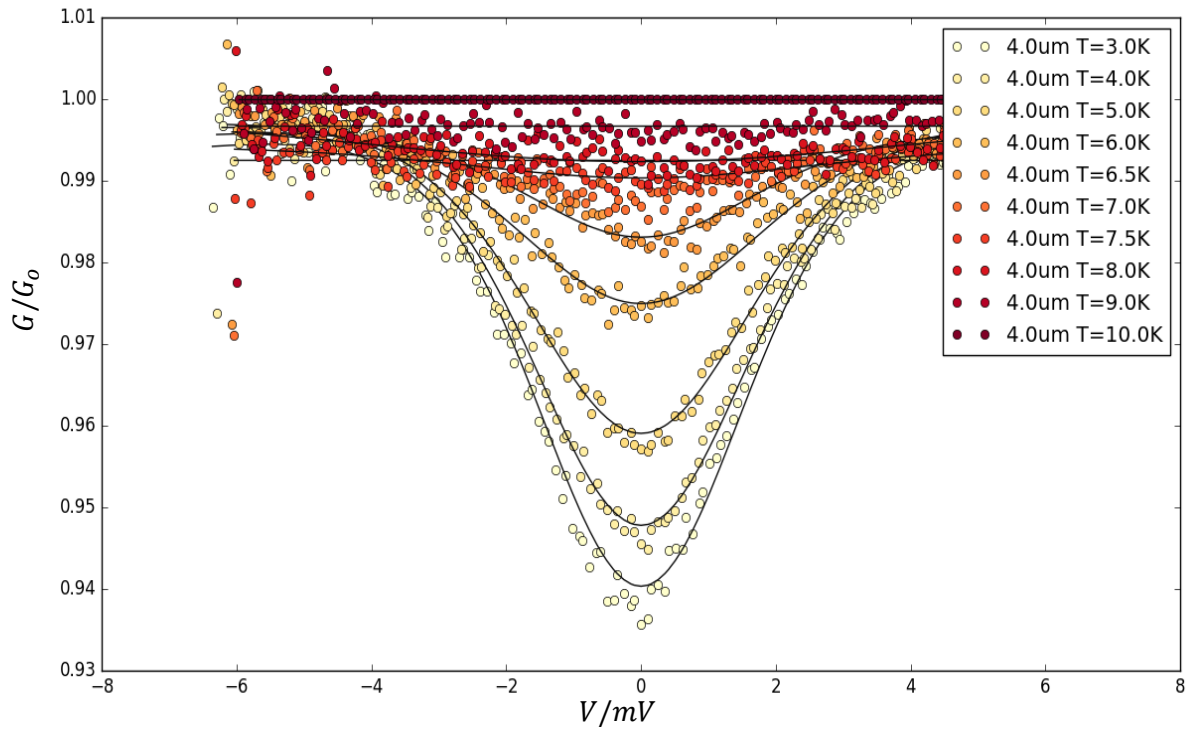
Figure 62: Normalised conductance as a function applied voltage of a 4.0μm gap.
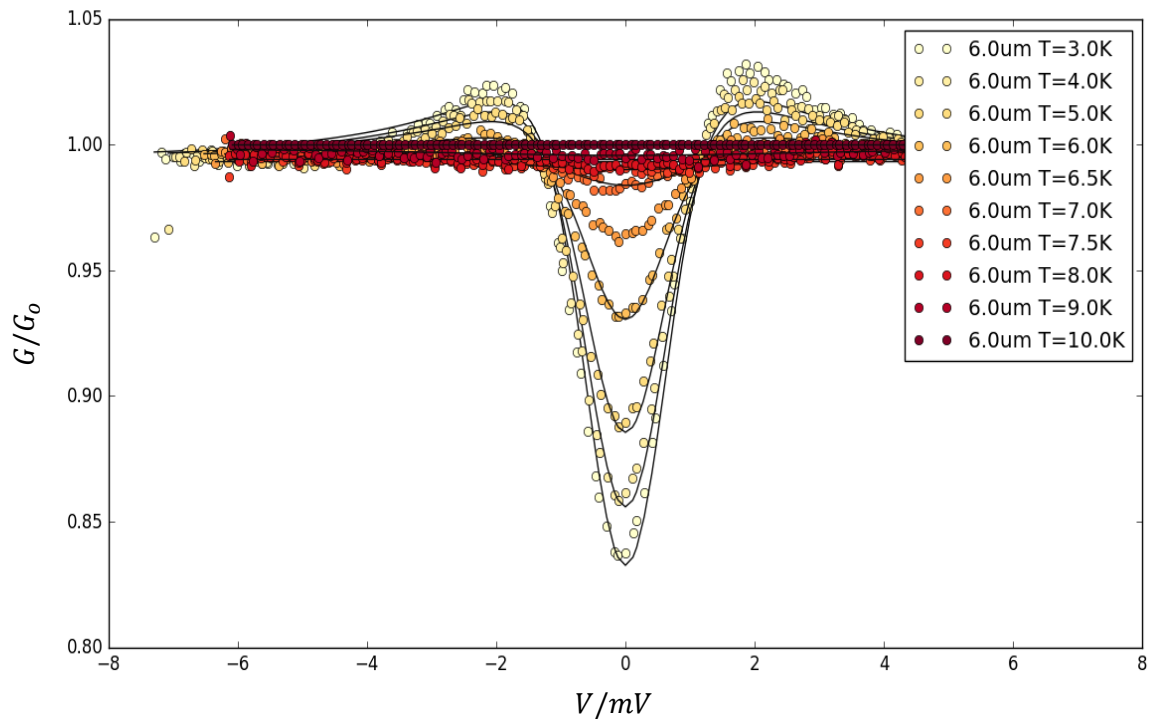
Figure 63: Normalised conductance as a function applied voltage of a 6.0μm gap.
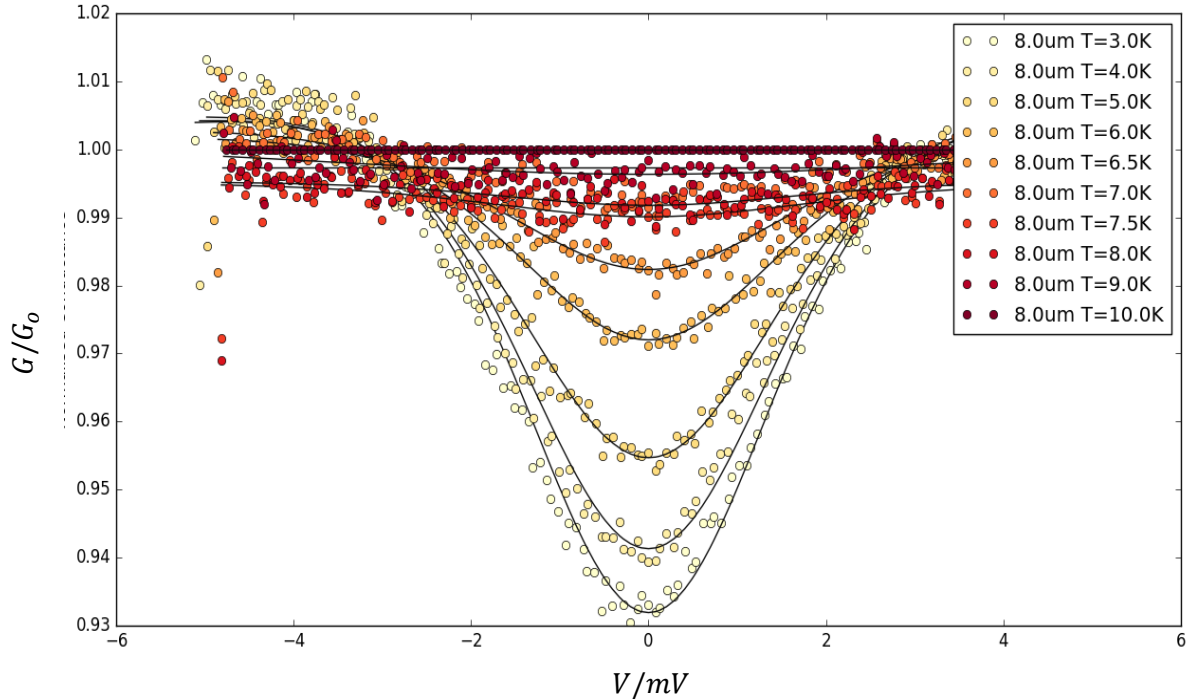
Figure 64: Normalised conductance as afunction applied voltage of an 8.0µm gap

For all gaps measured (Figure 59-Figure 64) the Dynes model provided a satisfactory fit. We can broadly separate the gaps measured into two groups from this. The first, (Figure 59, Figure 60, Figure 61 and Figure 64) consist of 'large' central conductance dip, and associated onset peaks. The other two, the $4\mu m$ and $8\mu m$ gaps, (Figure 62 and Figure 64) possess wide but shallower dips, and no onset peaks. However, despite the lack of onset features, they are still adequately fit by the Dynes model. Evidence of superconductivity in all these gaps is notable – $8\mu m$ is extremely large length scale for proximity superconductivity. Typical length scales for proximity superconductivity in metals are on the order of $\approx 10 - 100$ of nm [216] [217] [218]. To exist on a μm length scale, the SC must have extended into the QW layer, where we expect μm scale ballistic lengths [195][58]. The proximity effect arises from the leakage of Cooper Pairs from the superconductor to the normal material – the length scale at which it extends will relate to the length scale at which a cooper pair can remain coherent within the N material [219] [220]. High mobility, and long ballistic length N materials, such as our QWs, should thus have long coherence lengths.
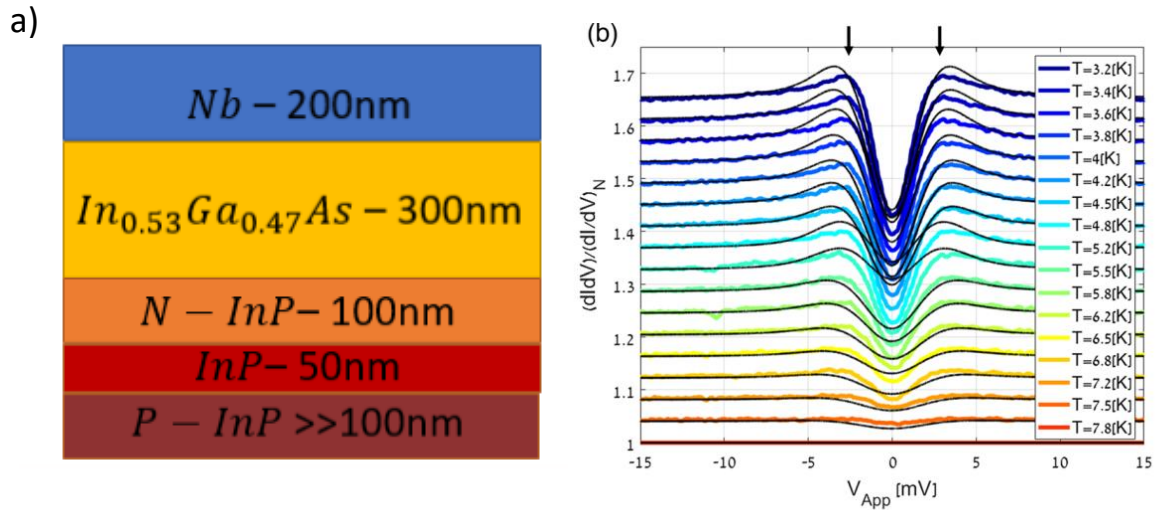
Figure 65: a) Layer details of $Nb/InGaAs/InP$ heterostructure. The QW in this structure is formed in the InP layer b) Measured differential conductance as a function of temperature [221].

A recent paper showed similar results in an $InGaAs/InP$ 2DEG [221]. The layer structure of their device is indicated in Figure 65a. Differential conductance measurements of there device showed a similar conductance dip, also modelled by a modified BTK equation. Specifically, rather than treat the interfacial barrier as a single δ function as per the Dyne's function, the barrier is treated as a series a successive step functions [222]. The paper deemed successful induction in the well with a thicker Nb film, through a thicker $InGaAs$ layer than the equivalent $AlInSb$ layer in ours. As such, this supports the hypothesis that our devices indicate successful proximity induction of superconductivity within an $InSb$ QW via top-down fabrication methods. This is a significant technological success for moving towards side gated devices. This opens a range of potential future options to improve the SC state, including thinning of the $AlInSb$ top cap.
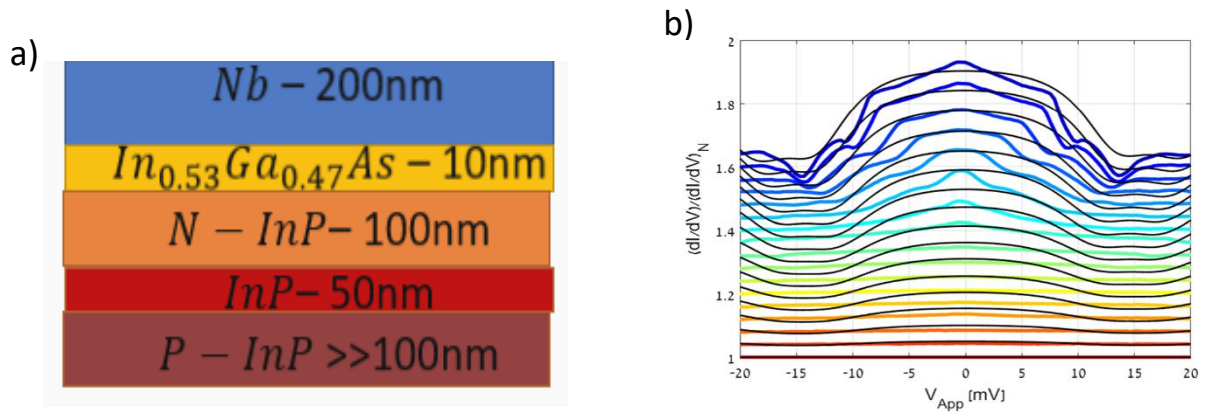
Figure 66: Layer details of resonant $Nb/InGaAs/InP$ heterostructure. The QW in this structure is formed in the InP layer b) Measured differential conductance as a function of temperature [221].

The same PRL shows an example of this enhancement, presenting a modified $InGaAs/InP$ heterostructure, designed with a significantly thinned $InGaAs$ top cap layer (Figure 66a). The thinner top cap was designed such that the first energy level within the QW would align with the superconducting gap. This would allow for resonant tunnelling of carriers from the SC into the N material, increasing the probability of carriers entering the QW. This would result in the sample feeling an effectively smaller interfacial barrier, as seen in Figure 66b. The lower barrier manifests itself in a radically different feature shape relative to Figure 65b, including a shift from a conductance dip to an increased conductance plateau. As observable in Figure 58, such a feature is associated with lower barrier heights. An equivalent thinning of the top cap in our $InSb$ devices would be a promising future direction for these devices.
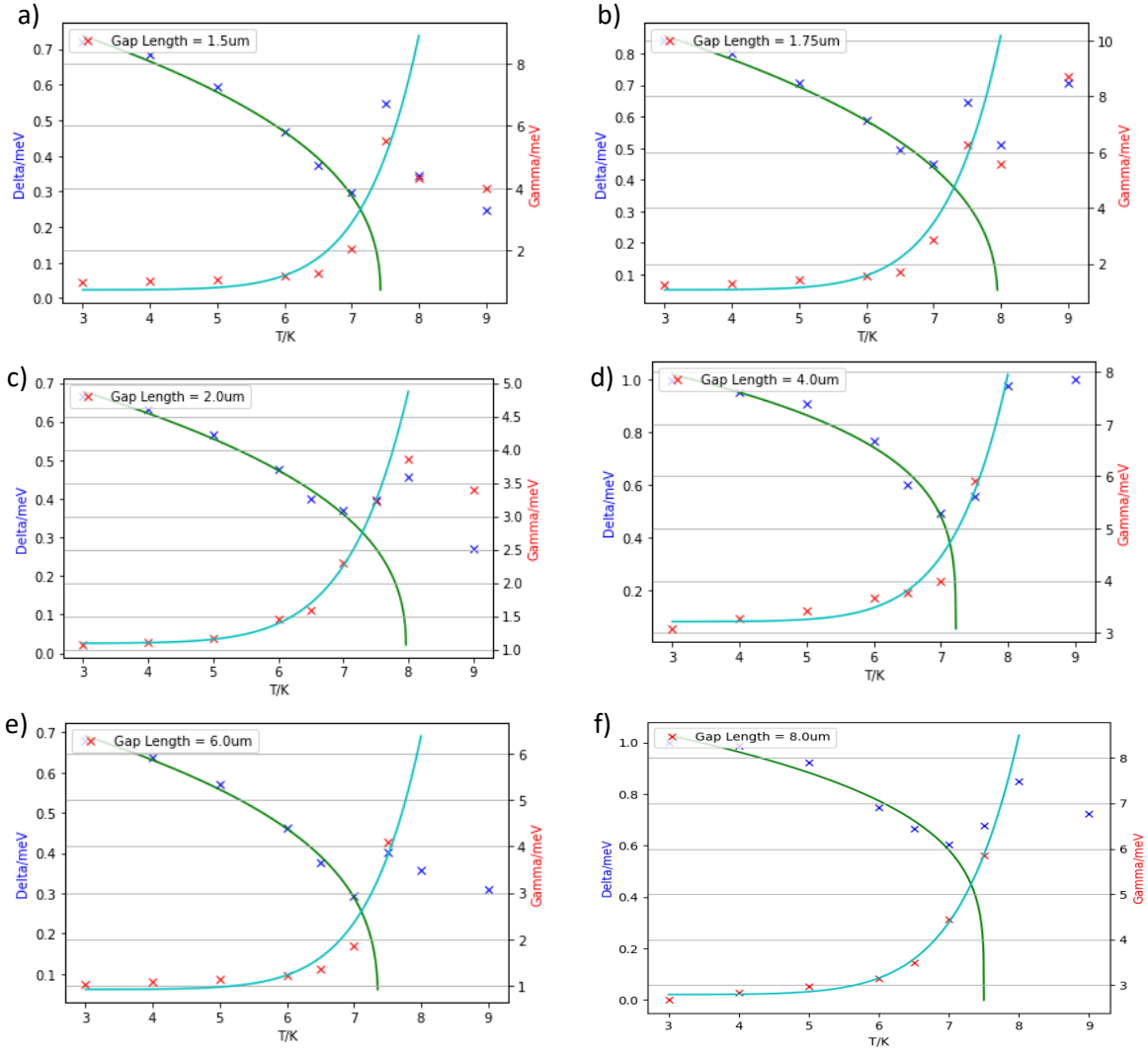
Figure 67: Extracted Dynes fit values Δ (Blue crosses) and Γ (Red crosses) as a function of temperature for each gap length. Solid lines (Δ green and Γ teal) represent fits to each parameter.

Figure 67 presents the extracted Δ and Γ for all gaps as a function of temperature. The induced gaps are significantly smaller than the nominal gap for Nb ($2.32 meV$), and the reduction is similar in scale to that observed in the $InGaAs/InP$ devices [221]. Extracted Δ were fit to eq. 2.33. T_c was allowed to vary between $T = 7.0K$ and $T = 8.0K$ in line with our measured values. We note that limitations in the number of datapoints around T_c may impact the quality of our fits, particularly given that the points above T_c at 8K and 9K cannot be included in these fits due to lying outside the SC state. Also presented are the Γ, which increased as a function of temperature. Γ were fit to a more general power law of the form:

$$\Gamma = \Gamma_o + \Gamma_1 T^p \qquad\qquad (4.6)$$

Where Γ_o is the temperature independent contribution to the broadening term, Γ_1 is the temperature dependant element, and p is an integer indicating the dependence. Similar treatment has been used to consider prior 2D superconducting systems [213]. The resulting fit parameters are presented in Table 3:

Table 3: Extracted parameters from fits of Δ and Γ presented in Figure 26.

Gap Size/μm	$\Delta(0)/meV$	T_c/K	n	Γ_o/meV	$\Gamma_1/meVK^{-p}$	p	$\dfrac{\Delta(0)}{k_bT_c}$
1.5	0.91 ± 0.04	7.43 ± 0.23	0.40 ± 0.07	0.71 ± 0.36	7.64 ± 0.54E − 09	10 ± 3.5	1.42
1.75	1.03 ± 0.06	7.95 ± 0.61	0.41 ± 0.12	1.06 ± 0.29	8.48 ± 0.44E − 09	10 ± 2.6	1.51
2.0	0.82 ± 0.04	7.97 ± 0.62	0.39 ± 0.11	1.09 ± 0.04	3.90 ± 0.57E − 08	8.84 ± 0.72	1.19
4.0	1.17 ± 0.07	7.22 ± 0.20	0.26 ± 0.06	3.21 ± 0.18	4.41 ± 0.28E − 09	10 ± 3.1	1.87
6.0	0.83 ± 0.03	7.36 ± 0.15	0.35 ± 0.04	0.92 ± 0.20	5.08 ± 0.30E − 09	10 ± 3.0	1.31
8.0	1.17 ± 0.04	7.49 ± 0.23	0.26 ± 0.03	2.79 ± 0.17	1.31 ± 0.78E − 08	9.57 ± 0.94	1.82

In addition to the fit parameters, we can also consider the ratio $\frac{\Delta(0)}{k_bT_c}$ as a further assessment of superconduting quality. Ideal BCS superconductors have a ratio of ~1.76. [223] [84]. In all cases, we see disagreement from this ideal. Additionally, although the fits to Γ were visually satisfying, it is likely this is a non-physical description of the system. The prior usage of it within the literature found $p \approx 2.2$, a

more reasonable dependence than ours. Many instances of the Dynes model literature within the literature do not model Γ, but do note an increase in Γ with temperature as per our data. [210] [211] [212] [213] [214] [215].
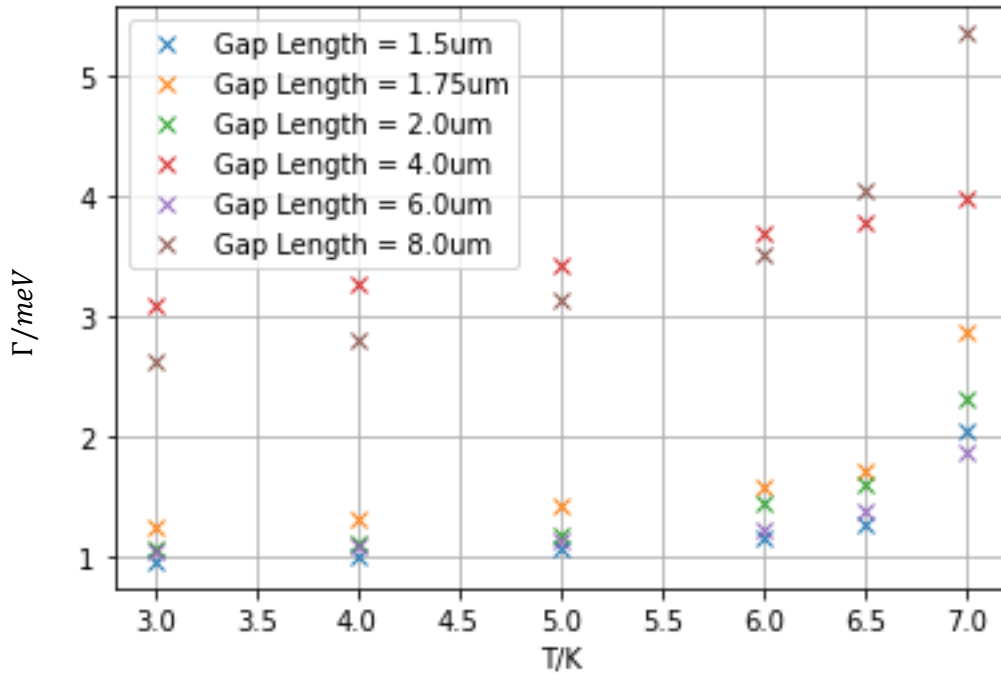
Figure 68: Extracted Γ as a function of temperature for all gaps.

As an aside, Γ also offers a possible qualitative explanation for the different responses we see in the 4.0 and $8.0\mu m$ gaps. Considering Γ as a function of temperature Figure 68 shows a large difference in Γ between these two gaps, which lack the onset features, and the other four. Higher Γ is indicative of increased broadening, or inelastic scattering between these gaps, and likely a worst interface local to those gaps.
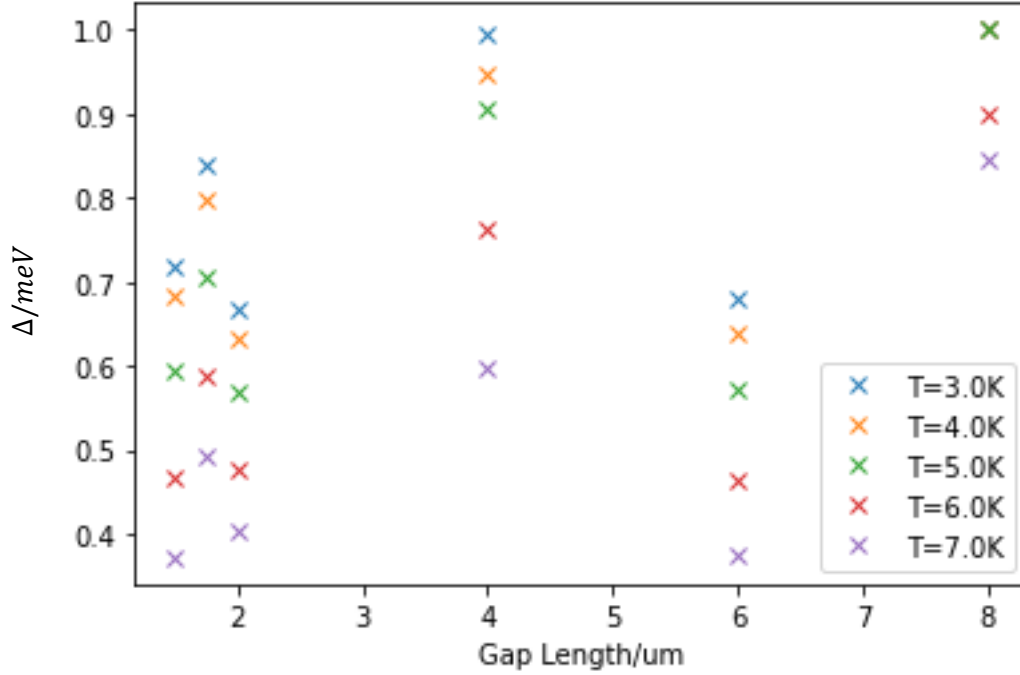
Figure 69: Δ as a function of gap length for different temperatures.

We can also consider the dependence of Δ as a function of gap length – In an ideal case, Δ should decrease as the gap length increases beyond λ_{prox}, and the junction becomes dominated by normal state material. Figure 69 shows Δ as a function of gap length for various temperature below T_c. There is no systematic dependence on with gap length visible, regardless of temperature. This precludes our ability to perform the TLM analysis as described in 4.1 with this set of devices.

4.6: Field sweeps of Nb/InSb structures:

Having considered the temperature variation of these Nb/InSb devices, to fully investigate the devices available, we also moved to consider the application of an external magnetic field. As discussed in Chapters 1 and 2, magnetic field is a critical component in the realisation of MZM devices. As such, to be able to use $InSb$ 2DEGs, we must characterise the field behaviour in our $Nb/InSb$ devices. The initial field measurement applied a 0.55T external B field perpendicularly to the sample cross section at $T = 3.0K$. The field was then decreased in 0.05T steps. At each field step, a full differential resistance curve is measured as per the electrical measurements in Section 4.5.
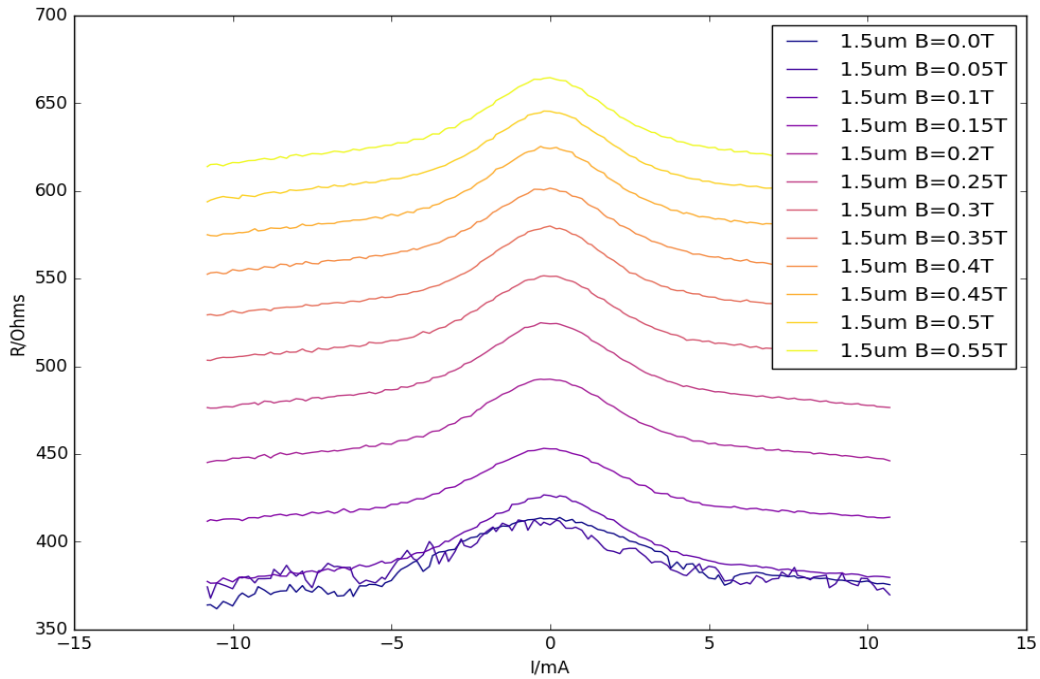
Figure 70: $3K$ Differential Resistance measurements of 1.5μm gapped junction for applied magnetic field. Raw data is presented within this curve – no offsets are applied .

A broad central peak was present in the resistance for all field values, suggesting no suppression of the SC state (Figure 70). The overall resistance also increased as a function of field, which is likely attributable to magneto resistance.
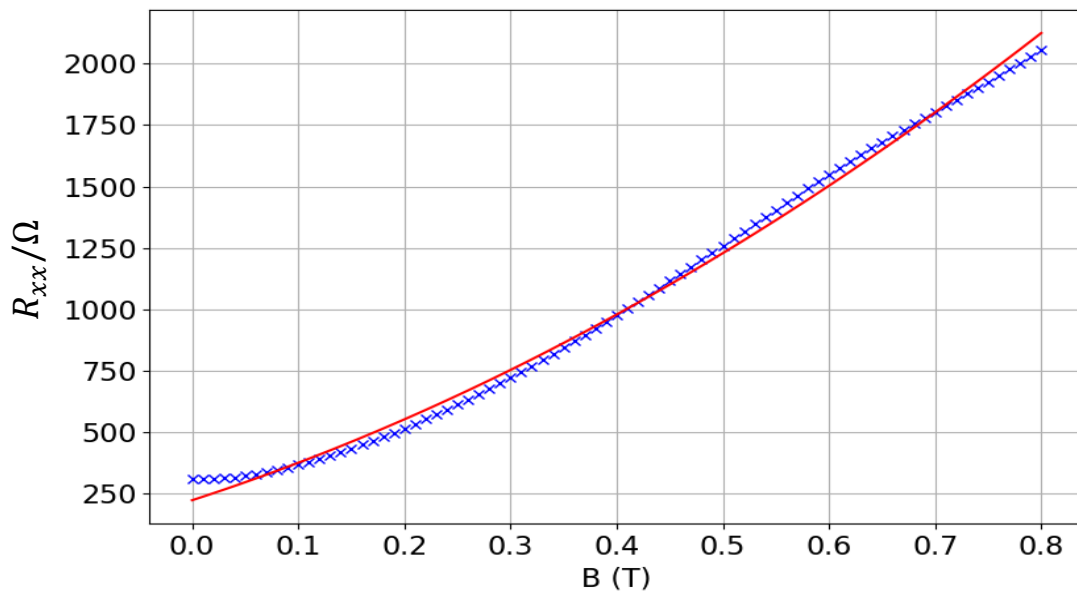
Figure 71: Measured resistance vs applied magnetic field for an InSb 2DEG Hall bar, fabricated from the same wafer as was used for the fabricated of the Nb TLM structure. Red line indicates a simple polynomial fit.

Magnetoresistance was seen in the $InSb\ 2DEG$ Hall measurements used for characterisation of the 2DEG (Figure 42). The $T = 3K$ magnetic field versus R_{xx} data is presented in Figure 71. A nearly four times increase in the measured resistance is seen in the Hall bar data at $B = 0.5T$ vs an approximate doubling in the TLM data (Figure 70).
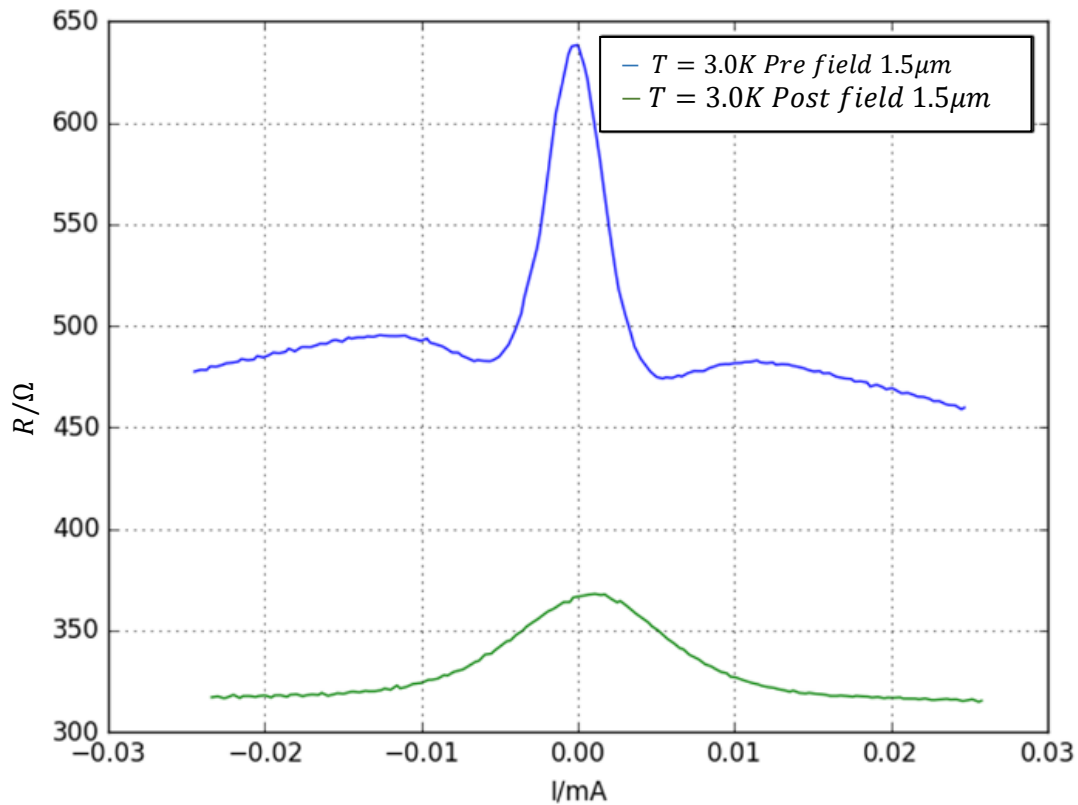
Figure 72: Comparison of measured differential resistance measured before and after application of an external B-field for the 1.5μm gap. Both measurements occurred at $T = 3.0K$. Sample temperature was nor raised above $10K$ between these two measurements.

Additionally, comparing $B = 0.0T$ curve to the initial measurements of the junction, the onset peak features visible in the initial measurement are now absent (Figure 72). The measured resistance is heavily supressed compared to the initial measurement ($R(0) = 400\ \Omega\ vs\ 65\ \Omega$). The application of the B field has caused some change within the sample, that has altered the physical properties measurable across the gap. To verify, all the gaps were remeasured with no applied external B field.
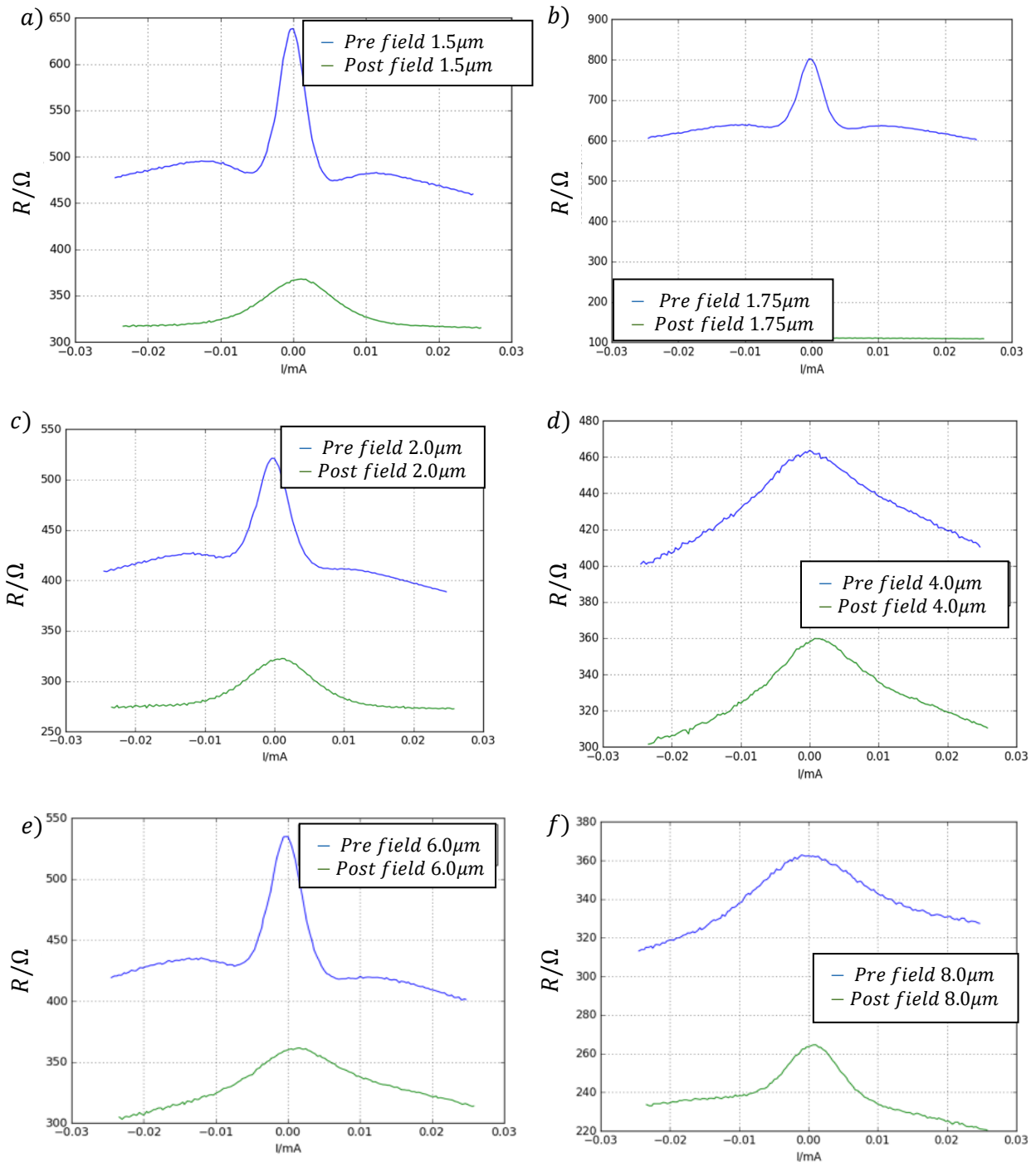
Figure 73: Comparison of measured differential resistance measured before (blue) and after (green) application of an external B-field. All measurements occurred at 3.0K as per electrical measurements. a-f): $1.5, 1.75, 2.0, 4.0, 6.0, 8.0\mu m$ respectively.

In all cases, (Figure 73) the measured features were altered relative to the initial measurements. The initial onset features are supressed, although large central features remain. Additionally, in all cases the measured resistance is supressed relative to the initial measurements.
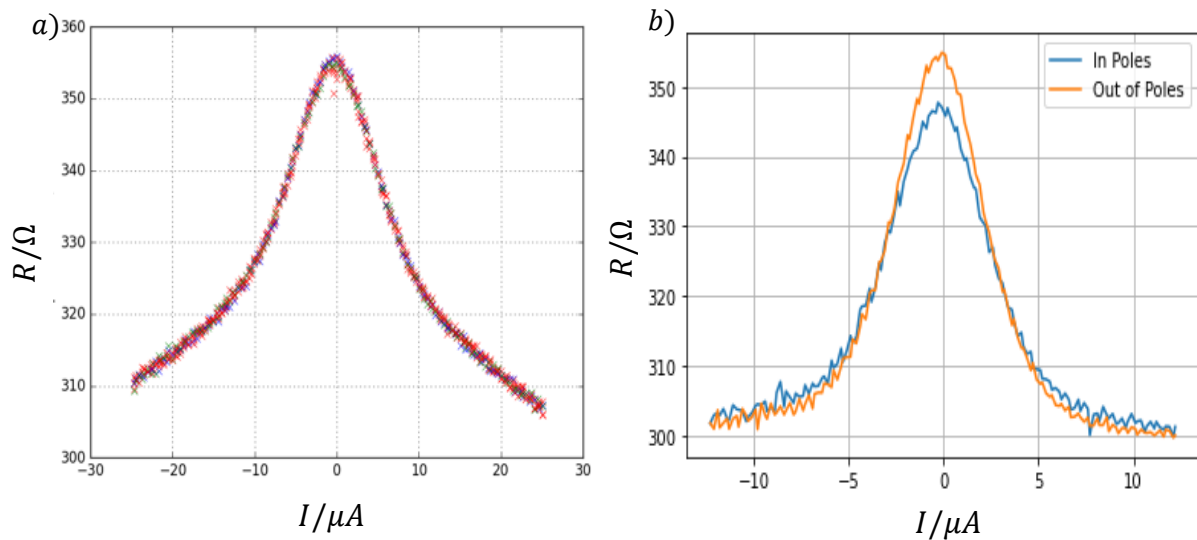
Figure 74: a) Four super imposed repeated differential resistance measurements of $1.5\mu m$ gap. b) Differential resistance measurement with the sample aligned in and out of magnetic poles in the absence of applied field.

To further investigate that this was a real observed phenomenon, the multiple differential resistance measurements of the $1.5\mu m$ junction were taken successively (Figure 74a). These measurements were repeatable, and indistinguishable, Finally, we considered the possibility of lingering magnetism within the poles. The magnet had undergone a degaussing procedure post measurement, cycling the field with decreasing amplitudes of current between positive and negative currents, however there was the possibility that this hadn't fully demagnetised the poles. As such the sample could still be within a magnetic field in the absence of a current flow through the poles. The differential resistance was remeasured with the sample out of the poles via rotation of the cold finger by 45°. Although a difference is observable, it is still broadly in-line with the post field measurement. We thus believe the application of a field has resulted in some physical alteration to the sample, most likely the interface, altering the proximity induced state.

The most likely possibility for this was deemed to be flux trapping within the superconductor. However, heating the sample to $15K$, well out of the SC state, and remeasuring, the system was still altered. This discounted flux trapping. It was then speculated that the change could result from within the semiconducting layers.

Material studies into surface oxides and the deposition of dielectric films onto $InSb$ and $AlInSb$ material layers have shown the possibility of interfacial charge trapping between the semiconductor and the dielectric [224] [225] [226] [227]. The intentional introduction of surface defects in a similar III-V heterostructure, $InAs/GaSb$, has shown the spatial make-up of such states can influence the resulting conduction characteristics [228]. As such, the barrier resulting in the initial features (Figure 59-Figure 64) likely resulted from this interfacial charge trapping, which is likely to differ between the different gaps. The application of a Magnetic field could have then supplied sufficient energy to the system to alter the distribution of those charges, changing the interface characteristics. Similar behaviour can be seen with hysteresis effects in response to gate voltage in gated 2DEG structures [229] [230]. As temperature supresses carrier concentration within the $InSb$ (Figure 42b), interfacial states either occupied or depleted by the application of the field may not be reoccupied at such low temperature as a result. As the exact temperature scale was unknown, to restore the charge environment, the sample was heated to room temperature, and then re-cooled and remeasured.
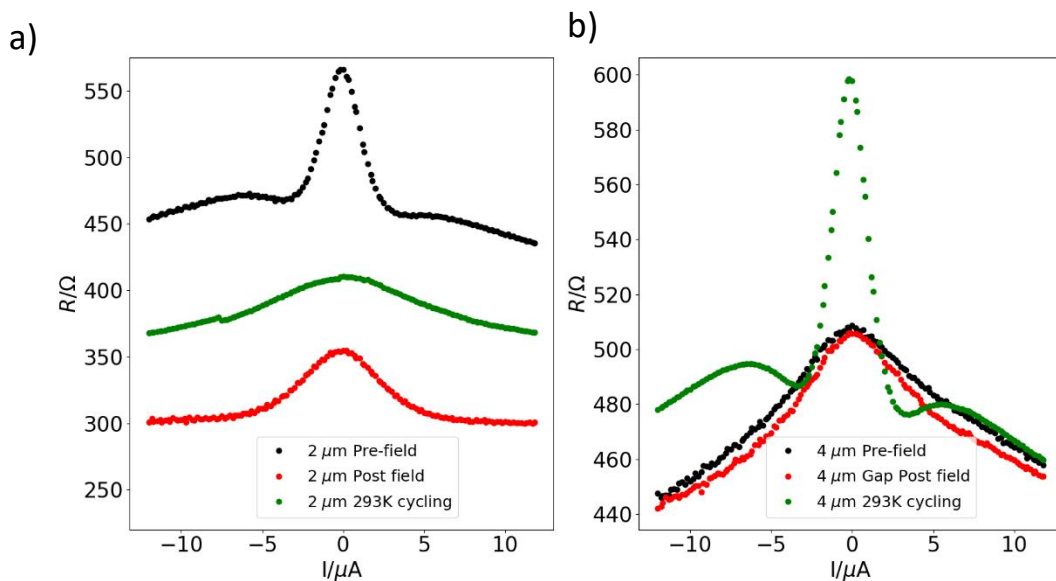
Figure 75: Post temperature cycling differential resistance measurements for the a) $2\mu m$ and b) $4\mu m$ gaps. Included are $T = 3.0K$ measurements prior to B-field exposure, the initial measurement after field exposure, and the measurement after cycling to room temperature.

Figure 75a shows that the temperature cycling through room temperature did not restore the initially observed traces in $2\mu m$ gap, nor the trace observed post field cycling. The onset features were not restored by this field cycling. This also true of all

the other gaps, except the $4\mu m$ gap. In the case of the $4\mu m$ junction (Figure 75b), whilst not restoring the initial trace, the cooling had established a signal trace with onset features. This occurred despite the initial $4\mu m$ trace not exhibiting such features in the first place. The emergence of this with temperature cycling in our view supports the argument for charge trapping. The distribution of these trapped charges would depend on the charge make-up within the sample at cooling, and as such would vary between different cooling processes.
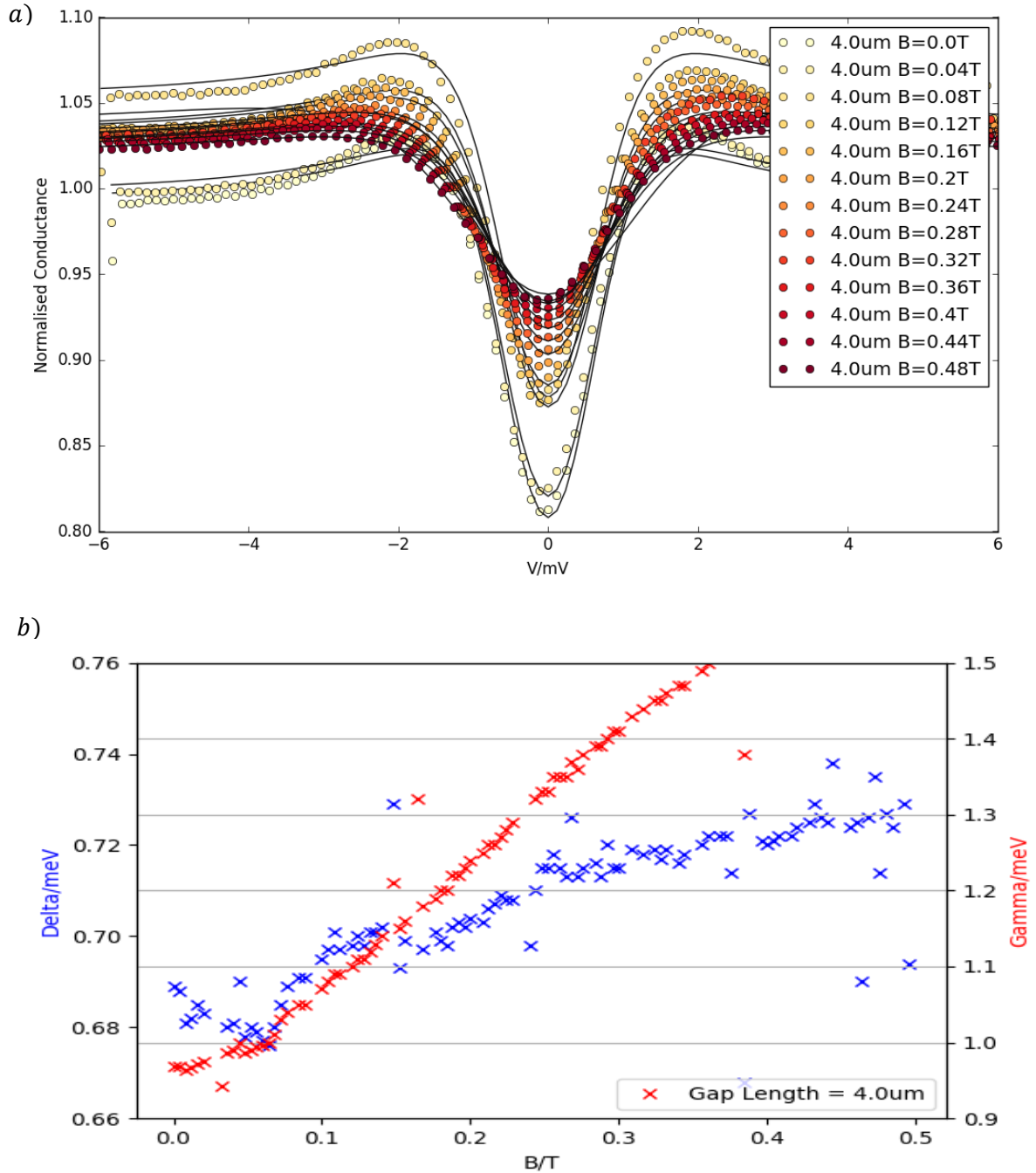
Figure 76: Field Measurement of 4μm junction. a) 2 terminal differential resistance as a function of I_{bias} with a lockin amplifier supplying an $0.01mA$ $13.7Hz$ ac current for increasing magnetic fields b) Extracted Dynes fit values Δ and Γ.

Field dependence measurements of this re-established feature were taken by gradually increasing the field in steps of 0.02T, and then performing a full differential resistance sweep, up to a maximum field of 0.5T. Once swept, the sample was heated to 10K, and another field sweep performed. This allowed normalisation of the conductance at each field step to account for the magnetoresistance and isolate the

evolution of the superconducting features. A selection of these curves are presented in Figure 76a. The features are seen to broaden out with the application of field - with onset features and central peak becoming broader and shorter. Even at the highest applied field, the feature is still present. The normalised conductance is fitted to the Dynes function eq. 4.5, and Δ and Γ are extracted (Figure 76b). Both are shown to increase with field, which is consistent with the broadening observed in the raw data. This is more significant for Γ than Δ, indicating that the scattering is enhanced by the application of a B field. As Δ also increases, this scattering is not likely to be directly supressing Cooper Pair formation. In either case, this supports the prior observation that the application of a B field can significantly alter the electrical environment of the sample. Further measurements and characterisation are required to fully understand the nature of the $InSb/Nb$ interface, and in particular the influence of an applied B field. This would include detailed temperature cycling to discover the 'reset' temperature required to cause the formation of these peaks post field exposure. Additionally, detailed gradual field cycling - applying a single field value, measuring, setting the field to zero, performing a differential conductance measurement at zero applied field, before increasing the field. Both of these measurements would allow characterisation of the energy scales involved in this alteration, as well as the required physical conditions to trigger it. Additionally, fabrication of alternative devices with a thinned top cap, similar to those in Figure 66, and performing comparative measurements could allow for optimisation of the interfacial quality to minimise both the interfacial scattering, and interfacial barrier.

4.7: Summary:

In order to begin the proximity induced SC state within $InSb$ 2DEGs, set of 6 TLM junctions with spacings varying from $1.5\mu m$ to $8\mu m$ was fabricated using a C_4F_8 dry etch. Low temperature electrical measurements exhibited the appearance of a peak in the measured differential resistance. The overall feature shape was consistent with other observations in the literature for superconducting features in the presence of an interfacial electrical barrier with a high degree of inelastic scattering, not unexpected given the minimal surface preparation used prior to $InSb$ deposition. The presence of such features over an $8\mu m$ length scale suggests successful proximity induction of superconductivity within the QW layer of the 2DEGs. Successful induction of proximity

SC in an InSb 2DEG via top-down deposition techniques, despite the poor quality of the SN interface, represents a major technology success.

The initial application of a magnetic field resulted in a permanent alteration to the sample behaviour. This alteration was robust against heating the sample above $2T_c$, and was unlikely to be trapped flux within the SC. Heating of the sample to room temperature and subsequent cooling did not rectify this, however it did lead to the emergence of the peak with onset features in a junction that previously did not exhibit it. Subsequent field measurements on this sample showed enhancement of inelastic scattering with the application of magnetic field. The combination of these behaviours is suggestive that the inelastic scattering at the interface arises in part from trapped states between the $InSb$ and Nb. Further work is required to further investigate and characterise these states.

Chapter 5: μSR of an Nb/InSb heterostructure:

5.0: Overview

Chapter 4 showed some experimental evidence for proximity induced SC within Nb/InSb 2DEG structures. The SC extended across large ($\sim \mu m$) junctions suggesting proximity induction of SC within the high mobility 2DEG layer. Of interest now is characterisation of this induction – the high SOC within the 2DEG should in theory lead to an induced state that exhibits elements of both s-wave and p-wave superconductivity, owing to the lifted spin degeneracy at finite k. In this section, we will discuss measurements directly probing the potentially proximity induced SC (PISC) state with Low Energy Muon Spin Relaxation spectroscopy (LE-μSR). The aim of these measurements is to investigate the local field across the interface of a conventional s-wave superconductor in proximity to a high SOC InSb 2DEG heterostructure.

5.1: Muons, and Muon Spin Relaxation:

μSR, or muon spin relaxation, resonance or rotation is a measurement technique that utilizes the decay of implanted spin polarised muons as a local material probe [231] [232] [233]. Experimental detection of muons was first recorded in detection of Cosmic Rays in 1936. [234]. Spin spectroscopy of muons as an experimental tool began later, with the measurement of the muon lifetime by Garwin [235]. In nature, both positively and negatively charged muons exist, possessing spin $\frac{1}{2}$ and a large mass compared to the electron, $m_\mu = 206.7 m_e$, and charge magnitude $|e|$. Negative muons are often more difficult to use as material probes, as their negative charge often leads to interaction and capture by atomic nuclei, which results in a loss of spin polarisation although many techniques and experiments successfully using negative muons [236] [237] [238] [239] [240]. However, moving forwards, we will focus on positive muons.

Positive muons (μ^+) can be generated via the decay of a pion, π^+ into a muon and a neutrino [235]. (v_μ):

$$\pi^+ = \mu^+ + v_\mu$$

The π^+ is a spin-0 particle. The spin and momentum of a v_μ intrinsically align opposite to each other owing to parity violations [241]. To conserve spin, the spin of μ^+ generated by this decay must then also align opposite to its momentum. A μ^+ population generated in this fashion will thus be spin polarised.
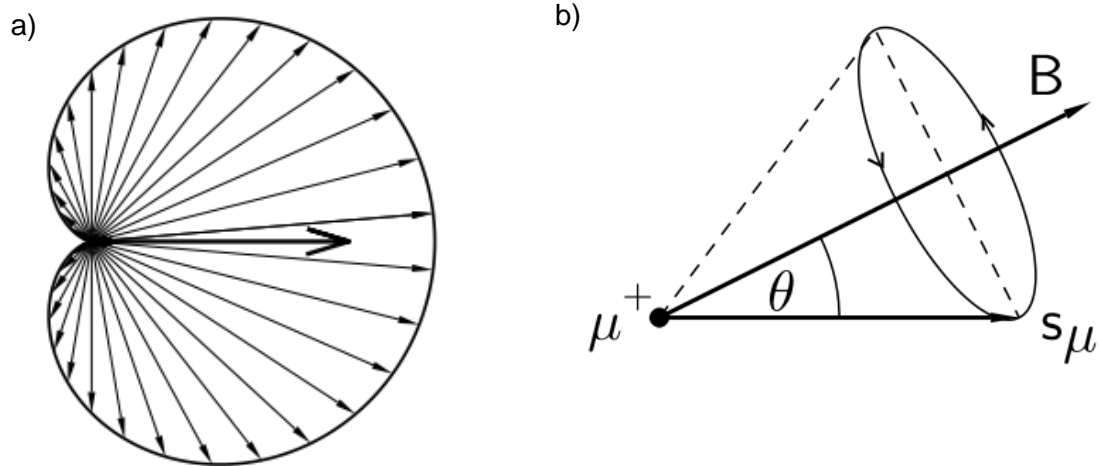
Figure 77: a) Directional distribution of Positron Emission from muon decay. b) Spin precession of a muon in the presence of a magnetic field,B aligned at an arbitrary angle θ to the muon spin orientation. Both figures are adapted from [242].

This spin polarised population can then be implanted within a sample. There, μ^+ will rapidly ($\sim 10^{-9}s$) lose energy through electrostatic interactions and collisions [243]. The energy loss will be sufficient to localise the muon within a sample, at a depth dependent upon the initial muon momentum. μ^+ will then be subject to any local conditions before decaying [244]. μ^+ decays into a positron and a neutrino-anti neutrino pair:

$$\mu^+ = e^+ + v_e + \overline{v_\mu}$$

The positrons emit preferentially along the direction of μ^+ spin (Figure 77a).

The ability to generate μ^+ in a spin polarised fashion is one of several properties of the μ^+ that make them desirable as material probes. μ^+ possess a large magnetic moment relative to the proton ($3.18\mu_p$), and a larger Gyromagnetic ratio ($\gamma_\mu =$

$135 MHz/T$) [231]. The combination of these, allow μ^+ to be more sensitive to small magnetic fields within materials than other techniques, such as X-ray scattering. In particular, it allows measurement of weak magnetisation, or systems with short-range magnetic orders, in the absence of an applied field. For instance, one can track the evolution and emergence of internal fields in a sample as a function of temperature [245] [246] [247]. Measurements of the spin dynamics within a material over the μ^+ lifetime, associated with time varying magnetic fields, as well as the diffusion of μ^+ within a sample are also extensively explored [248] [249]. This work is focused on samples within a static external magnetic field and will largely focus on that example, but for more information of zero field measurements, the interested reader is referred to the following review articles, and several experimental publications of zero field measurements [232] [250] [242] [251] [252].

If the localised muons within the sample experience a magnetic field, either internally in the sample due to local magnetic domains or from an externally applied field, depending on the alignment of the field to the spin (Figure 77b) the muon will undergo Larmor precession. The precession occurs with a frequency $\omega = -\gamma_\mu B$ where γ_μ is the muon gyromagnetic ratio (135.6 MHz/T), and B is applied field. As the spin precesses, the net direction of positron emission will also precess with the same frequency.
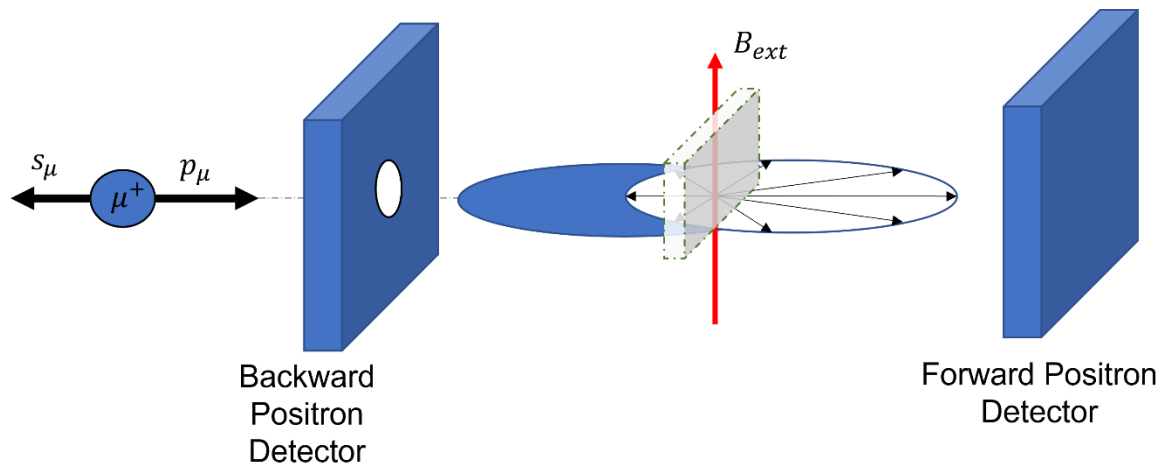
Figure 78: Example experimental set-up. A spin polarised beam of muons is directed towards a sample. An external transverse magnetic field is applied B_{ext}. Two positron detectors are arranged upstream (Forward) and downstream (Backward) of the sample. Positrons emitted from the muon decay are detected and logged as a function of time.

If the spin polarisation direction of the muon is known, then the field can be aligned perpendicularly to it. With a suitably orientated set of positron detectors (Figure 78), one can, as a function of time, measure the net 'spin direction' of positron emission changing in a sample in response to B. This change in beam polarisation, can be tracked by a polarisation, or relaxation function, P(t). The exact form of $P(t)$ depends upon both the alignment of the initial spin direction with the B field, and its spatial distribution throughout a sample. For instance, if the field was aligned parallel to initial muon spin, precession would not occur and thus:

$$P(t) = 1 \qquad (5.1)$$

As the field is aligned with the spin, it cannot precess, and thus the polarisation will remain unchanged. If however, the field were to align perpendicularly to the muon polarisation:

$$P(t) = \cos\left(-\gamma_\mu B\right) \qquad (5.2)$$

The net polarisation oscillates proportionally to the field as previously described. More complex field distributions can be described by further modifications to the $P(t)$. In many cases, there will be some additional relaxation of the polarisation over time, arising from local B fields, tending the net polarisation towards zero. Muons localised in different locations, either within different material layers, or localised around different atoms within a crystal lattice, can experience different fields. Their spins will precess at different frequencies due to experiencing different fields. The relaxation of the whole population will require some degree of summation over these fields to model. For instance, in the zero-field case, the static Gaussian Kubo-Toyabe function can be used [253]:

$$P^{static}(t) = \frac{1}{3} + \frac{2}{3}(1 - \sigma_{kt}^2 t^2)e^{-\frac{1}{2}\sigma_{kt}^2 t^2} \qquad (5.3)$$

σ_{kt} describes the average local field within the sample. Eq. 5.3 is often used to describe fields obeying a Gaussian distribution. Modification of this formula can be used to describe systems exhibiting time varying fields, [254]

$$P(t) = P^{static}(t)e^{-vt} + v \int_0^t dt' \, P(t-t') \, P^{static}(t')e^{-vt'} \qquad (5.4)$$

Where v is the fluctuation rate of the magnetic field. This function allows characterisation of the timescale and magnitude of any such dynamics. This the Dynamic-GKT function. Both static and dynamic versions of the Kubo-Toyabe function are often used in Zero-Field μSR measurements [253]. Even otherwise ideal cases, such as eq. 5.2, often require modification in the measurement of real samples. Small, local magnetic fields will contribute to the total field felt by the muon term, adding an effective damping term to the relaxation function:

$$P(t) = P_o e^{-(\sigma t)^2} \cos(\gamma_\mu B t + \phi) \qquad (5.5)$$

where σ is the depolarisation rate resulting from the internal fields, P_o is the initial polarisation γ_o is the gyromagnetic frequency, B is local field felt by a muon, and ϕ is the detector phase.

The counts measured by a given positron detector, $N(t)$, can be described by:

$$N(t) = N_o e^{-\frac{t}{\tau_\mu}}\big(1 + a_o P_z(t)\big) \qquad (5.6)$$

Where N_o is the initial count, a_o is an intrinsic detector property representing the maximum possible detector reading, τ_μ is the μ^+ lifetime, and $P_z(t)$ is the polarisation in the detector orientation [242].
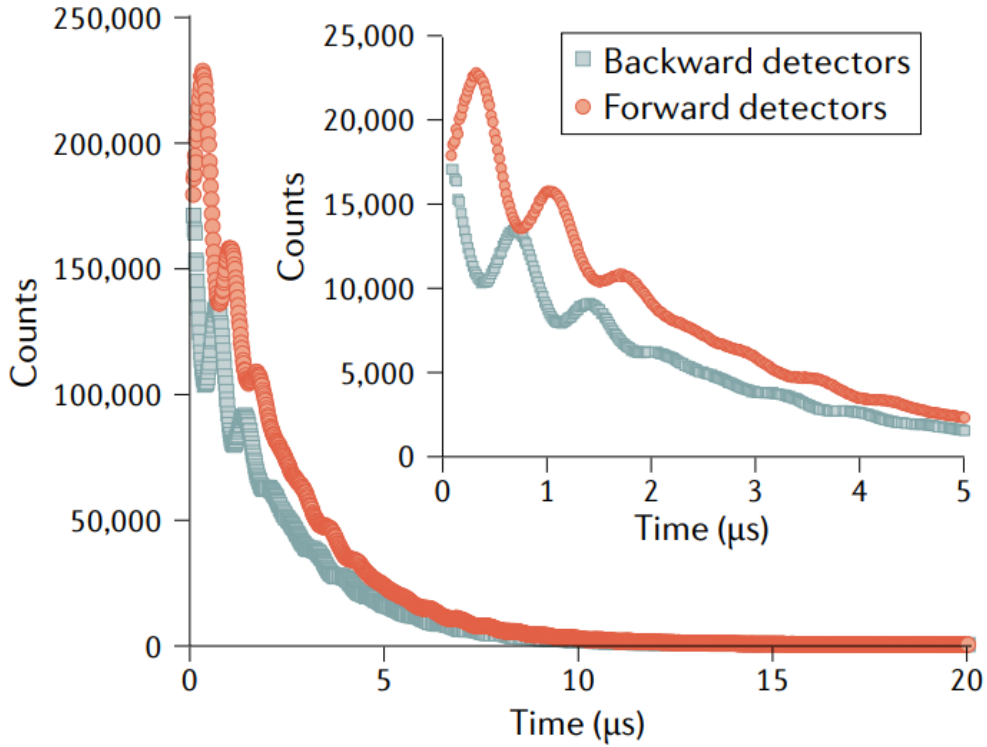
Figure 79: Detector population statistics measured in CdS in an external B field. Presented are statistics from detectors placed forwards and backwards of the sample for the same measurement. The inset is a zoom-in of the same dataset. Adapted from [231]

Figure 79 shows an example measurement using such a detector pair [231]. The sample is in an external field aligned perpendicularly to the muon polarisation. There is an oscillatory component in both traces. This is indicative of the precession: the maxima of the forward detector correspond to the minima of the backwards detector and vice versa. The net spin direction, and thus positron emission, is being rotated in a coherent fashion by the presence of a magnetic field.

From the individual detector statistics, the muon lifetime can be removed, and an asymmetry function, $A(t)$ can be constructed.

$$A(t) = a_o P(t) = \frac{N_f(t) - N_b(t)}{N_f(t) + N_b(t)} \qquad (5.7)$$

Where $N_f(t)$ is the number of detections on the forward detector, and $N_b(t)$ the number of detections on the backward detector. a_o is an experimental parameter

indicating the maximum possible measurable asymmetry for a given detector pair. Such a function can also be constructed for other detector pairs (e.g. Left and Right). $A(t)$ is in essence, the polarisation function adjusted for the maximum sensitivity of the detector set-up used.
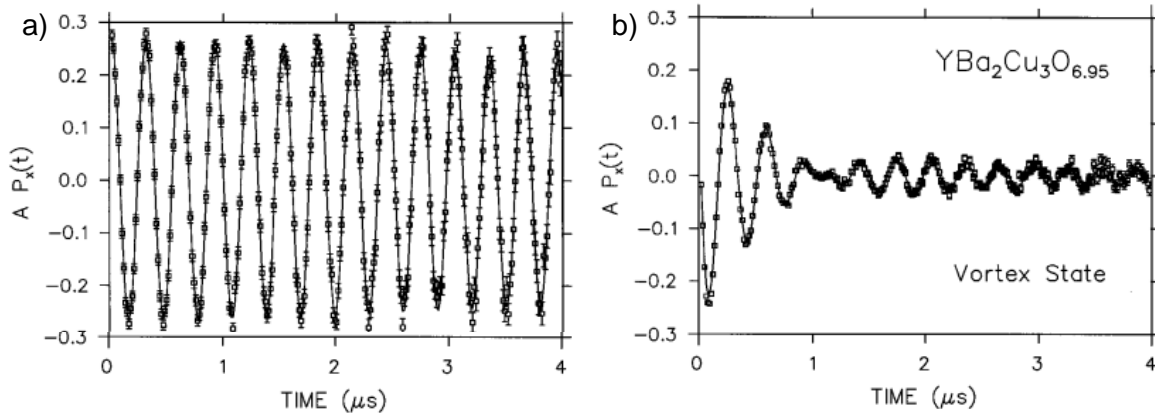
Figure 80: uSR measurements of YBCO superconducting sample ($T_c = 93.2K$) in an external magnetic field of $\mu_o H = 0.5T$ a) measurement at T=120K b) measurement at T=2.4K [263]

Figure 80a shows an example of the measured Asymmetry within a sample of $YBa_2Cu_3O_7$ (YBCO), a high temperature superconductor, in the normal state with an external magnetic field. Figure 80b shows the same sample measured well below T_c. Whilst an oscillatory signal is still visible, the oscillations are heavily damped below T_c. There is a significant increase in depolarisation below T_C. This increased depolarisation directly results from magnetic field screening within the SC state, and as such, we will now consider μSR in SCs in greater depth to understand this.

5.2: Muon Spectroscopy of Superconductors:

To briefly summarise the field behaviour of SCs discussed in Chapter 2.8, within a conventional type-I s-wave superconductor, the field within the bulk of the sample is expelled.
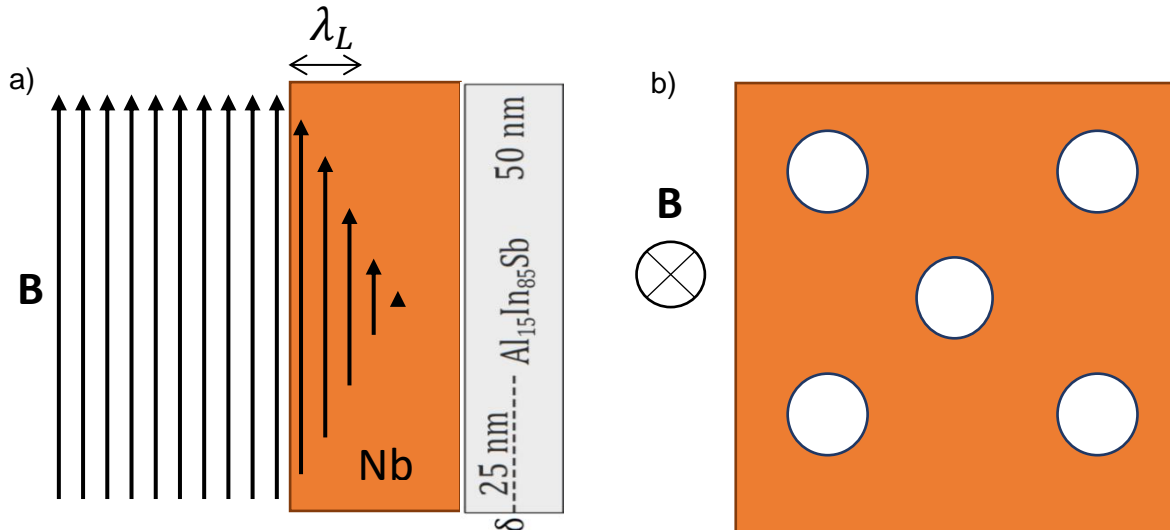
Figure 81: Schematic diagram of a) a parallel orientated field, highlighting the decreasing field with depth from the sample surface. b) Perpendicular field, indicating the formation of magnetic regions of normal material threaded through the sample cross section.

There exists some finite length scale, or penetration depth, λ_L, from the surface over which an external field is screened (Figure 81a). The local field within the superconductor will decrease exponentially away from the surface, leading to zero field within the bulk.

For a type-II SC, spatial distribution of the field depends on the field orientation and field size. Below a certain critical field, H_{c1}, a type-II will behave as per a type-I. If we consider a field above H_{c1} but below H_{c2} that is orientated parallel to the sample surface (Figure 81a), the field will again be screened as per a type-I. However, if the field is rotated, and instead aligned to be transverse with the sample surface (Figure 81b), the field will not be totally expelled. There will exist truncated cylinders of normal state material containing flux of a flux quanta ϕ_o, surrounded by superconducting state. The flux within the N regions will be screened within the remaining SC bulk via screening currents, again over some length scale λ. In either case, the type-I or type-II SC, the screening will vanish above T_c.

μSR of SCs can examine many properties of the SC state. As an example, zero field, or $ZF - \mu SR$ can be used to examine the presence and distribution of magnetic impurities via the Gaussian Kubo-Toyabe functions [254] [255]. The absence of an external field, and thus precession, means the measured depolarisation will correspond to internal magnetic features, or impurities.
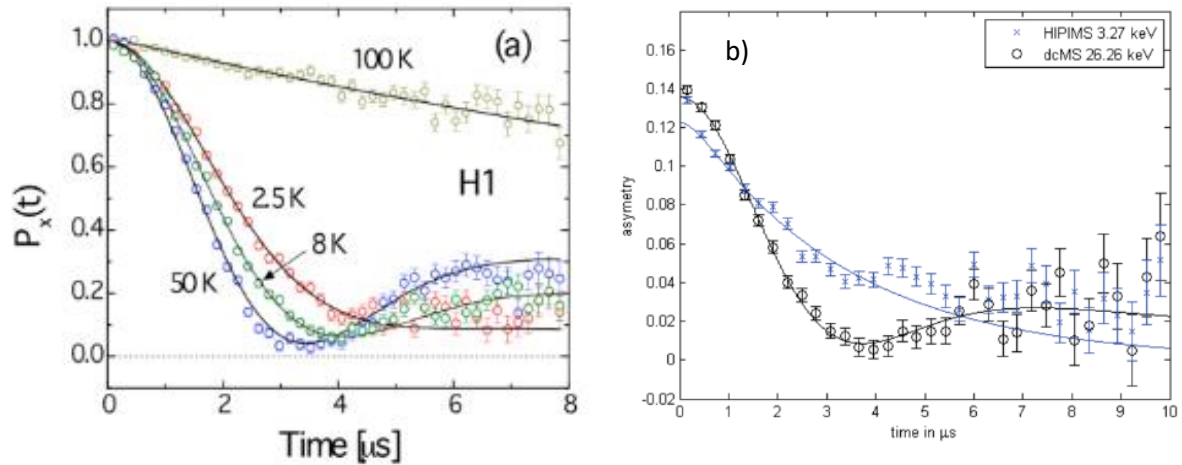
Figure 82: ZF-uSR measurements of an Nb sample at various temperatures. Data modelled to Dynamic-GKT described by (6.4). Figure adapted from [256] b) Figure adapted from [257] tracking magnetic impurities in two Nb samples via different implantation energies.

Figure 82 shows examples of this kind of characterisation in two different Nb samples. Figure 82a tracks the evolution of defect states in an Nb film as a function of temperature, considering how magnetic impurities can evolve and change within these materials. For $T < 100K$, depolarisation can be seen to be drastically enhanced vs $T = 100K$. For low energy, or $LE - \mu SR$ μ^+ can be injected at very shallow depths within a sample, allowing consideration and characterisation of surface defects within thin films. An example of this is shown in Figure 82b, where μ^+ are implanted at two different depths within Nb films, showing a difference in the resulting depolarisation. Modelling with dynamic GKBT allows further characterisation as to the effect these defects have on spin-dynamics [256]. ZF measurements allow characterisation of these innate defect states, but in this case, the case of externally applied fields for $LE - \mu SR$ is of greater interest.
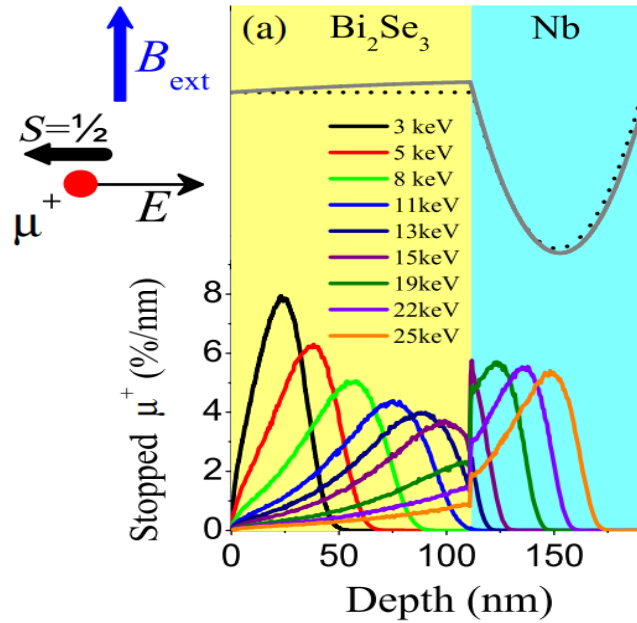
Figure 83: Muon stopping profiles as a function of implantation energy a) Stopping profile calculated for a $BiSe_2/Nb$ heterostructure. Top-most solid and dotted lines show calculated local field within each material. [258]

Below T_c the expulsion of field applied parallel to the sample surface within SC samples, provided the sample was cooled with the external field applied (known as field cooling) [259], result to a spatially non uniform field profile through the sample (Figure 83). The field a μ^+ experiences depends upon where in the SC it localises. There will be a calculable stopping profile, dependant on μ^+ implantation energy, that will shift deeper into samples with increasing energy. Correspondingly, the higher the μ^+ implantation energy, the greater the fraction of μ^+ stopping deeper into the sample, and thus for a superconductor the greater the field screening felt. For type-II SC, in addition to the parallel field case, you can also consider the case of a field applied perpendicular to the sample surface. Below H_{c1} two signals will experience similar behaviour.
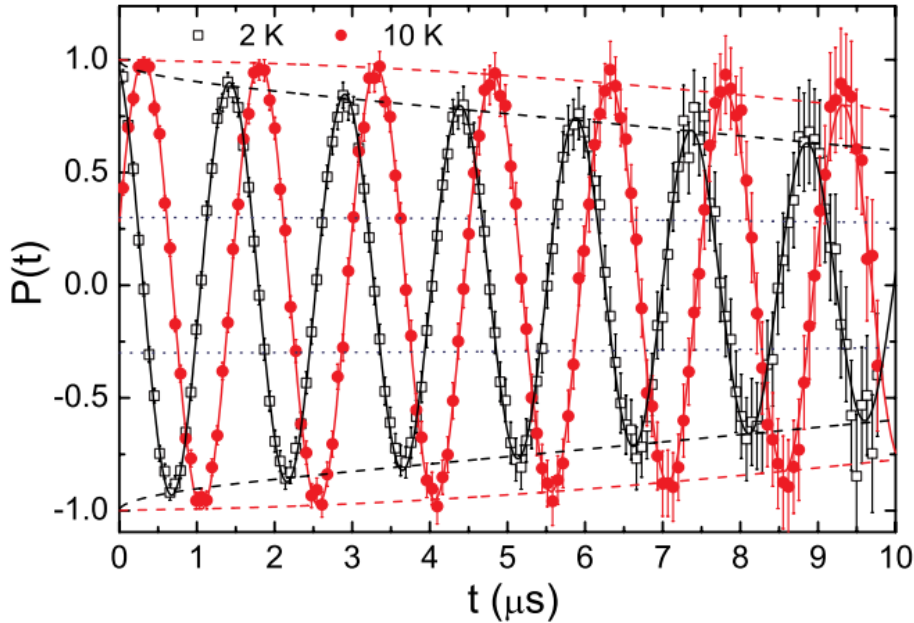
Figure 84: Measured Polarisation of Ga_{84} sample, a type-II SC, $T_c = 7.8K$. Measurement was performed with an external field applied perpendicular to the sample surface $B_{TF} = 60mT$. Figure adapted from [260].

The decreased field within the SC will result in the net μ^+ precession frequency also decreasing, shifting the trace. Additionally, the spread of felt fields, arising from the spread of the stopping profile through the sample means the measured positron decay will consist of many μ^+ experiencing many different fields. This will result in enhanced depolarisation below T_c. Increasing the implantation energy, and thus implanting deeper within a sample, allows direct measurement of Meissner Screening within SC thin films via $LE - \mu SR$. [261] [258] Figure 84 gives an example of this behaviour in a Type-II SC. Above T_c, the data is well modelled by eq. 5.5 with minimal damping. When taken below T_c, both the characteristics we previously saw are present. The frequency is shifted, Additionally, there is some enhancement of depolarisation owing to an increased distribution of fields, visible in shrinking of the envelope of the signal.

This field alignment has further advantages for measurement of thin films. In such cases, particularly for LE-μSR, λ_l can be large relative to the film thickness, meaning the measurable screening in the parallel field may be negligible. Instead, one can consider the vortex state within a perpendicular field orientation. Within a type II SC, held in a field above H_{c1} there will be a mixed distribution of N and S, due to the formation of superconducting vortices and associated field screening surrounding them. As such, the emitted positrons will also represent a distribution of different

effective fields, arising from the N regions, S regions, and screened regions surrounding the vortices.
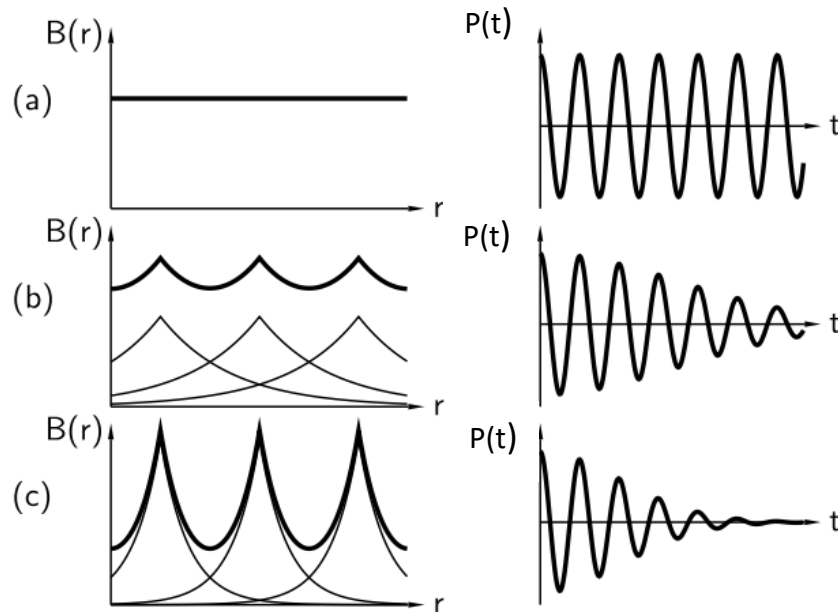
Figure 85: left – all) Local field distribution within a superconductor. Right – all) Corresponding μSR polarisation trace. a) Normal state b) Superconducting state, long penetration depth c) Superconducting state short penetration depth. Figure adapted from [242]

Figure 85 illustrates the three different cases for a Type-II SC experiencing an externally applied field. The first, (Figure 85a) and its corresponding relaxation function indicate the SC held above T_c. There is minimal depolarisation, and $P(t)$ is approximately constant (as per eq. 5.2). When the sample is brought below T_c, (Figure 85b) vortices form, and screening begins, decreasing the field over λ_L surrounding the vortexes. As with the Meissner state above, the non-uniform fields cause damping, and adds depolarisation to $P(t)$. The size of this damping is inversely proportional to λ_L – as λ_L gets shorter (Figure 85c), the field around the vortex cores decays more rapidly, and the faster the muon population depolarises. There will also be some dependence on the density and size of vortices, which has been measured via μSR previously [262]. The distribution of field values can be modelled by considering the depolarisation, σ, which can be related to λ_L via: [263] [264].

$$\sigma = \gamma_\mu \phi_o \sqrt{0.00371}\,\frac{1}{\lambda_L^2} \tag{5.8}$$

Where ϕ_o is the magnetic flux quanta. This has been used to directly measure the magnetic screening length as a function of temperature [265] [264] [266]. An example of these measurements can be seen below:
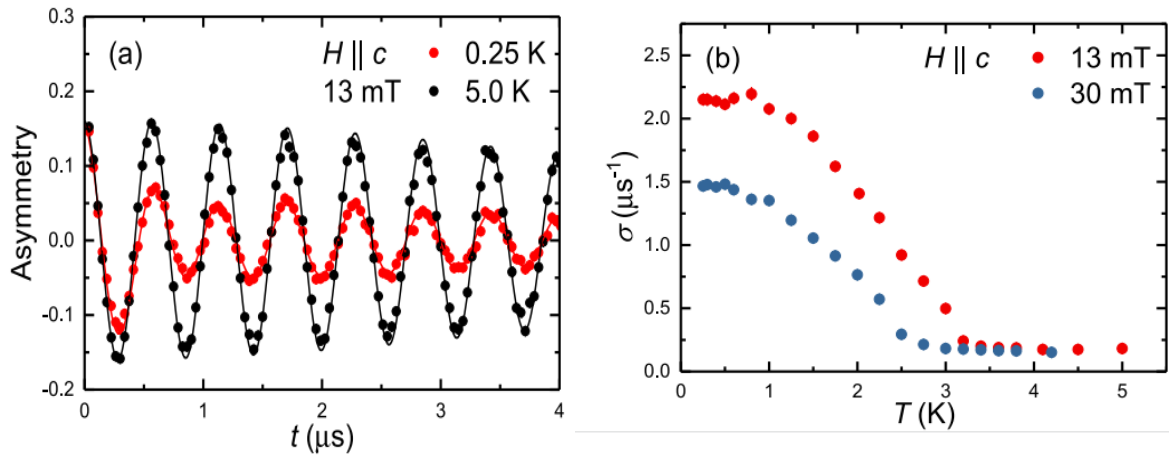
Figure 86: *μSR measurements of $PbTaSe_2$ a type II superconductor a) Detector asymmetry measured above and below T_c via TF-uSR. b) Extracted σ as a function of Temperature for two fields. Adapted from* [267]

Figure 86a shows a measurement of $PbTeSe_2$ above and below T_c, showing the strongly enhanced depolarisation below T_c. In Figure 86b σ was extracted from the datasets via eq. 5.8 and plotted as a function of increased temperature to illustrate its temperature variation. Modelling of the temperature variation of either σ or λ_L directly allows characterisation of the SC state and has been used to assist in the classification of SC materials [268] [269].
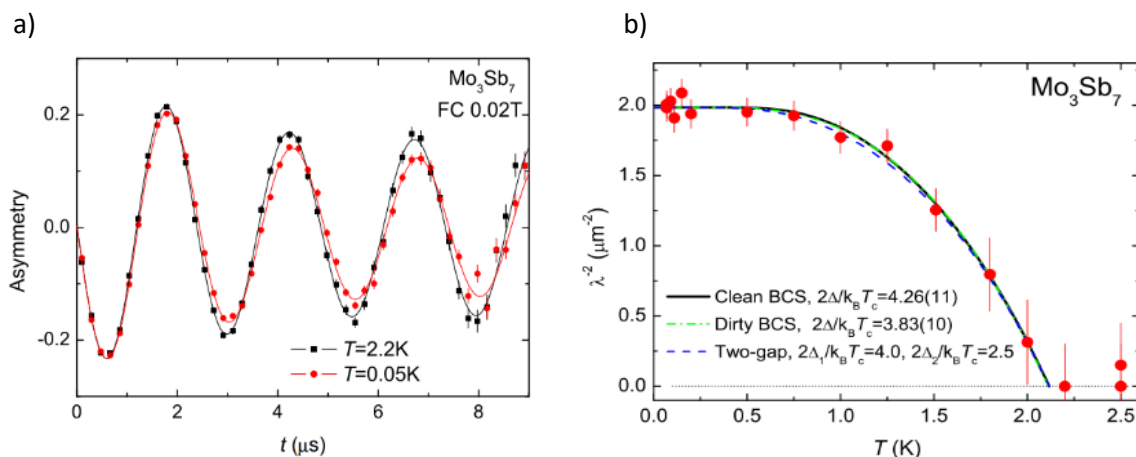
Figure 87: *μSR measurements of Mo_3Sb_7, a type II superconductor a) Detector asymmetry measured above and below T_c b) Extracted λ^{-2} as a function of Temperature fit to various models for different gap functions. Adapted from* [266]

Figure 87 illustrates an example of this. As with Figure 86 μSR was performed (Figure 87a), from which σ was extracted and used to extract λ_L via 5.7 (Figure 87b). This temperature dependence was then modelled for various conventional BCS energy gaps. As well as classification of SC, this analysis can also be used to assess the quality of an SC sample. In Figure 87b for instance, the data is modelled by a 'clean':

$$\frac{\lambda_L^{-2}(T)}{\lambda_L^{-2}(0)} = 1 + 2 \int_{\Delta(T)}^{\infty} \left(\frac{\partial f}{\partial E}\right) \frac{E}{\sqrt{E^2 - \Delta(T)^2}} dE \qquad (5.9)$$

Where f is the fermi function. And dirty superconductor dependence:

$$\frac{\lambda_L^{-2}(T)}{\lambda_L^{-2}(0)} = \frac{\Delta(T)}{\Delta(0)} \tanh\left(\frac{\Delta(T)}{2k_b T}\right) \qquad (5.10)$$

In this instance, the similarity between the 'clean' and 'dirty' function fits was taken as evidence that the measured sample was a heavily defected SC sample [266]. Similar analysis can also be done directly with λ rather than λ^{-2}. A defect free s-wave SC in that case can be modelled via:

$$\lambda_L(T) = \lambda_L(0) + \sqrt{\frac{\pi \Delta(0)}{2k_b T}} e^{-\frac{\Delta(0)}{k_b T}}. \qquad (5.11)$$

Where $\lambda(0)$ is the penetration depth at $T = 0K$ [270]. For defected s-wave fits, a power law fit,

$$\lambda_L(T) - \lambda_L(0) \; \alpha \; T^n \qquad (5.12)$$

where n is an integer, and α is a proportionality constant [263] [271] The exact power of n is indicative of the type of defects present in a non-clean SC, and thus allows a qualitative analysis of the SC state.

Finally, it is worth considering $LE - \mu SR$ as a probe of proximity induced SC. As discussed, by varying the implantation energy and extracting the field, we can find the local field at increasing depths from the sample surface. If material layers are thin on the length scale of μ^+ implantation, which for $LE - \mu SR$ can be on the order of $\sim 10s$ of nm, then doing so will sweep implantation through material layers. This is shown in the stopping profiles in Figure 83a, Through this, we can measure the field screening profile, both in the SC layer and any proximity induction in other material layers [272] [273]. This allows measurement of the length scale of the induced SC, as well as its local field behaviour. For instance, μSR measurements in a Bi_2Se_3/Nb heterostructure [258] measured evidence of an anti-screening effect within the Bi_2Se_3.
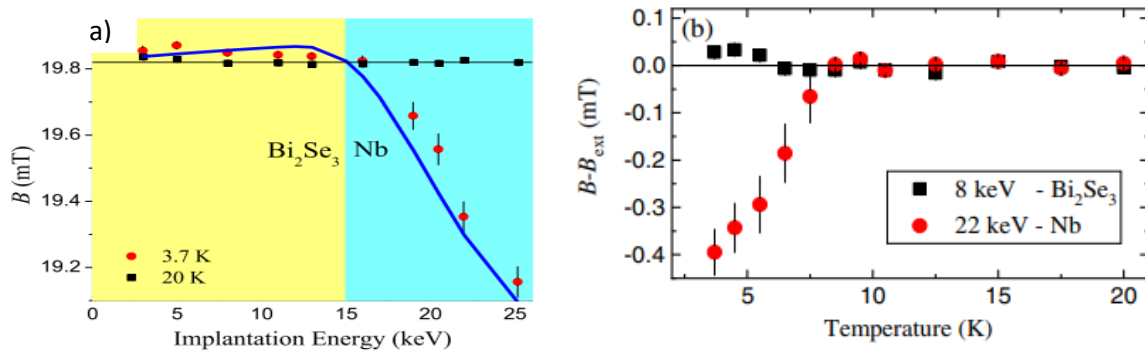
Figure 88: uSR measurements of Bi_2Se_3 from [258] Black line indicates externally applied field. a) Measured B-field as a function of implantation energy for temperatures above and below sample T_c. B) Measured B field as a function of temperature . In both cases, the solid black line indicates the externally applied field.

Bi_2Se_3 is thought to be a topological insulator, exhibiting fully lifted spin-degeneracy, like the case of SOC discussed in chapter 2. This lifted spin degeneracy allows the formation of proximity induced SC with unconventional SC pairing, predominantly spin triplet p-wave. The p-wave pairing causes the formation of an anti-screening Meissner effect owing to the odd frequency nature, enhancing the local field [128]. This anti-screening will manifest itself as an increase in the local field.

The μSR measurements undertaken observed a decrease in local field within the Nb (Figure 88a). Within the Bi_2Se_3 however there is instead a slight enhancement of field. In both cases, the change from the externally applied field was supressed with increasing temperature. It was supressed entirely as the sample temperature was driven above T_c and well into the normal state (Figure 88b). Similar behaviour should

be observable within high SOC InSb 2DEGs experiencing proximity SC [274] [10]. Both InSb and Nb have been previously measured using μSR, but measurements of our heterostructure devices are novel [275] [276] [256] [277] [278]. Additionally, because the commonly used side deposition of SC films is incompatible with the required experimental geometry. The μ^+ beam passes through the sample cross section, spread across a broad (~mm) area. A thin film deposited on the side of a sample on the order of a few 10s of nm would have a negligible contribution to the measurement. The top-down SC film used in this work thus allows us to perform this novel investigation.

The aim of this chapter's measurements was thus to measure the local field across the interface of a conventional s-wave superconductor in proximity to a high SOC InSb 2DEG heterostructure.

5.3: Experimental Apparatus:

Measurements were undertaken on the Low Energy Muon beamline (LEM) at the Paul Scherrer Institute (PSI) in Switzerland [279] [280]. The muon beam is generated by first producing protons from a source of hydrogen atoms which are sent through a successive series of accelerators. These accelerate the proton beam to ~80% the speed of light. The protons are then transported through a series of channels towards a graphite target. A variety of interactions between the proton beam and nuclei in the target leads to the formations of π_+, π_0 and π_-. [231] π created at or near the surface of the target then decay [279]. This produces 'low energy' (~4MeV) muons emitted in a ~100% spin polarised population, with spins aligned opposing the muon momentum [281].
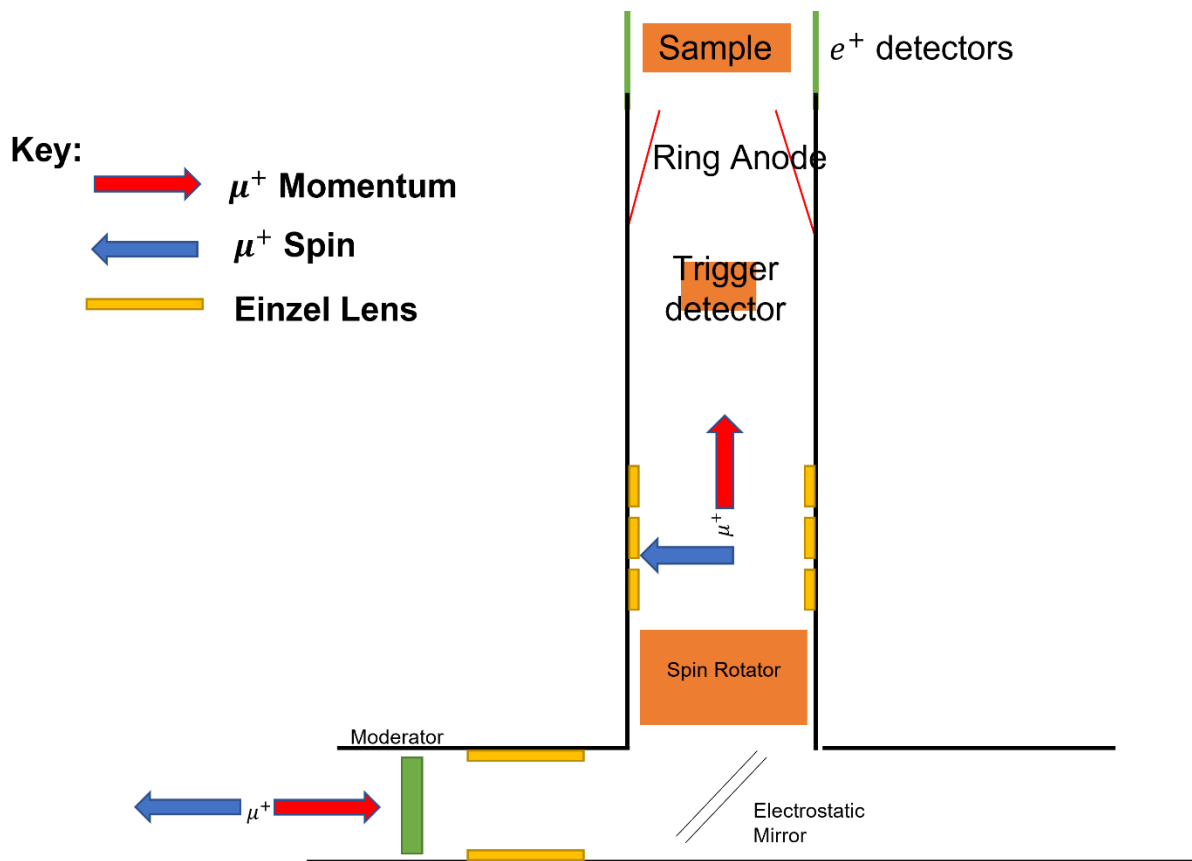
Figure 89: Schematic representation of the LEM Beamline.

The so called 'surface muons' generated from this target are then directed to a cryogenic moderator (Figure 89), which serves to slow the muons via coulomb interactions and ionization of atoms in the target [231] [280]. The moderators are typically wide-band gap insulators. Once the muon energy reaches approximately the band gap energy, interactions are suppressed, and the rate of energy loss is lowered, allowing control of muon energies [282]. These 'epithermal' muons then exit the moderator, with the initial polarisation of the muon being strongly conserved.

The generated muon beam is then directed towards an electro-static mirror (Figure 13) to filter out any remaining high energy muons exiting the moderator. The mirror is aligned such that only μ^+ with low energy are reflected onto the sample. These are sent through a spin rotator allowing re-alignment of the spin as is necessary for different field orientations, without impacting the percentage polarisation of the muon beam. The beam is then focused via a series of Einzel lenses towards the sample, with a final beam rate of $\sim 4.5 \times 10^3 \ s^{-1}$. A set of ring anodes allows adjustment of the final beam position via biasing to deflect the beam. For externally applied fields, this

allows compensation for any induced bending of the beam and allows maximization of the initial asymmetry.

A 10 nm carbon film is placed along the beam path [283]. Muons passing through this foil cause the generation of electrons, which are channelled towards a detector. This serves to act as a trigger detector with minimal interference to the muon beam (Overall energy reduction of ~1keV and a deviation of ~0.4keV). Finally, muon energy can be controlled at the sample by applying a voltage at the sample plate to further accelerate or decelerate the beam. Final muon energies can be varied in the range 1keV to 30keV depending upon the appropriate plate voltage. With the appropriate cryostat, it has a measurable temperature range of $2.2 - 300K$.
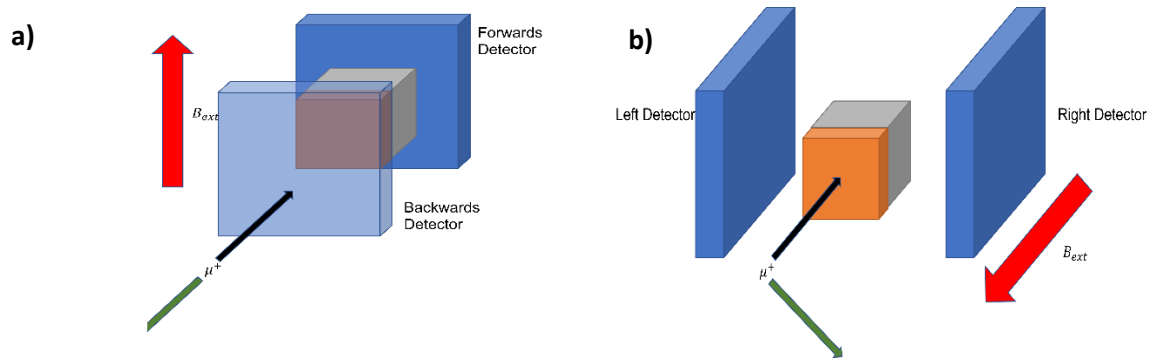
Figure 90: LEM Field and Detector Orientations a) Parallel orientation b) Perpendicular orientation. Rotation of μ^+ spin, and the detectors is necessary with adjustment of the field to allow measurement of the precession.

As discussed in section 5.1, the μ^+ spin must be aligned perpendicular to the magnetic field in order to have a measurable precession. Further to this, the detectors must also be aligned along the axis of precession to be able to measure this. In the initial case, where μ^+ is aligned anti-parallel with the beam momentum, and perpendicular to the cross section of the sample. (Figure 90a). The magnetic field, B_{ext} must then be aligned parallel to the sample surface. This is known as the parallel measurement orientation.

To instead orient the field through the sample cross section, as is necessary to measure the vortex state in a type-II SC, the muon spin must be rotated. This is the function of the spin rotator in Figure 89 [284]. The spin can be rotated such that is

aligned perpendicularly with the muon beam, without significantly impacting the overall polarisation muon population. This is known as the perpendicular orientation. LEM supports fields aligned parallel to the sample surface (Figure 90a) of up to $0.34T$ and perpendicular fields (Figure 90b) of up to $30mT$.
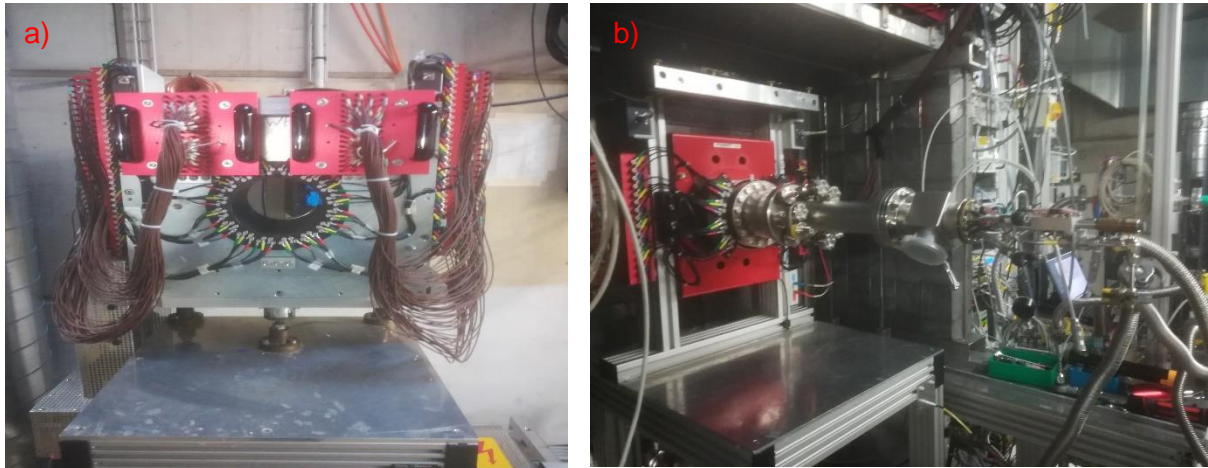
Figure 91: a) Muon detector array used at LEM b) Sample and cryogenic environment mounted into the beamline.

Figure 91a shows an example detector array utilised in the apparatus. Each lead corresponds to a set of detectors, leading to 16 possible detector channels for utilisation. Pictured is the transverse field array – the LEM array is modular, allowing for rapid change between detector orientations at room temperature. The sample plate is then attached to a He cold-head and mounted in the detector array as visible in Figure 91b.

5.4. Sample design:

The sample design used for the electrical measurements (Chapter 5) was likely to be unsuitable for these LEM measurements. For low energy μSR experiments, depending upon the target material density, the expected stopping distances can be as low as ~ 10 −to hundreds of nm, versus μSR which can extend to several μm [272].
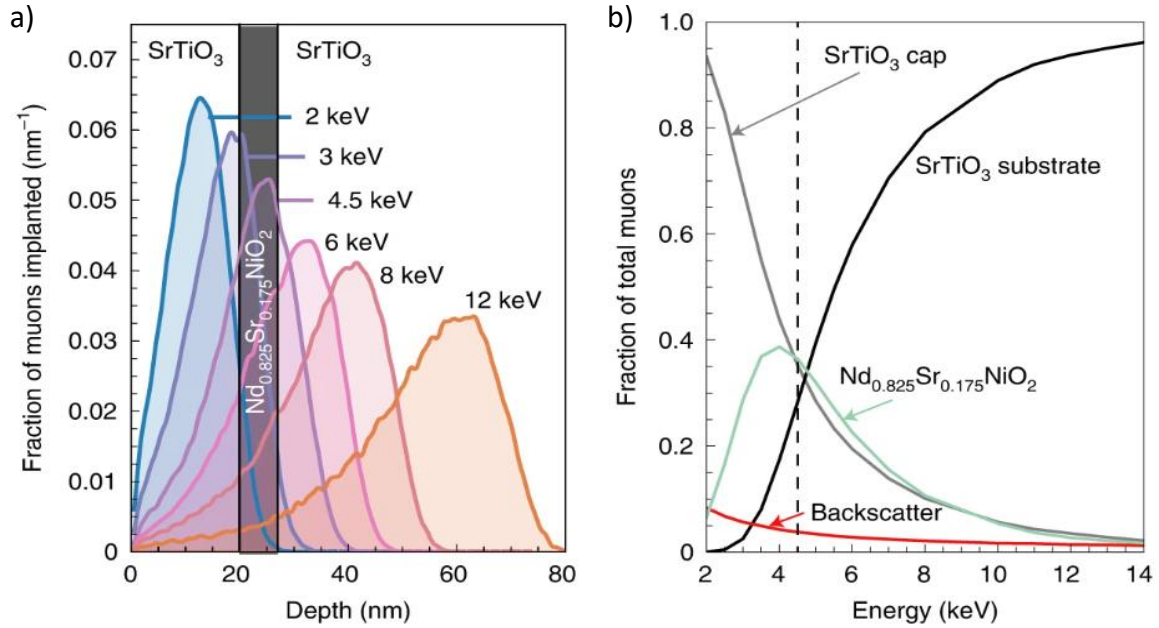
Figure 92: a) Muon stopping profile calculated for various implantation energies within a $Nd_{0.825}Sr_{0.175}NiO_2$ heterostructure. b) Fraction of μ^+ stopping within a given material layer of a) as a function of implantation energy. Adapted from [261]

The muon beam passes through the sample cross section; even for high implantation energies there will be some fraction of the muons stopping in the initial materials layers. Figure 92 shows this. Figure 92a shows the muon stopping profile for a $SrTO_3/Nd_{0.825}Sr_{0.175}NiO_2$ heterostructure for various implantation energies. Figure 92b then shows from this the fraction of μ^+ stopping within a given material layer. Even at the highest energies, with the peak of the stopping profile well into the substrate, there is a non-zero fraction of μ^+ from the initial capping layer. If for instance, a SC is the first material layer, below T_c there will be some fraction of μ^+ stopping within there, and thus some field screening arising in all measurable energies. Ideally, the top-most layers should be those of lowest density to allow greater penetration in deeper layers. Additionally, for measurements investigating proximity superconductivity, it is preferable to place the bulk SC as the bottom most layer.
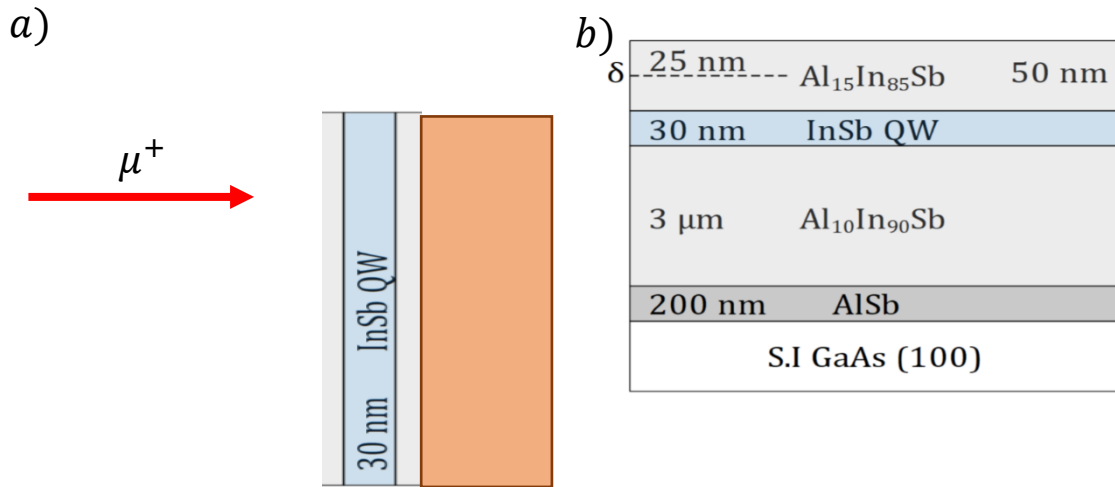
Figure 93: a) Idealised sample design, orientated relative to the incident μ^+ beam. b) InSb 2DEG Heterostructure schematic. Noted are the various material layers, and corresponding thicknesses.

An ideal sample, for our purposes, (Figure 93a) would have the InSb active layers on top, and the Nb below, allowing for thick Nb layers to be used. The InSb 2DEGS (Figure 93b) are grown on a thick ($\sim 350\mu m$) GaAs substrate, with a further $3\mu m$ buffer layer. The substrate and buffer layers are sufficiently thick to preclude any muon implantation in the QW in that orientation. Additionally, it cannot be etched away without risk of compromising the quality of the 2DEG. As such the Nb layer must be the top layer for these experiments. Because the range of muon energies available is limited ($30keV$ at maximum), the Nb layer would have to be thin enough to allow a significant fraction of μ^+ to stop in the QW layer within our energy range.

To calculate appropriate film thickness, numerical calculations of muon stopping profiles were performed using TRIM.SP [285]. TRIM.SP is part a wider part of SRIM (Stopping Range of Ions in Matter [286] [287]. It is a numerical software capable of simulating the stopping profiles via Monte Carlo simulations of freely chosen ions within up to 10 material layers. It has been widely used in the simulation of atomic and ionic implantation [288], particle sputtering [289] [290, 291] [292], and calculation of

muon stopping profiles [258] [128] [293]. Muons are simulated by treating them as hydrogen ions H^+ with a mass of m_u.

Table 4:TRIM.SP Simulation Parameters used to calculate stopping profiles for different Nb thicknesses.

Material layer:	Density (g/cm^3):	Layer Thickness/nm
Nb	8.57	Variable
$Al_{15}In_{85}Sb$	5.552	50
$InSb\ QW$	5.78	30
$Al_{10}In_{90}Sb$	5.628	3000

The chosen material layers, and the densities used for the simulations are listed in Table 4. Muon stopping was calculated on a monolayer-by-monolayer basis, considering the collisions and interactions between muons and the atoms of each layer to estimate final stopping position. 100,000 muon stopping events were simulated for each generated stopping profile.
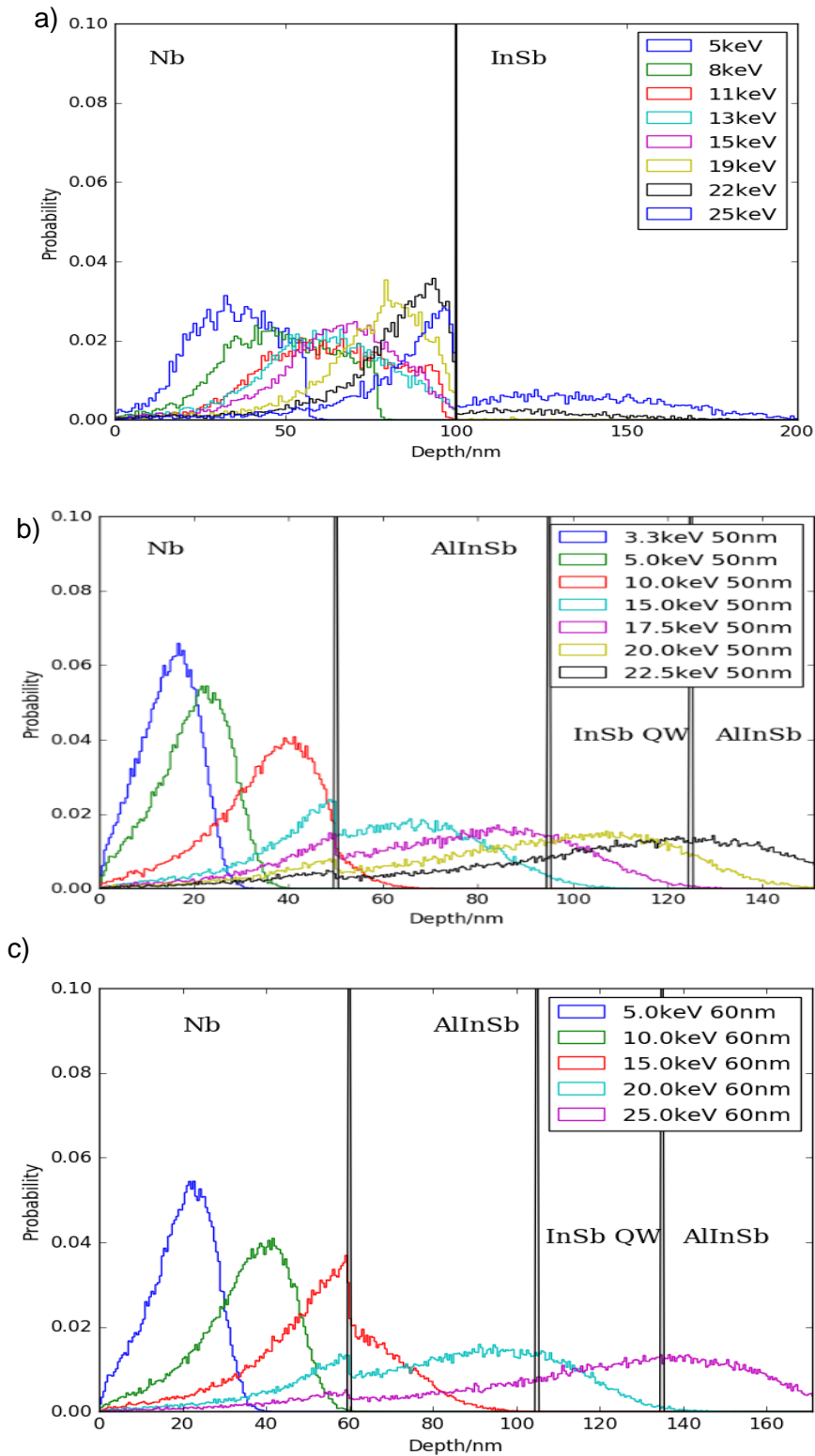
Figure 94: TRIM simulations for our sample for different implantation energies. A) 100 nm Nb thin film b) 50nm Nb thin film c) 60nm Nb thin film.

Figure 94 presents numerical simulations for, 100nm, and 50nm and 60nm films. The simulations suggested that use of a 50nm Nb layer. The 100nm films (Figure 94a) used for prior electrical measurements was too thick for our purposes – even the

highest energies accessible available had a negligible fraction of muons stopping within the InSb. Both the 50nm (Figure 94b) and 60nm (Figure 94c) films showed sufficient stopping within the QW layer. Of these, the thinner 50nm was preferred due to the access of a larger range of energies within the InSb layers. A thinner 30nm film was trialled experimentally and found to have T_c outside of measurable range of the LEM cryostat. 50nm (Figure 94a) was thus the chosen thickness as a compromise between a desirable stopping profile and a workably high T_c.

5.5: Sample Characterisation:
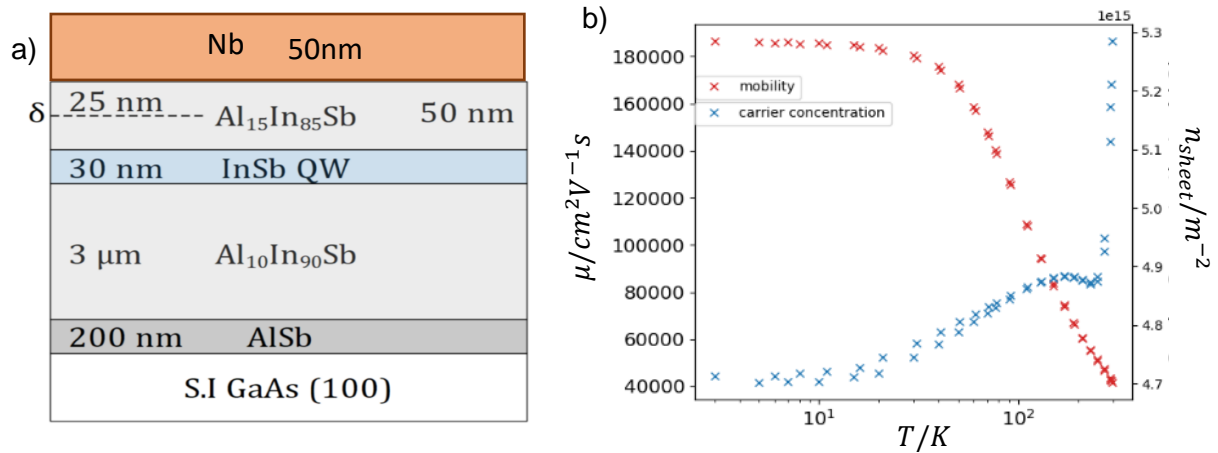
Figure 95: a) Sample cross section –4 1cm^2 pieces of an epitaxially grown InSb/Al$_x$In$_{1-x}$Sb QW heterostructure. δ indicates the location of Te-modulation doping layer. b) Mobility and Carrier Concentration calculated as a result Hall Effect measurements performed during a temperature sweep from 293K to 3K. Measurements were performed prior to this work by previous students [137] [37].

The finalised sample (Figure 95a) consisted of a mosaic of 4 $1 \times 1 \ cm^2$ of a 50nm Nb film, deposited by sputtering on a Te-doped InSb/Al$_x$In$_{1-x}$Sb 2DEG. The 2DEG consists of an InSb quantum well (QW) electrically confined by layers of Al$_x$In$_{1-x}$Sb either side of it. As with prior samples discussed, the quality of the 2DEG was assessed via Hall Effect measurements, prior to Nb deposition (Figure 95b), giving single carrier mobilities and carrier concentrations of $n = 4.71 \times 10^{15} \text{m}^{-2}$ and $\mu = 187{,}000 \ \text{cm}^2\text{V}^{-1}\text{s}^1$ respectively. The 2DEG was grown epitaxially at the National Epitaxy Facility at Sheffield University. The Nb was deposited at Bristol university – the film thickness was measured in-situ and confirmed via surface profilometry after deposition. The

same wafer, and thus 2DEG design, was chosen for this work as was for the electrical measurements undergone in Chapter 4 to allow for comparison..

The superconducting film was characterised via AC magnetic susceptibility measurements in a Physical Properties Measurement System (PPMS). [294] This technique has wide applications in materials research particularly in investigating the sensitive magnetic responses of magnetic materials in extreme conditions (ultra-low temperatures, or extreme frequencies for example [295] [296] [297]). Magnetic susceptibility is defined as:

$$\chi = \frac{M}{H} \tag{5.13}$$

Where M is the magnetisation within the sample, and H is the applied external magnetic field. If the external magnetic field applied is varying, by applying a small external AC field for instance, then we can instead measure the ac susceptibility:

$$\chi_{ac} = \frac{\partial M}{\partial H} \tag{5.14}$$

Where M is the measured amplitude of the change in magnetic moment to an external field.

In this work, this can be used to measure the superconducting state within the sample – owing to the expulsion of flux within the bulk, an SC below T_c behaves as a perfect diamagnet i.e. $\chi' = -1$. By measuring χ' as a function of temperature, we can estimate T_c. [298] [299]
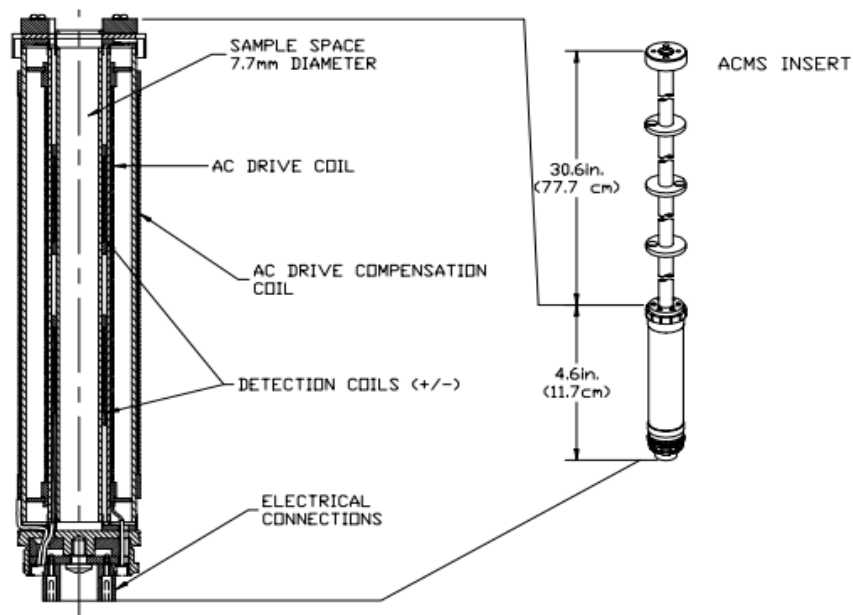
Figure 1-1. ACMS Insert and Coil Set

Figure 96: ACMS Schematic Diagram showcasing the ACMS insert, and the coil locations. Adapted from [300].

The measurement was performed using an AC Measurement System (ACMS), an added measurement option for the PPMS. The ACMS allows direct measurement of the real and imaginary components of the AC moment response. A piece of Nb/InSb deposited in the same process as the full sample, was mounted into a sample holder and zero field cooled to base temperature of 2K. A 0.1mT reference field was applied at a 1000Hz frequency via the drive coils (Figure 96), and temperature gradually swept.

The detection coils have equal numbers of turns, N, but are wound in opposite directions relative to each other. Centred within each detector coil are additional single turn calibration coils. This is a feature unique to the ACMS. The field outside the detection coils is supressed via the compensation coil, which is counter-wound relative to the drive coil. This reduces interaction with and interference from other conductive parts of the system in the measured signal. At each temperature point, the sample is placed within the centre of each detection coil in turn and measured.

The sample is also placed and measured between the two coils. An additional two measurements are taken by reversing the polarity of the two calibration coils. Through

comparison to the known driving signal, the real and imaginary parts of the moment response can be measured.
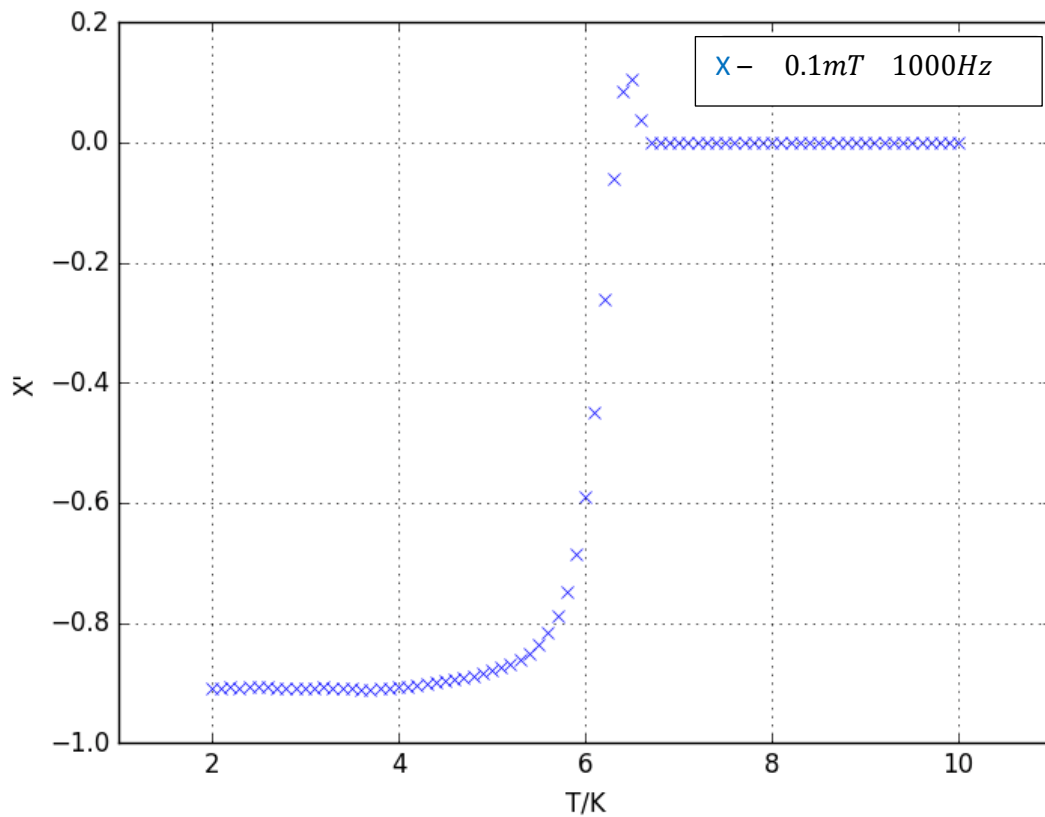
Figure 97:SC Characterisation of 50nm Nb/InSb sample via magnetic susceptibility measurements in a 0.1mT 1000Hz magnetic field.

χ' was found for a 0.1mT amplitude AC field (Figure 97). From these, T_c was estimated to be 6.25K, corresponding to the sharp transition in χ' from a negative value. This is lower than the T_c for bulk Nb ($T_c = 9.26K$), and lower than the 100nm Nb films previously measured in Chapter 4 ($T_c = 8.0K$ on InSb) [301].

5.6: Initial Measurements:

After calibrating the beamline via adjustment of the ring anode voltages, implantation energy scans were undertaken at $T = 15K$ and $T = 2.36K$. Additionally, temperature scans at selected energies within the Nb ($E = 9.97keV$) and the InSb ($E = 19.97keV$) were performed to establish temperature dependence. In all these cases, measurements were field cooled – an external field applied to the sample above T_C

before cooling to base temperature- to ensure flux is present within the bulk of the sample.
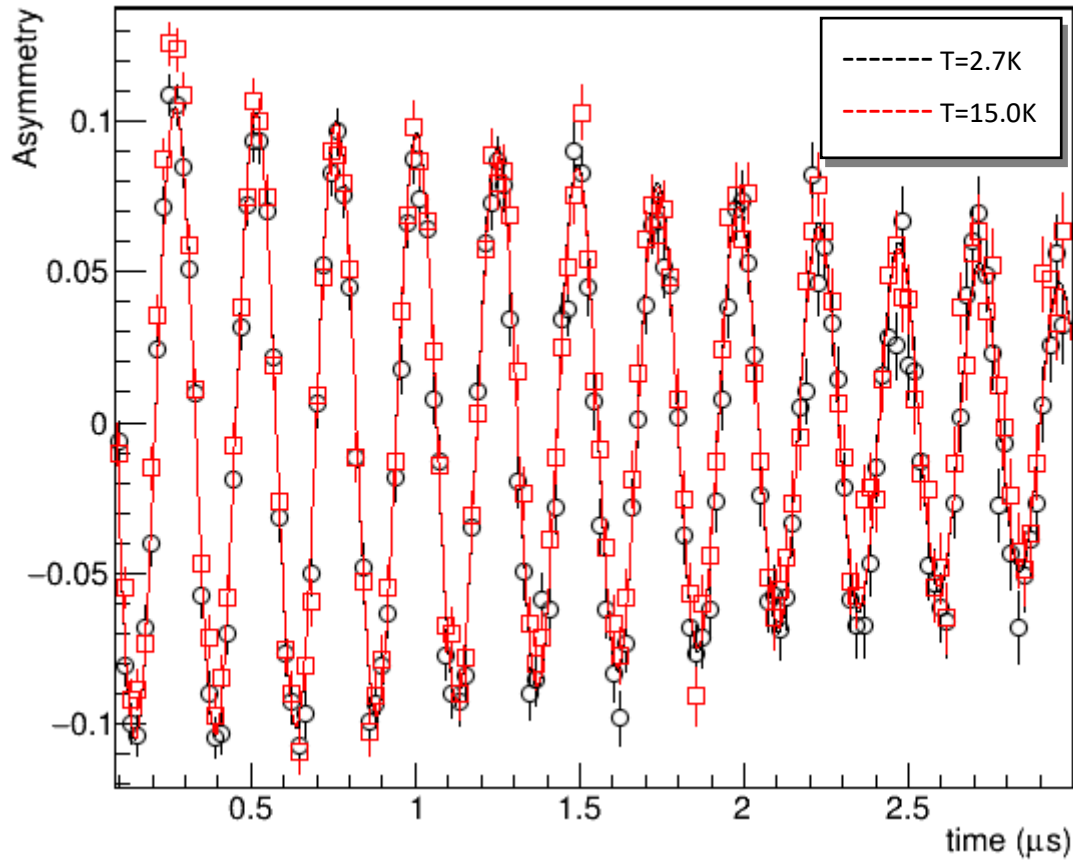
Figure 98: Measured detector asymmetry for an Nb/InSb heterostructure with $LF - \mu SR$ with a 30mT applied external field, above and below T_c.

Detector asymmetry was extracted from the raw histograms and fit to eq. 5.5. Figure 98 considers two measurements at an implantation energy $E = 9.97 keV$ at different temperatures. No clear difference in frequency, or signal envelope can be seen in the asymmetry between above and below T_c. This suggests a lack of field screening within the Nb. To confirm this, the measured local field, initial asymmetry, and depolarisation rate were extracted from the fits. All datasets within a given scan (e.g. all energies at 15K) were fitted globally.
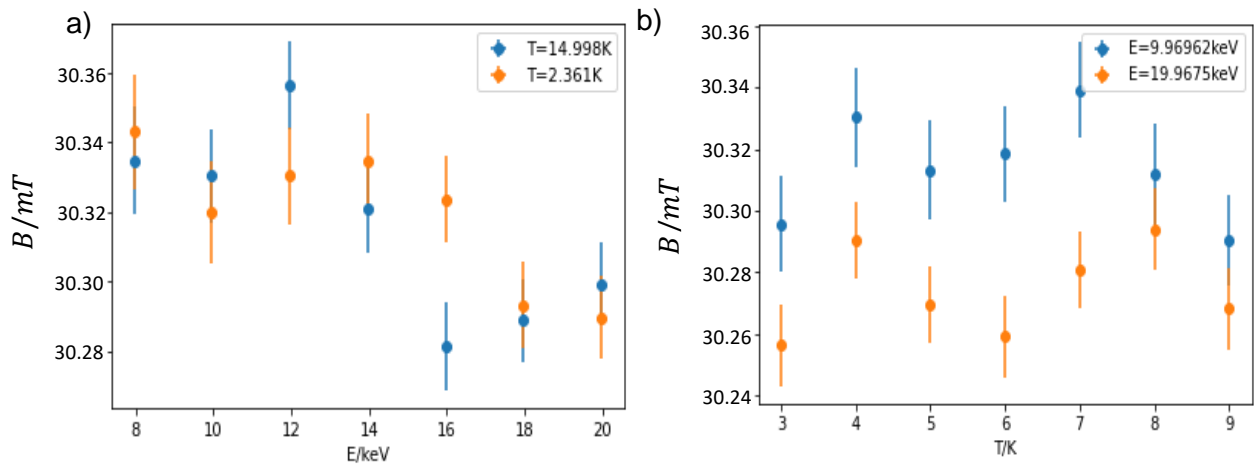
Figure 99: Field extracted from LEM measurements with an 30mT field orientated parallel with the sample surface. a) Energy sweeps above and below Tc. b) Temperature sweeps within the Nb (E=9.96keV) and the QW (E=19.9keV)

Figure 99a shows the extracted local fields as a function of implantation energy above and below T_c. Although there is a slight decrease through the sample, there is no statistically significant difference in behaviour above and below T_c. This is confirmed by the Temperature Scans (Figure 99b). Although the fields have different values between the two implantation points, there is no systematic behaviour with temperature, nor is there a transition as T rises above T_c. These two results again suggest that the Meissner screening was not observable in the Nb layers. Additionally, there is no evidence of screening at the higher energies corresponding to within the $InSb$ layers.
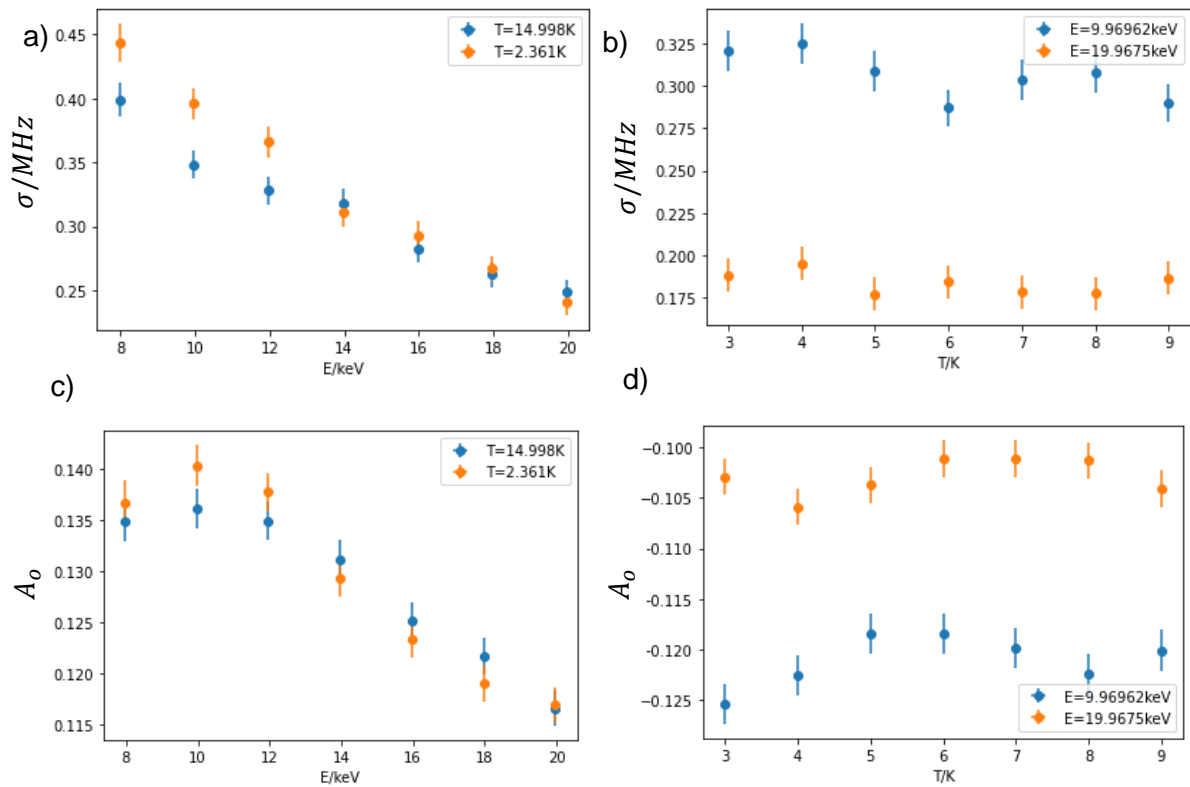
Figure 100: σ extracted from LEM measurements with an 30mT field orientated parallel with the sample surface. a) Energy sweeps above and below Tc. b) Temperature sweeps within the Nb (E=9.96keV) and the QW (E=19.97keV) Asymmetry extracted from LEM measurements with an 30mT field orientated parallel with the sample surface. c) Energy sweeps above and below T_c d) Temperature sweeps within the Nb (E=9.96keV) and the QW (E=19.9keV)

Figure 100 shows the other fit parameters extracted from the parallel field measurements, σ and A_o. σ shows a trend of decreasing as a function of implantation depth. Additionally, within the Nb (energies below 12keV), there is some discrepancy between the values above and below T_c (Figure 100a), which would suggest some enhancement in depolarisation within the superconducting state as would be expected. The absence of this at higher energies is suggestive of a lack of SC induced Nb. This is mirrored in the temperature scans (Figure 100b). There is minimal temperature variation for $E = 19.97keV$ (within the InSb), and no clear transition in either trace as T rises above T_c. This suggests a lack of induced SC within the InSb owing to a lack of enhanced screening. Minimal difference in temperature is observed within A_o (Figure 100c). Both above and below Tc it seems to peak as the muon population begins to peak at the interface between the Nb and $AlInSb$ top-cap. It then, in both cases, decreases as throughout the sample. There is from these no evidence of screening linked to the superconducting state with a parallel field alignment.

5.7: Zero-Field cooled measurement:
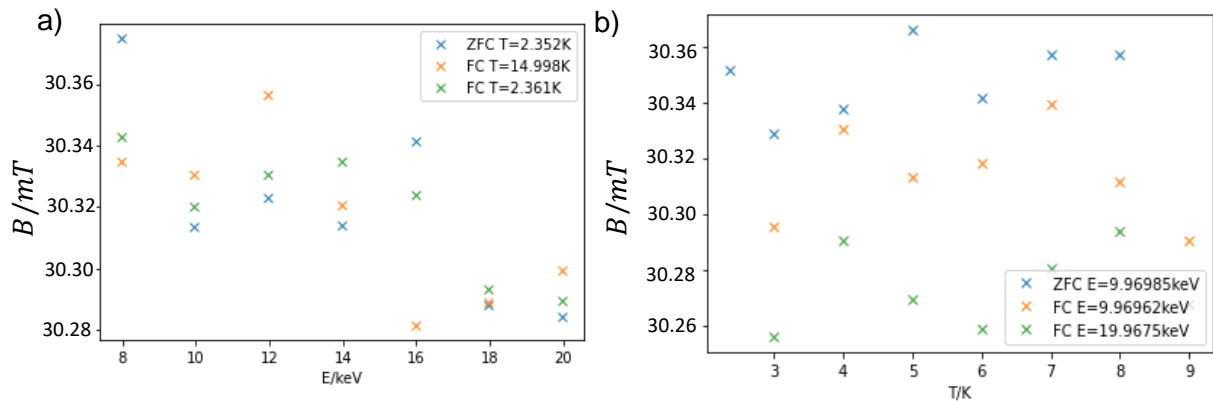
Figure 101: Field extracted from LEM measurements with an 30mT field orientated parallel with the sample surface. A) Energy sweeps above and below Tc. B) Temperature sweeps within the Nb (E=9.96keV) and the QW (E=19.9keV)

In addition to the field cooled measurements above, we also performed the same procedure with zero field cooling – The external field is switched off whilst the sample temperature is being changed (Figure 101). Both an energy scan and a temperature scan were performed, again at a 30mT field applied parallel to the sample surface. This again exhibited no evidence of screening as a function of temperature (Figure 101b).

5.8: Secondary Measurements:

Owing to the poor T_c of the sample, it was thought likely that the penetration depth, λ_L, within the Nb layers of our sample was long relative to the film thickness. To verify, the experiment apparatus was adjusted to align the field perpendicular with the sample cross section as per section 5.3. The spin rotator was utilised to re-orientate the net polarisation of the μ^+ and allow for measurable precession. Energy scans were performed at two different temperatures (T=15K and T=2.36K). Following that, temperature was swept at 4 energies three of these were chosen to consider the changing behaviour within the Nb approaching the $Nb/AlInSb$ interface. The final energy (E=19.97keV) would directly probe the QW. In all cases measurements were field cooled and performed at 10mT.
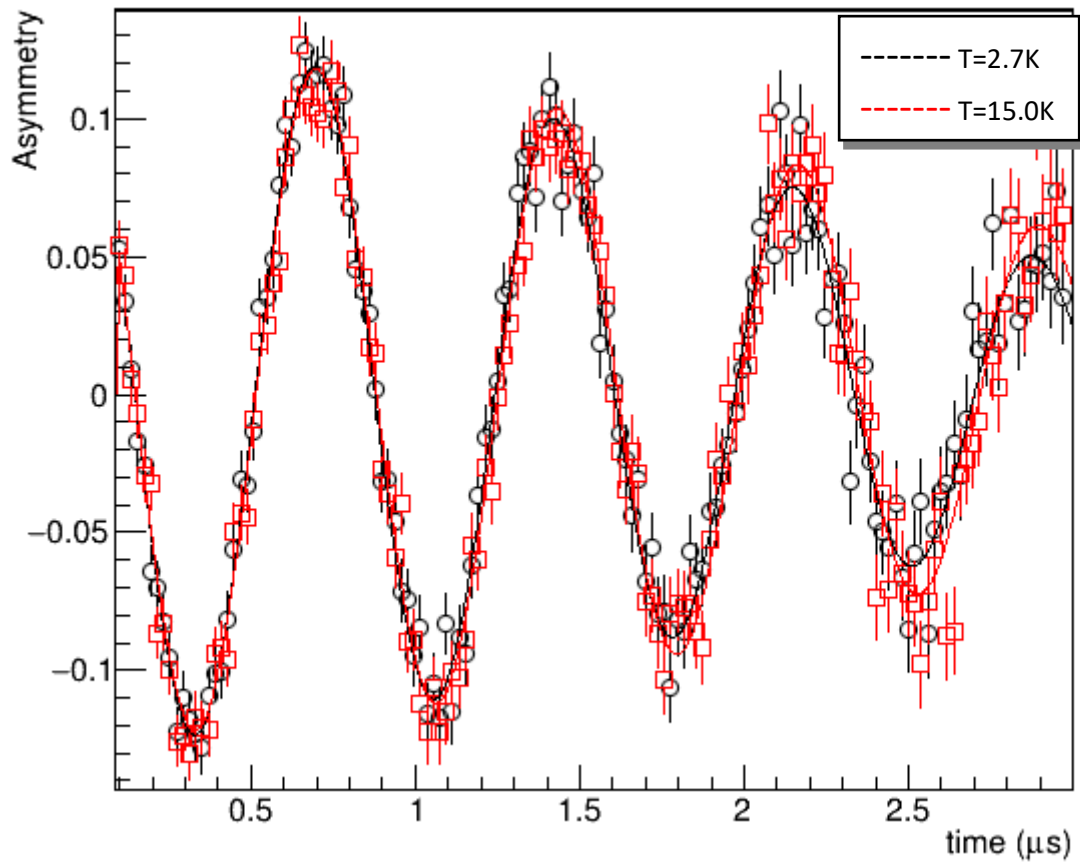
Figure 102: Measured detector asymmetry for an Nb/InSb heterostructure with μSR with a 10mT applied external field applied perpendicular to the sample surface, above and below T_c.

As with the initial measurements (Figure 98), we can first consider the measured asymmetry directly at $E = 9.97 keV$ (Figure 102). This shows an enhancement of depolarisation below T_c, most visible at the minima at $\sim 2.5 \mu s$. This initial measurement is consistent with our expectations (Figure 87). Once again, all datasets within a given scan (e.g. all energies at 15K) were fitted globally to equation 5.5. From these fits, a_o, B and σ are extracted.
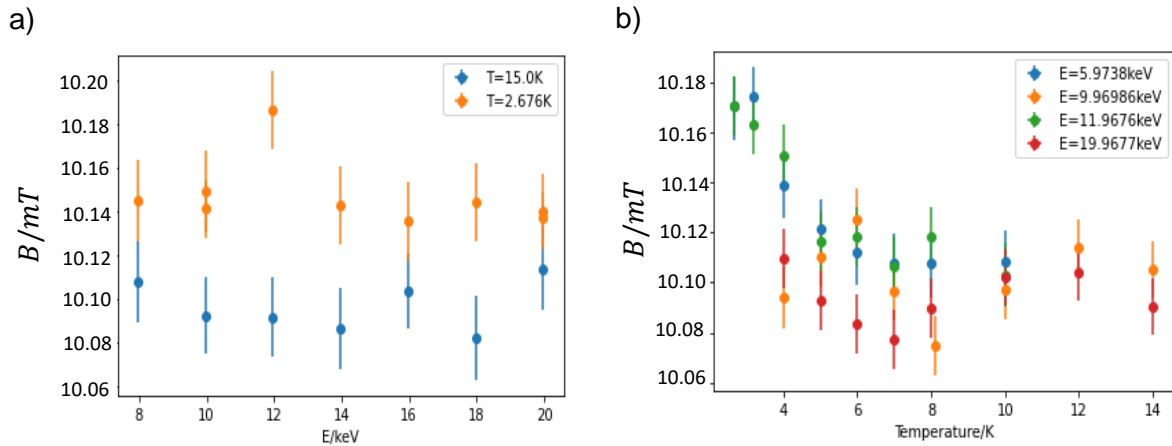
Figure 103: Field extracted from LEM measurements with an 10mT field orientated perpendicular with the sample surface. a) Energy sweeps above and below Tc. b) Temperature sweeps within the Nb (E=9.96keV) and the QW (E=19.9keV)

The energy scans (Figure 103a) showed minimal change in the field throughout the material, although there was a more significant difference between the two temperatures compared to the parallel field (Figure 99a). The temperature sweep (Figure 103b) shows more of a response as a function temperature for all four energies in comparison to the parallel field (Figure 99b) and is suggestive of some screening present in the Nb.
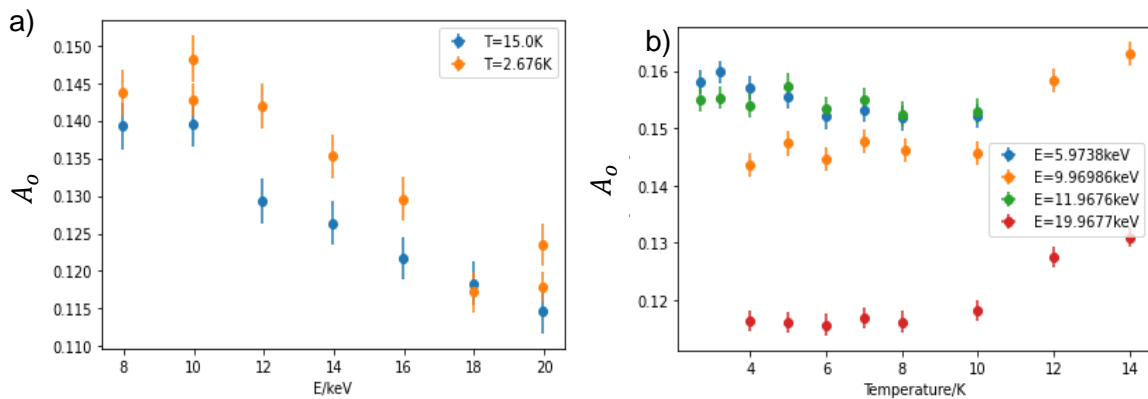
Figure 104: Asymmetry extracted from L-R asymmetry with an 10mT field orientated perpendicular with the sample surface. A) Energy sweeps above and below Tc. B) Temperature sweeps within the Nb (E=9.96keV) and the QW (E=19.9keV)

A_o showed a similar trend to the parallel field, although as for the extracted field, there is a more prominent disparity between the temperatures (Figure 104a). However, from the temperature sweeps (Figure 104b) this does not appear to be related to the

superconducting state. There is an increase mirrored in the Nb and the $InSb$ beginning at $T = 10K$, which begins well above T_c.
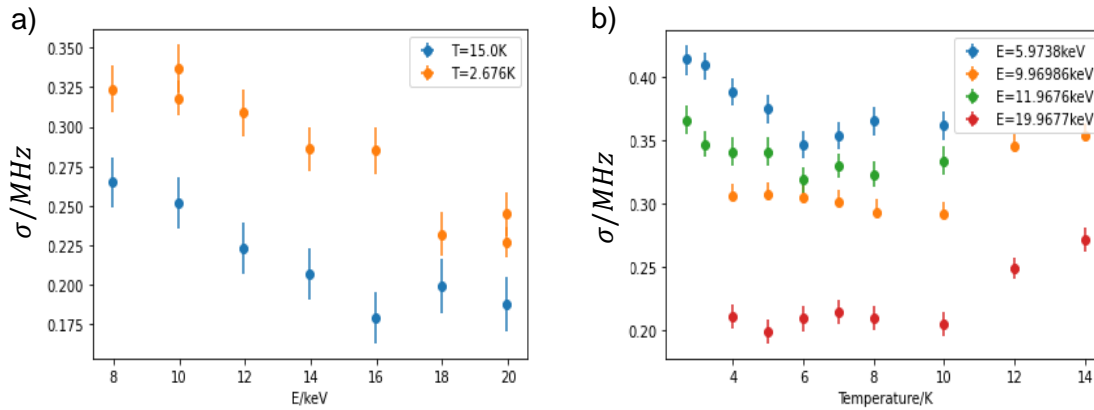
Figure 105: σ extracted from the L-R asymmetry of 10mT field orientated perpendicular with the sample surface. A) Energy sweeps above and below Tc. B) Temperature sweeps within the Nb (E=9.96keV) and the QW (E=19.9keV)

As with Figure 100a, σ is seen to decrease as a function of implantation depth (Figure 105a). There is a disparity between the two temperature values at all energies that was not present for the highest energies in Figure 100a. σ was seen to decrease as a function of temperature below T_c. This enhancement in depolarisation, and subsequent decrease, is attributed to the SC state. High temperatures, well above T_c, exhibited a similar increase as A_o. With σ, characterisation of the quality of the SC sample is possible. λ_L was extracted via eq. 5.8, and then data was fit to both the clean and dirty SC (eq. 5.11 and eq. 5.12) to definitively assess the defects within the Nb.
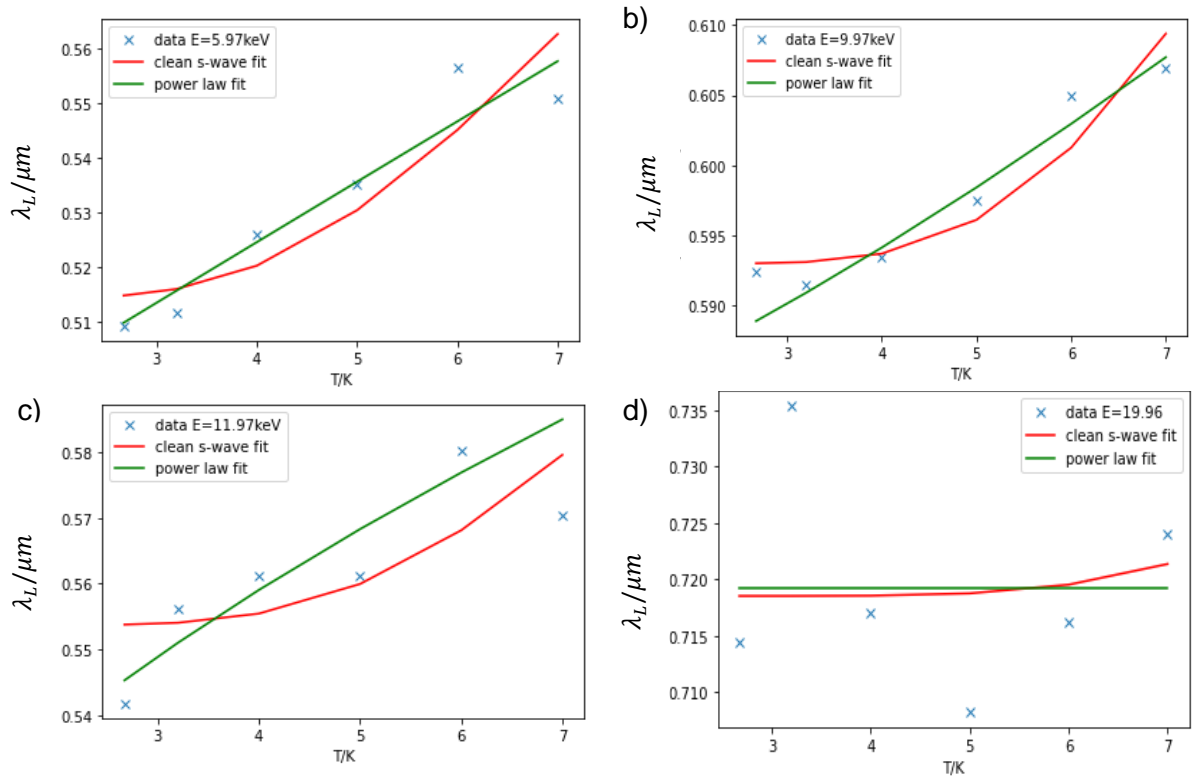
Figure 106: Penetration depth modelling for the 4 different energies swept as part of the Temperature scans, fitting to both.

Fit parameters in all cases are presented below in Table 5:

Table 5: Fit parameters of Figure 9. In each case, the extracted parameters for both the "clean" s-wave fit and the power law are included.

Energy/keV	"Clean" s-wave fitting parameters		Power Law fitting parameters		
	$(\lambda(0)/\mu m)$	$\Delta(0)$ /meV	$\alpha \, (\frac{K}{\mu m})$	n	$\lambda(0)/\mu m$
5.97	0.51 ± 0.06	1.09 ± 0.01	0.011 ± 0.001	0.989 ± 0.002	0.48 ± 0.06
9.97	0.59 ± 0.03	2.75 ± 0.01	0.022 ± 0.007	1.27 ± 0.12	0.58 ± 0.02
11.97	0.55 ± 0.04	2.40 ± 0.03	0.025 ± 0.02	0.635 ± 0.03	0.50 ± 0.24
19.97	0.718 ± 0.005	4.0 ± 2.6	0.232 ± 0.01	$1.07e - 16 \pm 0.06e - 16$	0.48 ± 0.01

As expected from the low T_c, and the lack of measured screening, we find the power law fit is more satisfactory than the 'clean' s-wave fit (Figure 106) within the Nb. This indicates the presence of point or line defects with the Nb. The $\Delta(0)$ found in the 'clean s-wave fits' (Table 1) do not agree with accepted value of ~2.32meV from the literature [302] [301], additionally supporting the presence of defects. Neither fit is satisfactory within the InSb (Figure 106d). This is direct evidence for the lack of induced SC within the QW layer in this sample.

For the three implantations within the Nb (Figure 106a-Figure 106c), it appears to be first order. Additionally, as the implantation energy increases, we get closer to the interface $Nb/InSb$, the fit becomes less satisfying, and the order deviates (Figure 106c). The length scale of $\sim 500nm$ is around 10x longer than our film thickness, and longer than expectation of high quality Nb [303]. This agreed with our expectations and explained the lack of observable screening with the parallel field measurements.
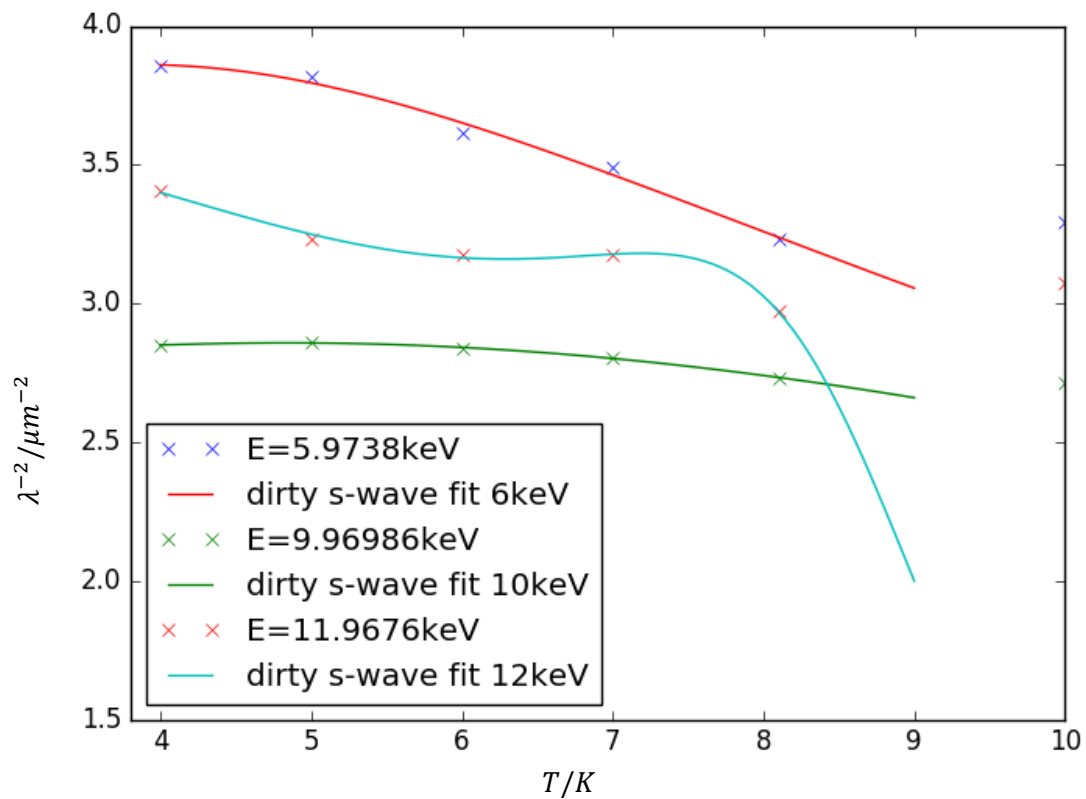
Figure 107: λ^{-2} extracted from transverse field $LE - \mu SR$ measurements as a function of temperature for three implantation energies.

We can also consider the variation in λ^{-2} as is considered in the literature previously (Figure 87). Figure 107 gives this for 3 implantation energies. Data is fit to the case for a 'dirty' s-wave superconductor eq. 5.11. Within eq. 5.10, $\Delta(T)$ is substituted for $\Delta(0)\left(1 - \frac{T}{T_c}\right)^n$, as used to assess the electrical measurements in Chapter 4.

Table 6: Extracted fit parameters from modelling of λ^{-2} as a function of temperature.

Fit Parameter	$E = 5.97keV$	$E = 9.96keV$	$E = 11.96keV$
$\lambda^{-2}(0)/\mu m^{-2}$	5.00 ± 0.08	2.78 ± 0.01	3.62 ± 0.04
$\Delta(0)/meV$	1.17 ± 0.02	1.78 ± 0.04	1.16 ± 0.01
n	1.48 ± 0.03	2.63 ± 0.06	6.69 ± 0.80

Fit parameters are presented in Table 6. Fits are obtained for all three cases, further supporting the argument for the Nb used possessing defects. Again, $\Delta(0)$ does not agree with the accepted energy gap of Nb in the literature. Additionally, n shows increasing disagreement with the accepted value of $n = 0.5$ for clean s-wave SC deeper into the sample. At all energies, n is significantly larger than that obtained during characterisation of the 100nm films characterised for the electrical measurements in Chapter 4, which were around the ideal value of $n = 0.5$ (Table 2). This agrees with the overall lower T_c of this 50nm film ($T_c = 6.25K$ vs $8.0K$). This also offers a possible explanation for the apparent lack of induced SC within the 2DEG layer compared to the $100nm$ film. Also of note, in comparison to the previously considered examples in the literature (Figure 87b), and as with (Figure 106) is the comparatively large finite λ existing above $T_c = 6.25K$. As λ_L is estimated from σ, there is either significant depolarisation occurring intrinsically within the Nb outside of the SC state, as can be seen in Figure 105, or the induced SC state is weak, and is causing minimal screening.

From both these analyses, and the overall low T_c of the Nb film, we conclude that the Nb film used here contains defects, that have adversely affected the film quality. The reduced film quality resulted in a long penetration depth relative to our film thickness, which precluded measurement of screening in the Nb layers. Additionally, in all

considered analysis, no evidence of SC was observed within InSb layers. As a result, there is no information to be gleamed about the potential pairing frequency of a high SOC material from this experiment. Overall, the lack of measurable SC extending into the InSb means this experiment must be regarded as a failure. However, as the primary cause of this failure extended from the poor quality of the Nb, it was thought that a higher quality SC film would be a viable experimental alternative. This will be the subject of the next chapters discussion.

Chapter 6: μSR of a $Pb/InSb$ heterostructure

6.1: Adjustments in light of prior experiments:

The previous μSR experiment on a Nb/InSb heterostructure failed to measure Meissner screening within the Nb layer. Extraction of λ_L from μSR measurements experiment suggested that the Nb used contained defects. The presence of these defects led to a long λ_L past that which allowed for measurable screening with our samples. Because the intended experiment was still of great interest, alternative superconductors were considered. Al, a common alternative SC in high SOC proximity superconducting devices was unviable due to the T_c being outside the measurable range for the LEM cryostat [41].
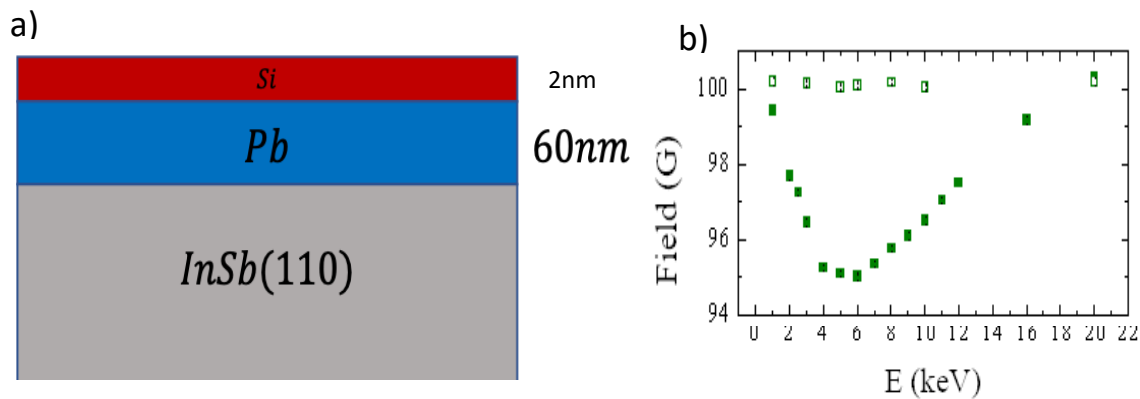
Figure 108: a) Previously measured sample structure – a 60nm Pb film deposited upon bulk InSb. b) Internal field extracted from μSR measurements of a 60nm Pb film deposited upon bulk InSb [304]. Solid blocks are below T_c at $T = 3.0K$, clear blocks above T_c at $10.5K$.

Another considered option was Pb. Pb has been shown to be a Type-I superconductor, with a $T_c \approx 7.2K$ for pure samples [305] [306]. Previous μSR measurements on a 60nm Pb film deposited on top of bulk $InSb$ had been performed by other groups (Figure 108). Energy scans showed a clear screening profile below T_c (Figure 108b). The Pb film in this sample was the top-most layer, analogous to the Nb films used in Chapter 5. The presence of a clear screening profile, when adjacent to $InSb$, made Pb our clear secondary choice of a superconductor.
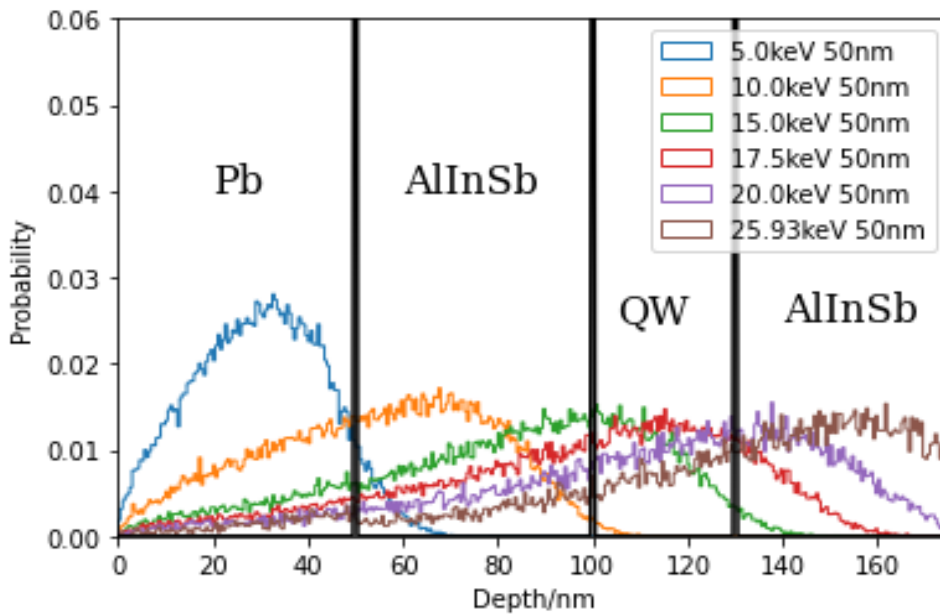
Figure 109: Muon stopping profile for a 50nm Pb film deposited on an InSb QW layer, simulated by TRIM SP.

Whilst a 60nm film was used for that bulk measurement, simulations were still required to find a workable film thickness for our purposes. Pb has a significantly higher density than Nb. As density is a major contributor to the muon stopping distance, it was expected that thinner Pb films would be required to ensure an adequately high proportion of μ^+ stopping within the quantum well. However, TRIM simulations of a $Pb/InSb$ structure again suggested 50nm would be sufficient for our purposes, even given this higher density.

6.2: Surface treatment of an InSb QW:

Simple substitution of the Nb for a Pb film had some basis for likely experimental success, as evidenced from the prior measurements and TRIM simulations. However, we also took steps to modify the InSb structure to further improve this likelihood. A full reworking of the sample to modify it such that the Pb would be the bottom most layer of the sample was impossible on our timescale. Facilities to grown new 2DEGs were not operational and could not be brought into operation during this time. Even if they were, modification and growth of new 2DEG wafers would require extensive characterisation and optimisation. This meant that existing 2DEG wafers were used.

Another possibility to achieve this same modification would be to etch the GaAs substrate, and in essence 'lift' the 2DEG layers from the sample. (Figure 13). However, this would still leave the $3\mu m$ $AlInSb$ buffer layer. This buffer layer would be too thick to allow μ^+ implantation in the QW layer. Additionally, the bulk $AlInSb$ would be insulating, and thus unlikely to exhibit long range proximity superconductivity. A controllable, uniform etch of this $3\mu m$ layer post 'lift' was possible in theory via dry etch methods, however this would again require extensive characterisation work non-viable on our time frame. As such it was not possible for this series of experiments to invert the positioning of the Pb and $InSb$.

Whilst this inversion was impossible, it was still possible to decrease the spatial separation between the SC and the QW by etching the top cap. A full etch down to the QW layer, placing the Pb flush against it was non-viable. This would both remove the doping and destroy the confinement of the QW and thus cripple the conductivity of the sample. However, within the existing designs, this left around $20nm$ of AlInSb top cap material that could be safely etched. For this, we considered an existing citric acid etch recipe, used as a surface treatment to create ohmic electrical contacts for Hall Bars. Experimental characterisation of this etch was performed by a prior PhD student in our group, the full details of which can be read here [162].
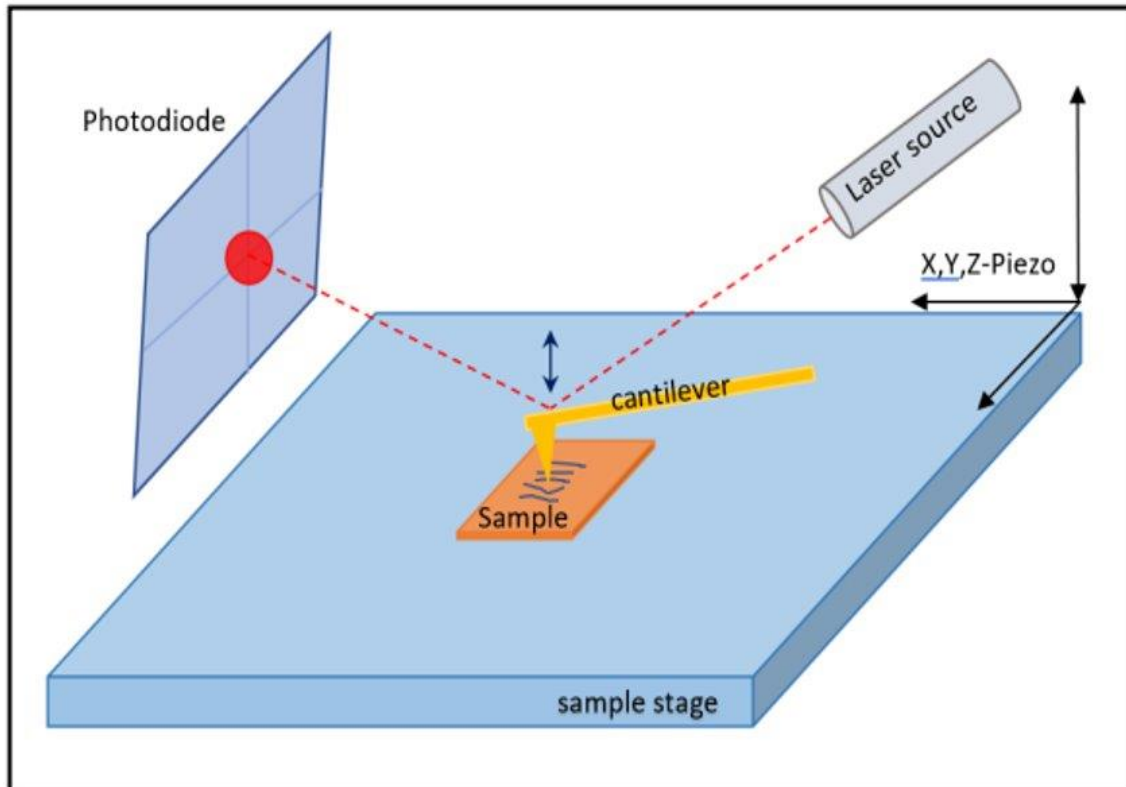
Figure 110: Schematic diagram of performed AFM measurements. A cantilever is moved across a sample surface. A laser is aligned with the back of the cantilever. Slight deflections of the cantilever are measured by tracking the laser intensity via a photodiode. [162]

As part of the work in characterising the role of the citric acid etching, Atomic Force Microscopy, or AFM, measurements of the surface roughness of a typical InSb sample were performed. AFM, as used in that work, utilises a cantilever moved across the surface of a sample (Figure 110) [307] [308]. As the cantilever is moved, electrostatic repulsion between the cantilever and the surface deflects the cantilever. As the surface of the sample changes in height, the cantilever will thus be deflected proportionately. In this case, deflections are monitored via laser interferometry [162] [309]. A laser beam is reflected off of the back of the cantilever, and the reflection monitored via a photodiode [310]. As the cantilever deflects, the path length of the reflection changes, changing the intensity incident on the photodiode. With a suitable calibration, measurement of the variation in photodiode signal as a function of cantilever motion will give the topography of a sample surface along the axis of cantilever motion. Successive movements of the cantilever can allow full mapping of a sample surface [311] [312].
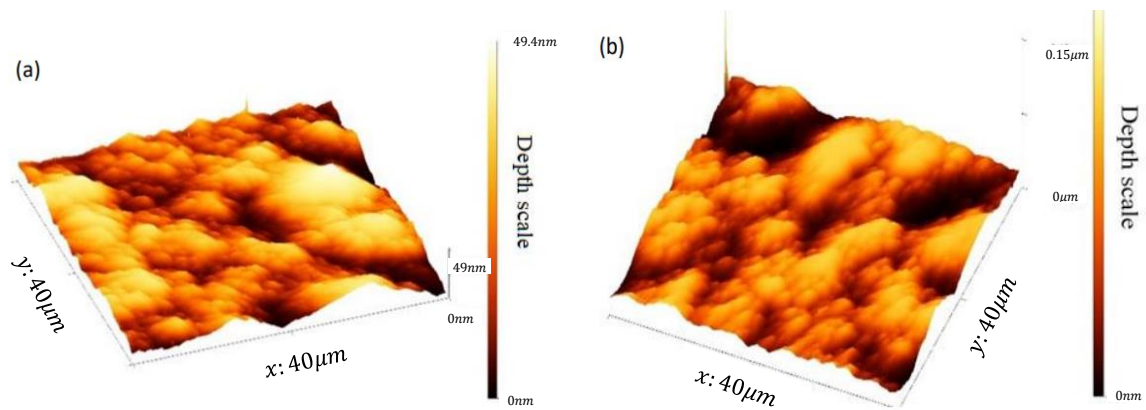
Figure 111: a) AFM measurements of surface roughness of untreated $40 \times 40 \mu m^2$ piece of an InSb 2DEG wafer. b) as a) but with the sample rotated 90°. [162]

Figure 111 presents such a mapping. AFM measurements were performed on a $40 \times 40 \mu m^2$ piece of a typical $InSb/AlInSb$ heterostructure. The typical samples show rough surfaces, prior to etching. A piece of this sample had a $60 \times 30 \mu m^2$ trench defined by optical lithography, and was then subject to a citric acid etch:
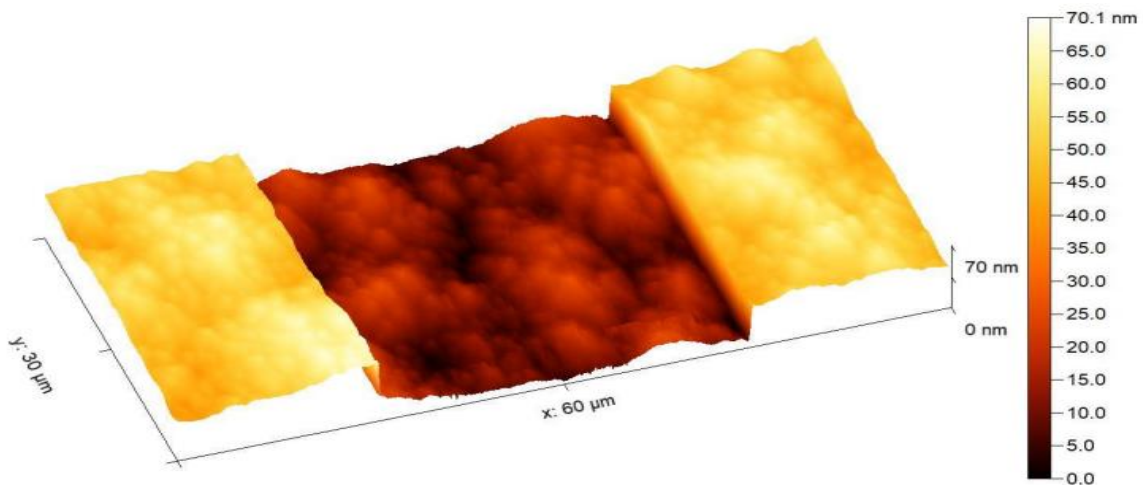
Figure 112: AFM of a piece of InSb subject to a citric acid surface treatment [162].

AFM confirmed the citric acid etched the InSb wafer (Figure 112). A series of samples were prepared and etched for various lengths of time. After the etch, each sample was measured via AFM, and used to calculate the r_{rms} surface roughness as a function of etch time. r_{rms} is a measure of the average surface roughness, given by:

$$r_{rms} = \frac{\sqrt{(z_1^2 + z_2^2 + z_3^2 + z_4^2 + \cdots . z_n^2)}}{\sqrt{n}} \qquad (6.1)$$

Where z_n is the roughness at a given sampling point, n. Additionally, for each sample, the total etch depth was calculated from the AFM measurements, by considering the step size between the trench and surrounding wafer.
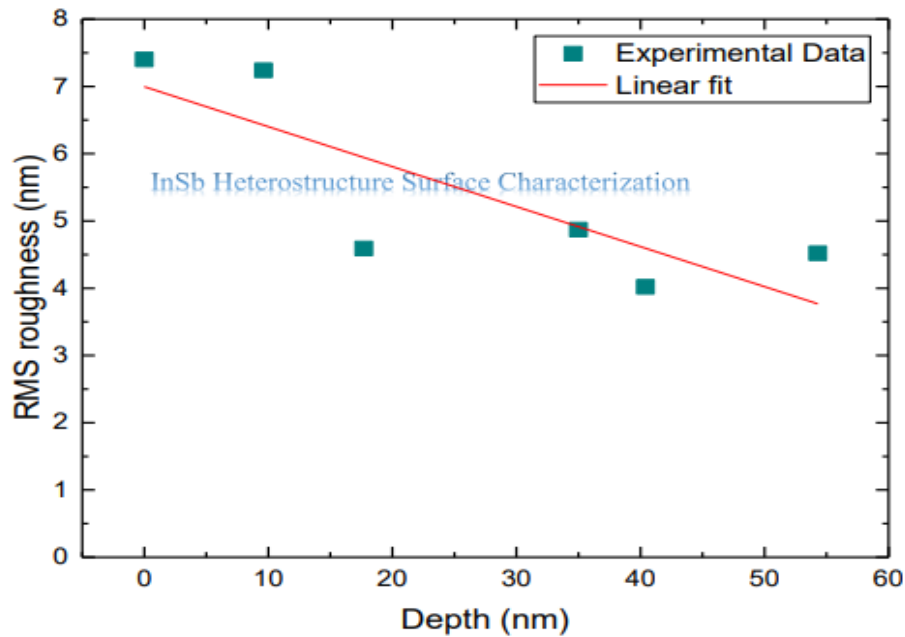
Figure 113: RMS roughness of InSb wafer as a function of total etch depth [162]

The RMS roughness estimated for each etch depth is shown in Figure 113. The original work performed a linear extrapolation of surface roughness as a function of depth; however it is arguable the roughness would more sufficiently obey a step function corresponding to the removal of the surface oxide layer on the AlInSb. In either case, Figure 113 showed that, for shallow etches of the AlInSb top cap, there is no increase in surface roughness.
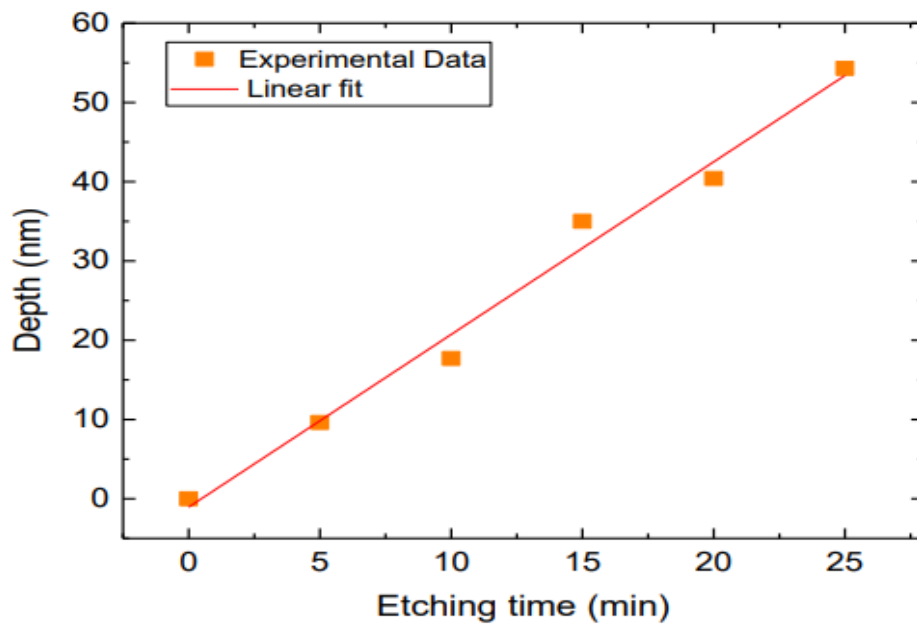
Figure 114: Etch depth as a function of total etch time for use of calibration of the overall etch rate [162].

Etch depth as a function of total etching is shown in Figure 114. This was estimated to be $\sim 2nm/\text{min}$. A shallow etch of the top cap layer was thus a controllable process. As such, it was thought a shallow etch of the InSb top cap with a citric etch could be performed, without impacting the deposited film quality, or compromising the conductivity of the underlying QW structure.

6.3 Redesigned Sample, Deposition and Characterisation:
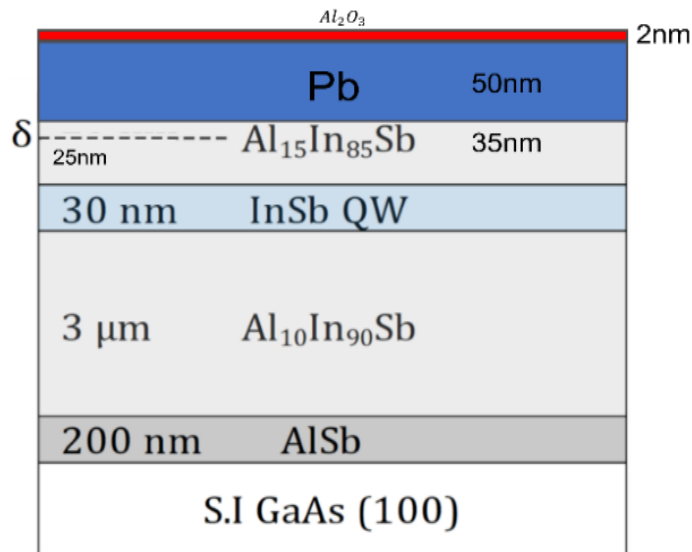
Figure 115: Redesigned SC/InSb 2DEG used in this section's measurements. A citric acid etch treatment applied to the bulk InSb removed $\sim 15nm$ of $Al_{15}In_{85}Sb$ top cap. Chosen etch depth should mean the Te doping is approximately $10nm$ from the Pb/InSb interface.

The finalised sample design is shown in Figure 115. Using the calibrated etch, the citric acid etch was timed to etch around 15nm of material, and the sample was quickly loaded (<5 mins) into an evaporator under vacuum to prevent re-oxidisation of the surface. Additionally, a separate test piece was prepared, with some of the sample coated with PMMA to serve as an etch mask, which was etched at the same time as actual sample. The PMMA was then removed with acetone, and the total etch depth measured via AFM to be 15nm. The etch, sample cleaning, and Pb deposition were all performed at the Neils Bohr Institute in Copenhagen. An additional 2nm thin Al_2O_3 layer was deposited to protect the sample surface.

6.3.1. Electrical characterisation:

In addition to the 4 $1 \times 1cm^2$ pieces required for the μSR measurements, additional smaller samples were made in the same deposition to allow for characterisation of the Pb film. From these, an $\sim 0.5mm^2$ piece was contacted with 4 terminals bonded to the sample surface with silver conductive paint. The sample was measured using the Pulse Tube Cryostat and a Keithley 6200/ 2100A current source/multimeter.
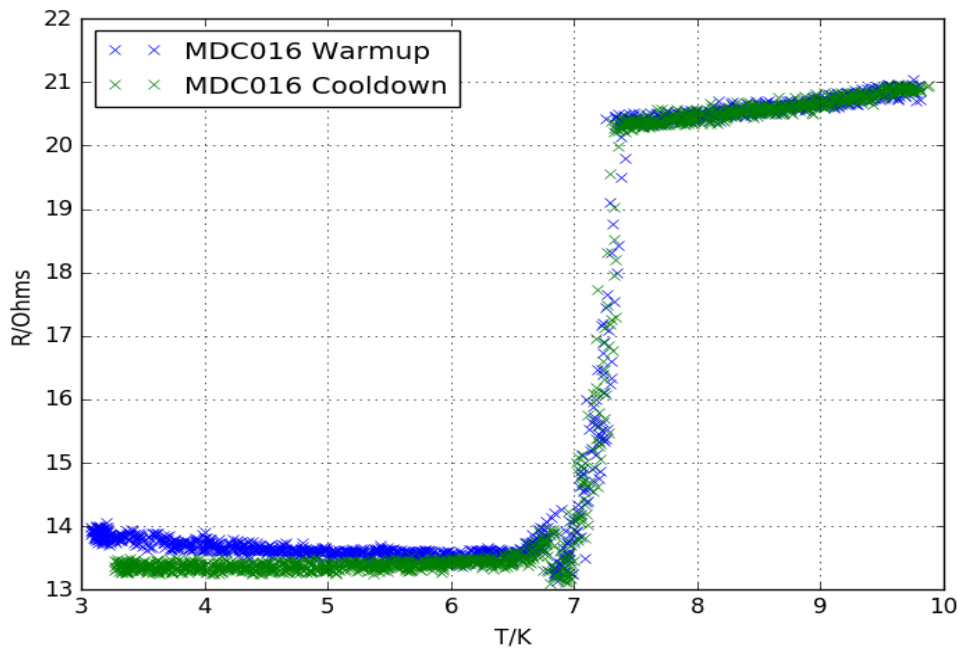
Figure 116: Electrical characterisation of the Pb/InSb Sample via 4-terminal R(T) measurements on a $1cm^2$ piece of Pb/InSb film.

Characterisation consisted of 4 terminal measurements R(T) measurements, setting a singular offset current, and recording the lock-in voltage multiple times. The temperature is raised gradually in 0.1s intervals, and voltage recorded continually. The temperature was swept up from base, and then lowered in a single continuous measurement. From this, T_c was estimated to lie between 6.7 and 7K, lower than the $T_c = 7.2K$ expected for pure Pb [313].

6.3.2. Self-Consistent Schrodinger-Poisson simulation.

In addition to characterisation of the Pb layer, it was also prudent to consider what effect the citric etch was likely to have on the semiconductor. The confinement of the energy levels within a QW depends upon the thickness of the surrounding confining material. Etching the top cap would, even without removing the δ doping layer, alter the resulting properties of the Quantum Well, and significantly reduce the confinement of electrons within it. In the worst case, the thinning could be sufficient to destroy the Quantum Well by entirely removing the confinement on one side.

Ideally, a full electrical study of this alteration would be performed to consider the effect this had on the mobility, μ and carrier concentration, n_s. However, fabrication of Hall bars to perform this was not possible in the time frame of this work. As such, a self-consistent Schrodinger-Poisson simulation was performed instead to give an indication as to the effects. This would calculate the resulting band structure and the first energy levels within the system. These simulations were performed using a FreeWare 1D Schrodinger-Poisson program [314]. This program had previously been used to for the calculations presented in Figure 40b.
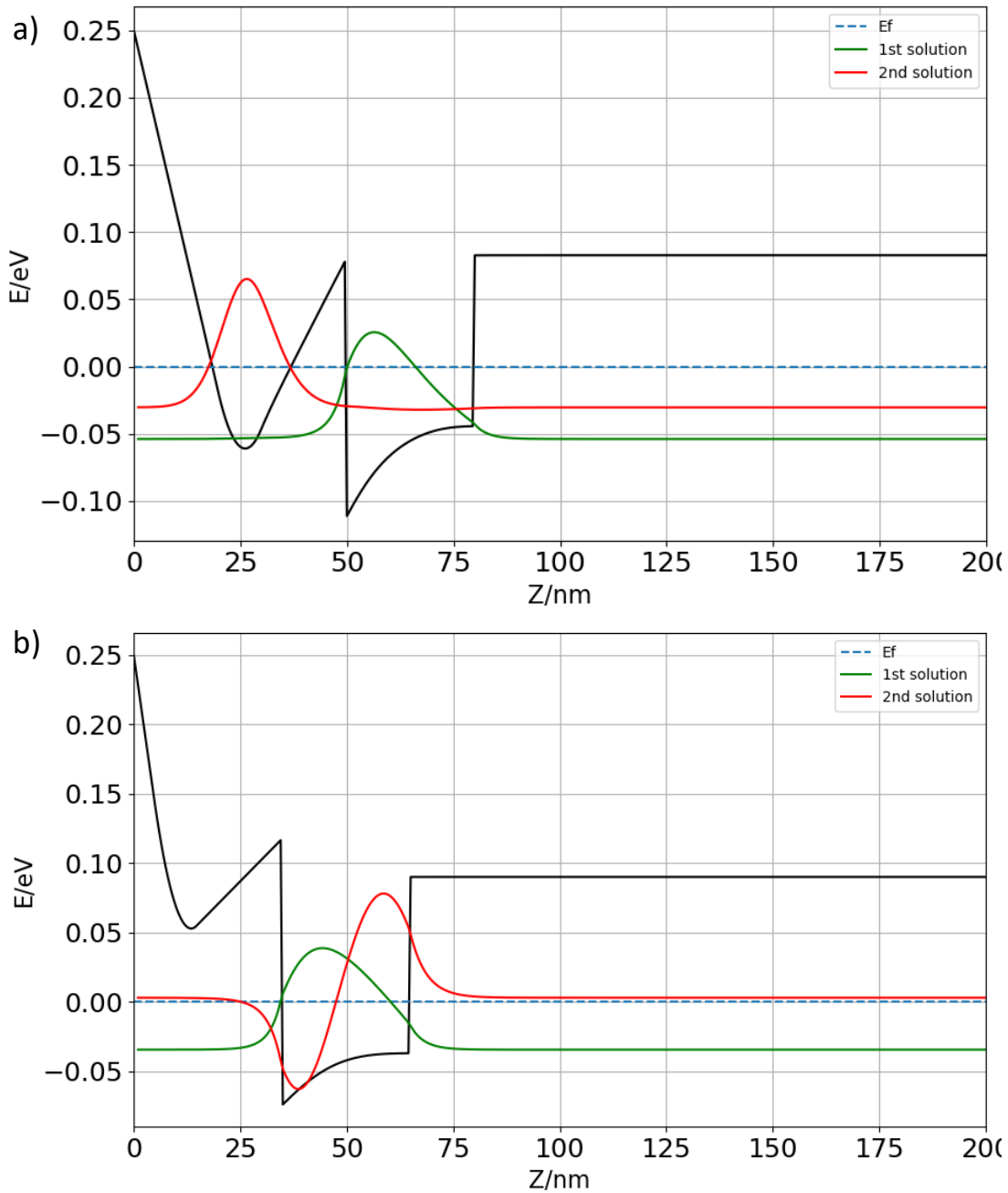
Figure 117: Self-Consistent Schrodinger Poisson simulations of the InSb elements within the Pb/InSb structure a) Comparative structure with no citric acid etching. b) Structure with citric acid thinned top cap. δ-doping concentrations of 2.2×10^{11} were used in both cases. Additionally, a Schottky barrier of 0.25eV at Z=0 was used in both calculations.

Figure 117 shows the results of simulations of the $InSb$ $2DEG$ structure (As depicted in Figure 40a and Figure 115). Figure 117a presents an un-etched example to serve as a comparative basis for the etched sample (Figure 117b). Thinning of the top cap primarily seems to render the secondary well, caused by the δ doping, shallower. This would be expected given that the thinning removed over half the confining material on this side. The thinning is sufficient for the first sub-band to now occupy the QW instead

of doping layer. The simulations suggest that although shallower, the Quantum Well still exhibits a good degree of confinement, and as such carriers within it likely to still exhibit high μ. As such, it can be compared to the previously used $2DEG$ samples in the discussion moving forwards, but we note a full electrical study would be an important piece of future work for future samples.

6.3.3: Muon Stopping Profile:
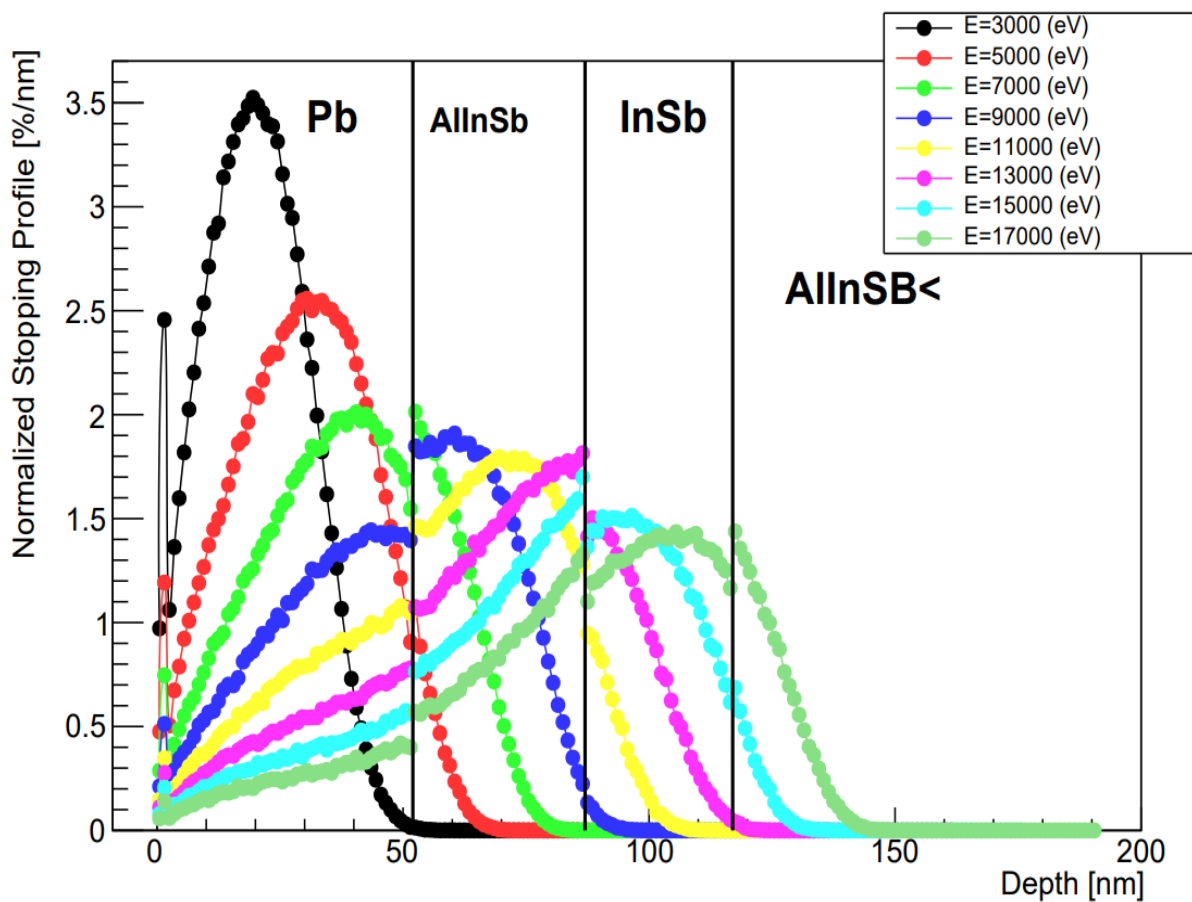
Figure 118: Muon Stopping Profile calculated via TRIM.SP for the InSb heterostructure featured in Figure 114.

The muon stopping profile was calculated for our modified heterostructure. The thinning of the top cap meant even with a high density Pb layer on top, we would have access to all layers of the sample within the range of available energies. However, there would be a significant fraction of muons stopping within the Pb layers at all energies.

6.4: Results:

6.4.1: 10mT μSR measurements:

As with the Nb measurements in Chapter 5, once the sample was loaded, the beamline was calibrated via adjustment of the ring anode voltages. Implantation energy scans were undertaken at $T = 15K$ and $T = 2.36K$. Additionally, temperature scans at selected energies within the Pb ($E = 6.0keV$) and the InSb ($E = 14.0keV$) were performed to establish temperature dependence. In all these cases, measurements were field cooled – an external field applied to the sample above T_C before cooling to base in order to ensure flux is present within the bulk of the sample.
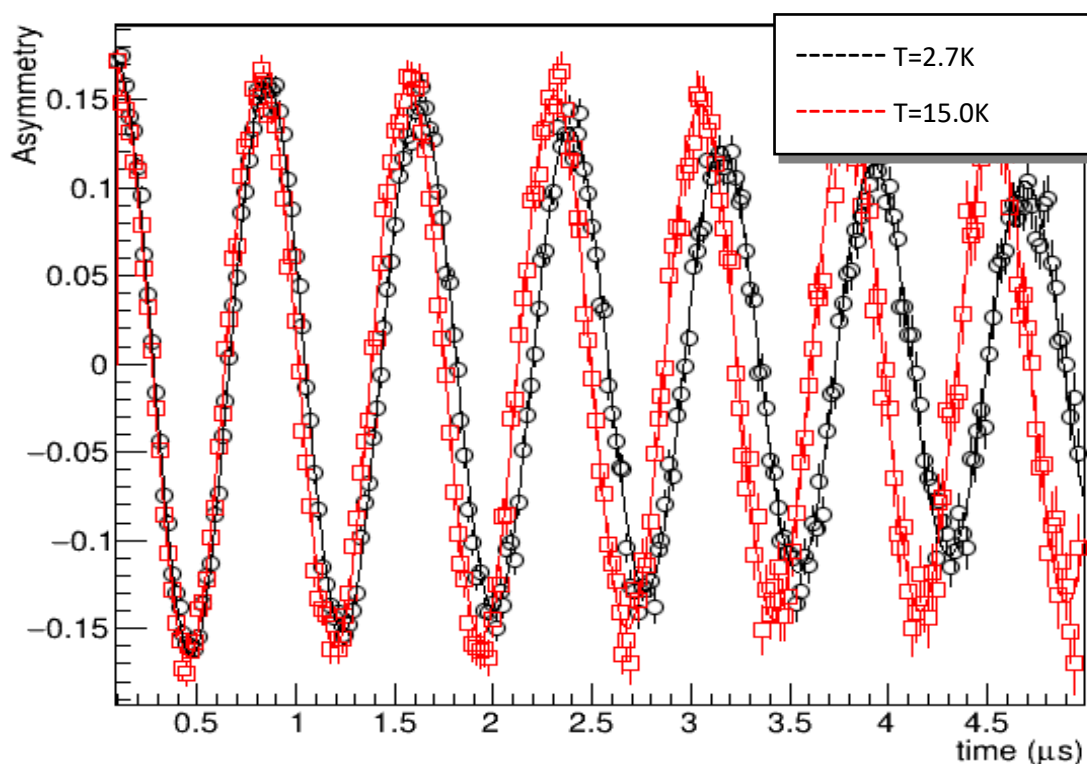
Figure 119: Measured detector asymmetry for an Pb/InSb heterostructure with a 10mT applied external field parallel to the sample surface, above and below T_c at $6.0keV$.

Detector asymmetry was extracted from the raw histograms and fit to eq. 5.5. All datasets within a given scan (e.g. all energies at 15K) were fitted globally. Figure 119 shows two measurements at an implantation energy $E = 6.0\ keV$ at different temperatures, above and below T_c. A clear frequency shift and increase in

depolarisation can be observed below T_c. The Pb is thus superconducting. For each of these asymmetry measurements, B, A_o and σ are extracted.
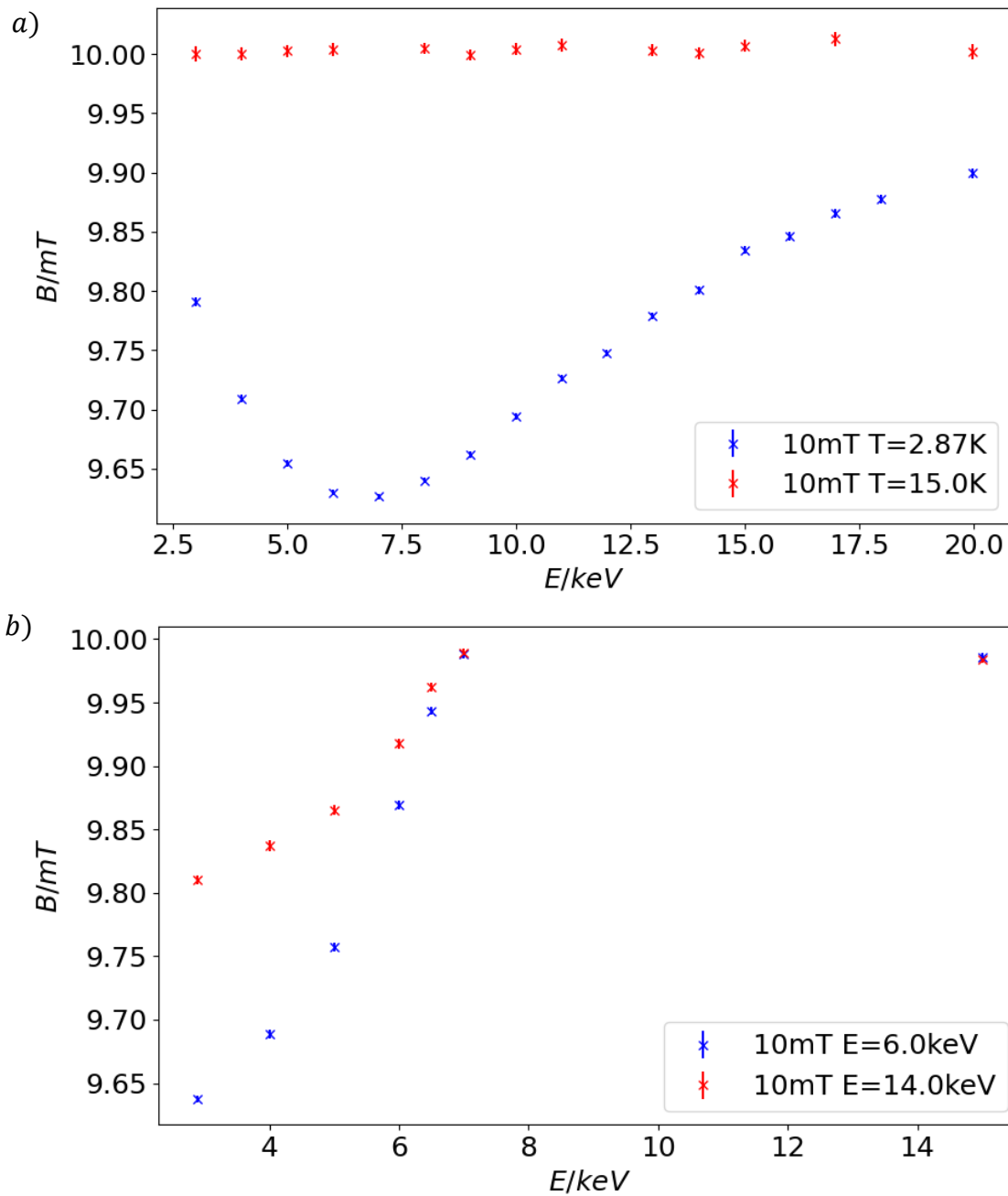
Figure 120: Magnetic field extracted for a 10mT external field as a function of a) Implantation energy above and below T_c b) Sample temperature at two energies – 6.0keV centered within the Pb and 14.0keV within the InSb.

Presented in Figure 120 are the fields extracted from energy scan and temperature scans for an 10mT field applied parallel to the sample surface. Clear screening is visible in the energy scans within the Pb and extended through all subsequent energies This contrasts with the bulk $InSb$ presented in Figure 108. In there, the

highest energies saw the field return to the external field, whereas here (Figure 120a) significant screening is still observable. As the highest energies centre within the InSb (Figure 118) this is strong evidence of SC extending well into the $InSb$ layers. Proximity SC has thus extended further into the $InSb$ 2DEG sample than has previously been seen on bulk InSb. This increased penetration likely results from the increased conductivity and μ^+ within the QW layer, which is indicative successful proximity induced SC in the 2DEG. As was the case with the electrical measurements, this is a significant experimental success.

Further supporting evidence can be seen in the temperature scans (Figure 120b). The temperature scans were chosen to occur at energies of $6keV$ and $14keV$ such that they would centre in the Pb and the $InSb$ respectively. The two traces exhibit different trends tending towards equivalence as T approaches T_c suggesting that the screening seen in each layer is different. Total suppression of the field screening by $T = 7.0K$ agrees with $R(T)$ characterisation of T_c (Figure 116).
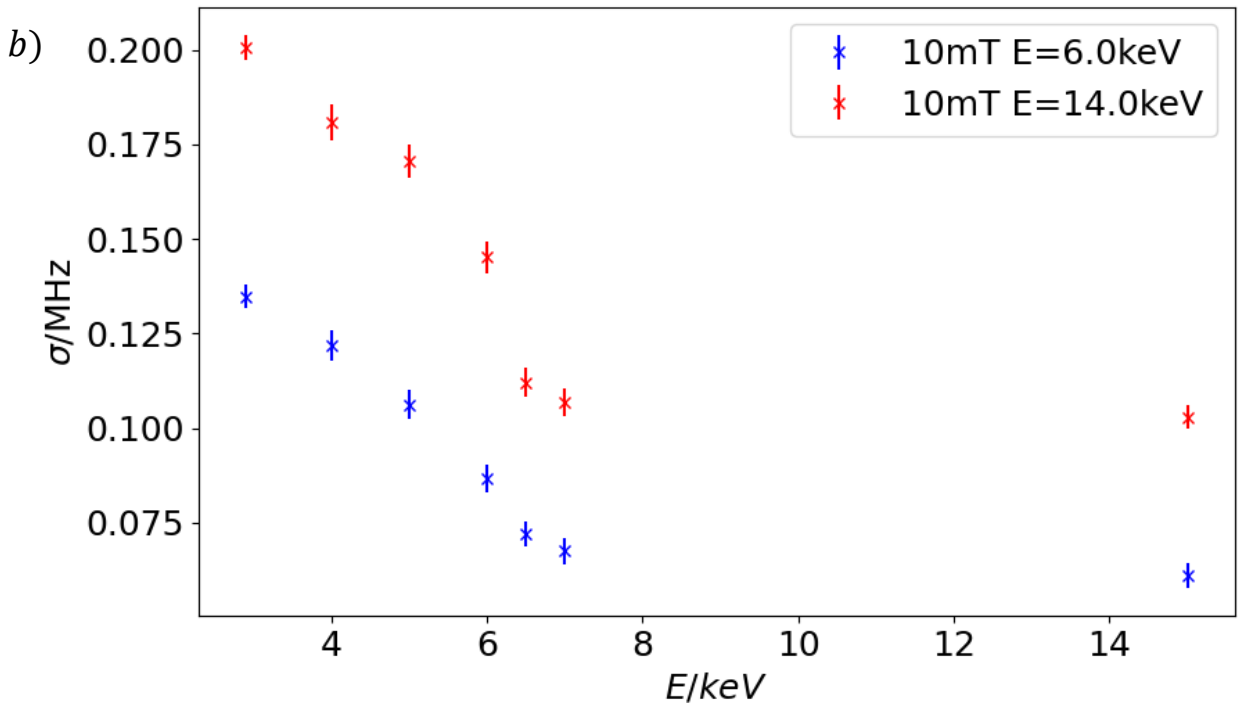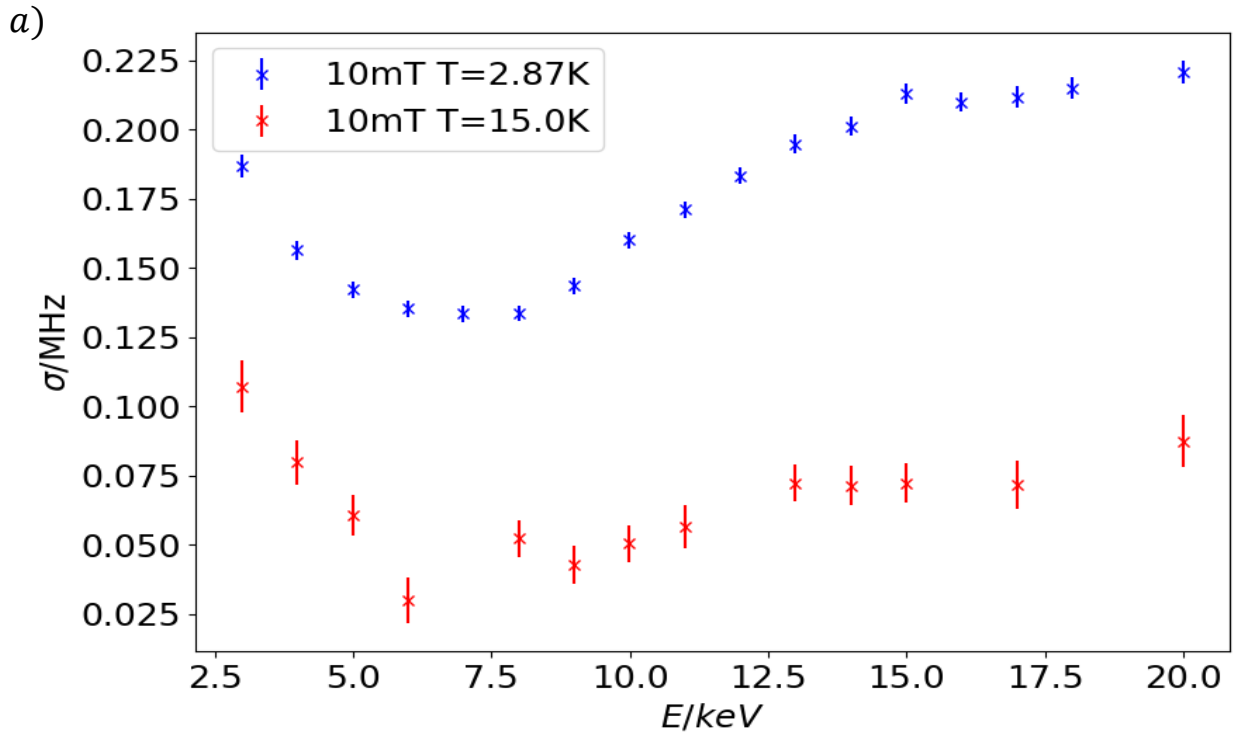
a)

b)

Figure 121: σ extracted for a 10mT external field as a function of a) Implantation energy above and below T_c b) Sample temperature at two energies – 6.0keV centred within the Pb and 14.0keV within the InSb.

The depolarisation measured within the sample is presented in Figure 121. As expected, we see an enhancement of depolarisation below T_c. This depolarisation is seen in each energy trace. Additionally, there is a clear trend visible (Figure 121b) in both the $InSb$ and the Pb, with the depolarisation then seemingly being constant as the temperature is increased further above T_c. The presence of this within the $E = 14.0keV$ data supports proximity induction within the $InSb$ layers.
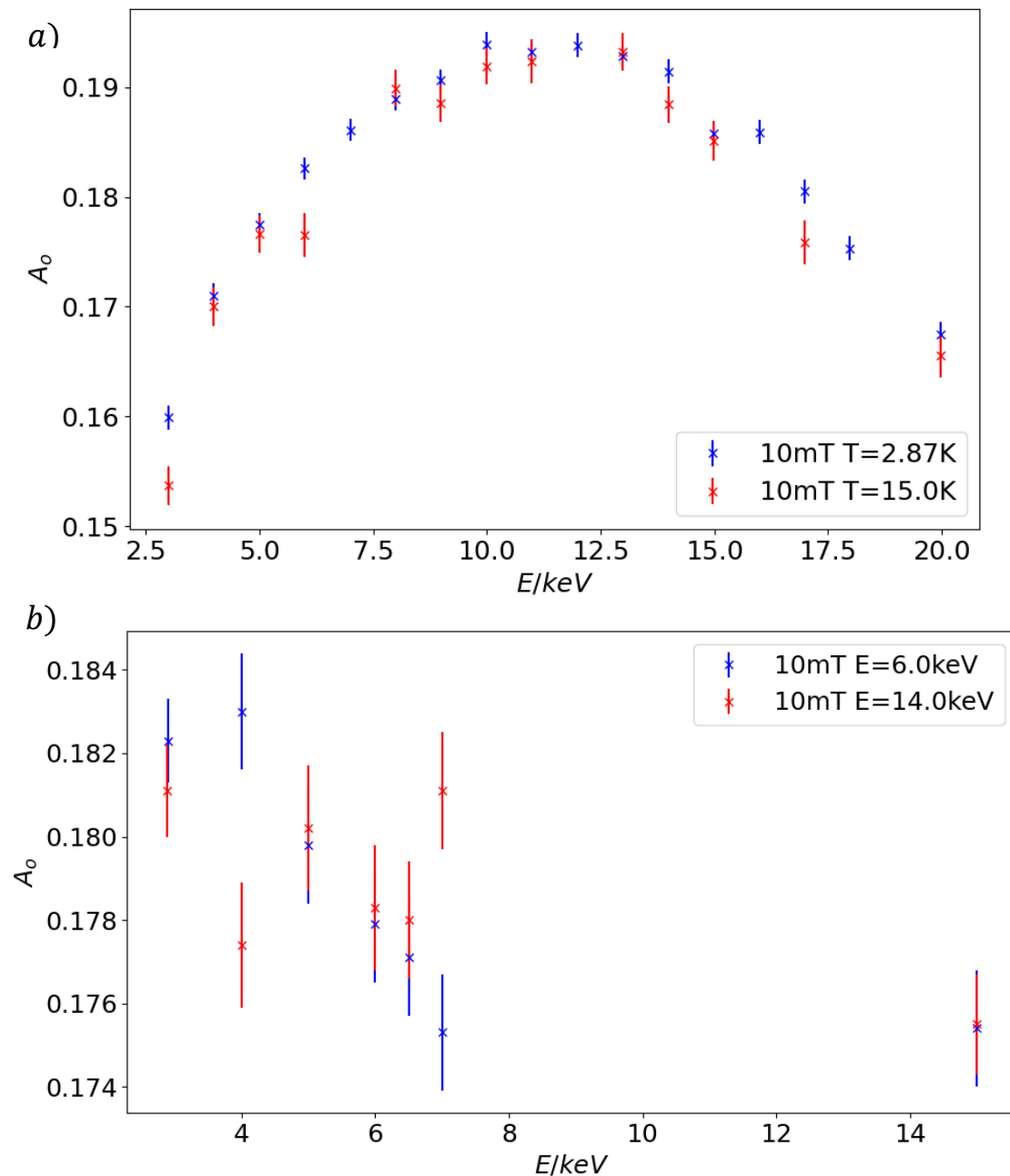
Figure 122: A_o extracted for a 10mT external field as a function of a) Implantation energy above and below T_c b) Sample temperature at two energies – 6.0keV centered within the Pb and 14.0keV within the InSb.

Finally, we can consider A_o (Figure 122). There was no systematic difference between the $InSb$ and Pb visible as a function of temperature. In general, the asymmetry increased as a function of Implantation depth.

6.4.2: 30mT μSR measurements

According to the theory, application of a larger field should enhance the p-wave elements and decrease the s-wave components within a high SOC proximity superconductor [121] [126]. As such, we also performed μSR measurements at 30mT. This was constricted to an energy scan at $T = 2.89K$ and $T = 15.0K$. As with the 10mT, the measurements were field cooled from 15.0K.
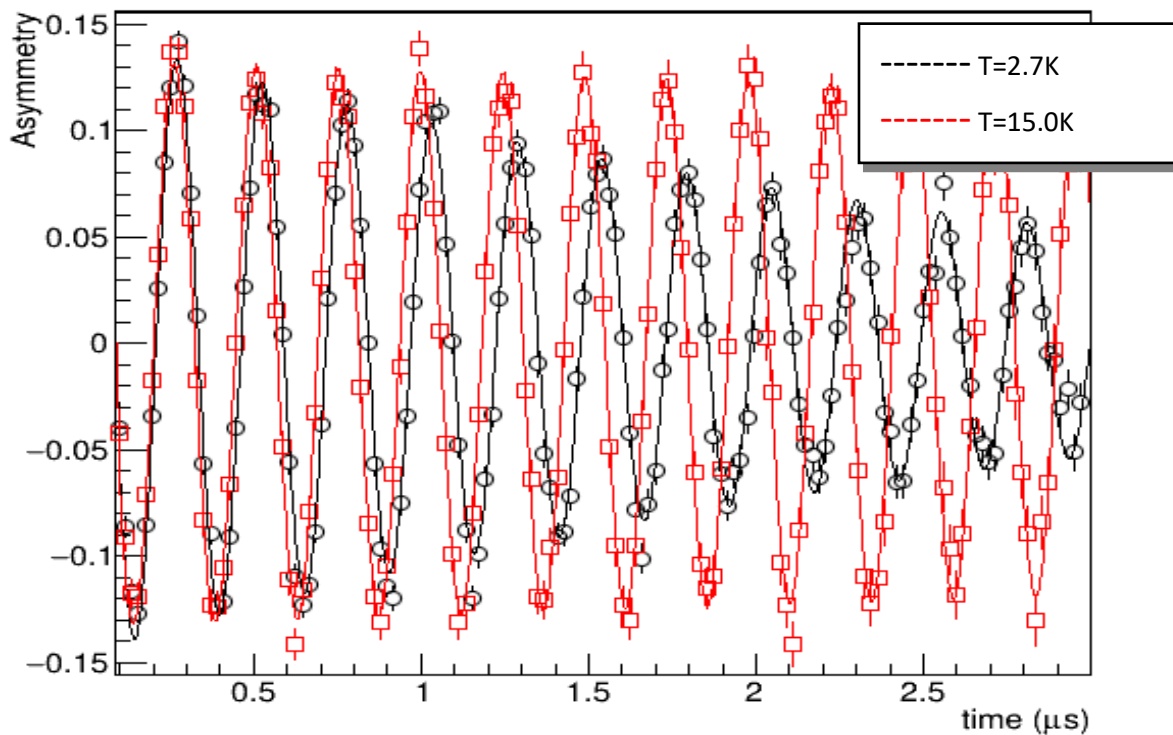
Figure 123: Measured detector asymmetry for an Pb/InSb heterostructure with with a 30mT field external field applied parallel to the sample surface, above and below T_c.

Once again, detector asymmetry was extracted from the raw histograms and fit to eq. 5.5 Figure 123 gives shows two measurements at an implantation energy $E = 6.0keV$ above and below T_c. Again, a clear frequency shift and increase in depolarisation can be observed below T_c. For each of these asymmetry measurements, B, A_o and σ are extracted.
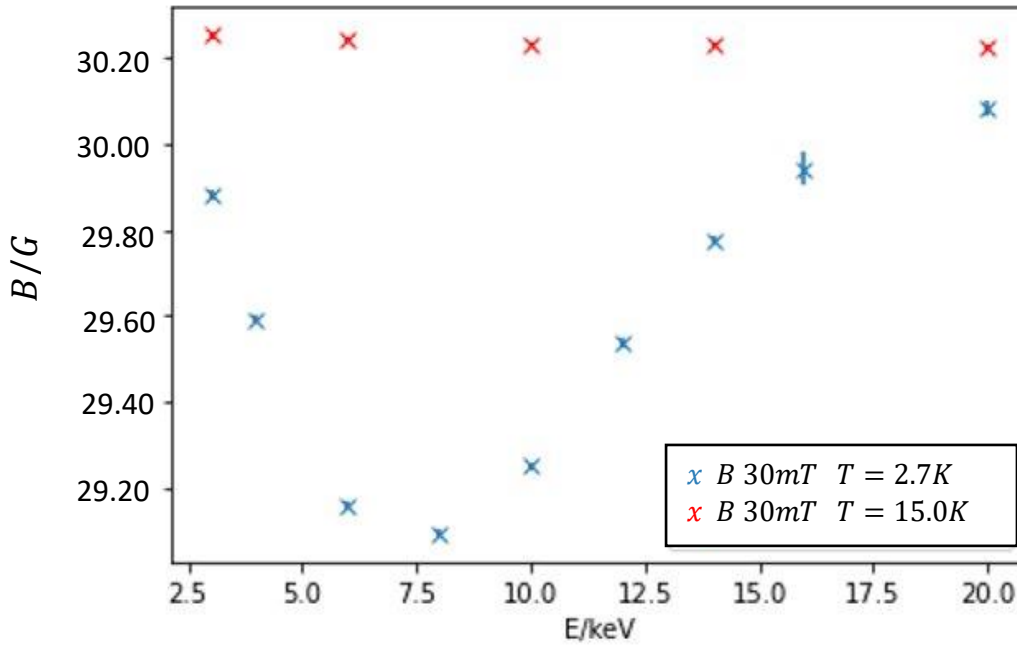
Figure 124: Magnetic field extracted for a 30mT external field as a function of implantation energy above and below T_c

The higher field also exhibits evidence of Meissner screening through the sample (Figure 124). As with the 10mT field, the screening extends to the higher energies, centering within the InSb.
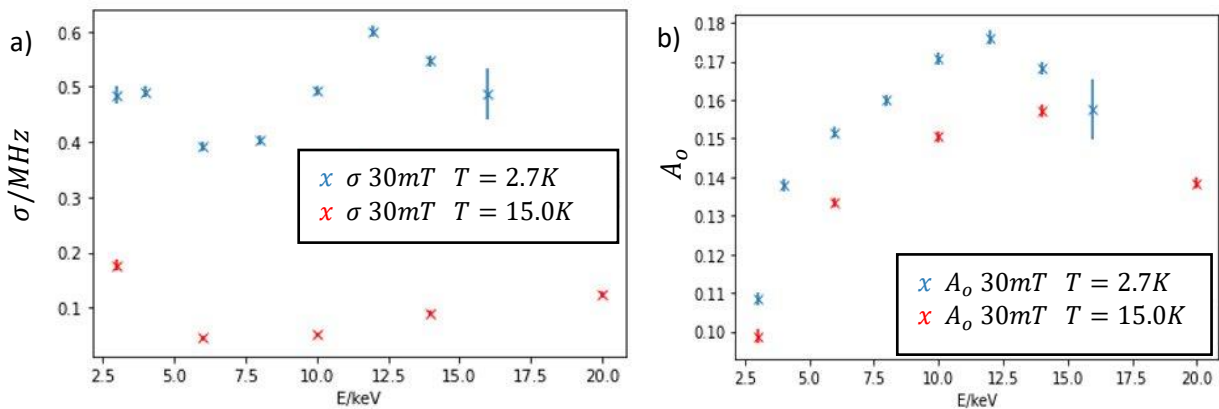
Figure 125: a) σ extracted for a 30mT external field as a function of Implantation energy above and below T_c b) A_o extracted for a 30mT external field as a function of implantation energy above and below T_c

σ and A_o are also extracted for the 30mT measurements (Figure 125). As with the 10mT field, σ is significantly enhanced below T_c consistent with the superconducting state. Additionally, it shows a similar dependence with implantation energy. The overall larger values are attributable to the larger field used, as observed in the Nb

measurements. In contrast however to the 10mT data (Figure 122), A_o observed a slight difference between the S and N states, but still exhibited a visibly similar trend with implantation energy.
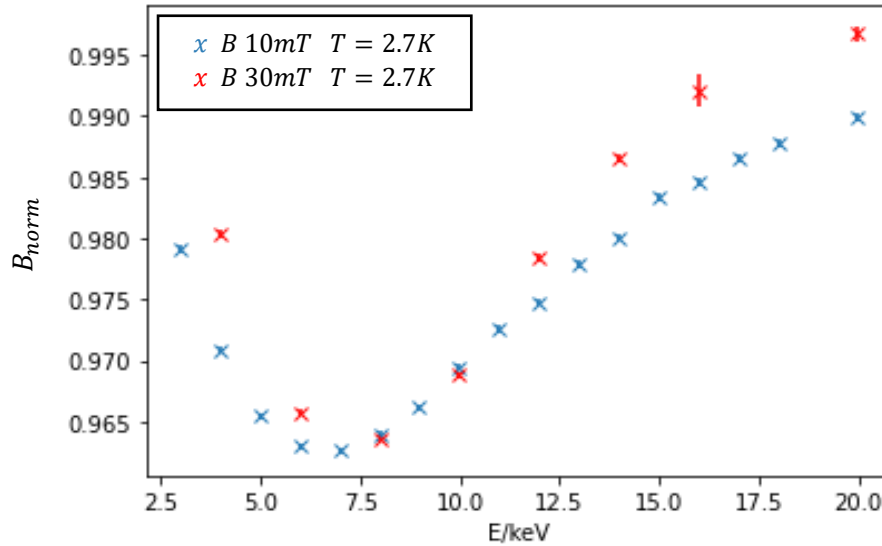
Figure 126: Normalised field extracted from the 10mT and 30mT measurements considered in Figure 118a and Figure 121 as a function of implantation energy.

Comparison between the field data normalised with respect to measurements at $15.0K$ for the two fields shows a distinct difference in field behaviour between the two fields. The measured local field is greater for the 30mT external field than the 10mT data. As a result, the local field screening profile within the sample has been suppressed, relative to the 10mT field, by the application of a 30mT field.

There are a few possible explanations for this. The first, most obvious, is that the higher field is sufficient to kill the superconductivity induced in the InSb. The electrical measurements undertaken in Chapter 4 showed that the SC induced in the InSb layers is weaker than that of the corresponding bulk superconductor, possessing a smaller energy gap. As such, it should be possible that the application of an external field could kill this proximity state, whilst not supressing the Pb. As such, the remaining screening seen at the high energy for 30mT could result solely from the fraction stopping within the Pb.
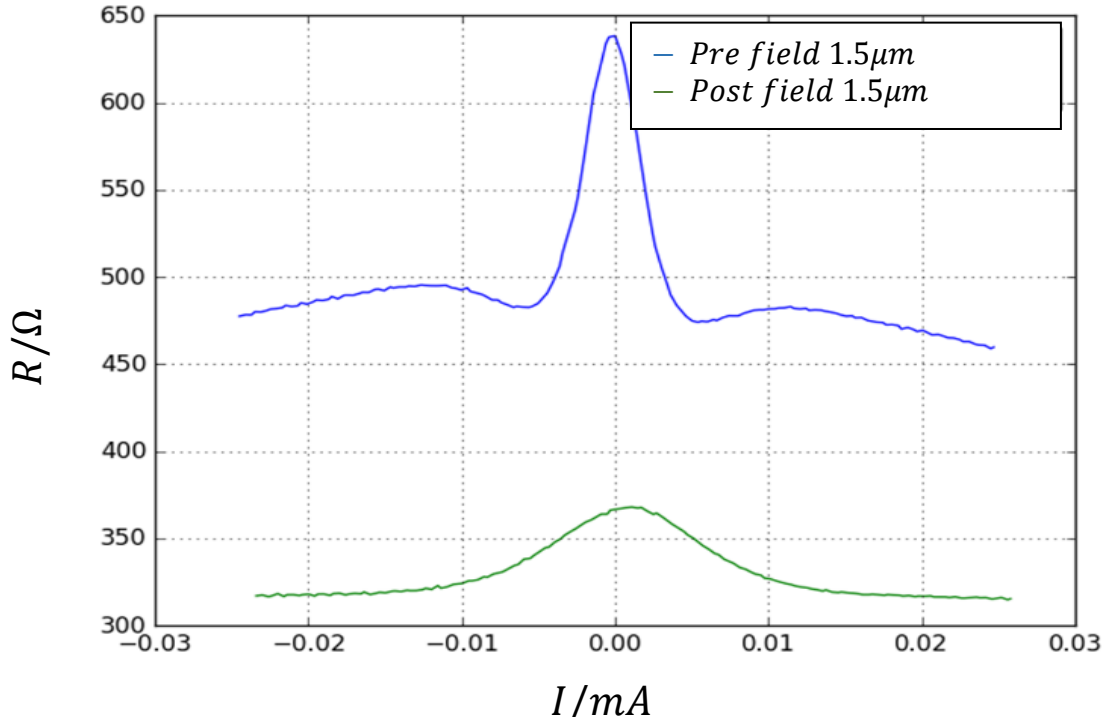
Figure 127: Comparison of measured differential resistance measured before and after application of an external B-field on 100nm Nb/InSb sample, as measured in Chapter 4. Measurement undertaken at 3.0K.

The second possibility, also suggested by the electrical measurements, is that the application of the magnetic field has altered the interface between the Pb and the $InSb$. As seen in 4.12, application of a field can permanently alter the proximity superconducting state in a $InSb/SC$ heterostructure, which can radically change the measured features (Figure 127). Although this sample received a citric acid surface treatment, and thus the exact conditions between the two samples will vary, it is not unlikely that the interfacial behaviour may be similar. As such, the altered behaviour may be due to a field induced alteration of the interface.

Finally, it is possible this behaviour results from the nature of the induced superconductivity. As discussed in chapter 2.11, high SOC can lead to the induction of a triplet superconductivity state. Additionally, because SOC doesn't fully lift spin degeneracy, the induced superconducting state should exhibit elements of both singlet and triplet pairing [121]. These two states should exhibit opposing field responses [122]. The singlet state will exhibit Meissner screening, expelling the external field from within the SC. The triplet state will exhibit anti-screening, seeking to enhance the induced SC state. Additionally, the relative strength of the singlet term will be

supressed by the field, and the triplet state will be enhanced. The reduced field screening in the 30mT trace could result from this. Confirmation of such behaviour would be a significant finding, providing direct experimental evidence of triplet superconductivity in high SOC materials. However, distinguishing between a purely s-wave induced state, and a mixed state that is predominantly s-wave may be challenging, and will require detailed theoretical modelling.

In order to distinguish between these three possibilities, two things are required. First, to consider potential alteration of the interface, we would need to verify if the system remained altered after the 30mT field is removed. There was insufficient time to perform this during the initial set of measurements. Additional experimental time was granted at a later date. Thus, to investigate this, a series of measurements applying $10mT \rightarrow 30mT \rightarrow 10mT$ fields would be required. At each field step, a measurement with varying implantation energy would be performed. Additionally, samples would then require heating to 15K before application of the higher field to ensure no flux is trapped within the superconducting state. As established in Chapter 4.12, temperature cycling over this low temperature scale wouldn't undo any field induced changes. As such, by cycling the field $10mT \rightarrow 30mT \rightarrow 10mT$, if the μSR signal restored itself to the initial $10mT$ measurement, then the observed change would be unlikely to be these interfacial effects.

6.4.4: Secondary measurements:

Secondary measurements on the same sample to perform this cycling were performed a few months after the initial measurements. The $Pb/InSb$ piece used for characterisation in 6.3 was remeasured to consider any possible degradation over this time frame. The sample was measured using the Optistat cryostat, and Keithley 6100/2100A current source/multimeter. Additionally, one of the four electrical contacts gave out during sample cooling. The re-characterisation measurements were thus undertaken via two terminal measurements.
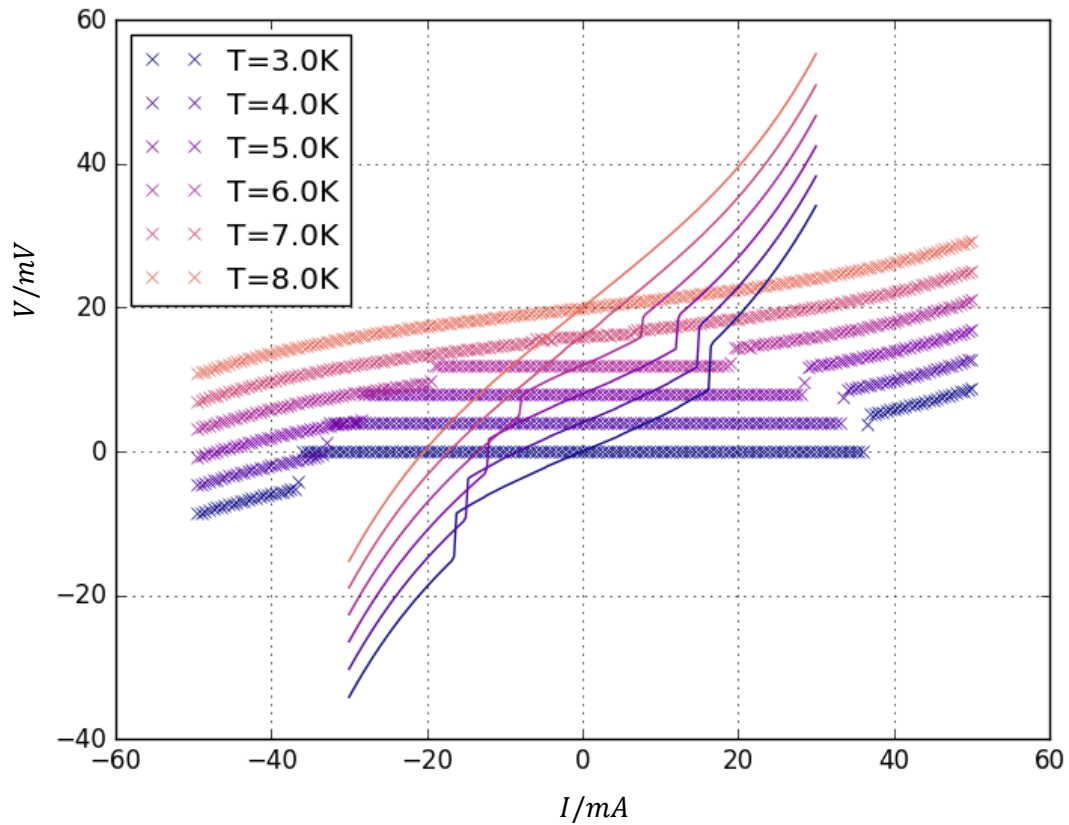
Figure 128: IV's measured for Pb/InSb characterisation piece. ×'s indicate data measured prior to initial μSR measurements. –'s indicate measurements performed prior to second experimental run. In both cases, data is offset from $T = 3.0K$ data for visual clarity – Equivalent temperature data sets for are offset by the same amounts.

IV's performed for this characterisation are presented in Figure 128 with the equivalent IV's measured during the initial characterisation included for reference. Although T_c can be seen to be broadly similar, there is a large suppression in I_c. This suggests the sample underwent some degradation during the interim. As the sample was stored in vacuum conditions during this period, it is likely this degradation is occurring at the interface between the InSb and the Pb. Interfacial degradation between InSb 2DEGs and SC thin films has been previously reported [202].
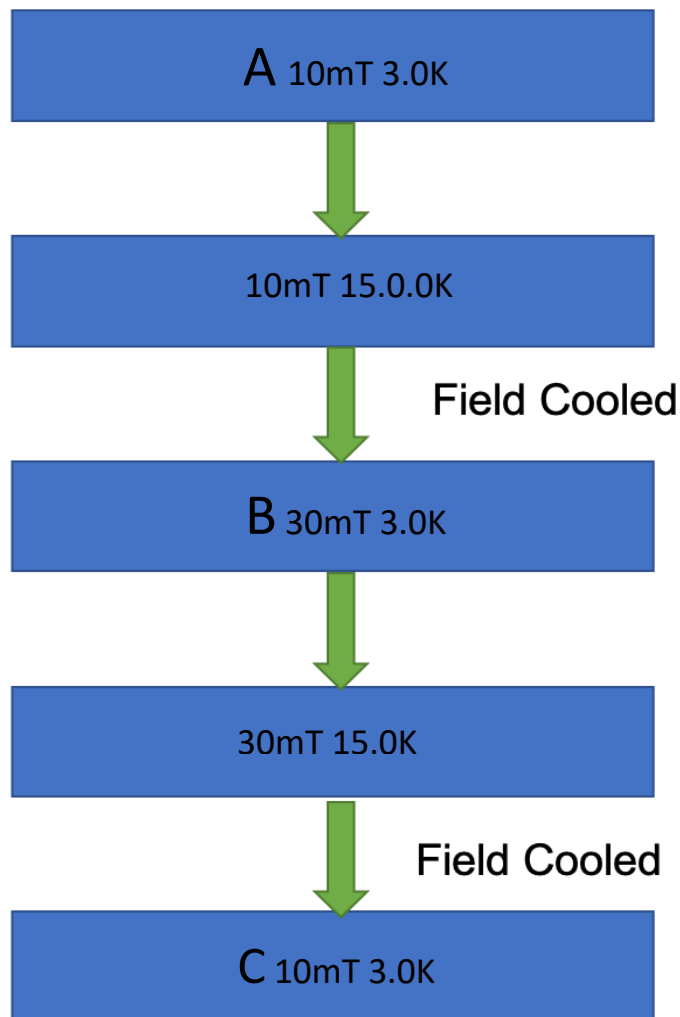
Figure 129: Field history of secondary $LE - \mu SR$ measurements. A, B and C are used to denote which measurements different datasets correspond to in future plots.

The original intention of the measurements was to perform a full $10mT \rightarrow 30mT \rightarrow 10mT$ sweep over the same energy range and spacing as used for the initial $30mT$ measurements (Figure 126). Unfortunately, the sample was found to insufficiently cool below T_c during measurement due to inadequate thermal contact. As such, the sample required heating, re-gluing and recooling. This was sufficient to bring the sample below T_c, however doing so halved total measurement time, and as such restricted the total measurement range in order to perform the expected cycling. The final procedure for temperature cycling with given field is shown in Figure 129. Additionally, this meant no temperature sweeps (e.g. Figure 121b) were performed for any field.
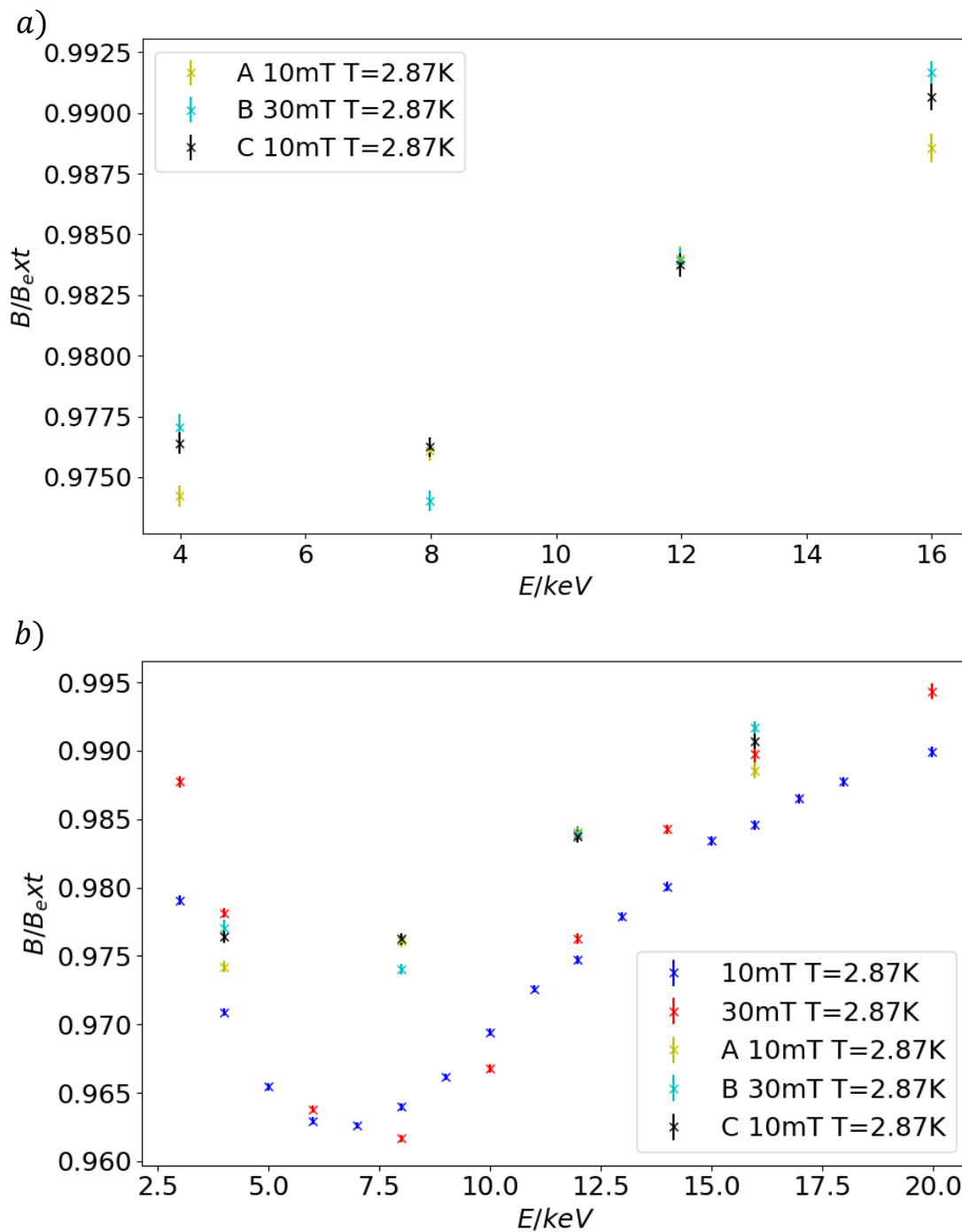
Figure 130: Normalised field extracted from the 10mT and 30mT measurements as a function of μ^+ implantation energy. Notation A, B and C correspond to measurements A, B and C in Figure 21. a) Measurements undertaken during these secondary measurements. b) All energy sweep measurements undertaken over both experimental periods.

Figure 130a shows the fields extracted from each of the secondary μSR measurements, normalised with respect to the applied external field. As with the initial measurements (Figure 126), magnetic screening can be observed, reducing as the

implantation energy increases. Application of the 30mT field causes a distinct alteration of the field profile relative to the 10mT, increasing the screening within the Pb (E = 8.0keV), and reducing screening at the high energies. When the field is cycled back to 10mT, this change in field relaxes, although the system does not fully return to the original measured behaviour. The relaxation of this phenomena is evidence that the altered screening profile has at least some direct field dependence and is not solely due to alteration of the surface states. The electrical measurements showed that cycling to $T = 15K$ was not sufficient to reset any field induced alteration, and as such the relaxation here cannot be due to the temperature cycling alone. It instead must result from the change in field amplitude.

Additionally, the values of screened field for this secondary set of measurements are significantly less than those in the initial (Figure 130b). We attribute this reduction to the sample degradation, evidenced by the reduction in I_c (Figure 128). λ_L, which describes the length scale of Meissner screening, has inverse dependence on the n_s, and thus Δ (2.23). As Δ and I_c within a superconductor are correlated, an observed reduction in I_c means λ_L will be longer. A longer λ_L, in the same sample will lead to less overall screening, leading to a reduced measured B.
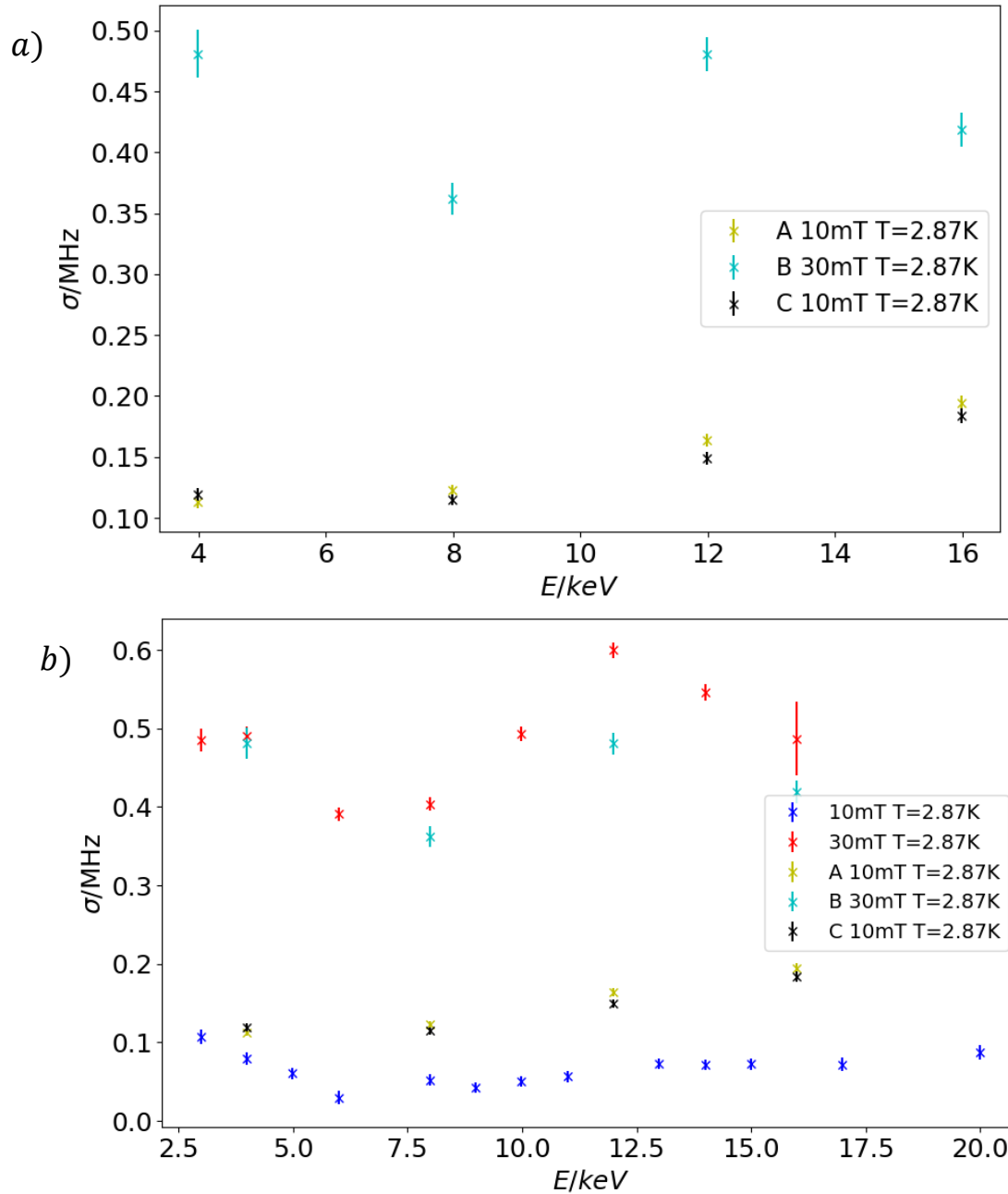
Figure 131: σ extracted from the 10mT and 30mT measurements as a function of μ⁺ implantation energy a) Measurements undertaken during these secondary measurements. b) All such measurements undertaken over both experimental periods.

As with the initial measurements, σ can be extracted (Figure 131a). Depolarisation was enhanced for the 30mT field. This enhancement is in line with the enhancement seen in the initial measurements (Figure 131b). σ mostly returned to the initial values seen pre-field cycling although there was a small difference, which was larger for the higher energies. As discussed in Section 5.1, below T_c the depolarisation, σ, arises from the distribution of fields within the sample. In the superconducting state, this will

be dictated by the screening profile within the sample, which at high energies will include the proximity superconductivity. For the values to remain similar, this suggests minimal alteration in the internal field distribution of the sample. As such, an alteration as seen in the electrical measurements of the Nb samples cannot have occurred. The field suppression seen at the higher energies must then be a direct response to the magnitude of the applied field.
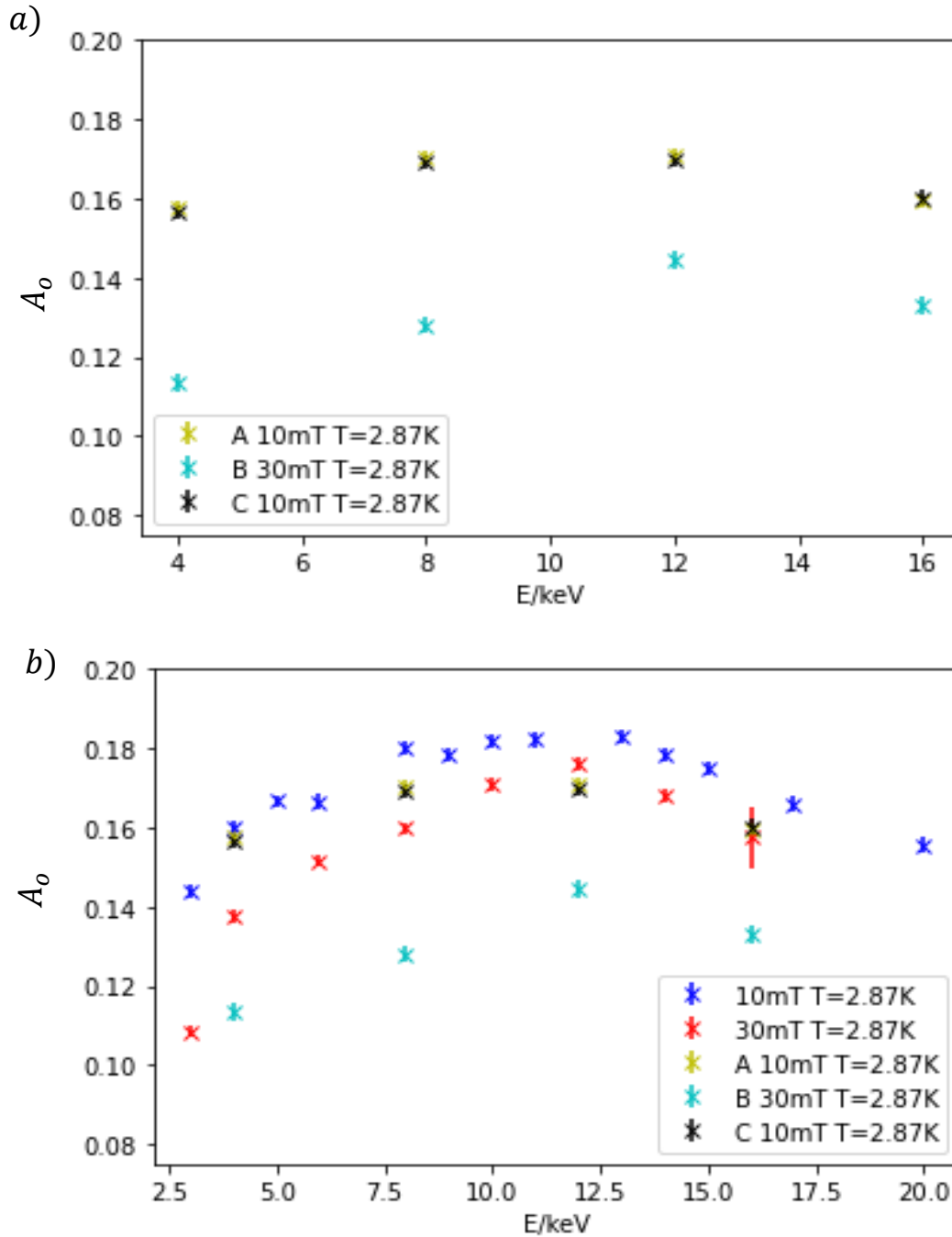
Figure 132: A_o *extracted from the 10mT and 30mT measurements as a function of* μ^+ *implantation energy a) Measurements undertaken during these secondary measurements. b) All such measurements undertaken over both experimental periods*

Finally, we can consider A_o (Figure 132a). A decrease is seen for the $30mT$ relative to the $10mT$ data. Additionally, field cycling did not change the measured A_o at $10mT$. Comparison of the full set of measured data (Figure 132b), a suppression of A_o was also observed between the $10mT$ and $30mT$ data. This suppression was greater for the secondary measurements than the initial ones.

6.5: Modelling of the Internal field profile:

Having experimentally established that the phenomena is unlikely to be due to charge alteration alone, we can also attempt to factor out the Pb contribution to the observed field screening. As discussed in 5.3, the sample orientation used in this measurement, that with the SC layer on top, will result in some energy dependant fraction of μ^+ stopping within the SC. This will likely result in there being some measurable screening for all implantation energies. For measurements of proximity superconductivity such as ours, this means the screening observed, particularly at the highest energies, may have significant contributions from the fraction of μ^+ stopping within the Pb.
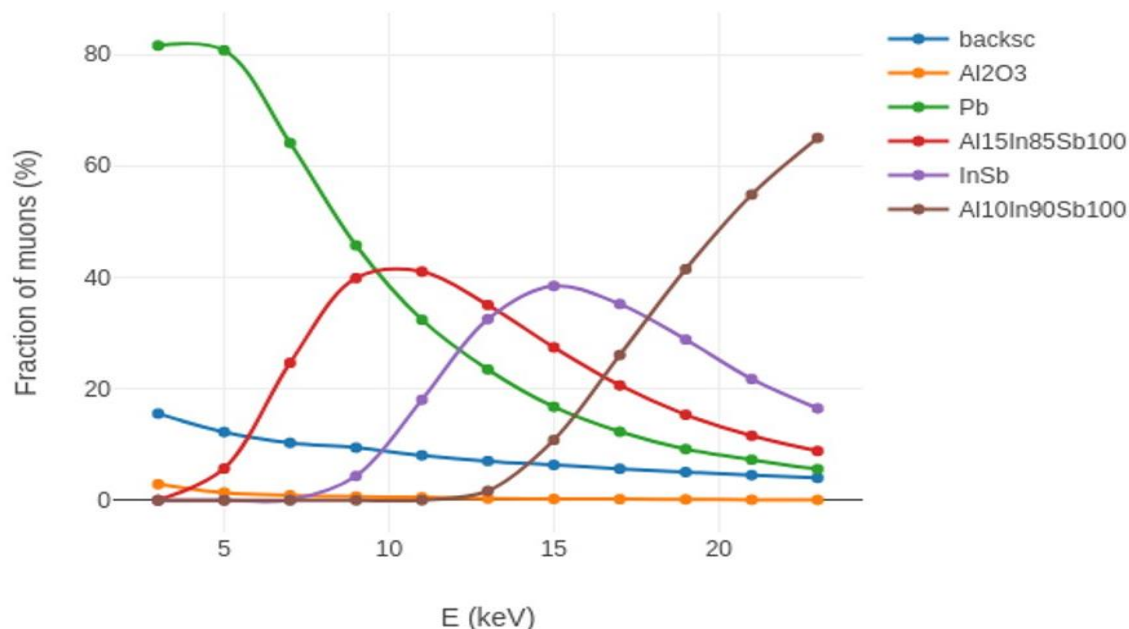
Figure 133: Muon Stopping fractions by material layer as a function of implantation energy.

To account for this, we can consider the μ^+ stopping distribution, $n(E)$ that serves as the basis of the stopping profiles (Figure 133). From this we can estimate the muon stopping fraction within each layer for a given energy. For each implantation energy, the number of μ^+ expected to stop in a given layer is summed, and then divided over the total of μ^+. Figure 133 gives these fractions. From this, we can see that even for the highest implantation energies used, $25keV$, around 10% of the total muon fraction will be contributions from the Pb. As such, we must account for this fraction to verify the observed screening is not purely due to the Pb stopping fraction.

6.5.1 "Worst-case" modelling:

In the first instance, we can consider the most extreme possible case – that of spatially uniform screening within the Pb and no proximity superconductivity i.e.:

$$B(z) = \begin{cases} B_{screen} & 2 < z < 52nm \\ B_{ext} & else \end{cases}$$

(6.2)

For μ^+ stopping within the Pb, the internal field they experience will be screened, such that it experiences a fractional value of B_{ext} . Otherwise, a μ^+ will experience B_{ext}. This is taken to be the most extreme possible estimate of Meissner screening possible within the Pb – a. For a given implantation energy, resulting average field felt by the total μ^+ population will thus be given by:

$$B(z) = \sum n(z)B(z)$$

(6.3)

From which, we can extract an overall B/B_{ext} value for each implantation value. This can then be compared to our measured values, for different values of B_{screen}. If there is no proximity screening, then a value of B_{screen} should correspond to our measurements, and our observed data could be explained by the Pb fraction alone.

The resulting 'worst-case' screening profile is given in:
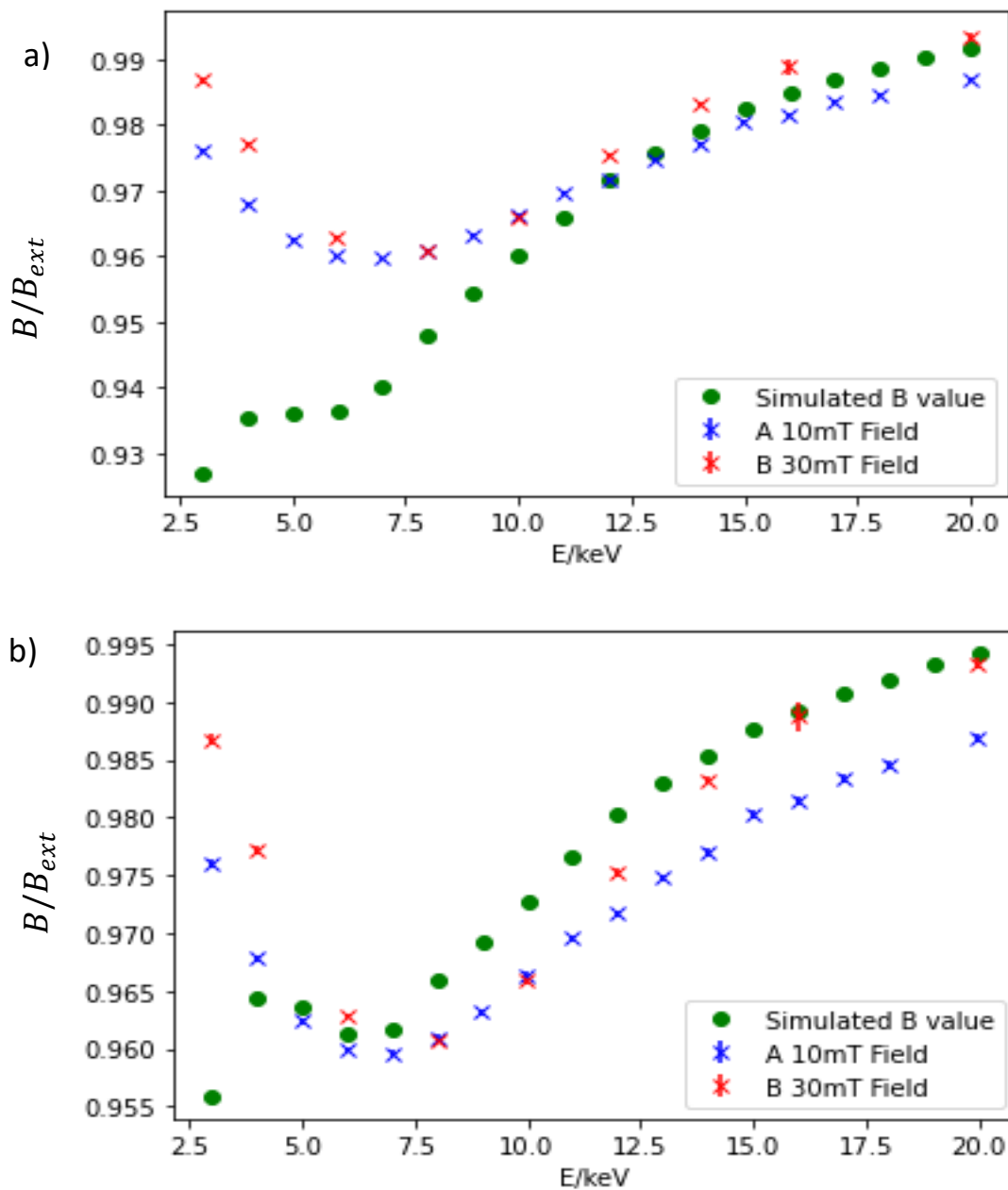
Figure 134: Simulated 'worst-case' screening profiles calculated for a) $B_{screen} = 0.9B_{ext}$ b) $B_{screen} = 0.96B_{ext}$. In both cases, normalised B-field measured for the 10mT and 30mT as a function of implantation are included for comparison.

Two cases for field screening are simulated. The first (Figure 134a) takes a screening value of $B = 0.96B_{ext}$, taken as the observed minima within from the energy scans. The second (Figure 134b) takes $B = 0.90B_{ext}$ as an example extreme screening case. In either case, the screening profile observed cannot be fully explained with this 'worst-case' example. In both cases, the highest energy behaviour for the 30mT

measurement appears explainable by this screening. However, the 10mT values cannot – If the observed field screening was purely due to the Pb fraction, both datasets should be explainable. Additionally, for both fields, the 'worst-case' is also insufficient to describe energies less than 15keV, which covers the majority implantation within the $AlInSb$ top cap. From these, given this was intended as a 'worst-case', it seems reasonable that there is some experimental evidence of proximity superconductivity within the AlInSb layers. The same treatment can be done for the secondary set of measurements.
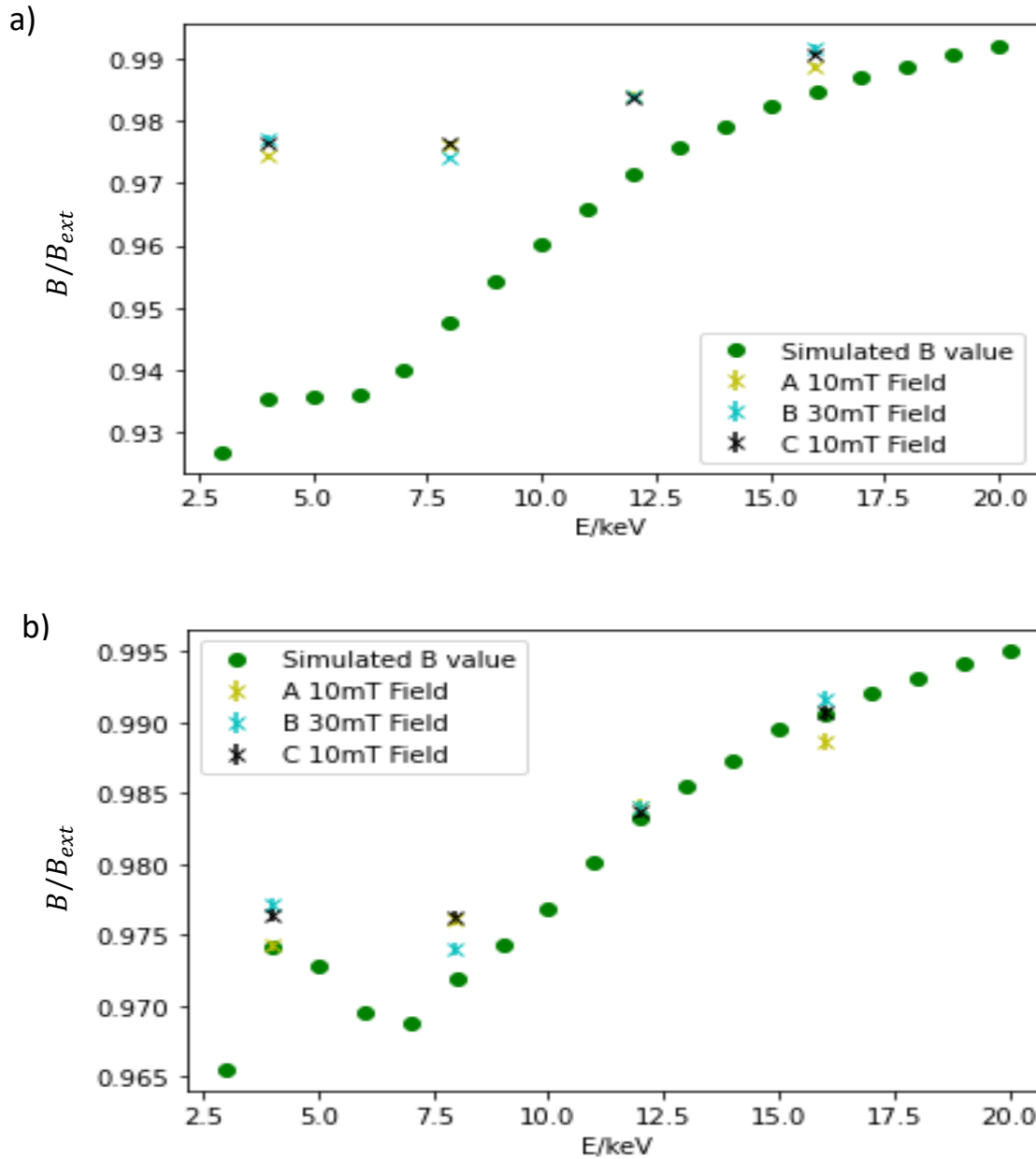
Figure 135: Simulated 'worst-case' screening profiles calculated for a) $B_{screen} = 0.96 B_{ext}$ b) $B_{screen} = 0.99 B_{ext}$. In both cases, normalised B-field measured for secondary measurements as a function of implantation are included for comparison.

Figure 135 gives two cases of this, for $B_{screen} = 0.96 B_{ext}$ and $B_{screen} = 0.9 B_{ext}$ respectively. Whilst the limited energy range restricts the ability to compare fully, In either case, the field profile can be insufficiently explained by the worse-case, either over estimating the field predominantly within the Pb, or that outside the Pb. .

6.5.2 Modelling of the Pb internal field

The 'worst-case' modelling gives likely gives an over-estimation of Pb contribution and is physically unrealistic. A more accurate description would be one where the field sample should be non-uniform. However, it is known that in the case of Meissner screening, the field distribution within the superconductor will vary away from the surface over the London penetration depth, λ_L, to a maximum screening value within approximately within the centre of the Pb film.

The previous analysis considered here of the μ^+ profile does not consider this directly, finding instead a single value of B_{screen}, and considering the depolarisation, σ, to find λ_L. However, by considering the stopping distribution of a μ^+, it has previously been shown that λ_L can be extracted as a direct fitting parameter [315].

Meissner screening occurs, as discussed, over a length scale of λ_L from the surface of the sample. For thin films, on a similar length scale to λ_L, the field profile has previously been modelled by:

$$B(z, \lambda_L) = \frac{B_o Cosh\left(\frac{t - z}{\lambda_L}\right)}{Cosh\left(\frac{t}{\lambda_L}\right)} \tag{6.3}$$

Where t is the thickness of the SC film, z is the thickness of an optional non-superconducting or 'deadlayer' on top of the SC, and λ_L is the London penetration depth [315]. With this field distribution, we can perform a similar treatment as with the 'worst-case' fitting. As with the 'worst case' fitting, $B(z)$ can be combined with the stopping distribution $n(E, z)$. However, instead of simply estimating B_{screen} from this, we can instead use it to describe the polarisation, $P(t, E)$ for a $B(z, E)$ via:

$$P(t, E) = \int n(E, z) \cos\left(\gamma_\mu B(z, \lambda_L) t + \phi\right) dz \tag{6.4}$$

Where $B(z)$ is given in eq. 6.3. Eq. 6.4 can be substituted into eq. 5.8 and fit directly to the asymmetry data as per the prior measurements in section 6.4.3. As $B(z)$ is determined by λ_L, this allows extraction of λ_L from the polarisation spectra directly as a fitting parameter.
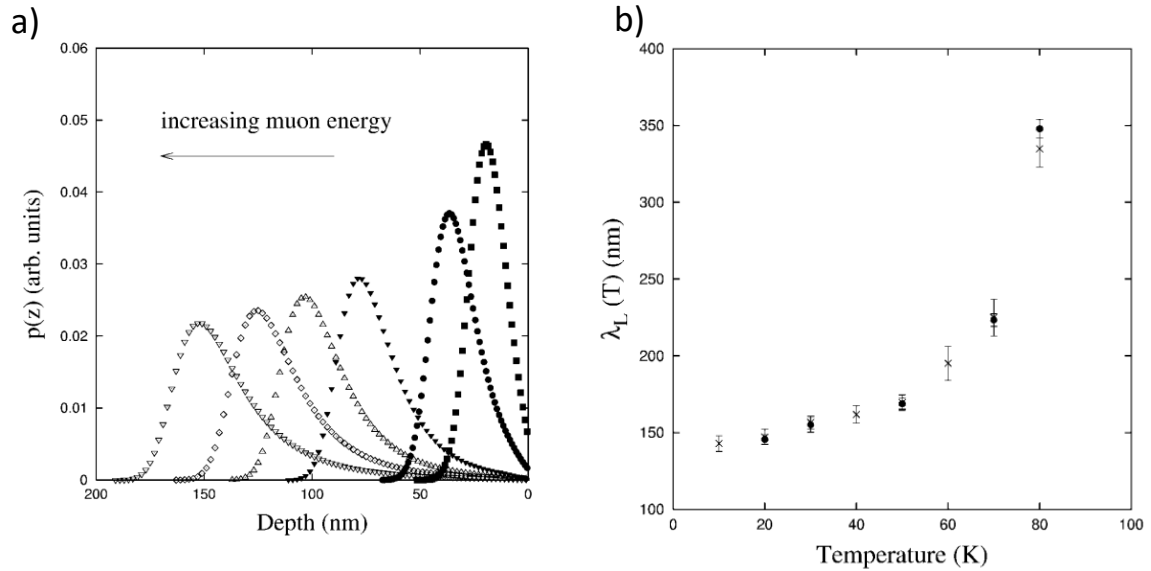
Figure 136: Both figures adapted from [315] a) TRIM.SP simulations of muon stopping probability as a function of sample depth for increasing implantation energies. b) Extracted λ_L as a function of Temperature. Crosses indicate values obtained via the fitting procedure in 7.4. Closed circles indicate values extracted from an alternative method.

This was previously used in the analysis of measurements of 700nm thick piece of YBCO superconductor [315]. Figure 136 shows the simulated muon distribution, showcasing the evolution of the field population with energy. From these, polarisation data was modelled and fit via the method described in (7.4) for increasing measurement temperatures, extracting λ_L. Values found here were found to agree strongly with those extracted from the mean field distribution of the sample sample [316], giving strong validity to this as an analytical approach. However as with the extreme case, this will only use to model the direct contributions of the Pb. The proximity SC cannot be modelled with this due an unknown field distribution within the InSb layers. As such, this will consider if it is possible to model our data with purely the fractional Pb stopping.
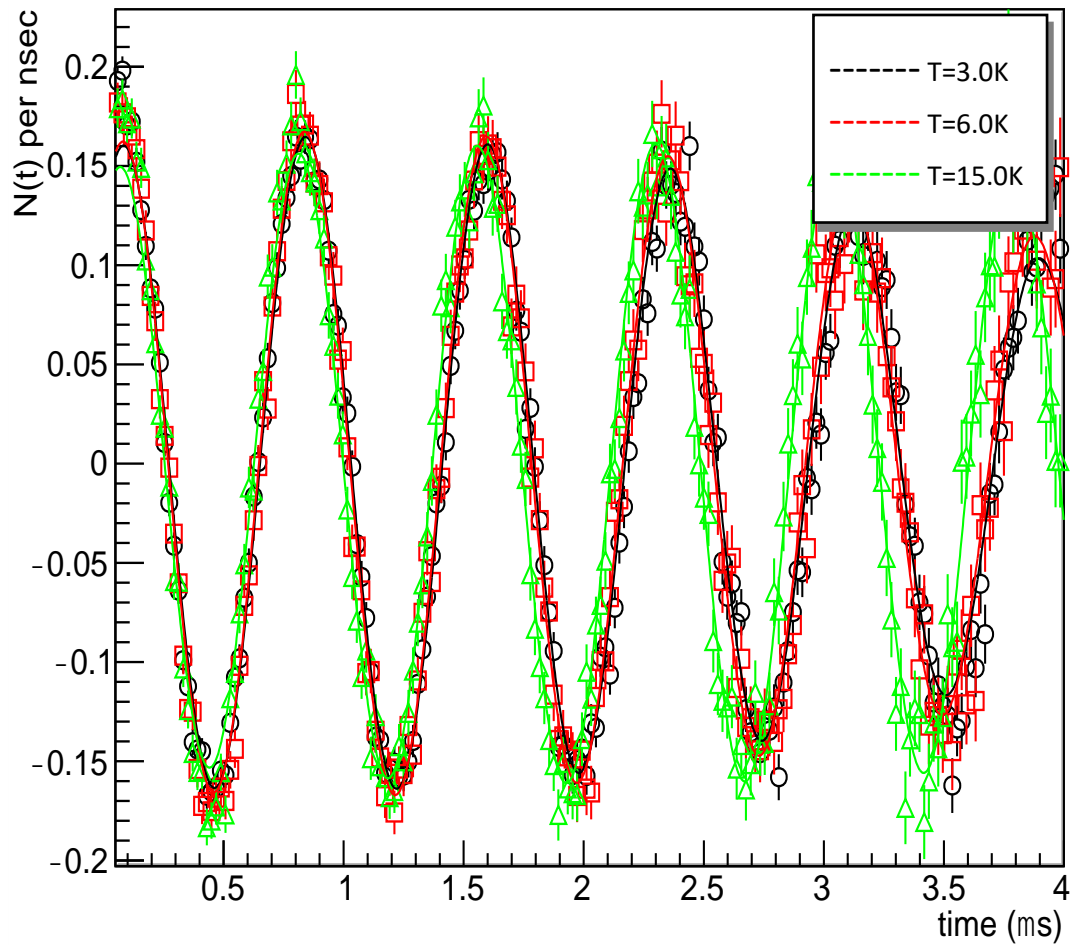
Figure 137:Polarisation data for 10mT μSR measurements performed with an implantation energy of $E = 6.0 keV$ at various temperatures. In all cases, data is fit to eq. 5.5.

In the first instance, we use this to model λ_L as a function of temperature as per [315]. Figure 137 shows fits to the temperature sweep data sets also used to generate Figure 120. Data sets are fit globally, and $\lambda_L(T)$ is extracted for each temperature point. The model well describes both the $E = 6.0 keV$, and the $E = 14.0 keV$ data as a function of temperature.
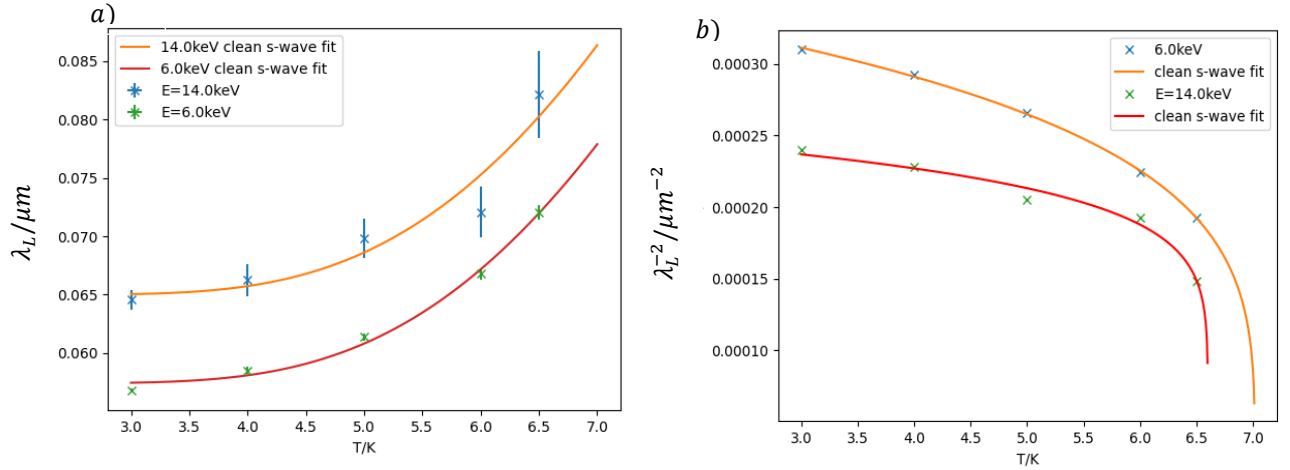
Figure 138: a) Modelling of temperature dependence of the λ_L as extracted from a fit to 6.4 b) as a) but considering λ_L^{-2}

Both the $6.0keV$ data and the $14.0keV$ parameters to the models for 'clean' s-wave superconductors given by 5.9 and 5.11, for both λ_L and λ_L^{-2}. As with the analysis of the Nb film within chapter 5, $\Delta(T)$ within 5.9 was substituted for $\Delta(0)\left(1-\frac{T}{T_c}\right)^n$. In both cases, λ_L can be fit too via this these models. Extracted fit parameters for these can be seen in Table 7.

Table 7: Fit values as a function of temperature for E=6.0keV and E=14.0keV

E/keV	Clean s-wave fitting parameters		Inverse λ fitting parameters		
	$(\lambda_L(0)/nm)$	$\Delta(0)$ /meV	$\lambda(0)^{-2}/\mu m^{-2}$	T_c	n
6.0	57.4 ± 0.4	2.96 ± 0.03	354.7 ± 3.1	7.02 ± 0.07	0.23 ± 0.01
12.0	65.0 ± 0.2	2.93 ± 0.12	256.1 ± 9.9	6.60 ± 0.10	0.13 ± 0.03

$\lambda_L(0)$ extracted from our fits are long relative to the $39nm$ expected from the literature [317] [318]. Our film had a lower T_c than pure Pb, and as evidence by the Nb films measured in Chapter 6, it is not unreasonable to expect a longer λ_L as a result. Additionally, this would be consistent with the deviation of n from $n \approx 0.5$ seen in the λ_L^{-2} fits. Overall, we can be confident in the ability of 6.3 to model our data in line with

the existing literature. Additionally, the two different energies give different λ_L. λ_L, being a physical property of the Pb film, should not vary as a function of energy. If the screening arises solely from the changing fraction of the Pb film, then λ_L should also not vary as a function of energy. That it does, is direct evidence that the screening cannot be fully modelled by the fractional Pb screening alone, and that there is proximity induced SC in the $InSb$ layers.

To further evidence this, we can consider the various energy scans undertaken, to consider $\lambda_L(E)$ directly. There are two approaches here. The first, will be to fit the datasets, that is allow λ_L to be a free variable as a function of implantation energy, $\lambda_L(E)$. The second approach will be to take λ_L as a global fit value (i.e. A shared fit parameter for each dataset), and instead assess the quality of fit at each energy. This will assess the degree to which, if any, a single value of λ_L fails to model the data.
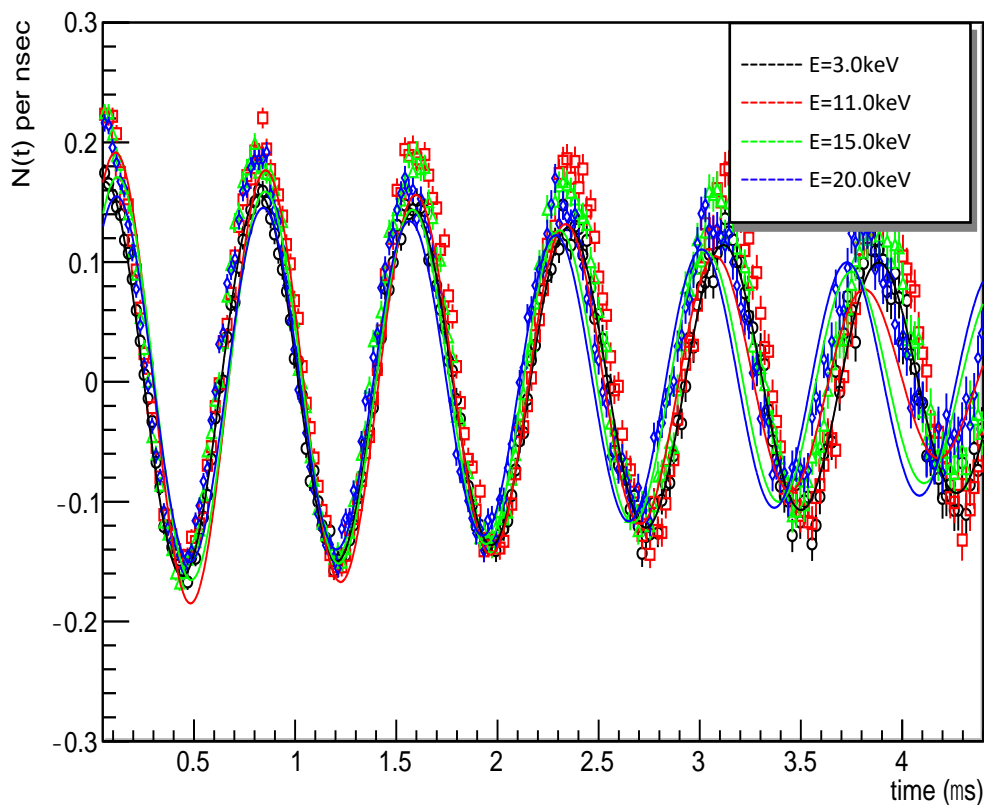
Figure 139: Polarisation data for 10mT μSR measurements performed at $T = 3.0K$ for various implantation energies. Data is fit globally to eq. 6.4, with a shared fit parameter of λ_L for all datasets.

The global fit of the initial 10mT polarisation data cannot be satisfactorily fit with a single value of λ_L. Figure 139 shows a selection of energies from this global fit. The higher energies, $E = 15.0 keV$ and $E = 20.0 keV$, show a frequency drift from the dataset, in contrast to the lower energies. As the higher energies correspond to an increasing fraction stopping within the $InSb$ layers, the failure of the fitting at higher energies is strong evidence of the Pb fraction being insufficient by itself. A value of $\lambda_L = 62.09 \pm 0.11 nm$ is given.
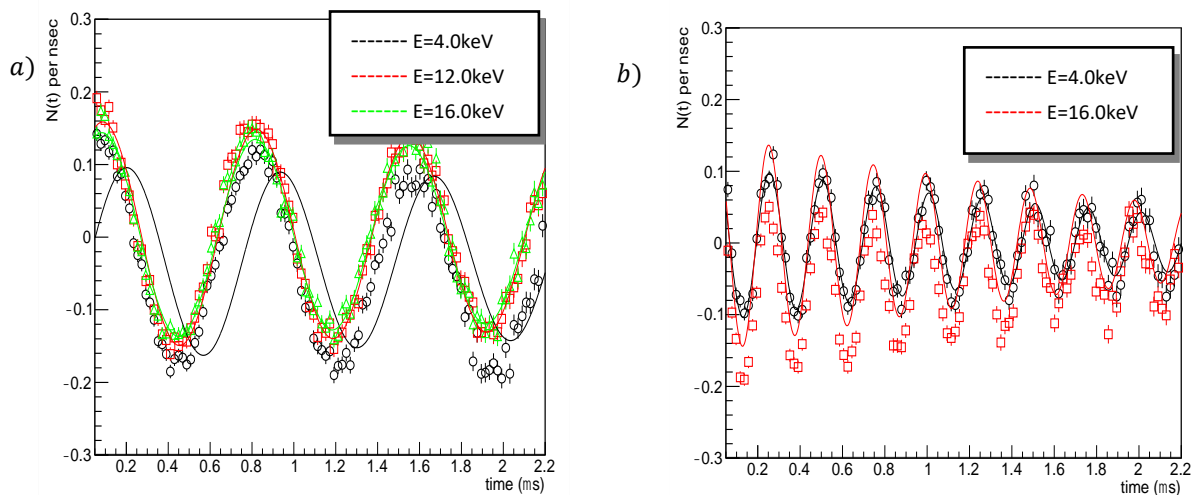
Figure 140: Polarisation data for secondary μSR measurements performed at $T = 3.0K$ for differing implantation energies. Data is fit globally to eq. 6.4, with a shared fit parameter of λ_L for all datasets. a) 10mT A dataset. b) 30mT B dataset.

This behaviour is mirrored in the secondary measurements, for both 10mT and 30mT datasets (Figure 140). A global fit, holding λ_L as a shared parameter between all runs, that solely considered the Pb fraction cannot adequately fit both the high and low energies.
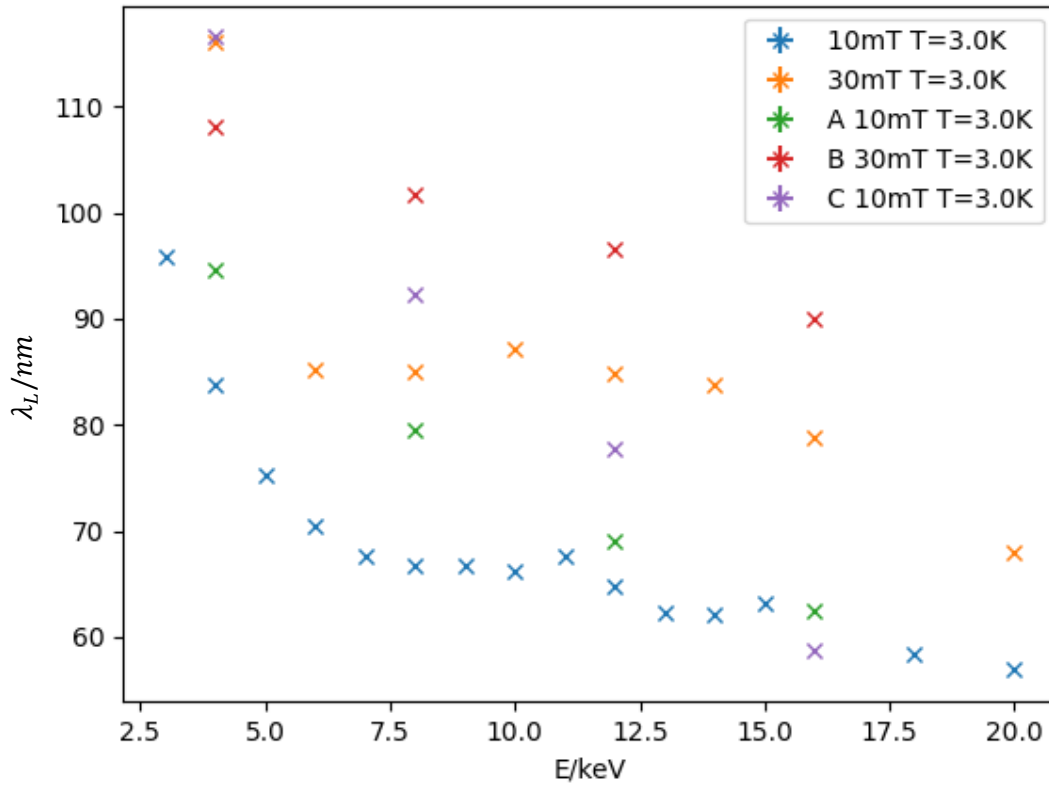
Figure 141:$\lambda_L(E)$ as a function of implantation energy extracted from polarisation data fit to 6.5 for all energy scans performed below T_c.

Considering $\lambda_L(E)$ instead, we can see λ_L decrease as a function of energy in all cases (Figure 141). The overall decrease is smaller for the 30mT data in both the initial and secondary measurements. As with our expectation from the field values, the secondary measurements (A, B and C) showed larger values of λ_L than those of the initial 10mT and 30mT measurements. The energy dependence of λ_L is sufficient to conclude that the fractional Pb stopping alone cannot explain our observed data - λ_L being a physical parameter of Pb should not strictly change as a function of implantation depth if it is the sole contributor to the screening. From this, it is the position of the author that the magnetic screening profiles observed must contain some proximity superconductivity extending into the $InSb$ layers.

We cannot, however, distinguish between the competing possibilities for the induced superconductivity, namely that of purely s-wave, or of a p-wave and s-wave mixed state. To do so would require further amendments to eq. 6.4, to factor in the proximity superconductivity. For instance, by modifying the field used in eq. 6.4:

$$B(z) = B_{Pb}(z) + B_{prox}(z) \qquad (6.5)$$

Where $B_{Pb}(z)$ is given by 6.3 as discussed, and $B_{prox}(z)$ describes the proximity superconductivity within the $InSb$. The exact form of $B_{prox}(z)$ is likely to be a complicated function, as the proximity superconductivity state should become weaker as the system moves further from the NS interface. In the case of mixed p-wave and s-wave, which proximity induced SC in InSb should theoretically be, this is further complicated. As shown in 2.7, triplet p-wave SC can arise from the lifting of spin degeneracy caused by Rashba SOC. The strength of the Rashba SOC will vary spatially through the 2DEG heterostructure, as it arises from Structural Inversion Asymmetry, and will thus be largest in the QW. As such, any p-wave component will have an additional competing spatial variance resulting from a non-uniform SOC term throughout. Additionally, the modelling must account for the competing field responses, i.e. the suppression of s-wave and enhancement of p-wave, for varying fractions of each. Modelling this is not part of this thesis, as it beyond both the available timescale to implement, and beyond the capacity of this author's theoretical knowledge. Several previous works have successfully modelled odd frequency SC in similar systems, including in prior μSR experiments [128] [258] [121] [10]. As such, this modelling represents an immediate direction to expand upon this work.

Despite this, these results still represent a significant success. Direct experimental confirmation of proximity superconductivity extending in the InSb supports our electrical measurements. This again represents a significant material success, via the top-down induction of proximity SC in an InSb 2DEG by thin films. Additionally, the success of this citric acid etch opens the possibility to perform similar treatment on electrical devices, with the potential to improve the SN interface as a result. Finally, though not possible as part of this work, the capacity to resolve more information about the properties of superconductivity within the high SOC material is there.

6.6: Summary

Following from the failure of the Nb/InSb μSR measurements, an alternative sample design featuring a $Pb/InSb$ device was proposed. As part of this, a $50nm$ Pb film was

deposited on an $InSb$ 2DEG heterostructure. $15nm$ of the top-most layers of the $InSb$ were etched via Citric acid to reduce the distance between the SC and the QW. The resulting structure was a high quality Pb film ($T_c \approx 6.7K$).

$LE - \mu SR$ measurements at 10mT exhibited evidence of Meissner Screening. The screening was seen to extend deeply into sample even at high energies, where the μ^+ population peaked in the $InSb$ layers. This suggested proximity induction of SC into the $InSb$ layers. At both low and high energies, the screening was supressed as a function of temperature, vanishing above T_c. Meissner screening was also observed for 30mT $LE - \mu SR$ measurements of the same sample, however the screening profile was supressed relative to 10mT.

Additional measurements further investigated this, by cycling the applied magnetic field $10mT \rightarrow 30mT \rightarrow 10mT$. These indicated this suppression was a response to the magnitude of the applied field, rather than any alteration akin to that seen in the electrical measurements. Consideration of the fraction of muons stopping in the Pb layers further suggested that the screening profile could not be explained by that alone. As such, our measurements are strongly indicative of proximity superconductivity induced in the InSb layers of our 2DEG. The observed field response is in principle consistent with either s-wave or a mixed s-wave and p-wave proximity state. Further theoretical analysis must be undertaken to distinguish between these two possible superconducting states.

Future Work and Conclusion

7.0: Conclusion:

Proximity superconducting induced in high SOC semiconductor materials, such as $InSb$, by conventional s-wave supercondutors are thought to be an ideal platform to host topological edge states, or Majorana Zero Modes. SOC lifts the spin degeneracy within the InSb, save for at $k = 0$. This lifted degeneracy opens the possibility of proximity superconductivity induced within the $InSb$ to exhibit a mix of spin-singlet and spin-triplet pairing. Triplet SC, in combination with an applied magnetic field are necessary components to generate MZMs. Work on creating nanowire platforms hosting this MZMs, and experimentally verifying them, have run into significant challenges. There remains significant scientific and technological interest in both verifying this mixed superconducting state and creating scalable QW structures capable of hosting them. This work attempts to integrate superconducting thin films with high spin orbit coupling $InSb$ quantum wells. Specifically, it looked at 'top down' induction of SC within the Quantum Wells. Such a material set-up is necessary to allow for the fabrication and usage of side gated devices.

Top-down induction of the SC would necessitate the superconductivity passing through ~50nm of material before reaching the QW layer, where the SOC would be strongest. Confirming induction of SC within the QW, and not simply within these top layers was needed moving forwards. The experimental work was intended to both characterise the induced SC state and measure the length scales it extended into the $2DEG$ material. This was done via two experimental techniques.

The first utilised electrical measurements of a TLM device. A TLM measurement is traditionally used to measure $R_{contact}$ and R_{sheet}, by considering the increase in resistance between the increasingly spaced pads. By utilising superconducting contact pads, below T_c, the effective resistive length would be reduced by proximity induced length, λ_{prox}. By measuring the resistance for all gap lengths as a function of

temperature, λ_{prox} could be inferred. A $100nm$ Nb film was deposited on top of a high mobility remote doped $InSb$ QW. From this, a TLM structure comprised of a set of increasingly spaced Nb contact pads was fabricated. Characterisation of the Nb film showed $T_c \approx 7.5K$. An etch procedure for etching the Nb film without etching the InSb substrate was established. Final gap sizes spanned the range $l = 1.5 - 8\mu m$.

Differential Conductance measurements of the resulting gaps showed a dip centred at zero applied bias. The dip was suppressed as a function of temperature, corresponding to T_c of the Nb film. Two distinct features were observed, the first, for gap sizes of $4\mu m$ and $8\mu m$, a broad conductance dip was observed. For all other gaps, a narrow dip was accompanied by a pair of onset peaks, consistent with superconductivity. All gaps were satisfactorily modelled to the Dynes function, a modification of the BTK theory, factoring in inelastic scattering at the SN interface. From this, the difference between the two observed feature types was attributable to significantly increased inelastic scattering. The presence of SC features in all gaps suggest a long proximity length, consistent with induction in the high mobility QW layer, and are comparable to recent results in an $InGaAs/InP$ heterostructure. These results suggest successful induction of proximity superconductivity in *InSb* QWs via top-down films, a significant technological success. This induction is successful in-spite of the poor quality of the interface, and with minimal surface preparation undertaken. A full TLM measurement of our device was not possible due to this inelastic scattering, as no systematic dependence of resistance with gap length was observed.

Application of a magnetic field perpendicular to the sample surface resulted in a total suppression of the conductance dip for all gaps. This suppression persisted even upon the removal of the field. Heating the sample above $2T_c$ did not restore the suppressed features, suggesting it was not simple flux trapping. Heating the sample to T_{room}, and re-cooling did not restore the original features, but did induce a narrow peak in the $4\mu m$ gap, that previously did not exhibit it. The high temperatures required for this suggested that the suppression resulted from alteration of trapped charge states in the interfacial layers between the Nb and InSb. Alteration of these states would alter the NS interface responsible for the Dynes-like feature observed. An exact understanding of these states, and characterization of the field induced alteration remains on-going.

The second half of this work sought to directly probe the NS interface via the use of low energy muon spin rotation measurements, or $LE - \mu SR$. $LE - \mu SR$ allows measurement of the local magnetic field within nm thin films, by implanting μ^+ at increasing energies and measuring the spin precession via the resulting e^+ decay. Increasing the implantation energy allows measuring at increasing sample depths. Previous measurements across the interface of a Superconductor-Topological Insulator, which exhibits similar lifting of the spin degeneracy, observed an increase in the local magnetic field within the topological insulator. This local field increase is consistent with the spin triplet superconductivity. As such, we sought to perform similar measurements across an Nb/InSb QW heterostructure to examine the same effect. This represented the first such $LE - \mu SR$ measurements on a high SOC/SC structure, providing a unique experimental insight into these materials. This alternative set of measurements is only possible because of the 'top down' film used – The more commonly used side-deposition is incompatible with the required $LE - \mu SR$ experimental geometry.

Initial measurements were performed on a Nb/InSb sample with a 50nm Nb film. However, the Nb film produced was found to be heavily defected. The defected films observed no evidence of Meissner screening within the Nb. This prevented measurement of the proximity superconductivity within the sample and was thus an experimental failure.

Subsequent alteration of the sample design replaced the 50nm Nb film with a 50nm Pb film. Additionally, the topmost layers of the InSb 2DEG were thinned by $15nm$ by a citric acid etch to reduce the distance between the Pb and the QW. This modified structure when measured with a 10mT external field exhibited a clear Meissner screening profile. This profile suggested magnetic screening extending well into the $InSb$ material layers. Measurement with a 30mT external field suppressed the Meissner screening profile at higher energies. Secondary measurements cycling the field from $10mT \rightarrow 30mT \rightarrow 10mT$ eliminated the possibility that this suppression was due to previously surface alteration observed in the electrical measurement, as the system was seen to relax. Modelling of the fraction Pb screening showed that the

observed field profile could not be solely explainable by this alone. As such, the μSR measurements experimentally confirmed proximity superconductivity extending into the $InSb$ from a Pb film, and likely into the QW. It is likely that the field dependence of the Meissner screening profile is either due to the suppression of the proximity effect at high energies, or due to competing field behaviours of triplet and singlet superconductivity. However, this work is not able to adequately resolve between these two possibilities. And as such, more analysis is required to be able to infer the nature of the proximity induced state in high SOC materials.

7.1 Future Work:

Experimental evidence of proximity SC from two different SC films opens many avenues of future work exploring these platforms. Of primary interest is optimizing the interface between the InSb and SC to successfully induce a so called 'Hard gap' proximity state. As part of this, overcoming the immediate material challenges present will be of importance.

An initial set of measurements considering the fabrication of an equivalent set of electrical devices on the $Pb/InSb$ films would be an initial aim as a first investigation of the impact of thinned top cap on the induced SC state. Following this, a systematic investigation into the relationship between top cap thinning and induced superconductivity would be warranted. This would give an 'optimised' thinning of the top cap, compromising between the impact on the semiconductor conductivity, and the induced state. Ideally, such an investigation would be performed with both SC considered here for completeness. Additionally, selective area etching of intended SC deposition areas prior to film deposition offers another route towards strong proximity induction. By etching the $InSb$ areas corresponding to the eventual contact pads, depositing, and then removing the excess SC film, one can effectively 'sink' the SC pad into the heterostructure. This would result in the superconductor being flush with the QW, minimising the potential surface defects. Such an approach has previously been used in InAs SC structures.

Further investigation into the observed field induced alteration of the electrical measurements is also necessary as a part of this optimization work. Characterisation of the exact field history required to induce it, and as such the corresponding energy scales at which it occurs. Likewise, characterization of the exact temperature scale required to reset the interface should also be taken. Factoring this work in with optimisation of the interface for the pursuit of a superconducting hard gap. Characterisation of this behaviour is required for future devices, as an external field is an essential component required to realise MZMs.

In either case, once the material interface is optimized, and field behaviour understood, fabrication of more sophisticated devices structures would follow. In the first instance, fabrication of another set of TLM devices should be undertaken to allow direct measurement of the proximity length via electrical measurements. Modification of the design to incorporate a significantly larger gap lengths, e.g. $50\mu m$ or $100\mu m$ to consider the limiting case for such an SC/InSb junction.

Fabrication of such a TLM network, with a successful induction of 'hard gap' superconductivity, will open the ability to perform Josephson Effect measurements as a function of magnetic field. Measurements of the change in I_c as a function of applied B to investigate the expected Fraunhoffer diffraction pattern would be further experimental evidence for proximity induction across the full gap width. Ideally, this would allow measurement of the evolution of these patterns as a function of gap length.

Aside from optimising the SC interface, new devices should also focus on control of the local electronic density via electrical gating. This will include the fabrication of side gated InSb structures, leading to the successful realization, control and measurement of Quantised Conductance steps at ultra-low temperatures consistent with 1D conductance. Integration and measurement of such a device with superconducting films would then follow. To realize MZM supporting systems, all elements of this must be shown to be controllable within the superconducting state.

More detailed analysis on the μSR measurements are also an immediate priority. Ideally, this would involve modelling of the internal field within the sample, including the proximity superconductivity. Modelling should factor both purely s-wave superconductivity, as well as a mixed state of spin-triplet spin singlet superconductivity. If necessary, as per this analysis, additional samples could be prepared, and further measurements undertaken to obtain a full implantation energy scan with the complete field and temperature cycling as required to distinguish between these possibilities. Accurate analysis of the local field within the sample, potentially offers one of the first direct experimental verifications of the $p_x + ip_y$ state within high SOC materials. Ultimately, whilst much work remains to be done, the work

undertaken as part of this thesis represents a potentially important starting point for the utilisation of superconductor/$InSb$ $2DEGs$ devices as a future technological platform.

Bibliography

[1]   T. Ladd, F. Jelezko, R. Laflamme, Y. Nakamura, C. Monroe and J. O'Brien, "Quantum Computers," *Nature,* vol. 464, pp. 45-53, 2021.

[2]   H. Huang, D. Wu, D. Fan and W. Zhu, "Superconducting quantum computing: a review," *Science China Information Sciences,* vol. 63, no. 180501, 2020.

[3]   S. Das Sarma, M. Freedman and C. Nayak, "Majorana zero modes and topological quantum computation," *npj Quantum Information,* vol. 1, p. 15001, 2015.

[4]   E. Majorana, "A symmetric theory of electrons and positrons," *Soryushiron Kenkyu Electronics,* vol. 63, no. 3, pp. 149-162, 1981.

[5]   A. Y. Kitaev, "Unpaired Majorana fermions in quantum wires," *Physics Upsekhi,* vol. 44, no. 131, pp. 131-136, 2001.

[6]   F. Wilczek, "Quantum Mechanics of Fractional-Spin Particles," *Physical Review Letters,* vol. 49, no. 14, pp. 957-959, 1982.

[7]   C. Nayak, S. Simon, A. Stern, M. Freedman and S. Starma, "Non-Abelian Anyons and Topological Quantum Computation," *Reviews of Modern Physics,* vol. 80, no. 1083, 2008.

[8]   J. Alicea, Y. Oreg, G. Refael, F. von Oppen and M. P. Fischer, "Non-Abelian stastitics and topological quantum information processing in 1D wire systems," *Nature Physics,* vol. 7, pp. 412-417, 2011.

[9]   L. Kauffman and S. Lomonaco Jr, "Braiding with Majorana Fermions," in *SPIE Commercial + Scientific Sensing and Imaging*, 2016.

[10] J. Linder and A. V. Balatsky, "Odd-frequency superconductivity.," *Reviews of Modern Physics,* vol. 91, no. 4, 2019.

[11] A. Makenzie and Y. Maeno, "The superconductivity of Sr_2RuO_4 and the physics of spin-triplet pairing," *Reviews of Modern Physics,* vol. 75, p. 657, 2003.

[12] J. Alicea, "New directions in the pursuit of Majorana fermions in solid state systems," *Reports on Progress in Physics,* vol. 75, no. 7, 2012.

[13] J. Sau, R. Lutchyn, S. Tewari and S. Sarma, "Generic New Platform for Topological Quantum Computation Using Semiconductor Heterostructures," *Physical Review Letters,* vol. 104, pp. 040502: 1-4, 2010.

[14] J. Alicea, "Majorana fermions in a tunable semiconductor device," *Physical Review B,* vol. 81, p. 125318, 2010.

[15] R. Lutchyn, J. Sau and S. Sarma, "Majorana Fermions and a Topological Phase Transition in Semiconductor-Superconductor Heterostructures," *Physical Review Letters,* vol. 105, p. 077001, 2010.

[16] J. Sau, S. Tewari, R. Lutchyn, T. Stanescu and S. Sarma, "Non-Abelian quantum order in spin-orbit-coupled semiconductors: Search for topological Majorana particles in solid-state systems," *Physical Review B,* vol. 82, p. 214509, 2010.

[17] M. Leijnse and K. Flensberg, "Introduction to topological superconductivity and Majorana fermions," *Semiconductor and Science Technology,* vol. 27, no. 12, 2012.

[18] V. Mourik, K. Zou, S. Frolov, S. Plissard, E. Bakkers and L. Kouwenhoven, "Signatures of Majorana Fermions in Hybrid Superconductor-Semiconductor Nanowire Devices," *Science,* vol. 336, pp. 1003-1007, 2012.

[19] H. Zhang, C.-X. Liu, S. Gazibegovic, D. Xu, J. Logan, G. Wang, J. van Loo, J. Bommer, d. M. M.W.A., D. Car, R. Op het Veld, P. van Veldhoven, S. Koeling, M. Verheijen, M. Pendharkar, D. Pennachio, B. Shojaei and J. Lee, "Quantised Majorana Conductance," *Nature,* vol. 556, pp. 74-79, 2018.

[20] H. Zhang, M. de Moor, J. Bommer, D. Xu, G. Wang *et al.* "Large zero-bias in InSb-Al hybrid semiconductor-superconductor nanowire devices," *arXiv preprint,* 2021.

[21] H. Zhang, C.-X. Liu, S. Gazibegovic, D. Xu, J. Logan, G. Wang *et al.* "Retraction: Quantized Majorana Conductance," *Nature,* no. 591, 2021.

[22] P. Brouwer, K. Ensslin, D. Goldhaber-Gordon, P. Lee, P. Kruit and R. Haverslag, "Nature paper "Quantized Majorana conductance" Report from independent experts".

[23] S. Frolov, M. Manfra and J. Sau, "Topological superconductivity in hybrid devices," *Nature Physics,* vol. 16, pp. 718-724, 2020.

[24] P. Yu, J. Chen, M. Gomanko, G. Badaway, E. Bakkers, K. Zuo, V. Mourik and S. Frolov, "Non-Majorana states yield nearly quantized conductance in proximatixed nanowires," *Nature Physics,* vol. 17, pp. 482-488, 2021.

[25] S. Gazibegovic, D. Car, H. Zhang, S. Balk, J. Logan, M. de Moor, M. Cassidy, R. Schmits, D. Xu, G. Wang, Krogstrup.P. *et al.* "Retraction Note: Epitaxy of advanced nanowire quantum devices," *Nature,* vol. 604, no. 786, 2022.

[26] G. Wang, T. Dvir, G. Mazur *et al.* "Singlet and triplet Cooper pair splitting in hybrid superconducting nanowires," *Nature,* vol. 612, pp. 448-453, 2022.

[27] T. Dvir, G. Wang, N. van Loo, C. Liu, G. Mazur, A. Bordin, S. Haaf, J. Wang, D. van Driel, F. Zateli, X. Li, F. Malinowski, S. Gazibegovic, G. Badawy, E. P. Bakkers, M. Wimmer and L. Kouwenhoven, "Realization of a minimal Kitaev chain in coupled quantum dots," *Nature,* vol. 614, no. 7948, pp. 445-450, 2023.

[28] W. Cole, J. Sau and S. Das Sarma, "Proximity effect and Majorana bound states in clean semiconductor nanowires coupled to disordered superconductors," *Physical Review B,* vol. 94, no. 14, p. 140505, 2016.

[29] T. Stanescu and S. Das Sarma, "Superconducting proximity effect in semiconductor nanowires," *Physical Review B,* vol. 87, no. 18, p. 180504, 2013.

[30] S. ten Haaf, Q. Wang, A. Bozkurt, C. Liu, I. Kulesh, P. Kim, D. Xiao, C. Thomas, M. Manfra, T. Dvir, M. Wimmer and S. Goswami, "Engineering Majorana bound states in coupled quantum dots in a two-dimensional electron gas," *Mesoscale and Nanoscale Physics,* 2023.

[31] A. Danilenko, A. PoschL, D. Sabonis, V. Vlachodimitropoulos, C. Thomas, M. Manfra and C. Marcus, "Spin spectroscopy of a hybrid superconducting nanowire using side-coupled quantum dots," *Physical Review B,* vol. 108, p. 054512, 2023.

[32] Q. Wang, S. ten Haaf, I. Kulesh, D. Xiao, C. Thomas, M. Manfra and S. Goswami, "Triplet correlations in Cooper pair splitters realized in a two-dimensional electron gas," *Nature Communications,* vol. 14, no. 4876, 2023.

[33] R. Lutchyn, E. P. Bakkers, L. Kouwenhoven, P. Krogstrup, C. Marcus and Y. Oreg, "Majorana zero modes in superconductor-semiconductor heterostructures," *Nature Reviews Materials,* vol. 3, no. 5, pp. 52-68, 2018.

[34] K. Flensberg, F. von Oppen and A. Stern, "Engineered Platforms for topological superconductivity and Majorana zero modes," *Nature Reviews Materials,* vol. 6, pp. 944-958, 2021.

[35] C. Ke, C. Moehle, F. de Vries, C. Thomas, S. Metti *et al.* "Balistic Superconductivity and tunable pi-junctions in InSb Quantum Wells," *Nature Communications,* vol. 10, no. 3764, pp. 1-6, 2019.

[36] C. Moehle, C. Ke, Q. Wang, C. Thomas, D. Xiao, S. Karwal, M. Lodari, V. van de Kerkhof, R. Termaat, G. Gardner, G. Scappucci, M. Manfra and S. Goswami, "InSbAs two-dimensional electron gases as a platform for topological superconductivity," *Nanoletters,* vol. 21, no. 23, pp. 9990-9996, 2021.

[37] G. Smith, "The characterisation of InSb quantum well heterostructures by electrical measurement," *PhD Thesis,* 2019.

[38] T. Hahn, U. Shumeli and J. Arthur, International Tables for Crystallography, Dordrechy: Reidel, 1983.

[39] N. Ashcroft and N. Mermin, Solid State Physics, Saunders College Publishing, 1976.

[40] T. Liu and E. Peretti, "The lattice parameter of InSb," *Transactions of the AIME,* 1951.

[41] C. Kittel, Introduction to Solid State Physics, John Wiley and Sons, 1953.

[42] K. Edagawa, "Photonic crystals, amorphus materials and quasicrystals," *Science and Technology of Advanced Materials,* vol. 15, no. 3, p. 034805, 2014.

[43] F. Bloch, "Uber die quantenmechanik der elektronen in kirstallgittern," *Zeitschrift fur physik,* vol. 52, no. 7, pp. 555-600, 1929.

[44] Y. Kim, K. Hummer and G. Kresse, "Accurate Band Structures and effective masses for InP, InAs, and InSb using hybrid functionals," *Physical Review B,* vol. 80, no. 3, p. 035203, July 2009.

[45] P. Drude, "Zur Elektronentheone der Mellae," *Annalen der Physik,* vol. 306, no. 3, pp. 566-613, 1900.

[46] C. McIndo, D. Hayes, A. Papageorgiou, L. Hanks, G. Smith, C. Allford, S. Zhang, E. Clarke and P. Buckle, "Determination of the transport lifetime limiting scattering rate in InSb/AlxIn1-xSb quantum wells using opitical surface micrscopy," *Physica E,* vol. 91, pp. 169-172, 2017.

[47] O. Pooley, A. Gilbertson, P. Buckle, R. Hall, M. Emeny, M. Fearn, M. Halsall, L. Cohen and T. Ashley, "Quantum well mobility and the effect of gate dielectrics in remote doped InSb/AlxIn1-xSb heterostructures," *Semiconductor Science and Technology,* vol. 25, no. 12, p. 125005, 2010.

[48] N. Goel, J. Graham, J. Keay, K. Suzki, M. Santos and Y. Hirayama, "Ballistic transport in InSb mesoscopic structures," *Physica E: Low-dimensional Systems and Nanostructures,* vol. 26, no. 1-4, pp. 455-459, 2005.

[49] B. Nedniyom, R. Nicholas, M. Emeny, L. Buckle, A. Gibertson, P. Buckle and T. Ashley, "Giant enchanced g-factors in an InSb two-dimensional gas," *Physical Review B,* vol. 80, p. 125328, 2009.

[50] L. Vegard, "Die Konstitution der Mischkristalle und die Raumfullung der Atome," *Zeitschrift fur Physik,* vol. 5, p. 1921, 1921.

[51] A. Denton and N. Ashcroft, "Vegard's law," *Physical Review A,* no. 43, p. 3161, 1991.

[52] A. Bett, F. Dimroth, G. Stollwerck and O. Sulima, "III-V compounds for solar cell applications," *Applied Physics A,* vol. 69, pp. 119-129, 1999.

[53] H. Stormer, R. Dingle, A. Gossard, W. Wiegmann and M. Sturge, "Two-dimensional electron gas at a semiconductor-semiconductor interferace," *Solid State Communications,* vol. 29, no. 10, pp. 705-709, 1979.

[54] M. Kantner, Electrically Driven Quantum Dot Based Single-Photon Sources, Springer, Cham, 2020.

[55] M. Grundmann, "Quantum Devices of Reduced Dimensionality," in *Encyclopedia of Condensed Matter Physics*, 2005, pp. 17-22.

[56] T. Mimura, "The early history of the high electron mobility transistor," *IEEE Transactions on Microwave Theory and Techniques,* vol. 50, no. 3, pp. 780-782, 2002.

[57] J. Faist, F. S. D. Capasso, C. Sirtori, A. Hutchinson and A. Cho, "Quantum Cascade Laser," *Science,* vol. 264, no. 5158, pp. 553-556, 1994.

[58] M. Vitiello, G. Scalari, B. Williams and P. De Natale, "Quantum cascade lasers: 20 years of challenges," *Optics Express,* vol. 23, no. 4, pp. 5167-5182, 2015.

[59] J.-I. Chyi, S. Kalem, N. Kumar, C. Litton and H. Morkoc, "Growth of InSb and InAs1-xSbx on GaAs by molecular beam epitaxy," *Applied Physics Letters,* vol. 53, no. 12, pp. 1092-1094, 1988.

[60] P. Caroff, M. Messing, B. Mattias Borg, K. Dick, K. Deppert and L.-E. Wernersson, "InSb heterostructure nanowires: MOVPE growth under extreme lattice mismatch," *Nanotechnology,* vol. 20, no. 49, p. 495606, 2009.

[61] N. Goel, S. Chung, M. Santos, K. Suzuki, S. Miyashita and Y. Hirayama, "Effect of temperature on ballistic transport in InSb quantum wells," *Physica E: Low-dimensional Systems and Nanostructures,* vol. 21, no. 2-4, pp. 761-764, 2004.

[62] O. Pooley, A. Gilbertson, P. Buckle, R. Hall, L. Buckle, M. Emeny, M. Fearn, L. Cohen and T. Ashley, "Transport effects in remote-doped InSb/AlxIn1-xSb heterostructures," *New Journal of Physics ,* vol. 12, p. 053022, 2010.

[63] J. Nitta, A. Tatsushi, H. Takayanagi and T. Enoki, "Gate Control of Spin-Orbit Interaction in an Inverted In_0.53Ga_0.47AsIn_0.52Al_0.48As Heterostructure," *Physical Review Letters,* vol. 78, no. 7, pp. 1335-1338, 1997.

[64] G. Dresselhaus, "Spin-Orbit Coupling Effects in Zinc Blende Structures," *Physical Review,* vol. 100, no. 2, pp. 580-586, 1955.

[65] Y. A. Bychkov and E. Rashba, "Properties of a 2D electron gas with lifted spectral degeneracy," *Journal of Eexperimental and Theoretical Physics Letters,* vol. 39, p. 78, 1984.

[66] J. Chen, K. Wu, W. Hu and J. Yang, "Spin-Orbit Coupling in 2D Semiconductors: A Theoretical Perspective," *Journal of Physical Chemistry Letters,* vol. 12, pp. 12256-12268, 2021.

[67] Y. Xing, Q. Sun and J. Wang, "Nature of spin Hall effect in a finite ballistic two-dimensional system with Rashba and Dresselhaus spin-orbit interaction," *Physical Review B,* vol. 73, p. 205339, 2006.

[68] A. Manchon, H. Koo, J. Nitta, S. Frolov and R. Duine, "New perspectives for Rashba spin-orbit coupling," *Nature Materials,* vol. 14, pp. 871-882, 2015.

[69] T. Jungwirth, J. Wunderlich and K. Olejnik, "Spin Hall effect devices," *Nature Materials,* vol. 11, pp. 382-390, 2012.

[70] F. Pulizzi, "Spintronics," *Nature Materials,* vol. 11, p. 367, 2012.

[71] P. Debray, S. Rahman, J. Wan, R. Newrock, M. Cahay, A. Ngo, S. Ulloa, S. Herbert, M. Muhammad and M. Johnson, "All-electric quantum point contact spin-polarizer," *Nature Nanotechnology,* vol. 4, pp. 759-764, 2009.

[72] J. Chen, K. Wu, W. Hu and J. Yang, "Tunable Rashba Spin Splitting in Two-Dimensional Polar Perovskites," *The Journal of Physical Chemistry Letters,* vol. 12, pp. 1932-1939, 2021.

[73] M. Schultz, F. Heinrichs, U. Merkt, T. Colin, T. Skauli and S. Lovold, "Rashba spin splitting in a gated HgTe quantum well," *Semiconductor Science and Technology,* vol. 11, no. 8, p. 1168, 1996.

[74] S. Datta and B. Das, "Electronic analog of the electro-optic modulator," *Applied Physics Letters,* vol. 56, no. 7, pp. 665-667, 1990.

[75] H. Koo, J. Kwon, J. Eom, J. Chang, S. Han and M. Johnson, "Control of Spin Precession in a Spin-Injected Field Effect Transistor," *Science,* vol. 325, no. 5947, pp. 1515-1518, 2009.

[76] G. Biswal and K. Mohanta, "A recent review on iron-based superconductor," *Materials Today: Proceedings,* vol. 35, pp. 207-215, 2021.

[77] Hirsch.J., "How Alfven's theorem explains the Meissner effect," *Physics,* 2019.

[78] H. Onnes, "Further experiments with liquid helium. d. on the change of electric resistance of pure metals at very low temperatures, etc. v. the disappearance of the resistance of mercury," *Comm. Phys. Lab. Univ. Leiden,* vol. 122b, 1911.

[79] D. Van Delft and P. Kes, "The discovery of superconductivity," *Physics Today,* vol. 63, no. 9, pp. 38-43, 2010.

[80] W. Meisneer and R. Ochensfeld, "Ein neuer Effekt bei Eintritt der Supraleitfähigkeit," *Die Naturwissenchaften,* vol. 21, no. 44, pp. 787-788, 1933.

[81] F. London and H. London, "The Electromagnetic Equations of the Supraconductor," *Proceedings of the Royal Society of London Series A, Mathermatical and Physical Sciences,* vol. 149, no. 866, pp. 71-88, 1935.

[82] V. Ginzburg and L. Landau, "On the Theory of Superconductivity," in *On Superconductivity and Superfluidity*, Springer, 2009, pp. 546-568.

[83] B. Rosenstein and D. Li, "Ginzburg-Landau theory of type II superconductors in magnetic fields," *Reviews of Modern Physics,* vol. 82, pp. 109-168, 2010.

[84] M. Tinkham, Introduction to Superconductivity second edition, New York: McGraw-Hill Inc, 2004.

[85] A. Fetter and J. Walecka, "Chapter 13, Superconductivity, Section 49, London-Pippard Phenomenological Theory," in *Quantum Theory of Many-Particle Systems*, New York, Dover Publications, 2003, pp. 420-430.

[86] A. Pippard, "Field Variation of the superconducting penetration depth," *The Royal Society Mond Laboratory,* vol. A203, no. 98, pp. 210-223, 1950.

[87] H. Kaper and H. Nordborg, "The frozen-field approximation and the Ginzburg-Landau equations of superconductivity," *Journal of Engineering Mathematics,* vol. 39, no. 1, pp. 221-240, 2001.

[88] J. Rjabinin and L. Shubnikov, "Magnetic Properties and Critical Currents of Superconducting Alloys," *Nature,* pp. 581-582, 1935.

[89] A. Abrikosov, "The magnetic properties of superconducting alloys," *Journal of Physics and Chemistry of Solids,* vol. 2, no. 3, pp. 199-208, 1957.

[90] A. Abrikosov, "Nobel Lecture: Type-II Superconductors and the vortex lattice," *Reviews of modern physics,* vol. 76, pp. 975-979, 2004.

[91] J. Bardeen, "Theory of the Miessner Effect in Superconductors," *Physical Review,* vol. 97, no. 6, pp. 1724-25, 1955.

[92] L. Cooper, "Bound Electron Pairs in a Degenerate Fermi Gas," *Physical Review,* vol. 104, no. 4, pp. 1189-1190, 1956.

[93] E. Maxwell, "Isotope Effect in the Superconductivity of Mercury," *Physical Review,* vol. 78, no. 477, p. 477, 1950.

[94] C. Reynolds, B. W. W. Serin and L. Nesbitt, "Superconductivity of Isotopes of Mercury," *Physical Review,* vol. 78, no. 4, p. 487, 1950.

[95] H. Frohlich, "Interaction of electrons with lattice vibrations," *Proceedings of the Royal Society A,* vol. 215, no. 1122, pp. 291-298, 1952.

[96] J. Bardeen, L. Cooper and J. Schrieffer, "Theory of Superconductivity," *Physical Review,* vol. 108, no. 5, pp. 1175-1204, 1957.

[97] N. Bogolijubov, "A new method in the theory of Superconductivity," *Journal of Experimental and Theoretical Physics,* vol. 34, no. 7, pp. 58-65, 1958.

[98] L. Gor'kov, "Microscopic Derivation of the Ginzburg-Landau equations in the theory of Superconductivity.," *Journal of Experimental and Theoretical Physics,* vol. 36, no. 6, pp. 1364-1267, 1959.

[99] H. Frohlich, "Theory of the Superconducting State I: The Ground State at the Absolute Zero of Temperature," *Physical Review,* vol. 79, no. 5, pp. 845-856, 1950.

[100] R. Wordenweber and J. Vanacken, Superconductors at the Nanoscale, De Gruyter, 2017, pp. 1-28.

[101] A. Andreev, "The Thermal Conductivity of the Intermediate State in Superconductors," *Journal of Experimental and Theoretical Physics,* vol. 19, no. 5, pp. 1828-1831, 1964.

[102] A. Prepelista, V. Zdravkov, E. Molchanova and A. Sidorenko, "Nonuniform Superconducting State in Superconducting/Ferromagnetic Nanoscale-Layered System," *Moldavian Journal of the Physical Sciences,* vol. 1, no. 5, pp. 71-77, 2013.

[103] B. Pannetier and H. Courtois, "Andreev Reflection and Proximity effect," *Journal of Low Temperature Physics,* vol. 118, pp. 599-615, 2000.

[104] T. Klapwijk, "Proximity Effect from an Andreev Perspective," *Journal of Superconductivity; Incorporating Novel Magnetism,* vol. 17, no. 5, pp. 593-611, 2004.

[105] C. S. Geuron, A. Chepelianskii and H. Bouchiat, "Full range of proximity effect probed with superconductor/graphene/superconductor junctions," *Physical Review B,* vol. 94, p. 115405, 2016.

[106] H. Takyanagi and T. Kawakami, "Superconducting Proximity Effect in the Native Inversion Layer on InAs," *Physical Review Letters,* vol. 54, no. 22, pp. 2449-2452, 1985.

[107] A. Kononov, V. Kostarev, B. Semyagin, V. Preobrazhenskii, M. Putyato, E. Emelyanov and E. Deviatov, "Proximity Induced Superconductivity within the

InAs/GaSb edge conducting state," *Physical Review B,* vol. 96, no. 245304, pp. 01-05, 2-17.

[108] C. Ke, C. Moehle, F. de Vries, C. Thomas, S. Metti, C. Guinn, R. Kallaher, M. Lodari, G. Scappucci, T. Wang, R. Diaz, G. Cardner, M. Manfra and S. Goswami, "Supplementary Information for: Ballistic superconductivity and tunable π-junctions in InSb quantum wells," *Nature Communications,* vol. 10, 2019.

[109] G. Blonder, T. Tinkham and M. Klapwijk, "Transition from metallic to tunneling regimes in superconducting microconstrictions: Excess current, charge imbalance and supercurrent conversison," *Physical Review B,* vol. 25, no. 7, pp. 4515-4532, 1982.

[110] M. Kjaergaard, Proximity Induced Superconducting Properties in One and Two Dimensional Semiconductors, Center for Quantum Devices: Copenhagen University, 2015.

[111] J. Demers and A. Griffin, "Scattering and Tunneling of Electronic Excitations in the Intermediate State of Superconductors," *Candadian Journal of Physics,* vol. 49, no. 3, pp. 285-295, 1971.

[112] O. Entin-Wohlman, "Effect of a barrier at the superconducting-normal metal interface," *Journal of Low Temperature Physics,* vol. 27, pp. 777-786, 1977.

[113] G. Strijkers, Y. Ji, F. Yang, C. Chien and J. Byers, "Andreev reflections at metal/superconductor point contacts: Measurement and analysis," *Physical Review B,* vol. 63, no. 10, p. 104510, 2001.

[114] M. Kupka, "Modification of the Blonder, Tinkham and Klapwijk theory of normal metal-superconductor point contact due to contact heterogeneity," *Journal of Physics: Condensed Matter,* vol. 2, no. 10, p. 10599, 1990.

[115] Y. Naidyuk, H. Lohneysen and I. Yanson, "Temperature and magnetic-field dependence of the superconducting order parameter in Zn studied by point-contact spectroscopy," *Physical Review B,* vol. 54, no. 16, p. 16077, 1996.

[116] R. Dynes, V. Narayanamurti and J. Garno, "Direct Measurement of Quasiparticle-Lifetime Broadening in a Strong-Coupled Superconductor".

[117] J. Rodrigo, N. Agrait and S. Vieira, "Conductance regimes in superconducting junctions of atomic size," *Physical Review B,* vol. 50, p. 374, 1994.

[118] H. Alpern, "Unconventional superconductivity induced in Nb films by adsorbed chiral molecules," *New Journal of Physics,* vol. 18, p. 113048, November 2016.

[119] J. Linder and A. Subdo, "Tunneling conductance in s- and d-wave superconductor-graphene junctions: Extended Blonder-Tinkham-Klapqijk formalism," *Physical Review B,* vol. 77, no. 06, p. 064507, 2008.

[120] L. Fu and C. Kane, "Superconducting Proximity Effect and Majorana Fermions at the Surface of a Topological Insulator," *Physical Review Letters,* vol. 100, pp. 1-4, 2008.

[121] C. Reeg and D. Maslov, "Proximity-induced triplet superconductivity in Rashba materials," *American Physical Society,* vol. 92, p. 124512, 2015.

[122] S. Ran, C. Eckberg, Q. Ding, Y. Furukawa, T. Metz, S. Saha, I.-L. Lio, M. Zic, H. Kim and N. Butch, "Nearly ferromagnetic spin-triplet superconductivity," *Science,* vol. 365, no. 6454, pp. 684-687, 2019.

[123] F. Bergeret, A. Volkov and K. Efetov, "Odd triplet superconductivity and related phenomena in supercondutor-ferromagnet structures," *Reviews of Modern Physics,* vol. 77, no. 4, pp. 1321-1373, 2005.

[124] L. Gor'kov and E. Rashba, "Superconducting 2D System with Lifted Spin Degeneracy: Mixed Singlet-Triplet State," *Physical Review Letters,* vol. 87, no. 3, p. 037004, 2001.

[125] V. Edelstein, "Characterisistics of the Cooper pairing in two-dimensional noncentrosymmetric electron systems," *Zh. Eksp. Teor. Fiz,* vol. 95, pp. 2151-2162, 1989.

[126] K. Zuo and V. Mourik, "Signatures of Majorana Fermions in Hybrid Superconductor-Semiconductor Nanowire Devices," *PhD Thesis,* 2016.

[127] J. Xia, V. Shelukhin, M. Karpovski *et al.* "Inverse proximity effect in superconductor-ferromagnetic bilayer structures," *Physical Review Letters,* vol. 102, no. 08, p. 087004, 2009.

[128] A. Di Bernardo, Z. Salman, X. L. Wang, M. Armado, M. Egilmez, M. Flokstra, A. Suter, S. Lee, J. Zhao, T. Prokscha, E. Morenzoni, M. Blamire and J. Robinson, "Instrinsic Paramagnetic Meissner Effect Due to s-Wave Odd-Frequency Superconductivity.," *Physical Review X,* vol. 5, no. 4, p. 041021, 2015.

[129] V. Arole and S. Munde, "FABRICATION OF NANOMATERIALS BY TOP-DOWN AND BOTTOM UP APPROACHES - AN OVERVIEW," *Journal of Advances in Applied Sciences and Technology: Material Science,* vol. 1, no. 2, pp. 89-93, 2014.

[130] R. Hobbs, N. Petkov and J. Holmes, "Semiconductor Nanowire Fabrication by Bottom-Up and top-Down Paradigms," *Chemical Materials,* vol. 24, no. 11, pp. 1975-1991, 2012.

[131] S. George, "Atomic Layer Deposition: An Overview," *Chemical Review,* vol. 110, no. 1, pp. 111-131, 2010.

[132] A. Cho and J. Arthur, "Molecular beam epitaxy," *Progress in Solid State Chemistry,* vol. 10, no. 3, pp. 157-191, 1975.

[133] C. Thelander, P. Caroff, S. Plissard and K. Dick, "Electrical properties of InAs1-xSb and Insb nanowires grown by molecular beam epitaxty," *Applied Physics Letters,* vol. 100, no. 23, p. 232105, 2012.

[134] Z. Lei, C. Lehner, E. Cheah, M. Karalic, C. Mittag, L. Alt, J. Schametzky, W. Wegscheider, T. Ihn and K. Ensslin, "Quantum transport in high-quality shallow InSb quantum wells," *Applied Physics Leters,* vol. 115, no. 1, p. 012101, 2019.

[135] F. Jabeen, S. Rubini and F. Martelli, "Growth of III-V semiconductor nanowires by molecular beam epitaxy," *Microelectronics Journal,* vol. 40, no. 3, pp. 442-445, 2009.

[136] R. Shyu, H. Yang, W.-R. Tsai and J.-C. Tsai, "Micro-ball lens array fabrciation in photoresist using PTFE hydrophobic effect," *Microsystem Technologies,* vol. 13, pp. 1601-1606, 2007.

[137] C. McIndo, "Transport Effects in InSb Quantum Well Heterostructures," *PhD Thesis,* 2019.

[138] T. Chao, Introduction to semiconductor manufacturing technology, Spie Press, 2001.

[139] J. Shaw, J. Gerlorme, N. LaBianca, W. Conley and S. Holmes, "Negative photoresists for optical lithography," *IBM Journal of Research and Development ,* vol. 41, no. 1.2, pp. 81-94, 1997.

[140] F. Dill, "Optical Lithography," *IEEE Transactions on Electrical Devices,* vol. 22, no. 7, pp. 440-444, 1975.

[141] H. Lee and J.-B. Yoon, "A simple and effective lift-off with positive photoresist," *Journal of Micromechanics and Microengineering,* vol. 15, no. 11, p. 2136, 2005.

[142] W.-M. Yeh, D. Noga, R. Lawson, L. Tolbert and C. Henderson, "Comparison of positive tone vs negative tone resist pattern collapse behavoir," *Journal of Vacuum Science & Technology B,* vol. 28, no. 6, pp. 6-11, 2010.

[143] M. Kelso, N. Mahenderkar, O. Chen, J. Tubbesing and J. Switzer, "Spin coating epitaxial films," *Science,* vol. 364, no. 6436, pp. 166-169, 2019.

[144] V. Chaplick, E. Degenkolb, D. Elliot *et al.* "Analysis of photoresist edge bead removal using laster light and gas," *Optical Microlithography XXIII,* vol. 7640, 2010.

[145] D. Widmann, "Metallization for intergrated circuits using a lift-off technique," *IEEE Journal of Solid-State Circuits,* vol. 11, no. 4, pp. 466-471, 1976.

[146] W.-M. Yeh, R. Lawson, L. Tolbert and C. Henderson, "A study of reactive adhesion promoters and their ability to mitigate pattern collapse in thin film lithography," in *Advances in Resist Materials and Processing Technology XXVIII*, San Jose, California, 2011.

[147] X. Hu, "Photolithography technology in electronic fabrication," in *2015 International Power, Electronics and Materials Engineering Conference*, Atlantis Press, 2015.

[148] M. Rothschild, "Photolithography at wavelengths below 200nm," in *Conference on Lasers and Electro-Optics*, San Fransisco, 1998.

[149] C. Gwyn, R. Stulen, D. Sweeney and D. Attwood, "Extreme ultraviolet lithography," *Journal of Vacuum Science & Technology B: Microelectronics and Nanometer Structures Processing, Measurement, and Phenomena,* vol. 16, pp. 3142-3149, 1998.

[150] D. Qin, Y. Xia, A. Black and G. Whitesides, "Photolithography with transparent reflective photomasks," *Journal of Vacuum Sciences & Technology B: Microelectronics and Nanometer Structures Processing,* vol. 16, pp. 98-103, 1998.

[151] J. Ruhe, "And There Was Light: Prospects for the Creation of Micro- and Nanostructures through Maskless Photolithography," *ACS Nano,* vol. 11, no. 9, pp. 8537-8541, 2017.

[152] R. Seisyan, "Nanolithography in microelectronics: A review," *Technical Physics,* vol. 56, pp. 1061-1073, 2011.

[153] M. Walsh, F. Zhang, R. Menon and H. Smith, "Maskless Photolithography," in *The Art of Fabricating Nanoelectronic and Nanophotonic Devices and Systems*, Woodhead Publishing, 2014, pp. 179-193.

[154] H. Huang, Z. Ren, C. Chan and X. Li, "Wet etch, dry etch and MacEtch of B-Ga_2O_3: A review of characteristics and mechanism," *Journal of Materials Research,* vol. 36, pp. 4756-4770, 2021.

[155] B. Balakrisnan, S. Paril and E. Smela, "Patterning PDMS using a combination of wet and dry etching," *Journal of Micromechanics and Microengineering,* vol. 19, no. 4, p. 047002, 2009.

[156] O. Cakir, "Review of etchants for copper and its alloys in wet etching processes," *Key Engineering Materials,* vol. 364, pp. 460-465, 2008.

[157] H.-C. Huang, Z. Ren, C. Chan and X. Li, "Wet etch, dry etch, and MacEtch of β-Ga2O3: A review of characteristics and mechanisms," *Journal of Materials Research,* vol. 36, pp. 4756-4770, 2021.

[158] N. Carlsson, N. Ikeda, Y. Sugimoto, K. Asakawa, T. Takemori, Y. Katayama, N. Kawai and K. Inoue, "Design, nano-fabrication and analysis of near-infrared 2D photonic crystal air-bridge structures," *Optical and Quantum Electronics,* vol. 34, pp. 123-131, 2002.

[159] K. Hjort, "Sacrificial etching of III-V compounds for micromechanical devices," *Journal of Micromechanics and Microengineering ,* vol. 6, no. 4, p. 370, 1996.

[160] K.-M. Chang, J.-J. Luo, C.-D. Chiang and K.-C. Liu, "Wet Etching Characterization of InSb for Thermal Imaging Applications," *Japanese Journal of Applied Physics,* vol. 45, no. 3R, p. 1477, 2006.

[161] T. Ashley, L. Buckle, S. Datta *et al.* "Heterogeneous InSb quantum well transistors on silicon for ulta-high speed low power logic applications," *Electronics Letters,* vol. 43, no. 14, pp. 777-779, 2007.

[162] S. Jubair, "Technology development for nanoscale InSb quantun split-gate structures," *PhD Thesis,* 2019.

[163] A. Dehzangi, J. Li, L. Gautam and M. Razeghi, "Avalanche Photodetector Based on InAs/InSb Superlattice," *Quantum Reports,* vol. 2, no. 4, pp. 591-599, 2020.

[164] R. Powell, "Dry etching for microelectronics," Elsevier, 2012.

[165] K. Nojiri, Dry Etching Technology for Semiconductors, Springer Chem, 2014.

[166] G. Oerhlein, "Reactive-Ion Etching," *Physics Today,* vol. 39, no. 10, pp. 26-33, 1986.

[167] M. Huff, "Recent Advances in Reactive Ion Etching and Applications of High-Aspect Ratio Microfabrication," *Micromachines,* vol. 12, no. 8, p. 991, 2021.

[168] K. Racka-Szmidt, B. Stonio, J. Zelazko, M. Filipiak and M. Sochacki, "A Review: Inductively Coupled Plasma Reactive Ion Etching of Silicon Cardbide," *Materials,* vol. 15, no. 1, p. 123, 2022.

[169] C. Welch, D. I Olynick, Z. Liu *et al.* "Formation of nanoscale structures by inductively coupled plasma etching," in *International Conference on Micro- and Nano- Electronics*, Zwenigorod, 2012.

[170] F. Karouta, "A practical approach to reactive ion etching," *Journal of Physics D: Applied Physics,* vol. 47, no. 23, p. 233501, 2014.

[171] S. Pearton, R. Shul and F. Ren, "A Review of Dry Etching of GaN and Related Materials," *Materials Research Society Internet Journal of Nitride Semiconductor Research,* vol. 5, no. 1, p. e11, 2000.

[172] S. Rohde, "Sputter Deposition," in *Surface Engineering*, 1994.

[173] W. Westwood, "Sputter Deposition Processes," *MRS Bulletin,* vol. 13, no. 1988, pp. 46-51, 2013.

[174] O. Abegunde, E. Akinlabi, O. Oladijo, S. Akinlabi and A. Ude, "Overview of the thin film deposition techniques," *Materials Science,* vol. 6, no. 2, pp. 174-199, 2019.

[175] K. Seshan, D. Schepis *et al.* Handbook of Thin Film Deposition, Fourth Edition, Elsevier Inc, 2018.

[176] S. Rossnagel, "Sputter deposition for semiconductor manufacturing," *IBM Journal of Research and Development,* vol. 43, no. 1, pp. 163-179, 1999.

[177] P. Kelly and R. Arnell, "Magnetron sputtering: a review of recent developments and applications," *Vacuum,* vol. 56, pp. 159-172, 2000.

[178] "Facility For Radioactive Materials Surfaces," [Online]. Available: https://nnuf-farms.bristol.ac.uk/about/.

[179] Y. Chen, D. van Driel, C. Lampadaris, S. Khan, K. Alattallah, L. Zeng, E. Olsson, T. Dvir, P. Krogstrup and Y. Liu, "Gate-tunable superconductivity in hybrid InSb-Pb nanowires," *Applied Physics Letters,* vol. 8, p. 123, 2023.

[180] C. Thompson, "Solid-State Dewetting of Thin Films," *Annual Review of Materials Research,* vol. 42, pp. 399-434, 2012.

[181] L. van der Pauw, "A method of measuring specific resistivity and hall effect of discs of arbitrary shape," *Philips Research Reports,* vol. 13, no. 1, pp. 1-9, 1958.

[182] F. Oliveira, R. Cipriano, F. da SIlva, E. Romao and C. dos Santos, "Simple analytical method for determining electrical resistivity and sheet resistance using the can der Pauw procedure," *Scientific Reports,* vol. 10, no. 1, p. 16379, 2020.

[183] R. Op het Veld, D. Xu, V. Schaller, M. Verheijen, S. Peters *et al.* "In-plane selective area InSb-Al nanowire quantum networks," *Communications Physics,* vol. 3, no. 59, 2020.

[184] P. Aseev, G. Wang, L. Binci, A. Singh, S. Marti-Sanchez, M. Botifoll, L. Stek, A. Bordin, J. Watson, F. Boekhout, D. Abel, J. Gamble, K. Van Hoogdalem, J.

Arbiol, L. Kouwenhoven, G. de Lange and P. Caroff, "Ballistic InSb Nanowires and Networks via Metal-Sown Selective Area Growth," *Nano Letters,* vol. 19, no. 12, pp. 9102-9111, 2019.

[185] Z. Lei, C. Lehner, E. Cheah, C. Mittag, M. Karalic, W. Wegscheider, K. Ensslin and T. Ihn, "Gate-defined quantum point contact in an InSb two-dimensional electron gas," *Physical Review Research,* vol. 3, no. 2, p. 023042, 2021.

[186] A. Poschol, A. Danilenko, D. Sabonis, K. Kristjuhan, T. Lindemann, C. Thomas, M. Manfra and C. Marcus, "Nonlocal conductance spectroscopy of Andreev bound states in gate-defined InAs/Al nanowires," *Physical Review B,* vol. 106, p. L241301, 2022.

[187] H. Berger, "Model for contacts to planar devices," *Solid-State Electronics,* vol. 15, pp. 145-158, 1972.

[188] S. Guo, G. Gregory, A. Gabor, V. Schoenfeld and K. Davis, "Detailed investigation of TLM contact resistance measurements on crystalline silicon solar cells," *Solar Energy,* vol. 151, pp. 163-172, 2017.

[189] L. Mak, C. Rogers and D. Northrop, "Specific contact resistance measurements on semiconductors," *Journal of Physics E: Scientific Instruments,* vol. 22, no. 5, p. 317, 1989.

[190] M. Lijadi, F. Pardo, N. Bardou and J.-L. Pelouard, "Floating contact transmission line modelling: An improved method for ohmic contact resistance measurement," *Solid-State Electronics,* vol. 49, no. 10, pp. 1655-1661, 2005.

[191] H. Berger, "Contact resistance and contact resistivity," *Journal of Electrochemical Society,* vol. 119, pp. 507-514, 1972.

[192] C. Nguyen, H. Kroemer and E. Hu, "Contact resistance of superconductor-semiconductor interfaces: The case of Nb-InAs/AlSb quantum-well structures," *Applied Physics Letters,* vol. 65, no. 1, pp. 103-105, 1994.

[193] J. Hrostowski, F. Morin, T. Geballe and G. Wheatley, "Hall Effect and Conductivity of InSb," *Physical Review,* vol. 100, no. 6, pp. 1672-1676, 1955.

[194] D. Haynes, C. Alford, G. Smith, C. McIndo, L. Hanks, A. Gilbertson, L. Cohen, S. Zhang, E. Clarke and P. Buckle, "Electron transport lifetimes in InSb/Al(1-x)In(x)Sb quantum well 2DEGS," *Semiconductor Science and Technology,* vol. 32, no. 085002, 2017.

[195] C. McIndo, D. Hayes, A. Papageorgiou, L. Hanks, G. Smith, C. Alford, S. Zhang, E. Clarke and P. Buckle, "Determination of the transport lifetime limiting scattering rate in InSb/Al(x)In(1-x)Sb quantum wells using optical surface microscopy," *Physica E,* vol. 91, pp. 169-172, 2017.

[196] P. Krogstrup, N. Ziino, W. Chang, S. Albrecht, M. Madsen, E. Johnson, J. Nygard, C. Marcus and T. Jespersen, "Epitaxy of semiconductor-superconductor nanowires," *Nature Materials,* vol. 14, pp. 400-406, 2015.

[197] A. Fornieri, A. Whiticar *et al.* "Evidence of topological superconductivity in planar Josephson junctions," *Nature,* vol. 559, pp. 89-92, 2019.

[198] T. Kanne, M. Marnauza, D. Olsteins, D. Carrad, J. Sestoft, J. de Bruikckere, L. Zeng, E. Johnson, E. Olsson, K. Grover-Rasmussen and J. Nygard, "Epitaxial Pb on InAs nanowires for quantum devices," *Nature Nanotechnology,* vol. 16, pp. 776-781, 2021.

[199] M. Z. B. Pendharkar, H. Wu, A. Zarassi, P. Zhang, C. Dempsey, J. Lee, S. Harrington, G. Badway, S. Gazibegovic, J. Jung, A. Chen, M. Verheijen, M. Hocevar, E. Bakkers, C. Palmstrom and S. Frolov, "Parity-preserving and magnetic field resilient superconductivity in indium antimonide nanowires with tin shells," *Mesoscale and Nanoscale Physics,* 2019.

[200] J. Cochran and D. Mapother, "Superconducting Transition in Aluminium," *Physical Review ,* vol. 111, p. 132, 1958.

[201] F. Boscherini, Y. Shapira, C. Capasso, C. Aldao, M. del Giudice and J. Weaver, "Exchange reaction, clustering and surface segragation at the Al/InSb(110) interface," *Physical Review B,* vol. 35, no. 18, pp. 9580-9585, 1987.

[202] C. Thomas, R. Diaz, J. Dycus, M. Salmon, R. Daniel, T. Wang, G. Gardner and M. Manfra, "Towards durable Al-InSb hybrid heterostructures via epitaxy of 2ML interfacial InAs screening layers," *Physical Review Materials,* vol. 3, no. 12, p. 124202, 2019.

[203] Gottscho.T, C. Jurgensen and D. Vitkavage, "Microscopic uniformity in plasma etching," *Journal of Vacuum Science and Technology,* 1992.

[204] Y. Lee and Z. Zhou, "Feature-Size Dependence of Etch Rate in Reactive Ion Etching," *Journal of the Electrochemical Society,* vol. 138, no. 8, p. 2439, 1991.

[205] V. Donnelly and A. Komblit, "Plasma etching: Yesterday, today and tomorrow," *Journal of Vacuum Scoemce amd Tecjmp;pgy,* vol. 31, p. 050825, 2013.

[206] M. Doemling, N. Ruger and G. Oehlein, "Observation of inverse reactive ion etching lag for silicon dioxide etching in inductively coupled plasmas," *Applied Physics Letters,* vol. 68, no. 10, pp. 10-12, 2996.

[207] T. Foxe, B. Hunt, C. Rogers, A. Kleinsasser and R. Burhrman, "Reactive ion etching of niobium," *Journal of Vacuum Science and Technology,* vol. 19, pp. 1394-11397, 1981.

[208] J. Sasserath, "Dry etching of niobium using CCl2F2 and CF4: A comparison," *Journal of Applied Physics,* vol. 68, no. 10, pp. 5324-5328, 1990.

[209] F. Herman and R. Hlubina, "Microscopic interpretation of the Dynes forumla for the tunneling of density of states," *Physical Review B,* vol. 94, no. 14, p. 144508, 2016.

[210] P. Szabo, T. Samuely, V. Haskova, J. Kacmarcik, M. Zemlicka, M. Grajcar, J. Rodrigo and P. Samuely, "Fermionic scenario for the destruction of superconductivity in ultrathin MoC films evidences by STM measurements," *Physical Review B,* vol. 93, p. 014505, 2016.

[211] M. Kuzmiak, M. Kopcik, F. Kosuth, V. Vano, P. Szabo, V. Latyshev, V. Komanicky and P. Samuely, "Supressed Superconductivity in Ultrathin Mo2N Films due to Pair Breaking at the Interface," *Journal of Superconductivity and Novel Magnetism,* vol. 35, pp. 1775-1780, 2022.

[212] W. Ko, J. Lado and P. Maksymvych, "Noncontact Andreev Reflection as a Direct Probe of Superconductivity on the Atomic Scale," *Nano Letters,* vol. 22, pp. 4042-4048, 2022.

[213] H. Boschker, E. Fillis-Tsirakis, C. Richter, D. Zhang, J. Smet and L. Kuerten, "Mircroscopic origin of the Dynes parameter Gamma of the LaAlO3-SrTiO3 supercondeuctor," *Physical Review B,* vol. 102, p. 134506, 2020.

[214] H. Kim, Y. Choi, C. Lewandowski, A. Thomson, Y. Zhang, R. Polski, K. Watanabe, T. Tanguichi, J. Alicea and S. Nadj-Perge, "Evidence for unconventional superconductivity in twisted trilayer graphene," *Nature,* vol. 606, 2022.

[215] E. Lechner, B. Dev Oli, J. Makita, G. Ciovati, A. Gurevich and M. Iavarone, "Electron Tunneling and X-Ray Photoelectron Spectroscopy Studies of the Superconducting Properties of Nitrogen-Doped Niobium Resonator Cavities," *Physical Review Applied,* vol. 13, p. 044044, 2020.

[216] G. S., H. Pothier, N. Birge, D. Esteve and M. Devoret, "Superconducting Proximity Effect Probed on a Mesocopic Length Scale," *Physical Review Letters,* vol. 77, no. 14, pp. 3025-3028, 1996.

[217] A. Stepniak, M. Caminale, A. Leon Vanegas *et al.* "Temperature depedance of the superconducting proximity effect quantified by scanning tunneling spectroscopy," *AIP Advances,* vol. 5, no. 017125, 2015.

[218] J. Clarke, "THE PROXIMITY EFFECT BETWEEN SUPERCONDUCTING AND NORMAL METALS IN ZERO FIELD," *Journal de Physique Colloques,* vol. 29, no. C2, pp. C2-3 - C2-16, 1968.

[219] B. Pannetier and H. Courtois, "Andreev Reflection and Proximity effect," *Journal of Low Temperature Physics,* vol. 118, no. 5, pp. 599-615, 2000.

[220] M. Klapwijk, "Proximity Effect From an Adreev Perspective," *Journal of Superconductivity: Incorporating Novel Magnetism,* vol. 17, no. 5, pp. 593-611, 2004.

[221] S. Bouscher, D. Panna, K. Balasubramanian, S. Cohen, D. Ritter and A. Hayat, "Enchanced Cooper-Pair Injection into a Semiconductor Structure by Resonant Tunneling," *Physical Review Letters,* vol. 128, p. 127701, 2022.

[222] S. Bouscher, R. Winik and A. Hayat, "Andreev reflection enhancement in semiconductor-superconductor structures," *Physical Review B,* vol. 97, no. 05, p. 054512, 2018.

[223] C. Tsuei, W. Johnson, R. Laibowitz and J. Viggiano, "The ratio of energy gap to transition temperature in amorphous superconductors," *Solid State Communications,* vol. 24, no. 9, pp. 615-618, 1977.

[224] R. Hung, "Surface Study of Anodized Indium Antimonide," *Journal of Applied Physics,* vol. 41, no. 5, p. 2185, 1969.

[225] T. Manago, S. Ishida, H. Geka and I. Shibasaki, "Interfacial trap states and improvement of low-temperature mobility by doping in InSb/AlInsb quantum wells," *Journal of Applied Physics,* vol. 117, no. 6, p. 065701, 2015.

[226] Y. Shapira and J. Bregman, "Origin and effects of interface traps in anodic native oxides on InSb," *Applied Physics Letters,* vol. 47, no. 5, p. 495, 1985.

[227] O. Vavasour, "Dielectrics for Narrow Bandgap III-V Devices," *PhD Thesis,* 2018.

[228] V. Ardakani, "Localization phenomena in InAs/GaAs Composite Quantum Wells with Disorder," *PhD Thesis,* 2019.

[229] S. Kim, H. Yoo and J. Choi, "Effects of Charge Traps on Hysteresis in Organic Field-Effect Transistors and Their Charge Trap Cause Analysis through Causal Inference Techniques," *Sensors,* vol. 23, no. 4, p. 2265, 2023.

[230] M. M. Uddin, H. Liu, K. Yang and K. Nagase, "Gate depletion of an InSb two-dimensional electron gas," *Applied Physics Letters,* vol. 103, no. 12, 2013.

[231] A. D. Hillier, S. J. Blundell *et al*. "Muon spin spectroscopy," *Nature Reviews Methods Primers,* vol. 2, no. 4, 2022.

[232] A. Schenck, Muon spin rotation spectroscopy: Principles and applications in solid state physics, 1985.

[233] A. Yaounac and P. de Reotier, Muon Spin Rotation, Relaxation and Resonance: Applications to Condensed Matter, Oxford Univwrsity Press, 2011.

[234] C. Anderson and S. Neddermeyer, "Cloud Champer Observation of Cosmic Rays at 4300 Meters Elevation and Near Sea-Level," *The Physical Review,* vol. 50, no. 4, pp. 263-271, 1936.

[235] R. Garwin, L. Lederman and M. Weinrich, "Observations of the Failure of Conservation of Parity and Charge Conjugation in Meson Decays: the Magnetic Moment of the Free Muon," *Physical Review,* vol. 105, no. 4, pp. 1415-1417, 1957.

[236] J. Sens, "Capture of Negative Muons," *Physical Review,* vol. 113, no. 2, p. 679, 1959.

[237] A. Hillier, D. Paul and K. Ishida, "Probing beneath the surface without a scratch — Bulk non-destructive elemental analysis using negative muons," *Microchemical Journal,* vol. 125, pp. 203-207, 2016.

[238] J. Sugiyama, I. Umegaki, H. Nozaki, W. Higemoto, K. Hamada, S. Takeshita, A. Koda, K. Shimomura, K. Ninomiya and M. Kenya Kubo, "Nuclear Magnetic Field in Solids Detected with Negative-Muon Spin," *Physical Review Letters,* vol. 121, p. 087202, 2018.

[239] T. Yamazaki, K. Nagamine, S. Nagamiya, O. Hashimoto, K. Sugimoto, K. Nakai and S. Kobayashi, "Negative Muon Spin Rotation," *Physica Scripta,* vol. 11, no. 133, 1975.

[240] I. Kazuki, K. Ohishi, T. Nakano, S. Nishimura, S. Takeshita, A. Koda, K. Ninomiya, M. Kenya Kubo and J. Sugiyama, "Negative Muon Spin Rotation and Relaxation Study on Battery Anode Material, Spinel Li4Ti5O12," *Journal of Physical Chemistry,* vol. 126, no. 25, p. 10506–10514, 2022.

[241] C. Wu, E. Ambier, R. Hayward, D. Hoppes and R. Hudson, "Experimental Test of Parity Conservation in Beta Decay," *Physical Review Latters,* vol. 105, no. 4, pp. 1413-1415, 1957.

[242] S. Blundell, "Spin-polarised muons in condensed matter physics," *Contempary Physics,* vol. 40, pp. 175-192, 1999.

[243] D. Groom, N. Mokhov and S. Striganov, "MUON STOPPING POWER AND RANGE TABLES," *Atomic Data and Nuclear Data Tables,* vol. 76, no. 2, 2001.

[244] A. Stoneham, "Kinetics and dynamics of muon localisation and trapping," *Hyperfine Interactions,* vol. 17, pp. 53-62, 1984.

[245] J. Budnick, A. Golnik, C. Niedermayer, E. Recknagel, M. Rossmanith, A. Weidinger, B. Chamberland, M. Filipowski and D. Yang, "Observation of magnetic ordering in La2CuO4 by muon spin rotation spectroscopy," *Physics Letters A,* vol. 124, no. 1-2, pp. 103-106, 1987.

[246] E. Kenny, B. Ortiz, C. Wang, S. Wilson and M. Graf, "Absence of local moments in the kagome metal KV3Sb5 as determined by muon spin spectroscopy," *Journal of Physics: Condensed Matter,* vol. 33, no. 23, p. 235801, 2021.

[247] M. Rutherford, "Weak transverse field uSR measurements as an experimental probe of magnetic materials," University of British Columbia , 2021.

[248] R. Johnson, B. Malkin, J. Lord, S. Giblin, A. Amato, C. Baines, A. Lascialfari, B. Babara and M. Graf, "Evolution of spin relaxation processes in LiY(1-x)HoxF4 studied via ac-susceptibility and muon spin relaxation," *Physical Review B,* vol. 88, no. 1, 2012.

[249] S. Lee, W. Lee, K. Lee, B. Kim, B. Suh, H. Zhang, J. Mitchell and K.-Y. Choi, "Muon spin relaxation study of spin dynamics in the extended kagome system YBaCo(4o7+d (d=0,0.1),)" *Physical Review B,* vol. 50, no. 20, 2018.

[250] F. Pratt, T. Sasaki, N. Toyota and K. Nagamine, "Zero Field Muon Spin Relaxation Study of the Low Temperature State in a-(BEDT-TTF)2KHg(SCN)4," *Physical Review Letters,* vol. 74, no. 19, 1995.

[251] R. Hayano, Y. Uemura, J. Imazato, N. Nishida, T. Yamazaki and R. Kubo, "Zero-and low-field spin relaxation studied by positive muons," *Physical Review B,* vol. 20, no. 3, 1979.

[252] H. Saadoui, Z. Salman, T. Prokscha, A. Suter, B. Wojek and E. Morenzoni, "Zero-field spin depolarization of low-energy muons in ferromagnetic," *Physics Procedia,* vol. 30, pp. 164-167, 2012.

[253] S. Blundell, R. De Renzi, T. Lancaster and F. Pratt, "Polarization functions," in *Muon Spectroscopy: An Introduction*, Oxford Academic Press, 2021, pp. 54-68.

[254] T. Junginger, S. Calatroni, A. Sublet, G. Terenziani, T. Prokscha, Z. Salman, A. Suter, T. Proslier and J. Zasadzinski, "A low energy muon spin rotation and point contact tunneling study of niobium films prepared for superconducting cavities," *Superconductor Science and Technology,* vol. 30, no. 12, p. 125013, 2017.

[255] J. Willwater, D. Eppers, T. Kimmel, E. Sadrollahi, F. Litterst, F. Grosche, C. Baines and S. Sullow, "Muon spin rotation and relaxation study on Nb1−yFe2+y," *Physical Review B,* 2022.

[256] A. Grassellino, C. Beard, C. Beard, P. Kolb, R. Laxdal, N. Lockyer, D. Longuevergne and J. Sonier, "Muon spin rotation studies of niobium for superconducting rf applications," *Physical Review Special Topics - Accelerators and Beams,* vol. 16, no. 062002, 2013.

[257] T. Junginger, S. Calatroni, T. Proschka, T. Proslier, Z. Salman, A. Suter, G. Terenziani and Zasadzinski, "Low Energy Muon Spin Rotation and Point Contact Tunneling Applied to Niobium Films for SRF Cavities," in *International Conference on RF Superconductivity*, 2015.

[258] J. A. Krieger, A. Pertsova, S. R. Giblin, M. Döbeli, T. Prokscha, C. W. Schneider, A. Suter, T. Hesjedal, A. V. Balatsky and Z. Salman, "Proximity-Induced Odd-Frequency Superconductivity in a Topological Insulator," *Physical Review Letters,* vol. 125, no. 2, July 2020.

[259] P. Joy and S. Date, "Comparison of the zero-field-cooled magnetization behavoir of some ferromagnetic and ferrimagnetic systems," *Journal of Magnetism and Magnetic Materials,* vol. 218, no. 2-3, pp. 229-237, 2000.

[260] D. Bono, A. Schnepf, J. S. H. Hartig, G. Nieuwenhuys, A. Amato and L. de Jongh, "Muon Spin Relaxation Studies of Superconductivity in a Crystalline Array of Weakly Coupled Metal Nanoparticles," *Physical Review Letters,* vol. 97, p. 077601, 2006.

[261] J. Fowlie, M. Hadjimichael, M. Martins, D. Li, M. Osada, B. Yang Wang, K. Lee, Y. Lee, Z. Salman *et al.* "Intrinsic magnetism in superconducting infinite-layer nickelates," *Nature Physics,* no. 18, p. 1043–1047, 2022.

[262] J. Sonier, R. Kiefl, J. Brewer, J. Chakhalian, S. Dunsiger, W. MacFarlane, R. Miller *et al.* "Muon-Spin Rotation Measurements of the Magnetic Field Dependence of the Vortex-Core Radius and Magnetic Penetration Depth in NbSe2," *Physical Review Letters,* vol. 79, no. 9, pp. 1742-1745, 1997.

[263] J. Sonier, J. Brewer and R. Kiefl, "mSR studies of the vortex state in type-II superconductors," *Reviews of Modern Physics,* vol. 72, no. 3, July 2000.

[264] T. Williams, A. Aczel, E. Baggio-Saitovitch, S. Bud'Ko, P. Canfield *et al.* "Muon spin rotation measurement of the magnetic field penetration depth in Ba(Fe0.926Co0.074)2As2:," *Physical Review B,* vol. 80, no. 9, p. 4501, 2009.

[265] D. MacLaughlin, J. Sonier, R. H. Heffner *et al.* "Muon Spin relaxation and isotropic pairing in superconducting PrOs4Sb12," *Physical Review Letters,* November 2002.

[266] R. Khasanov, P. Klamut, A. Shengelaya, Z. Bukowski, I. Savic, C. Baines and H. Keller, "Muon-spin rotation measurements of the penetration depth of the Mo3Sb7 superconductor," *Physical Review B,* vol. 78, 2008.

[267] Z. Zhu, C. Tan, T. Zhang, P. Biswas, A. Hillier, M. Wang, Y. Yang, C. Chen, Z. Sing, S. Li and L. Shu, "Muon spin rotation and relaxation study on topological non centresymmetric superconductor PbTaSe2," *New Journal of Physics,* vol. 24, no. 023002, 2022.

[268] A. Hillier and R. and Cywinski, "The classification of superconductors using muon spin rotation," *Applied Magnetic Resonance,* vol. 13, pp. 95-109, 1997.

[269] D. Adroja, A. Bhattaharyya, M. Smidman, A. Hillier *et al.* "Nodal Superconducting Gap Structure in the Quasi-One-Dimensional Cs2Cr3As3 Investigated Using uSR measurements," *Journal of the Physical Society of Japan,* vol. 86, p. 044710, 2017.

[270] B. Mushlschlegel, "Die thermodynamischen Funktionen des Supraleiters," *Zeitschrift fur Physik ,* vol. 155, pp. 313-327, 1959.

[271] J. Annett, N. Goldenfeld and S. Renn, "Interpretation of the temperature dependence of the electromagnetic penetration depth in YBa~Cu3O," *Physical Review B,* vol. 43, no. 4, 1991.

[272] A. Simoes, H. Alberto, R. Vilao, J. Gil, J. Cunha, M. Curado, P. Salome, T. Prokscha, A. Suter and Z. Salman, "Muon implantation experiments in films: Obtaining depth resolved information," *Review of Scientific Instruments,* vol. 91, no. 02, p. 023906, 2020.

[273] M. Flokstra, S. Ray, S. Lister, J. Aarts *et al.* "Measurement of the spatial extent of inverse proximity in a Py/Nb/Py superconducting trilayer using low-energy muon-spin rotation," *Physical Review B,* vol. 89, no. 5, p. 054510, 2014.

[274] S.-P. Lee, R. M. Lutchyn and J. Maciejko, "Odd-frequency superconductivity in a nanowire coupled to Majorana zero modes," *Physical Review B,* vol. 95, 2017.

[275] D. Herlach, K.-P. Doring, N. Haas, K. Furderer, M. Gladisch *et al.* "Muon Spin Relaxation Study of Defect Reactions in Electron-Irradiated Nb, Ta and Al," *Materials Science Forum,* Vols. 15-18, pp. 71-80, 1987.

[276] V. Storchek, D. Eshchenko, J. Brewer, B. Aronzon, S. Cottrel, R. Lichti, A. Savici and Y. Uemura, "Deep muonium state in InSb: Recomination center vs trapping centre," *Physica B,* pp. 387-389, 2006.

[277] S. Gheldi, T. Buck, M. Dehn, L. R. Kiefl, G. Morris and T. Junginger, "Muon Spin Rotation on Treated Nb Samples in Parallel Field Geometry," *Proceedings of SRF2015,* 2015.

[278] A. Romanenko, A. Grassellino, F. Barkov, A. Suter, Z. Salman and T. Prokscha, "Strong Meissner screening change in superconducting radio frequency cavities due to mild baking," *Applied Physics Letters,* vol. 104, no. 07, 2014.

[279] P. T., E. Morenzoni, K. Deiters, F. Foroughi, D. George, R. Kobler and V. Vrankovic, "A New High-Intensity, Low-Momentum Muon Beam for the

Generation of Low-Energy Muons at PSI," *Hyperfine Interactions,* vol. 159, pp. 385-388, 2004.

[280] T. Prokscha, E. Morenzoni, K. F. F. Deiters, D. George, R. Kobler, A. Suter and Vrankovic, "The new mE4 beam at PSI: A hybrid-type large acceptance channel for the generation of a high intensity surface-muon beam," *Nuclear Instruments and Methods in Physics Research A,* vol. 595, pp. 317-331, 2008.

[281] F. Foroughi, E. Morenzoni, T. Prokscha, M. Daum, K. Deiters, D. George, D. Herlach, C. Peritjean, D. Renker and V. Vrankovic, "Upgrading the PSI Muons Facility," *Hyperinfe Interactions,* vol. 138, pp. 483-488, 2001.

[282] P. Bakule and E. Morenzoni, "Generation and applications of slow polarized muons," *Contemporary Physics,* vol. 45, no. 3, pp. 203-225, 2004.

[283] K. Khaw, A. Antognini, P. Crivelli, K. Kirch, E. Morenzoni, Z. Salman, A. Suter and T. Prokscha, "Geant4 simulation of the PSI LEM beam line: energy loss and muonium formation in thin foils and the impact of unmoderated muons on the µSR spectrometer," *Journal of Instrumentation,* vol. 10, 2015.

[284] Z. Salman, A. Suter and T. Prokscha, "LEM Operation Instructions," Paul Scherrer Institute, 2020.

[285] W. Eckstein and J. Biersack, "Sputtering investigations with the Monte Carlo program TRIM SP," *Nuclear Instruments and Methods in Physics Research Section B: Beam Interactions with Materials and Atoms,* vol. 2, no. 1-3, pp. 550-554, 1984.

[286] J. Zeigler, M. Ziegler and J. Biersack, "SRIM - The stopping and range of ions in matter (2010)," *Nuclear Instruments and Methords in Physics Research B,* vol. 268, pp. 1818-1823, 2020.

[287] J. Zeigler, J. Biersack and M. and Zeigler, SRIM - The Stopping and Range of Ions in Matter, Ion Implantation Press, 2008.

[288] J. Biersack and L. Haggmark, "A Monte Carlo computer program for the transport of energetic ions in amorphous targets," *Nuclear Instruments and Methods,* vol. 174, no. 1-2, pp. 257-269, 1980.

[289] Biersack, J.P and W. Eckstein, "Sputtering studies with the Monte Carlo Program TRIM.SP," *Applied Physics A,* vol. 34, pp. 73-94, 1984.

[290] W. Eckstein, "Calculated sputtering, reflection and range values," IPP-Report, 2002.

[291] T. Prokscha, K.-H. Chow, Z. Salman, E. Stilp and A. Suter, "Direct Observation of Hole Carrier-Density Profiles and Their Light-Induced Manipulation at the Surface of Ge," *Physical Review Applied,* vol. 14, no. 01, p. 014098, 2020.

[292] E. Stilp, A. Suter, T. Prokscha, Z. Salman, E. Morenzoni, H. Keller *et al.* "Controlling the near-surface superfluid density in underdoped YBa2Cu3O6+x by photo-illumination," *Scientific Reports,* vol. 4, p. 6250, 2014.

[293] N. Hermandez, Z. Salman, T. Prokscha, A. Suter, J. Mardegan, S. Moser, A. Zakharova, C. Piamonteze and U. Staub, "Magnetic order of tetragonal CuO ultrathin films," *Physical Review B,* vol. 103, no. 22, p. 224429, 2021.

[294] A. Karki, Y. Xiong, I. Vekhter, D. Browne, P. Adams, D. Young, K. Thomas, J. Chan, H. Kim and R. Prozorov, "Structure and physical properties of the noncentrosymmetric superconductor Mo3Al2C," *Physical Review B,* vol. 82, no. 6, 2010.

[295] E. Riodan, J. Blomgren, C. Jonasson, F. Ahrentorp, C. Johansson, D. Margineda, A. Elfassi, S. Michel, F. Dell'ova, G. Klemencic and S. Giblin, "Design and implentation of a low temperature, inductance based high frequency alternating current susceptometer," *Review of Scientific Instruments,* vol. 90, 2019.

[296] E. Dahlberg, M. Hardiman, R. Orbach and J. Souletie, "High-Frequency ax Susceptibility and ESR of a Spin-Glass," *Physical Review Letters,* vol. 42, no. 6, p. 401, 1979.

[297] D. Billington, C. Paulsen, E. Lhotel, J. Cannon, E. Riordan, M. Salman, G. Klemencic, C. Cafolla-Ward, D. Prabhakaran, S. Giblin and S. Bramwell, "Experimental measurement of the isolated magnetic susceptibility," *Physical Review B,* vol. 104, no. 1, p. 014418, 2021.

[298] G. Ghigo, M. Fracasso, R. Gerbaldo, L. Gozzelino, F. Laviano, A. Napolitano *et al.* "High-frequency AC susceptibility of Iron-based supercondutors," *Materials,* vol. 29, no. 15, 2022.

[299] M. Qin and X. Yao, "ac susceptibility of high temperature superconductors," *Physical Review B,* vol. 54, no. 10, p. 7536, 1996.

[300] C. Topping and S. Blundell, "A.C. susceptibility as a probe of low-frequency magnetic dynamics," *Journal of Physics: Condensed Matter,* vol. 31, no. 01, 2019.

[301] V. Novotny and P. Meincke, "Single superconducting energy gap in pure niobium," *Journal of Low Temperature Physics,* vol. 18, pp. 147-157, 1975.

[302] D. Bonnet, S. Erlenkamper, H. Germer and H. Rabenhorst, "A new measurement of the energy gap in superconducting niobium," *Physics Letters A,* vol. 25, no. 6, pp. 452-453, 1967.

[303] B. Maxfield and W. McLean, "Superconducting Penetration Depth of Niobium," *Physical Review,* vol. 139, no. 5A, 1965.

[304] Z. Salman, *Internal communication,* 2021.

[305] P. Townsend and J. Sutton, "Investigation by Electron Tunneling of the Superconducting Energy Gaps in Nb, Ta, Sn, and Pb," *Physical Review Journals,* vol. 128, p. 591, 1962.

[306] I. Bihuega, A. Garcia-Garcia, P. Ribeiro, M. Ugeda, C. Michaelis, S. Bose and K. Kern, "Experimental observation of thermal fluctuations in single superconducting Pb nanoparticles through tunneling measurements," *Physical Review B,* vol. 84, no. 10, p. 4525, 2011.

[307] D. Rugar and P. Hansma, "Atomic Force Microscopy," *Physics today,* vol. 43, no. 10, pp. 23-30, 1990.

[308] F. Giessibl, "Advance in atomic force microscopy," *Reviews of modern physics,* vol. 73, no. 5, p. 949, 2003.

[309] R. Erlandsson, G. McClelland, C. Mate and S. Chiang, "Atomic force microscopy using optical interferometry," *Journal of Vacuum Science and Technology A,* vol. 6, pp. 266-270, 1988.

[310] G. Meyer and N. Amer, "Erratum: Novel optical approach to atomic force microscopy," *Applied Physics Letters,* vol. 53, no. 24, p. 2400, 1988.

[311] C. Ruppe and A. Duparre, "Roughness analysis of optical films and susbtractes by atomic force microscopy," *Thin Solid Films,* vol. 288, no. 1-2, pp. 8-13, 1996.

[312] K. Goldammer, W. Liu, G. Khodaparast, S. Lindstrom, M. Johnson, R. Doezema and M. Santos, "Electrical properties of InSb quantum wells remotely doped with Si," *Journal of Vacuum Science and Technology B: Microelectronics and Nanometer ~Structures Processing, Measurement and Phenomena,* vol. 16, pp. 1367-1371, 1998.

[313] W. Pearson and I. Templeton, "Superconducting Transition of Lead," *Physical Review Journals,* vol. 109, no. 1094, 1958.

[314] G. Snider, "Gregory Snider," [Online]. Available: https://www3.nd.edu/~gsnider/.

[315] T. Jackson, T. Riseman, E. Forgan, H. Gluckler, T. Prokscha, F. Morenzoni, M. Pleines, C. Niedermayer, G. Schatz, H. Luetkens and J. Litterst, "Depth-Resolved Profile of the Magnetic Field beneath the Surface of a Superconductor with a Few nm Resolution," *Physical Review Letters,* vol. 84, no. 21, pp. 4958-4961, 2000.

[316] M. Plienes, M. Birke, E. Forgan *et al.* "TEMPERATURE DEPENDENCE OF THE MAGNETIC PENETRATION DEPTH IN AN YBa2Cu3Or7-a FILM," *PSI Scientific Report,* vol. 1, p. 93, 1999.

[317] R. Gasparovic and W. McLean, "Superconducting Penetration Depth of Lead," *Physical Review B,* vol. 2, no. 2519, 1970.

[318] J. Lock and W. Bragg, "Penetration of magnetic fields into superconductors III. Measurements on thin films of tin, lead and indium," *Proceedings of the Royal Society A,* vol. 208, no. 1094, 1951.